



**HAL**  
open science

## Virtual histopathology of Alzheimer's disease

Matthieu Chourrout

► **To cite this version:**

Matthieu Chourrout. Virtual histopathology of Alzheimer's disease. Image Processing [eess.IV]. Université Claude Bernard - Lyon I, 2023. English. NNT : 2023LYO10192 . tel-04617110

**HAL Id: tel-04617110**

**<https://theses.hal.science/tel-04617110>**

Submitted on 19 Jun 2024

**HAL** is a multi-disciplinary open access archive for the deposit and dissemination of scientific research documents, whether they are published or not. The documents may come from teaching and research institutions in France or abroad, or from public or private research centers.

L'archive ouverte pluridisciplinaire **HAL**, est destinée au dépôt et à la diffusion de documents scientifiques de niveau recherche, publiés ou non, émanant des établissements d'enseignement et de recherche français ou étrangers, des laboratoires publics ou privés.



# THESE de DOCTORAT DE L'UNIVERSITE CLAUDE BERNARD LYON 1

**Ecole Doctorale N°205  
Interdisciplinaire Sciences Santé**

**Discipline** : Ingénierie pour le vivant

Soutenue publiquement le 11/10/2023, par :  
**Matthieu CHOURROUT**

---

## Histopathologie virtuelle de la maladie d'Alzheimer

---

Devant le jury composé de :

|   |                        |
|---|------------------------|
| Pr David MEYRONET<br><i>Professeur des universités, praticien hospitalier, Université Claude Bernard Lyon 1</i> | Président              |
| Dr Anne BONNIN<br><i>Chercheure, Paul Scherrer Institut</i>   | Rapporteure            |
| Dr Asunción CARMONA<br><i>Chargée de recherche, CNRS Bordeaux</i>   | Rapporteure            |
| Pr Sam BAYAT<br><i>Professeur des universités, praticien hospitalier, Université Grenoble Alpes</i>             | Examineur              |
| Pr David ROUSSEAU<br><i>Professeur des universités, Université d'Angers</i>                                     | Examineur              |
| Dr Marlène WIART<br><i>Directrice de recherche, CNRS Lyon</i>   | Examinatrice           |
| Dr Fabien CHAUVEAU<br><i>Chargé de recherche, CNRS Lyon</i>   | Directeur de thèse     |
| Dr Isabelle QUADRIO<br><i>Praticienne hospitalière, Hospices Civils de Lyon</i>                                 | Co-directrice de thèse |
| Dr Emmanuel BRUN<br><i>Chargé de recherche, Inserm Grenoble</i>   | Invité                 |



## Résumé de la thèse

La maladie d'Alzheimer est la maladie neurodégénérative la plus fréquente chez les personnes âgées. Dans sa progression, 2 protéines anormales s'agrègent : l'amyloïde- $\beta$  en plaques amyloïdes, et la protéine tau phosphorylée en dégénérescences neurofibrillaires. Deux hypothèses décrivent la progression de la maladie : la cascade amyloïde et la dérégulation des métaux. Son diagnostic est difficile ; des techniques in vivo existent mais la confirmation se fait au décès du patient, à partir de lames de microscope : c'est l'histologie. Dans cette thèse, les échantillons de cerveau sont imagés en 3D et étudiés numériquement : c'est l'histologie virtuelle. Pour cela, nous utilisons la tomographie par contraste de phase des rayons X. Après l'introduction à la maladie d'Alzheimer et à la tomographie X, quatre études sont rapportées. La première étude s'intéresse aux faisceaux de matière blanche. Nous avons démontré que leur signal dans nos images provient de la myéline, et étudié les lésions dans 3 modèles pathologiques. Dans la deuxième étude, nous avons mesuré en 3D les plaques amyloïdes dans des souris transgéniques grâce à des outils libres. La troisième étude nous a appris que nous voyons les plaques grâce aux métaux qu'elles accumulent. Dans la dernière étude (en cours), nous avons constitué une cohorte de patients atteints d'angiopathie cérébrale amyloïde : l'amyloïde se retrouve dans les vaisseaux sanguins, que nous étudions par histologie virtuelle.

Sur l'ensemble de ces travaux, nous avons montré le potentiel (pré-)clinique de la tomographie à contraste de phase des rayons X dans l'étude de la maladie d'Alzheimer. Nous avons développé des outils spécifiques au traitement de ces données, qui pourront servir à la communauté.

## Mots-clés

maladies neurodégénératives ; imagerie par rayons X ; traitement d'images ; histologie

## Title of the thesis

Virtual histopathology of Alzheimer's disease

## Abstract of the thesis

Alzheimer's disease is the most frequent dementia among the elderly, as it affects more than 30 million people worldwide. Its pathological pathway involves the aggregation of two abnormal proteins: amyloid- $\beta$  into amyloid- $\beta$  plaques and phosphorylated tau into neurofibrillary tangles. Two hypotheses describe Alzheimer's pathology: the amyloid cascade and the metal dysregulation. Its diagnosis is difficult; a few *in vivo* techniques but it is only confirmed at death, upon the analysis of microscope slides: this is histology.

In this thesis, the brain samples were not sliced; instead, they were imaged in 3D and studied digitally: this is virtual histology. To do so, we used x-ray phase-contrast tomography. Following an introduction to Alzheimer's Disease and x-ray phase-contrast tomography, four studies from the thesis are reported in the manuscript. The first study focused on white-matter-tracts. We proved that their signal in our images comes from myelin, and we studied lesions from 3 pathological models. In the second study, we performed 3D measurements on amyloid- $\beta$  plaques in the brains of transgenic mice with free open-source software. The third study revealed that the amyloid- $\beta$  plaques are detected in our images because of the metals they entrap. In the (ongoing) fourth study, we built a cohort of patients with cerebral amyloid angiopathy: amyloid deposits are found in the blood vessels, that we could study by virtual histology.

Through this work, we highlighted the contribution of x-ray phase-contrast tomography to the (pre-)clinical study of Alzheimer's disease. We also developed specific tools and processing pipeline for the analysis of these data.

## Keywords

dementia; x-ray imaging; image processing; histology

---

## Laboratoire / Laboratory

Centre de Recherche en Neurosciences de Lyon — INSERM U1028 – CNRS UMR 5292 – Université Claude Bernard Lyon 1 – Université Jean Monnet; 95, boulevard Pinel, 69675 Bron Cedex; <https://www.crnl.fr>

L'équipe BIORAN (biomarqueurs radiopharmaceutiques et neurochimiques) est hébergée au Cermep :

Cermep – Imagerie du vivant, 59, boulevard Pinel, 69677 Bron Cedex; <https://cermep.fr/>

# Résumé substantiel de la thèse

La maladie d'Alzheimer est la maladie neurodégénérative la plus fréquente chez les personnes âgées, puisqu'elle touche plus de 30 millions de personnes dans le monde. Ses symptômes comprennent la perte de mémoire et la confusion. Dans la plupart des cas, elle apparaît sporadiquement vers 65 ans ; toutefois, 5 % des cas sont héréditaires.

La maladie progresse avec le développement et l'agrégation de deux protéines anormales : l'amyloïde- $\beta$  et la protéine tau phosphorylée. L'amyloïde- $\beta$  s'agrège en plaques amyloïdes situées autour des neurones ; la protéine tau phosphorylée s'agrège en dégénérescences neurofibrillaires situées dans les neurones. Les plaques amyloïdes apparaissent avant les neurofibrilles et ces agrégats interagissent — deux hypothèses décrivent ces interactions : la cascade amyloïde et la perturbation de l'homéostasie des métaux.

De nombreux types de maladies neurogénératives présentent des symptômes confondants avec ceux de la maladie d'Alzheimer, qui se développe souvent avec des pathologies associées telles que les synucléinopathies, les maladies frontotemporales et les maladies cérébrovasculaires. Cela rend le diagnostic difficile et réduit les chances de succès de la thérapie. Des techniques ont été mises au point pour détecter l'amyloïde- $\beta$  et la protéine tau phosphorylée par imagerie médicale *in vivo* et à partir d'échantillons de liquides biologiques. Toutefois, le diagnostic n'est confirmé qu'au décès, lors de l'autopsie, lorsque le neuropathologiste atteste par microscopie la présence des lésions caractéristiques : c'est l'histologie.

Ce travail de thèse avait pour objectif général de démontrer la valeur ajoutée de l'histologie virtuelle, une méthode d'analyse 3D post-mortem du cerveau, pour l'étude de la maladie d'Alzheimer au plan fondamental (sur modèles animaux) et clinique (sur patients autopsiés). Les échantillons de cerveau ne sont pas examinés sous la forme de coupes déposés sur lames de microscopie, mais imagés en 3D à haute résolution et étudiés numériquement. L'anatomie du cerveau est préservée, de même que la structure 3D des objets pathologiques tels que les plaques amyloïdes. La thèse se concentre sur une technique d'imagerie appelée tomographie par contraste de phase des rayons X, disponible majoritairement dans les installations de rayonnement synchrotron — d'imposants équipements de recherche qui produisent des rayons X à l'aide d'un accélérateur de particules. Plus sensible que les tomodensitomètres classiques, la tomographie par contraste de phase des rayons X détecte les changements locaux et légers dans les tissus mous : elle peut révéler les plaques amyloïdes dans les images 3D du cerveau sans aucun agent de contraste. Quatre études de la thèse sont rapportées dans le manuscrit ; deux d'entre elles ont été publiées, une est en ligne en tant que préprint et vient d'être publiée, la quatrième est à un stade précoce avec des résultats préliminaires.

Pour la première étude de cette thèse, nous avons utilisé la tomographie par contraste de phase des rayons X pour évaluer les lésions de la matière blanche — des structures cérébrales qui assurent le flux d'informations dans le réseau neuronal. Les cerveaux

de modèles animaux présentant trois pathologies différentes ont été scannés : accident vasculaire cérébral ischémique, sclérose en plaques et hypoxie néonatale. Nous avons conçu une analyse d'image originale des faisceaux de matière blanche et des lésions associées. Avec un partenaire privé, nous avons développé un logiciel permettant de récupérer des données analogues à celles de l'imagerie du tenseur de diffusion, la méthode de référence pour l'étude des lésions de la matière blanche. Nous avons également mis en évidence que la tomographie par contraste de phase des rayons X détecte spécifiquement la myéline (un mélange lipidique qui protège les neurones). À cet égard, nous avons optimisé la préparation de l'échantillon pour augmenter le signal de la matière blanche.

La deuxième étude a porté sur les plaques amyloïdes dans le cerveau de souris transgéniques modèles de la maladie d'Alzheimer. Les cerveaux de trois souches différentes ont été acquis et scannés par tomographie à contraste de phase des rayons X après une simple préparation sans marquage. Nous avons conçu et rendu public un procédé de segmentation d'images avec un logiciel libre. Les plaques amyloïdes ont été segmentées à l'aide de ce procédé et des mesures 3D jusqu'alors inaccessibles via l'immunohistochimie ont été effectuées sur les plaques marquées. Nous avons dévoilé des distributions spécifiques à chaque souche transgénique de la morphologie et de l'intensité du signal des plaques.

La troisième étude a été conçue pour comprendre le signal spécifique des plaques amyloïdes dans nos images sans marquage de la tomographie à contraste de phase des rayons X. Nous avons testé deux hypothèses : le signal provenait-il des métaux endogènes piégés dans les plaques ou des fibrilles amyloïdes insolubles des plaques ? Nous avons acquis et scanné des échantillons de cerveau de deux patients humains atteints de la maladie d'Alzheimer, ainsi que des cerveaux de quatre modèles de rongeurs différents (souris et rats). Parallèlement, nous avons traité des échantillons de cerveau provenant des mêmes patients et animaux afin d'analyser la composition métallique et moléculaire des plaques amyloïdes à l'aide de deux techniques spécifiques (la microscopie à fluorescence à rayons X pour les métaux et la spectroscopie infrarouge à transformée de Fourier pour les fibrilles). Grâce à la tomographie à contraste de phase des rayons X, nous avons pu détecter des plaques amyloïdes chez l'un des deux patients, un cas familial rare de maladie d'Alzheimer ; les plaques amyloïdes de deux des quatre souches de rongeurs présentaient un signal jamais décrit par notre modalité d'imagerie. Nous avons constaté que les niveaux élevés de métaux étaient en corrélation avec les différents signaux des plaques amyloïdes.

Pour la quatrième étude, nous avons constitué une cohorte de patients atteints d'angiopathie amyloïde cérébrale, où des dépôts d'amyloïde- $\beta$  sont présents dans les parois des vaisseaux sanguins. Nous avons scanné des échantillons de cerveau de 11 patients humains à l'aide de la tomographie à contraste de phase à rayons X. L'analyse des images 3D est en cours. Nous pouvons déjà détecter l'angiopathie amyloïde cérébrale dans nos images, grâce à des signes communs à diverses maladies cérébrovasculaires. Les résultats préliminaires sont présentés et discutés. La prochaine étape, l'analyse des parois des vaisseaux sanguins, pourrait permettre de détecter directement les dépôts d'amyloïde- $\beta$ .

Sur l'ensemble de ces travaux, nous avons montré le potentiel clinique et pré-clinique de la tomographie à contraste de phase des rayons X dans l'étude de la maladie d'Alzheimer.

Nous avons notamment développé des outils spécifiques au traitement de ces données, qui pourront servir à la communauté.



# Remerciements / Acknowledgments

Je tiens à remercier un grand nombre de personnes qui m'ont suivi de près (ou de loin) pendant ces trois années et parfois depuis plus longtemps.

Pour commencer cette liste, un grand merci à mon directeur et à ma directrice de thèse : **Fabien** et **Isabelle**, j'ai beaucoup apprécié travailler sous votre direction et à vos côtés.

**Fabien**, ton tempérament calme et amical, accessible pour tes étudiants et tes autres collègues, fait oublier les statuts hiérarchiques et rend nos échanges dynamiques et agréables (et en plus ça déstresse!). **Isabelle**, ta bienveillance et ta rigueur sur les aspects cliniques m'auront aussi beaucoup apporté.

Merci, **Anne Bonnin** et **Asuncion Carmona**, pour votre relecture minutieuse et bienveillante en votre rôle de rapporteuses sur ce manuscrit, ainsi qu'aux autres membres du jury pour les échanges stimulants lors de la soutenance.

**Marlène** et **Emmanuel** : tout comme Fabien, vous m'avez encadré pendant 4 ans, en me proposant de travailler sur cette mine de données synchrotron qui dort dans un placard du B13. C'est parce que j'ai pris également du plaisir à vous côtoyer et à travailler avec vous que je me suis lancé dans cette aventure! Vous trois êtes une super équipe et j'ai hâte de voir où nos projets communs nous mèneront!

**Gabriel**, avec qui j'ai pu collaborer, tu as aussi continué de t'impliquer dans ma thèse en participant à mes comités de suivi de thèse (CSI pour les intimes) : merci!

Merci, **David Meyronet**, pour nos sessions de travail et de discussions, et pour le temps précieux que tu as pu consacrer à ce projet. Nos sessions nocturnes d'acquisition au synchrotron et nos heures de segmentation ne sont pas vaines, on met du *manpower* dessus! Merci également aux collaborateurs-trices des HCL, en particulier **Corinne Perrin** et **Dominique Bourchany** du Centre de Ressources Biologiques.

Les synchrotrons, ces bijoux de technologie, ne tourneraient pas sans les superbes équipes de leurs lignes de lumière. Ainsi, merci à **Christophe Sandt**, **Timm Weitkamp**, **Jonathan Perrin** du Synchrotron SOLEIL et à **Sylvain Bohic** de l'ESRF (et de STROBE), pour vos conseils dans les phases de planification, d'acquisition et d'analyse de ces données riches.

Merci à mes deux « tuteurs pédagogiques », **Yvan Duroc** et **Fabien Millioz**, pour cette opportunité de donner des cours via l'ACE à l'ISTR et Polytech Lyon et l'accompagnement sur ces trois années.

Merci à mes collègues de l'équipe BIORAN et du Cermep : **Luc**, **Sandrine**, **Élise**, **Sophie**, **Wael**, **Radu**, **Danielle**, **Nicolas**, **Inès**, **Marco** et **Benjamin** (« chef » du bureau Theranexus et bassiste d'un groupe de rock!). Et bien sûr, mes « ami-es du travail » : **Louis**, **Pierre**, **Sarah**, **Violette**, **Louise**, **Mickaël**, **Joshua**, **Fatima** et **Léa** (la représentante de la future génération de doctorant-es BIORAN). Et merci à mon voisin de bureau, **Louis** (oui, oui, tu y es deux fois!), pour nos discussions complices et tout à fait productives!

Merci **Clément** (que j'ai suivi de Buc à Lyon/Grenoble), **Laurène** (car on peut parler de Fourier de façon décomplexée), **Shifali** et **Clara** de l'équipe STROBE. Petite pensée pour « *X ray help* » à Thessalonique puis pour les rattrapages en physique via WhatsApp.

Pour se détendre après une grosse journée, rien de mieux qu'un... NeuroApéro! Merci pour ces beaux moments à parler de galères de manips autour d'une bière (je caricature un peu...), notamment la team NeuroApéro, en particulier **Inès**, **Anna**, **Laëtitia** et **Blandine**, et les (autres) piliers d'apéro **Ondine** et **Siloé**.

Je passe maintenant à mes proches et à mes amis (hors ceux du travail, j'entends). Merci **Maman** pour ton soutien sans faille et merci **Papa** de m'avoir poussé dans cette voie. Merci **Camille**, la meilleure des *sis'*, pour notre complicité que la distance n'ébranle jamais.

Merci à mes meilleur-es ami-es (que j'appelle « les Albigeois-es ») : **Aksel**, **Marie-France**, **Maxime** (coucou Docteur!), **Marie**, **Louis**, **Alexia**, **Elouan**, **Floriane**, **Iannis**, **Cyril**, **Jean-François**, **Aurélie**, **Aïny**, **Maguelone**. Cette thèse, je vous la dédie!

Merci aux **Phonies Polies**, des co-choristes et des ami-es : **Apolline**, **Cécile**, **Romain B.**, **Romain L.**, **Delphine** (grâce à qui je vous ai connu-es!!), **Blaise**, **Hortense**, **Lucas**, **Claire V.**, **Claire D.**, et tous-tes les autres. Rien de mieux qu'une virée au vert de temps en temps et des quintes justes pour rythmer les semaines (en chantant *doum doum la la*)! Et merci à **Maude** d'avoir créé cette jolie bulle. Ça fait redite mais merci les colocs **Delphine** et **Blaise**!

Et je termine avec les amis de l'école. Merci à vous aussi! Notamment ceux qui ont ouvert la voie : **Raphaël**, **Léo** et **Léonce**. Et le CFC : **Hicham**, **Yohann**, **Mahmoud**, **André**, **Cyril**, **Jamal**, **Quentin**, **Antoine**.

# Contents

|  |           |
|--|-----------|
| Résumé substantiel de la thèse en français                       | v         |
| Remerciements / Acknowledgments                                  | ix        |
| Contents   | xi        |
| <b>BACKGROUND</b>  | <b>1</b>  |
| Contexte de la thèse / Context of the thesis                     | 3         |
| <b>1. Alzheimer's disease</b>                                    | <b>5</b>  |
| 1.1. Pathology . . . . .   | 5         |
| 1.1.1. Symptoms and evolution . . . . .                          | 5         |
| 1.1.2. Forms and prevalence . . . . .                            | 7         |
| 1.1.3. Comorbid neuropathologies . . . . .                       | 9         |
| 1.2. Mechanisms . . . . .  | 11        |
| 1.2.1. Amyloid cascade . . . . .                                 | 11        |
| 1.2.2. Metal dysregulation . . . . .                             | 15        |
| 1.3. Diagnosis . . . . .   | 17        |
| 1.3.1. Cognitive tests . . . . .                                 | 18        |
| 1.3.2. <i>In vivo</i> techniques . . . . .                       | 20        |
| 1.3.3. <i>Postmortem</i> diagnosis of certainty . . . . .        | 23        |
| 1.4. Recent developments in A $\beta$ imaging . . . . .          | 29        |
| 1.4.1. Research models for AD . . . . .                          | 29        |
| 1.4.2. <i>In vivo</i> imaging . . . . .                          | 31        |
| 1.4.3. <i>Postmortem</i> imaging of individual plaques . . . . . | 32        |
| <b>2. X-ray phase-contrast tomography (XPCT)</b>                 | <b>35</b> |
| 2.1. Physics . . . . .   | 35        |
| 2.1.1. Synchrotron radiation . . . . .                           | 35        |
| 2.1.2. X-ray interaction with matter . . . . .                   | 40        |
| 2.2. Reconstruction . . . . .                                    | 44        |
| 2.3. Phase retrieval . . . . .                                   | 46        |
| 2.4. Current biomedical applications . . . . .                   | 48        |
| 2.4.1. Benefits of the technique . . . . .                       | 48        |
| 2.4.2. Applications on soft-tissue imaging . . . . .             | 49        |
| 2.4.3. Other applications . . . . .                              | 51        |

|  |            |
|--|------------|
| 2.5. Other synchrotron-based techniques . . . . .                                  | 51         |
| 2.5.1. X-ray fluorescence (XRF) . . . . .  | 52         |
| 2.5.2. Fourier-transform infrared spectroscopy (FTIR) . . . . .                    | 53         |
| <br>   |            |
| <b>PHD PROJECT</b>   | <b>55</b>  |
| <br>   |            |
| <b>3. Browsing brain structures with XPCT</b>                                      | <b>57</b>  |
| 3.1. Introduction . . . . .  | 57         |
| 3.2. Associated published work . . . . .   | 58         |
| 3.3. Discussion . . . . .  | 85         |
| <br>   |            |
| <b>4. Morphological study of amyloid-<math>\beta</math> plaques with XPCT</b>      | <b>89</b>  |
| 4.1. Introduction . . . . .  | 89         |
| 4.2. Associated published work . . . . .   | 89         |
| 4.3. Discussion . . . . .  | 108        |
| <br>   |            |
| <b>5. The origin of the contrast of amyloid-<math>\beta</math> plaques in XPCT</b> | <b>111</b> |
| 5.1. Introduction . . . . .  | 111        |
| 5.2. Associated published work . . . . .   | 112        |
| 5.3. Discussion . . . . .  | 149        |
| <br>   |            |
| <b>6. Cohort study of human cerebral amyloid angiopathy (CAA) with XPCT</b>        | <b>153</b> |
| 6.1. Introduction . . . . .  | 153        |
| 6.2. Material & Methods . . . . .  | 154        |
| 6.2.1. Cohort selection . . . . .  | 154        |
| 6.2.2. Immunohistochemistry . . . . .  | 154        |
| 6.2.3. Sample preparation . . . . .  | 156        |
| 6.2.4. X-ray phase-contrast tomography . . . . .                                   | 156        |
| 6.2.5. XPCT image analysis . . . . .   | 158        |
| 6.3. Preliminary results . . . . .   | 159        |
| 6.3.1. CAA hallmark detection . . . . .  | 159        |
| 6.3.2. Watershed-based segmentation . . . . .                                      | 160        |
| 6.3.3. Machine learning segmentation . . . . .                                     | 161        |
| 6.4. Discussion . . . . .  | 161        |
| <br>   |            |
| <b>SYNTHESIS</b>   | <b>165</b> |
| <br>   |            |
| <b>7. Discussion</b>   | <b>167</b> |
| 7.1. Multi-scale imaging . . . . .   | 167        |
| 7.2. Multi-modal imaging . . . . .   | 167        |
| 7.3. Standardization . . . . .   | 168        |

|  |            |
|--|------------|
| <b>8. Conclusion &amp; perspectives</b>      | <b>169</b> |
| 8.1. Methodological contributions . . . . .  | 169        |
| 8.1.1. Sample preparation . . . . .          | 169        |
| 8.1.2. Software development . . . . .        | 169        |
| 8.1.3. Data analysis . . . . .               | 170        |
| 8.2. Results provided by this work . . . . . | 170        |
| 8.3. Limitations of the studies . . . . .    | 171        |
| <br>   |            |
| <b>APPENDIX</b>                              | <b>173</b> |
| <br>   |            |
| <b>A. List of publications</b>               | <b>175</b> |
| <b>B. List of oral communications</b>        | <b>177</b> |
| <b>C. Curriculum vitae</b>                   | <b>179</b> |
| <br>   |            |
| <b>Bibliography</b>                          | <b>181</b> |
| <br>   |            |
| <b>List of Terms and Acronyms</b>            | <b>227</b> |



# List of Figures

|      |   |    |
|------|---|----|
| 1.1. | Amyloid- $\beta$ plaques and neurofibrillary tangles in the brain. Amyloid- $\beta$ plaques develop in the extracellular space and NFTs develop within the neurons. . . .   | 6  |
| 1.2. | Alzheimer's related pathophysiology converges to neurodegeneration through multiple cellular pathways. Pathognomonic changes of AD (in gray squares) are considered to consist only of amyloid and tau pathologies. The pathological changes considered unspecific to AD are represented in yellow boxes. Risk and protective factors, specified as aging, genetics, lifestyle and environmental are represented in blue circles (cf. subsection 1.1.2). Disease-modifying drugs target one or several mechanisms to block, these are represented with red flat-head arrows. APOE: apolipoprotein E; BBB: blood-brain barrier; PART: primary-age-related tauopathy; TREM2: triggering receptor expressed on myeloid cells 2. Adapted from [10]. . . . . | 7  |
| 1.3. | Schematic representation of the brain perivascular Virchow-Robin space and surrounding tissues at the surface of the brain cortex ( $\sim 5$ mm-depth). The brain is enveloped by three protective layers called meninges; cerebrospinal fluid (CSF) circulates between the arachnoid mater and the pia mater meninges. The cortical perivascular space of penetrating arteries (bounded by the adventitia of the vessel and the astrocyte end-feet) is filled with CSF from the subarachnoid space. Metabolic waste such as $A\beta$ is thought to accumulate around the blood vessel, possibly resulting in perivascular blockage and enlargement of the space, as shown on the right vessel. Adapted from [35]. . . . .                              | 11 |
| 1.4. | Cleavage of the APP protein into amyloid- $\beta$ peptides. (A) Whole domain architecture of the neuronal splice variant APP695. Dashed lines represent unknown domain structures. When APP is at its transmembrane location (gray), tethered by its transmembrane domain (TMD), its N-terminus (left) is outside the cell and its C-terminus (right) is in the cytoplasm. (B) Amino acid sequences of juxtamembrane, TMD and AICD domains. Vertical arrows point precise cleavage sites of $\alpha$ , $\beta$ , $\gamma$ and $\epsilon$ secretases. The different breakdown products are labelled. Adapted from [45]. . . . .  | 12 |
| 1.5. | Folding and stepwise aggregation of $A\beta_{1-42}$ peptides. Amino acid sequences are detailed for the monomers. The dashed rectangles show the $\beta$ -folding pattern. Adapted from [50]. . . . .   | 13 |
| 1.6. | The formation of NFTs. (1) Healthy neuron, in which normal tau proteins stabilize the microtubules. (2) Pre-tangle state by phosphorylation of tau monomers that change into $\beta$ sheets. (3) Aggregation and nucleation of oligomers inside the neuron. (4) Neuron death leaving flame-shaped "ghost tangles". Adapted from [70, 72]. . . . .   | 14 |

|   |    |
|---|----|
| 1.7. Copper and zinc in the physiological brain. Cu interacts with actin filaments (F-actin) for the synapse formation and Zn contributes to the stability of the post-synaptic density (yellow area) through interaction with the SHANK3 proteins. Zn also acts as a neurotransmitter [86]. Adapted from [87]. . . . .   | 16 |
| 1.8. Chronology of the AD biomarkers. The threshold for biomarker detection of pathophysiological changes is denoted by the black horizontal line. The grey area denotes the zone in which abnormal pathophysiological changes lie below the biomarker detection threshold. In this figure, tau pathology precedes A $\beta$ deposition in time, but only early on at a subthreshold biomarker detection level. A $\beta$ deposition then occurs independently and rises above the biomarker detection threshold (purple and red arrows). This induces acceleration of tauopathy and CSF tau then rises above the detection threshold (light blue arrow). Later still, FDG PET and MRI (dark blue arrow) rise above the detection threshold. Finally, cognitive impairment becomes evident (green arrow), with a range of cognitive responses that depend on the individual's risk profile (light green-filled area). These pathophysiological changes can span over decades. CSF=cerebrospinal fluid. FDG=fluorodeoxyglucose. MCI=mild cognitive impairment. MRI=magnetic resonance imaging. PET=positron emission tomography. From [5]. . . . . | 18 |
| 1.9. Clock-Drawing Test results from 4 subjects at risk for dementia of Alzheimer type. From left to right: Conceptual error (the hands are not placed correctly); Stimulus-bound error (the hands point 10 and 11); Perseverative behavior (supplementary lines are drawn and hands are drawn in multiple strokes); Planning difficulties (the clockface is small and spaces between numbers are inconsistent). Adapted from [129]. . . . .  | 19 |
| 1.10. First A $\beta$ PET imaging with [ <sup>11</sup> C]PiB along with the chemical structure of [ <sup>11</sup> C]PiB. SUV: standardized uptake value. Adapted from [144]. . . . .  | 21 |
| 1.11. Chemical structure of flortaucipir and representative uptake images in an AD patient (74 years old, MMSE 14). SUVR: SUV ratio (cerebellar cortex as reference). Adapted from [146]. . . . .   | 21 |
| 1.12. T <sub>2</sub> <sup>*</sup> -weighted MRI of a 77-year-old female patient without hypertension. Microbleeds are present only in lobar brain regions, meeting criteria for probable CAA. From [164]. . . . .   | 23 |
| 1.13. Sampling of the brain hemisphere from a vertical-frontal plane parallel to the view of Charcot [168]. 1A&1B: frontal lobe; 2: white matter in the frontal lobe; 3: lenticular nucleus; 4A: superior temporal sulcus; 4B: inferior temporal sulcus; 5: hippocampus. Courtesy of Pr D. Meyronet. . . . .  | 23 |

|  |    |
|--|----|
| 1.14. Schematic representation of the categories of hippocampal pathology seen in the aged population, as defined by Rauramaa et al. [169]. Type + corresponds to recent diffuse hypoxic/ischemic degeneration of cornu ammonis (CA) neurons. Type 1 is characterized by small focal infarcts (single or multiple). Type 2 corresponds to an extensive infarction of the CA1 sector. Type 3 has patchy diffuse neuronal degeneration in CA sectors, mainly in CA1, with some vacuolization. Type 4 accounts for a complete neuronal loss in CA1 because of neurodegeneration, most frequently associated with NFT; moderate to severe gliosis and corpora amylacea may be seen in CA sectors. Adapted from the original article. . . . . | 24 |
| 1.15. Types of A $\beta$ deposits. (A) A $\beta$ -positive cells and small plaques; (B–D) Multiple diffuse A $\beta$ plaques; (E) Senile (cored) A $\beta$ plaque. Immunohistochemistry with 6F3D clone of anti-A $\beta$ antibody, dilution 1 : 100. Adapted from [170]. . . . .  | 25 |
| 1.16. Different stainings and revealed features. (A) Bielschowsky staining with neuritic plaques (arrow) where the dark thickened neurites (arrowhead) are seen; (B) Gallyas staining with black NFTs (arrow) and neuropil threads or neurites (arrowhead); (C) Immunohistochemical (IHC) staining of A $\beta$ -labeled protein aggregates, i.e. plaques (arrow); (D) IHC of P-tau-labeled NFTs (arrow) and neuropil threads/neurites (arrowhead). Adapted from [180]. . . . .  | 25 |
| 1.17. Cartoon for semiquantitative assessment of the density of senile and neuritic plaques under a $\times 100$ magnification after histochemistry or IHC. Adapted from [181]. . . . .  | 26 |
| 1.18. Phases of $\beta$ -amyloidosis. Regions which exhibit A $\beta$ plaques are shown in black and gray shades. Arrows show the development towards new regions. Adapted from [182]. . . . .   | 27 |
| 1.19. Stages I–VI of cortical neurofibrillary pathology in 100 $\mu$ m polyethylene glycol-embedded hemisphere sections immunostained for hyperphosphorylated tau (AT-8, Innogenetics). From [184]. . . . .  | 28 |
| 1.20. Comparison of a selection of research models of AD with a timeline of observed pathophysiological changes. 3xTg, APPPS1, APP <sup>swe</sup> /PSEN1 <sup>dE9</sup> (line 85), ArcA $\beta$ and J20 are mouse models while TgF344-AD is a rat model. J20 and ArcA $\beta$ are mono-transgenic models (J20 with 2 mutations on the same gene), APPPS1, APP <sup>swe</sup> /PSEN1 <sup>dE9</sup> (line 85) and TgF344-AD are double-transgenic models and 3xTg is a triple-transgenic model with a tau co-pathology. Generated from [195]. . . . .   | 30 |
| 2.1. Evolution of the average brightness of x-ray and synchrotron-radiation sources throughout the years (left) and relationship between photon energy and brightness of a few facilities (right). From [241] (left) and [242] (right). . . . .  | 36 |
| 2.2. Schematic of a synchrotron showing the linac, booster and storage rings, and the magnetic devices that produce the synchrotron radiation. Adapted from [243]. . . . .   | 37 |

|       |  |    |
|-------|--|----|
| 2.3.  | At relativistic speed, an electron radiates a tangent beam within a cone of half-angle $\psi$ . From [239]. . . . .  | 37 |
| 2.4.  | Insertion device on the storage ring. From [246]. . . . .  | 38 |
| 2.5.  | The ANATOMIX beamline (SOLEIL, Gif-sur-Yvette, France) as an example of beamline for phase-contrast imaging. The transfocator is a set of refractive lenses which collimate the beam. The M1–M2 mirror pair acts as a secondary source. The DMM and DCM are two different monochromators. EH3 is for propagation-based XPCT and EH4 for grating-interferometer XPCT. From [250].   | 39 |
| 2.6.  | The principle of a monochromator. . . . .  | 39 |
| 2.7.  | The interaction of X rays with matter. (A) Primary, unattenuated beam does not interact with material. (B) Photoelectric absorption results in total removal of incident x-ray photon with an energy greater than the binding energy of an electron in its shell, with excess energy distributed to kinetic energy of photo-electron. (C) Rayleigh scattering is an interaction with an electron (or whole atom) in which no energy is exchanged and the incident x-ray energy equals the scattered x-ray energy with a small angular change in direction. (D) Compton scattering interactions occur with essentially unbound electrons, with transfer of energy shared between recoil electron and scattered photon, with energy exchange described by Klein–Nishina formula. From [256]. . . . . | 40 |
| 2.8.  | Cross-sections of the different interactions of X rays with matter for two elements: carbon (left) and iodine (right). p.a.: photoelectric absorption; R: Rayleigh scattering; C: Compton scattering; nucl.: nuclear pair production; elec.: electron pair production. The gray area is the summed cross-section. Note that the photoelectric absorption cross-section of iodine has discontinuities; the K-edge of carbon is at a lower energy, 282 eV [258]. 1 barn = $1 \times 10^{-24}$ cm <sup>2</sup> . Redrawn from [259]. . . . .  | 42 |
| 2.9.  | Schematics of parallel-beam x-ray tomography. From [266]. . . . .  | 44 |
| 2.10. | The projection geometry in 2D based on line integrals, with the source detector gantry $(x, y)$ rotated with respect to the Cartesian object frame $(x', y')$ by $\theta$ . From [267]. . . . .  | 44 |
| 2.11. | Visualization of the Fourier slice theorem. The 1D Fourier transform $\tilde{P}_z(\theta, k)$ of a projection $P_z(\theta, x)$ obtained as shown in (a) corresponds to a line cut in the 2D Fourier transform $\tilde{f}_z(k \cos \theta, k \sin \theta)$ of the object plane $f_z(x', y')$ , as sketched in (b). (c) The density of (discrete) data points falls off as $1/k$ , posing a challenge to sample the high spatial frequencies. Provided there is sufficient number of projections and suitable regridding, 2D fast Fourier transform (FFT) algorithms can be used to reconstruct $f_z(x', y')$ in each plane. From [267]. . . . .   | 46 |
| 2.12. | The principle of propagation-based XPCT. From Wikipedia, CC BY-SA 3.0. . .   | 46 |
| 2.13. | The principle of grating-interferometry XPCT. From Wikipedia, CC BY-SA 3.0.  | 47 |
| 2.14. | Dependence of in-line phase-contrast images on the distance between object and detector. Here, given numerical data for $D$ are only illustrative, which, in practice, will depend on the specific system setup. Adapted from [282]. . . .   | 50 |

|   |    |
|---|----|
| 2.15. Contour plot of the critical propagation distance $D_{crit} = (2\Delta)/\lambda$ to fulfill the near-field condition, for pixel sizes $\Delta$ ranging between 0.1 and 50 mm and photon energies from 5 to 120 keV. The actual sample–detector distance $D$ should be chosen well below $D_{crit}$ to fulfill the near-field condition even for the smallest features that the detector can resolve. From [287]. . . . .  | 50 |
| 2.16. Representative images of one osteoarthritis knee sample observed by each imaging technique. (A) MRI with an ultra-short echo time sequence (echo time = 0.008 13 ms; repetition time = 4.0 ms; flip angle = 5°; voxel size = 50×50×50 $\mu\text{m}^3$ ). (B) Conventional x-ray micro-tomography image (source voltage = 60 kVp; voxel size = 6.06 × 6.06 × 6.06 $\mu\text{m}^3$ ). (C) Synchrotron x-ray phase-contrast image (source energy = 52 keV; voxel size = 6.1 × 6.1 × 6.1 $\mu\text{m}^3$ ). (D,E) Phase-contrast image magnification with a soft (D) and hard (E) tissue contrast window. From [302]. . . . . | 51 |
| 2.17. The principle of XRF. The incident x-ray beam creates 2D hyperspectra which can be converted into 2D elemental maps of the sample. From [208]. . . . .  | 52 |
| 2.18. Vibrational modes of common biomolecular bonds. Inherent vibrational motion of molecules gives rise to distinct, fingerprint-like absorption bands in the mid-infrared region. Different stretching or bending vibrational bands commonly encountered in biological samples are shown. Infrared spectroscopy is sensitive to the presence of many chemical functional groups (structural fragments) in molecules, and taken together the set of vibration modes are unique for every molecular configuration. From [314]. . . . .   | 54 |
| 2.19. Infrared spectrum of a single human cell with color bands highlighting absorption peaks associated with constituent macromolecules (left) and lipid distribution within MCF-7 living cells — chemical changes can be monitored in time (right). From [314] (left) and [315] (right). . . . .  | 54 |
| 3.1. Tractography of the corpus callosum from an XPCT image in a multiple sclerosis model (LPC injection) using our pipeline and TrackVis. The corpus callosum contains long fibers (along the plain arrow); the empty region corresponds to the white-matter injury (dashed area). Unpublished results. . . . .  | 86 |
| 3.2. Dehydration kinetics of a full mouse brain immersed in 96% ethanol. (A) Snapshots of the same mouse brain imaged at different timepoints during dehydration. (B) Ratio of signal intensities between the anterior commissure and the thalamus. Unpublished results. . . . .  | 87 |

|  |     |
|--|-----|
| 6.1. Schematic representation of CAA stages in a coronary section through the human brain at the level of the basal ganglia. CAA changes are indicated in red. The first stage of CAA shows vascular A $\beta$ deposits only in a few neocortical areas and involves leptomeningeal and cortical vessels. Stage 2 is characterized by additional vascular A $\beta$ in the hippocampus, amygdala, hypothalamus, midbrain, and in the cerebellum; midbrain and cerebellum are not shown in this figure. In stage 3, CAA is also seen in vessels of the basal ganglia, the thalamus, and the basal forebrain. A $\beta$ deposition in the lower brainstem, another feature of CAA stage 3, is not depicted. Adapted from [37]. . . . . | 155 |
| 6.2. Vascular disease hallmarks found while browsing through the XPCT volume. Left: large blood vessel in the cortex surrounded by a high concentration of hemosiderin (red arrows) with a locally-enlarged perivascular space (blue arrow) in patient 13EJ00001. Right: artery in a fissure towards a sulcus presenting double barreling (green and yellow arrows) and variations in the vessel wall intensity from patient 16EH01503. Scale bars equal 100 $\mu$ m. . . . .  | 159 |
| 6.3. Immunohistochemistry with anti-A $\beta_{1-42}$ antibodies (left) and raw XPCT images (right) from the patient 16EH01503. Scale bars equal 100 $\mu$ m. . . . .   | 159 |
| 6.4. Results from watershed-based segmentation on a large vessel from patient 16EH01503. Measurements on segments with labels 1 and 2 are shown in Table 6.4. . . . .  | 160 |
| 6.5. Comparative segmentation of a slice with machine learning algorithms. Left: raw XPCT image. Middle: output with a random forest algorithm. Right: output with a U-Net. The parenchyma class is in red, the EPVS class in blue, the vessel wall class in green and the lumen class in purple. Scale bar equals 50 $\mu$ m. . .   | 161 |

## List of Tables

|  |    |
|--|----|
| 1.1. Risk of short-term cognitive decline based on the AT(N) biomarker profile and cognitive stage. A <sup>+</sup> : evidence of amyloid pathology; T <sup>+</sup> : evidence of tauopathy; (N) <sup>+</sup> : evidence of neurodegeneration or neuronal injury. From [3]. . . . . | 6  |
| 1.2. Level of AD neuropathological change. *: particular cases apply, please refer to the original article. From [26]. . . . .   | 28 |

|  |     |
|--|-----|
| 2.1. A few characteristic energies of a few elements, with their symbols and atomic numbers $Z$ . The binding energies of each shell indicate the incident energy that is required for a photoelectric absorption to occur, which in turn emits a new x-ray radiation that is detected in x-ray fluorescence. Iron, copper and zinc are extensively studied for their physiological involvement in subsection 1.2.2 and in Chapter 5; carbon and iodine cross-sections were shown in Figure 2.8; K-L <sub>2</sub> and K-L <sub>3</sub> spectral lines of argon are frequently used to normalize spectra. The IUPAC notations [312] K-L <sub>2</sub> through K-M <sub>3</sub> correspond to the former Siegbahn notations [313] K $\alpha_2$ , K $\alpha_1$ , K $\beta_3$ and K $\beta_1$ , respectively. Values were retrieved from PyMca [311]. | 53  |
| 6.1. Overview of the cohort with patient ID, age in years at death and histopathological scorings for CAA and AD. CAA scorings are: Thal–Braak stages for regional assessment [37], Vonsattel score for local severity [167] and Thal–Braak type for capillary involvement [396]. AD scorings are in the same order as for the NIA–AA "ABC" descriptors [3]: A $\beta$ Thal phases [182], CERAD score for neuritic plaques (NP) [181] and Braak stages for neurofibrillary tangles (NFT) [184]. F: female; M: male; N/A: not applicable.<br>✕: rare familial case also studied in Chapter 5;<br>†: patient without CAA nor AD, with mild tauopathy;<br>‡: patient without CAA nor AD, diagnosed with Parkinson’s disease. . . . .  | 155 |
| 6.2. Summary of the samples per patient and per region. The CAA Thal-Braak stage [37] for regional assessment is recalled here for each patient.<br>✕: rare familial case also studied in Chapter 5;<br>#: 2 paraffin-embedded frontal cortex samples from this patient were also scanned;<br>†: patient without CAA nor AD, with mild tauopathy;<br>‡: patient without CAA nor AD, diagnosed with Parkinson’s disease. . . . .  | 157 |
| 6.3. Acquisition and reconstruction parameters for XPCT . . . . .  | 157 |
| 6.4. Extracted metrics per segment of the segmented vessel from patient 16EH01503. Tortuosity is the ratio between curved length and straight length (not reported). Labels 1 and 2 refer to Figure 6.4. . . . .   | 160 |



# BACKGROUND



# Contexte de la thèse / Context of the thesis

The PhD thesis focused on Alzheimer's Disease, the most frequent dementia in the world. Although biomarkers have been identified and associated with the different evidences of the pathological mechanisms, the diagnosis of the disease is performed *postmortem* by a neuropathologist after a laborious process of sampling, slicing and staining. A formerly large set of different neuropathological scorings were pooled ten years ago into an ABC score but it still requires the analysis of microscope slides with three different stainings. Using a synchrotron technique called x-ray phase-contrast tomography, the scope of the thesis was to advance towards a contrast-agent-free 3D imaging technique for *ex vivo* extraction of 3D parameters relevant for the study of AD.

In detail, our goal was to develop tools such as image analysis pipelines, in order to provide quantitative results out of x-ray phase-contrast tomography. We obtained various samples from either rodent models of Alzheimer's Disease or deceased donor patients who were diagnosed with Alzheimer's Disease. 3D scans preserve the integrity of the samples and enable the extraction of 3D parameters that would be lost if the standard histopathology routine. Designing a labour-free sample preparation was also of interest for the clinicians; while a common approach has been to work with their usual samples — which are either frozen or paraffin-embedded —, we have shifted to a sample preparation by fixation–dehydration. We have also investigated the origin of the contrast of the amyloid-beta plaques, which are the main pathological hallmark of Alzheimer's Disease and we have built a cohort about amyloid deposits in the cerebral amyloid angiopathy.



# Alzheimer's disease

# 1.

## 1.1. Pathology

### 1.1.1. Symptoms and evolution

Alzheimer's disease (AD) is a neurodegenerative disease which appears and progresses with ageing. Signs of AD include [1]:

- ▶ Memory loss;
- ▶ Challenges in planning or solving problems;
- ▶ Difficulty completing familiar tasks;
- ▶ Confusion with time or place;
- ▶ Trouble understanding visual images and spatial relationships;
- ▶ New problems with words in speaking or writing;
- ▶ Misplacing things and losing the ability to retrace steps;
- ▶ Decreased or poor judgment;
- ▶ Withdrawal from work or social activities;
- ▶ Changes in mood, personality and behavior.

Reisberg [2] first detailed how these *clinical* signs appear by stages. Current definitions are based on *biomarkers*: Jack et al. [3] then defined multiple stages for patients presenting AD-specific biomarkers:  $A^+$ ,  $T^+$  and  $(N)^+$  (cf. Table 1.1), along with the differences between AD and mild cognitive impairment (MCI).

Two types of lesions form in the brain and cause neuronal death; these can precede the first symptoms by a few years and up to decades [5, 6].

Amyloid- $\beta$  ( $A\beta$ ) plaques (cf. Figure 1.1) are the first type of lesion to appear. They are located in the extracellular space — or neuropil. They contain mainly amyloid- $\beta_{1-42}$  peptides — i.e. peptides of 42 amino acids — which fold themselves and aggregate as fibrils. They often entrap biometals such as zinc, iron and copper. These last two points will be further detailed in section 1.2. They account for the  $A^+$  biomarker profile (cf. Table 1.1).

|   |    |
|---|----|
| <b>1.1 Pathology</b> . . . . .                                | 5  |
| 1.1.1 Symptoms and evolution . . . . .                        | 5  |
| 1.1.2 Forms and prevalence . . . . .                          | 7  |
| 1.1.3 Comorbid neuropathologies . . . . .                     | 9  |
| <b>1.2 Mechanisms</b> . . . . .                               | 11 |
| 1.2.1 Amyloid cascade . . . . .                               | 11 |
| 1.2.2 Metal dysregulation . . . . .                           | 15 |
| <b>1.3 Diagnosis</b> . . . . .                                | 17 |
| 1.3.1 Cognitive tests . . . . .                               | 18 |
| 1.3.2 <i>In vivo</i> techniques . . . . .                     | 20 |
| 1.3.3 <i>Postmortem</i> diagnosis of certainty . . . . .      | 23 |
| <b>1.4 Recent developments in <math>A\beta</math> imaging</b> | 29 |
| 1.4.1 Research models for AD . . . . .                        | 29 |
| 1.4.2 <i>In vivo</i> imaging . . . . .                        | 31 |
| 1.4.3 <i>Postmortem</i> imaging of individual plaques         | 32 |

The same group recently re-designed the set of biomarkers from AT(N) to ATX(N), “where X represents novel candidate biomarkers for additional pathophysiological mechanisms such as neuroimmune dysregulation, synaptic dysfunction and blood-brain barrier alterations” [4].

**Table 1.1.:** Risk of short-term cognitive decline based on the AT(N) biomarker profile and cognitive stage. A<sup>+</sup>: evidence of amyloid pathology; T<sup>+</sup>: evidence of tauopathy; (N)<sup>+</sup>: evidence of neurodegeneration or neuronal injury. From [3].

| Syndromal Cognitive Stage |  |   |  |   |
|---------------------------|--|---|--|---|
| Biomarker Profile         |  | Cognitively unimpaired  | MCI  | dementia  |
|                           | A <sup>-</sup> T <sup>-</sup> (N) <sup>-</sup> | normal AD biomarkers, cognitively unimpaired  | normal AD biomarkers with MCI  | normal AD biomarkers with dementia  |
|                           | A <sup>+</sup> T <sup>-</sup> (N) <sup>-</sup> | Preclinical Alzheimer's pathologic change   | Alzheimer's pathologic change with MCI   | Alzheimer's pathologic change with dementia   |
|                           | A <sup>+</sup> T <sup>+</sup> (N) <sup>-</sup> | Alzheimer's and concomitant suspected non Alzheimer's pathologic change, cognitively unimpaired | Alzheimer's and concomitant suspected non Alzheimer's pathologic change with MCI | Alzheimer's and concomitant suspected non Alzheimer's pathologic change with dementia |
|                           | A <sup>+</sup> T <sup>+</sup> (N) <sup>+</sup> | Preclinical Alzheimer's disease   | Alzheimer's disease with MCI (Prodromal AD)                                      | Alzheimer's disease with dementia   |
|                           | A <sup>+</sup> T <sup>+</sup> (N) <sup>+</sup> |   |  |   |
|                           | A <sup>+</sup> T <sup>+</sup> (N) <sup>+</sup> |   |  |   |

Non-Alzheimer's continuum profiles are not included in table because the risk associated with different combinations of T+(N)-, T+(N)+, T-(N)+ among A- individuals has not been established

- rate of short term clinical progression expected to be low  
 rate of short term clinical progression expected to be high



**Figure 1.1.:** Amyloid- $\beta$  plaques and neurofibrillary tangles in the brain. Amyloid- $\beta$  plaques develop in the extracellular space and NFTs develop within the neurons.

Neurofibrillary tangles (cf. Figure 1.1) are the second type of lesion. Contrary to A $\beta$  plaques, they develop in the neurons and mainly contain hyperphosphorylated tau proteins. The tau (tubulin-associated unit) protein plays a key role in maintaining the microtubule integrity in the axons of the neurons. Because of hyperphosphorylation, the tau protein leaves the microtubules — they will then collapse and lose their role in neuronal polarization. Then, the hyperphosphorylated tau (P-tau) proteins accumulate and aggregate within the neurons until neuronal death by apoptosis. They account for the T<sup>+</sup> biomarker profile (cf. Table 1.1).

Neurodegeneration leads to an atrophy of the brain areas and a reduced activity. This accounts for the (N)<sup>+</sup> biomarker profile (cf. Table 1.1).

While the symptoms of AD can be common to most dementia, these lesions are considered AD-specific (A<sup>+</sup> and T<sup>+</sup> biomarker profiles from Table 1.1, also shown in gray in Figure 1.2). These lesions are both based on proteins — amyloid- $\beta_{1-42}$  or tau — which become pathological as they undergo a conformation change. Besides, they have the ability to alter normal proteins in the vicinity by transconformation [7, 8], in a way similar to prions from Creutzfeldt-Jakob disease (prion-like mechanisms). Thus, Alzheimer's disease can be defined as a proteinopathy. Blocking these mechanisms (in red in Figure 1.2) is the main target for disease-modifying

drugs; these drugs have a higher outcome when used preventively as they usually slow the progression of the disease — biomarker profiles from Table 1.1 are not sufficient for a diagnosis (cf. subsection 1.3.3) but they can guide the therapeutic decision-making [9].

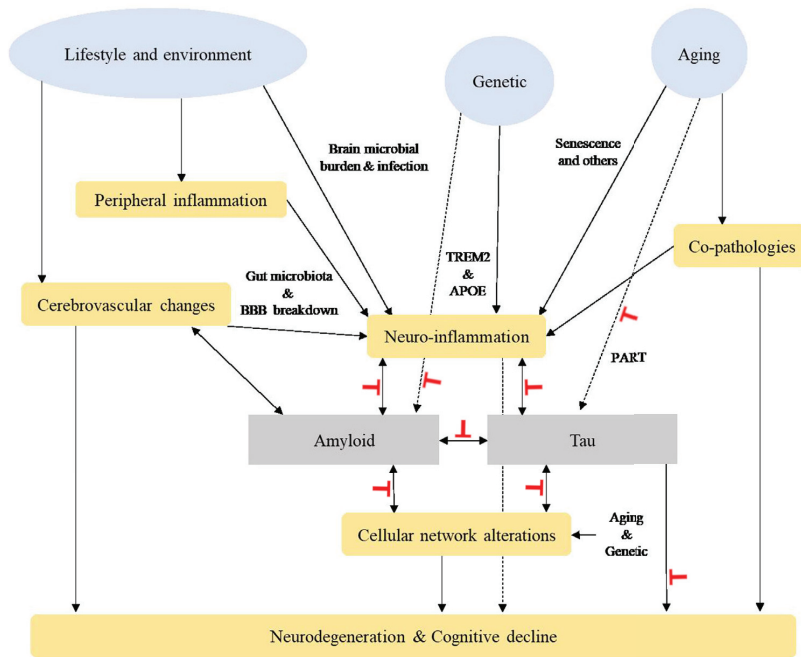


**Figure 1.2.:** Alzheimer’s related pathophysiology converges to neurodegeneration through multiple cellular pathways. Pathognomonic changes of AD (in gray squares) are considered to consist only of amyloid and tau pathologies. The pathological changes considered unspecific to AD are represented in yellow boxes. Risk and protective factors, specified as aging, genetics, lifestyle and environmental are represented in blue circles (cf. subsection 1.1.2). Disease-modifying drugs target one or several mechanisms to block, these are represented with red flat-head arrows. APOE: apolipoprotein E; BBB: blood–brain barrier; PART: primary-age-related tauopathy; TREM2: triggering receptor expressed on myeloid cells 2. Adapted from [10].

### 1.1.2. Forms and prevalence

Alzheimer’s disease is the most common dementia, with an estimated prevalence of 10.8% among the people aged 65 and above in the USA [1]. Rajan et al. [11] estimate the number of cases of AD and mild cognitive impairment in this population will double between 2020 and 2050 in the USA. In Europe, the pooled prevalence of dementia among the people aged 65 and above is 12.4% [12] — AD would account for  $\frac{2}{3}$  of these dementia cases.

Risks of developing AD are higher in some populations depending on multiple factors (cf. Figure 1.2):

**Education:** low education attainment may be a key factor [11];

**Country of residency:** low-income and developing countries account for 60% of people with dementia [13];

**Sex:** prevalence is higher for women compared to men [14];

**Health behaviors:** moderate alcohol consumption seems to have a protective outcome but high consumption and alcoholism increase AD risk [15]; healthy diets [16] and physical activity [17] both decrease AD risk;

**Genes:** AD can be either inherited or sporadic; while inherited AD is solely caused by mutations, genetic risk factors have also been identified for sporadic AD [18]; other genetic conditions may increase AD risk: people with Down's syndrome have a higher amyloid burden — both in the brain and in the cerebrospinal fluid — and are more prone to develop AD than the general population [19, 20].

AD has different forms with specific prevalences, presented below.

**Autosomal dominant forms of AD (ADAD)** The inherited forms of Alzheimer's disease, or autosomal dominant forms of AD (ADAD), have a prevalence of less than 5 % of total AD cases. However, ADAD patients can show signs of AD from 35 years old. Multiple genes are involved [21]: *APP*, *PSEN1*, *PSEN2*, *TREM2*, *MAPT*.

The gene *APP* is responsible for the production of the amyloid- $\beta$  precursor protein (APP), which is a transmembrane protein of 600–700 amino acids. When cleaved by  $\beta$  and  $\gamma$  secretases, its fragments become amyloid- $\beta$  peptides of 36 to 43 amino acids, including the  $A\beta_{1-42}$  peptide present in amyloid- $\beta$  plaques. The genes *PSEN1* and *PSEN2* encode subunits of the  $\gamma$  secretase complex [22]. These interactions will be further detailed in subsection 1.2.1.

The gene *TREM2* is related with microglial activity. For instance, the R74H variant of the *TREM2* gene decreases the functional effects of TREM2, such as phagocytosis [23], and people with this variant have a 3-fold increased risk of developing AD [24].

Finally, the gene *MAPT* (Microtubule-Associated Protein Tau) encodes the tau protein, present in NFTs in its hyperphosphorylated state (cf. subsection 1.2.1).

**Late-onset and early-onset Alzheimer's disease (LOAD / EOAD)** The main forms are the late-onset Alzheimer's

disease (LOAD) and the early-onset Alzheimer's disease (EOAD), whether the diagnosis was after or before age 65. They are said sporadic because they are not genetic, although multiple genetic risk factors have been identified, such as *TOMM40*, *APOE* and the aforementioned *TREM2*, among the 695 identified genes [18].

The *TOMM40* gene encodes a mitochondrial protein that enables protein exchange between the mitochondria and the cell cytoplasm.

The *APOE* gene (apolipoprotein E) is the most important of these risk factors. It has 3 alleles  $\epsilon 2$ ,  $\epsilon 3$  and  $\epsilon 4$  and people homozygoteous  $\epsilon 4/\epsilon 4$  have a higher risk of AD than the general population, while people with  $\epsilon 2/\epsilon 2$  have a lower risk. People with one or two alleles  $\epsilon 4$  of the *APOE* gene also develop AD at an earlier age [25]. This gene codes for a fat-binding protein produced in the liver, in macrophages and in astrocytes; the latter use this protein to transport cholesterol to neurons.

Site [www.alzgene.org](http://www.alzgene.org) associated with [18] visited on April 3, 2023.

### 1.1.3. Comorbid neuropathologies

Multiple diseases are associated with AD [26]. Some of them share biomarkers and symptoms with AD, requiring a differential diagnosis (cf. section 1.3).

#### 1.1.3.1. Synucleinopathies

Lewy body dementia (LBD) and Parkinson's disease (PD) are defined by the aggregation of the  $\alpha$ -synuclein ( $\alpha$ -syn) protein into Lewy bodies inside the neurons — they are also proteinopathies [27] with prion-like mechanisms — and by the degeneration of the dopaminergic neurons. The symptoms include dementia, recurrent visual hallucinations, sleep disorders and movement impairments (rigidity, rest tremors, slowed movement response, altered gait) [27], the latter being attributed to PD [28].

In a cohort study by Irwin et al. [29], 75% of autopsy-confirmed synucleinopathy patients ( $n = 213$ ) had neuropathological signs of AD; up to 50% of LBD patients might have AD [27, 30]. Interactions between  $\alpha$ -syn, P-tau and  $A\beta$  have been identified [27].

### 1.1.3.2. Frontotemporal dementia

Frontotemporal disorders or dementia (FTD) are a group of brain diseases with a common degeneration of neurons in the frontal and temporal lobes. Both sporadic and familial forms exist [31] — the first identified gene has been the *MAPT* (tau protein) gene [32], also linked with AD. FTDs are a set of pathologies with tau aggregates — such as Pick's bodies [33] and NFTs — or ubiquitin aggregates.

### 1.1.3.3. Cerebral amyloid angiopathy (CAA)

#### Context of the thesis

The last study that is reported in the manuscript — as an article draft — (cf. Chapter 6) is a cohort study about CAA. The section below gives general information. The introduction of Chapter 6 goes into more detail but it builds upon knowledge that is developed in the following sections (from section 1.2).

Cerebral amyloid angiopathy (CAA) is a vascular dementia caused by  $A\beta$  deposition in the walls of blood vessels. These deposits will eventually cause cerebral microbleeds [34]. In CAA, the main peptide within the  $A\beta$  deposits is  $A\beta_{1-40}$  instead of  $A\beta_{1-42}$ . Enlarged perivascular spaces (a.k.a. Virchow–Robin spaces) are a hallmark of CAA (cf. Figure 1.3) that is shared with other vascular diseases, along with hemosiderin deposits — small blood clots containing iron — within the brain. The diagnosis to discriminate CAA from other vascular diseases (e.g. arteriosclerosis) requires an autopsy where immunohistochemistry will reveal  $A\beta$  deposits in the blood vessel walls.

AD patients show distinct patterns of CAA [36] and they have a more severe and widespread CAA [37].

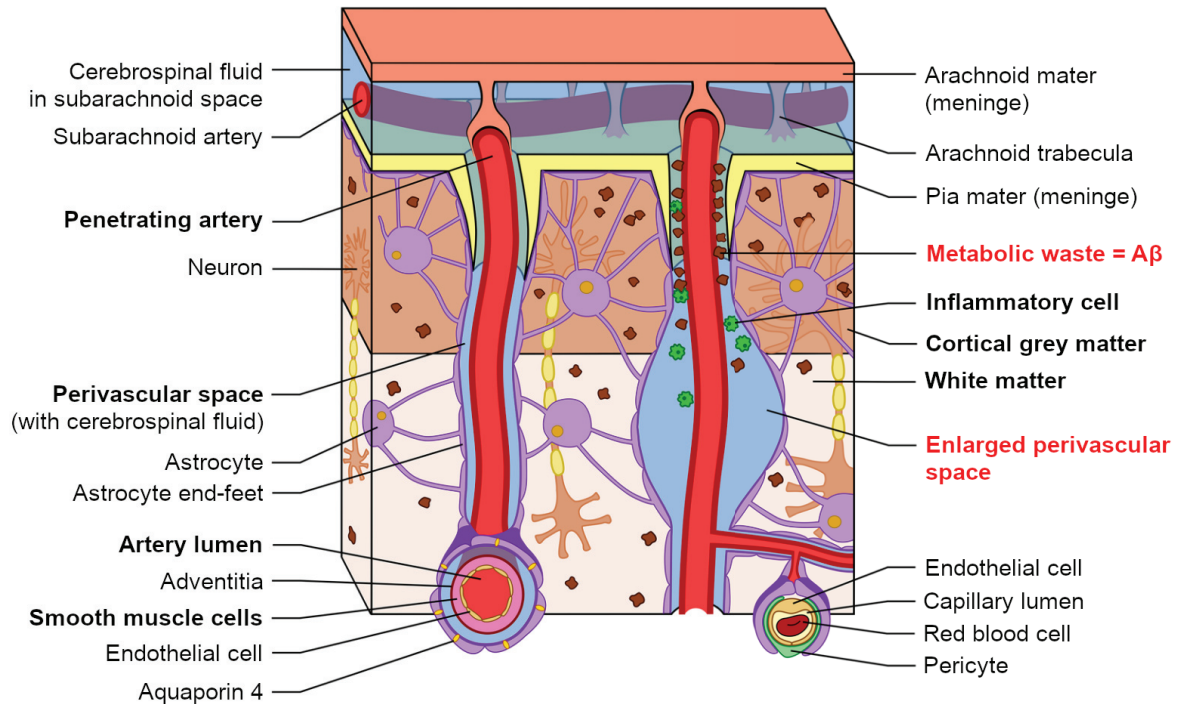


**Figure 1.3.:** Schematic representation of the brain perivascular Virchow–Robin space and surrounding tissues at the surface of the brain cortex ( $\sim 5$  mm-depth). The brain is enveloped by three protective layers called meninges; cerebrospinal fluid (CSF) circulates between the arachnoid mater and the pia mater meninges. The cortical perivascular space of penetrating arteries (bounded by the adventitia of the vessel and the astrocyte end-feet) is filled with CSF from the subarachnoid space. Metabolic waste such as A $\beta$  is thought to accumulate around the blood vessel, possibly resulting in perivascular blockage and enlargement of the space, as shown on the right vessel. Adapted from [35].

## 1.2. Mechanisms

### 1.2.1. Amyloid cascade

The amyloid cascade hypothesis is the most widely studied mechanism of AD pathogenesis, in which amyloidosis — the spreading of abnormal A $\beta$  — is the origin of the whole pathway leading to the development of the disease [10, 38, 39].

As previously stated, the amyloid- $\beta$  peptides are fragments of the APP protein released by the action of two enzymes —  $\beta$  and  $\gamma$  secretases. The APP protein is a transmembrane protein present on multiple cells; in the brain, it is highly concentrated within neurons, around synapses, as it plays a key role in synaptic formation and repair [40]. The cleavage of APP into A $\beta$  is a two-step process (cf. Figure 1.4) [41]:

1. The  $\beta$ -secretase cleaves the N-terminal part of APP, yielding soluble APP- $\beta$  (sAPP $\beta$ ) and a  $\beta$ -cleaved carboxy-

terminal fragment of APP ( $\beta$ -CTF). The  $\beta$ -secretase, more abundant in the neurons, competes with the  $\alpha$ -secretase, more abundant in the other cells; cleaving by  $\alpha$ -secretase prevents the  $A\beta$  pathological pathway [42]. Alternative (mutation-induced) cleavage sites of  $\beta$ -secretase may increase the amyloid burden and increase the risks of AD [43].

2. The  $\gamma$ -secretase further cleaves the  $\beta$ -CTF from the other end into an  $A\beta$  peptide of variable length — depending on the cleaving site — including the  $A\beta_{1-42}$  peptide. The remaining peptides from the amyloid intracellular domain (AICD) play a possible role into cellular pathways such as activation of nuclear signalling [44].

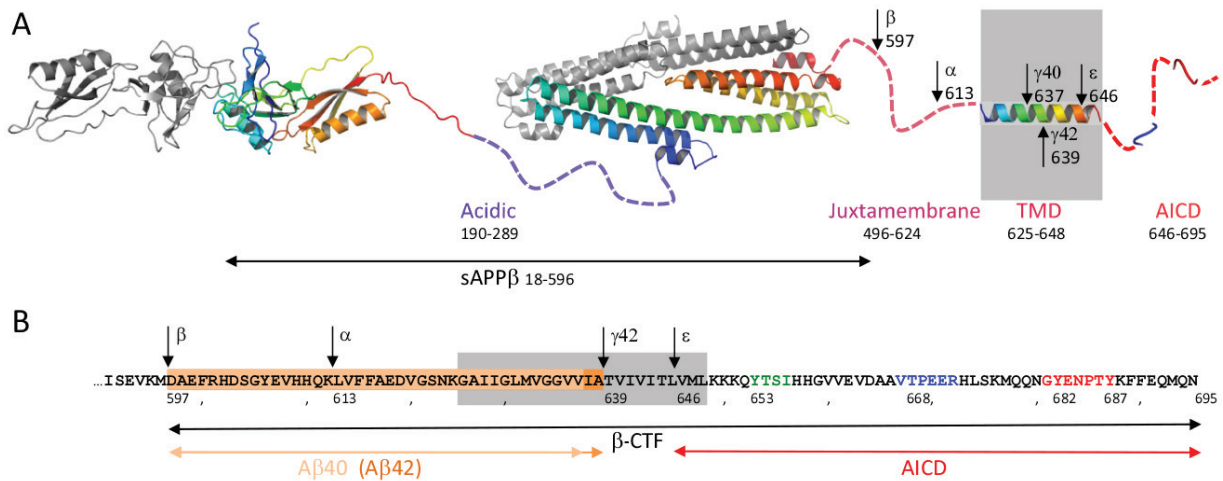


**Figure 1.4.:** Cleavage of the APP protein into amyloid- $\beta$  peptides. (A) Whole domain architecture of the neuronal splice variant APP695. Dashed lines represent unknown domain structures. When APP is at its transmembrane location (gray), tethered by its transmembrane domain (TMD), its N-terminus (left) is outside the cell and its C-terminus (right) is in the cytoplasm. (B) Amino acid sequences of juxtamembrane, TMD and AICD domains. Vertical arrows point precise cleavage sites of  $\alpha$ ,  $\beta$ ,  $\gamma$  and  $\epsilon$  secretases. The different breakdown products are labelled. Adapted from [45].

Amyloid- $\beta$  peptides exist at low concentrations in healthy individuals: while the  $A\beta_{1-40}$  peptides are preponderant under normal physiological conditions, the  $A\beta_{1-42}$  peptides accumulate in AD patients [46]. The underlying mechanism for this abnormal accumulation is either an excessive production of  $A\beta$  [47] or an impaired  $A\beta$  clearance [48].

The  $A\beta_{1-42}$  peptides eventually undergo a conformation change, which can be triggered by transconformation [7, 8, 49]: they shift from a disordered monomeric form to a  $\beta$ -style folding, first as monomers, then dimers, then multimeric  $\beta$ -amyloid protofibrils or insoluble fibrils (cf. Figure 1.5). These insoluble fibrils precipitate into  $A\beta$  plaques.

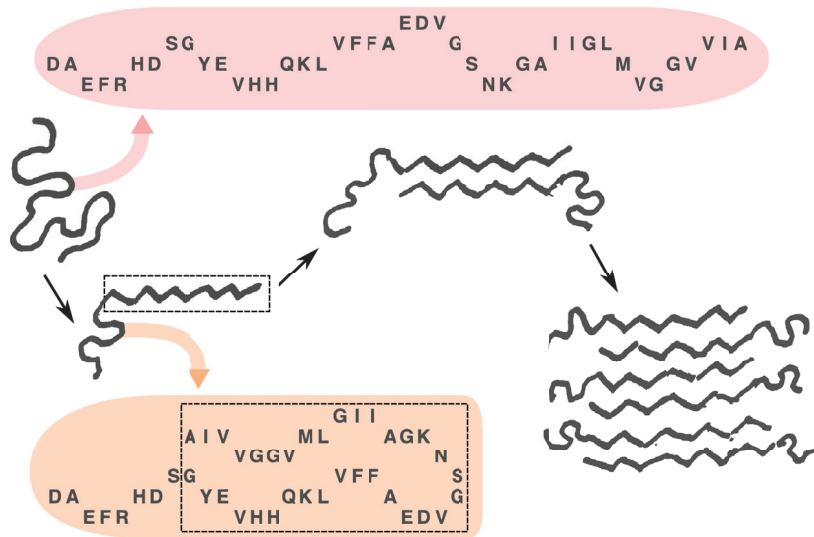


**Figure 1.5.:** Folding and stepwise aggregation of Aβ<sub>1-42</sub> peptides. Amino acid sequences are detailed for the monomers. The dashed rectangles show the β-folding pattern. Adapted from [50].

Contrary to the first amyloid cascade hypothesis, new evidences show that intermediate forms of Aβ may have a higher toxicity compared to fibrils [51, 52, 53]. These oligomers accumulate both in the extracellular space and in the neurons [54]. Among the studied pathways, Aβ oligomers may stimulate the excessive formation of reactive oxygen species (ROS) [55] — leading to cell damage —, cause synaptic dysfunction through impaired synaptic vesicle endocytosis [56], or disrupt the homeostasis of calcium and other ions by cell membrane permeabilization [57, 58].

Aβ oligomers activate microglia when they bind to a subclass of cell surface receptors named pattern recognition receptors (PRR) [59]. An acute short-term activation has a beneficial effect on Aβ clearance [60]. However, following an acute activation, the primed microglia were shown to increase vulnerability to inflammation from unrelated events — such as brain trauma or midlife obesity [61]. With a sustained exposure to Aβ, a chronic activation of PRRs leads to a chronic inflammation because of a persistent microglial release of inflammatory mediators (cytokines). This chronic activation causes a deleterious microglial proliferation and reduces the Aβ clearance by microglia [61, 62, 63]; it also induces neurotoxicity and neurodegeneration [64]. To support these hypotheses, chronically activated microglia have been observed in the vicinities of synapses [65] and of Aβ plaques [66].

There is currently no consensus on how Aβ interacts with tau and P-tau [67], but it is accepted that Aβ spreading precedes P-tau spreading [5]. Aβ oligomers may trigger

phosphorylation of tau, either through the disruption of calcium ion homeostasis [68] or inflammation [58]. This is in agreement with findings that blocking A $\beta$  affects tau spreading [69].

Soluble P-tau form  $\beta$  sheets and aggregate as oligomers inside the neurons [70] (cf. Figure 1.6), in a similar way than A $\beta$  (cf. Figure 1.5); P-tau protomers combine into a structure referred as paired helical filaments (PHF), which aggregate into the final NFTs. These P-tau oligomers are neurotoxic [71]. The P-tau oligomers and the successive forms are mainly intracellular but they will be released in the extracellular space upon apoptosis of the neurons, leaving flame-shaped "ghost tangles" [72] (cf. Figure 1.6).

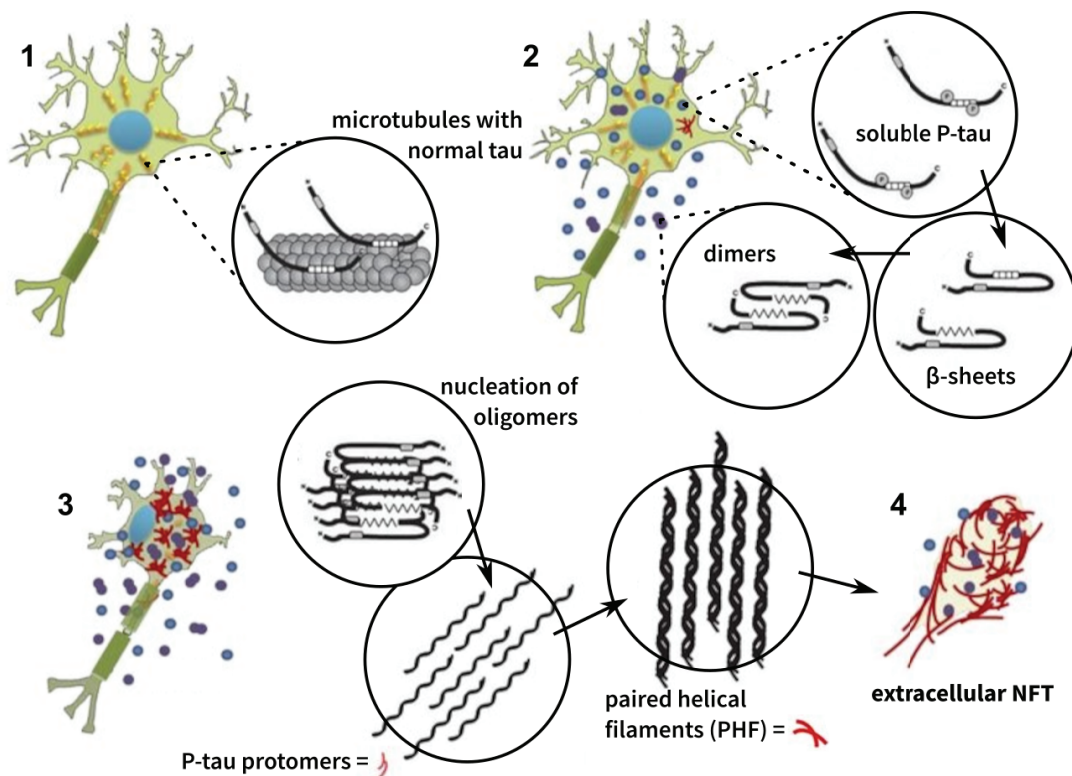


**Figure 1.6.:** The formation of NFTs. (1) Healthy neuron, in which normal tau proteins stabilize the microtubules. (2) Pre-tangle state by phosphorylation of tau monomers that change into  $\beta$  sheets. (3) Aggregation and nucleation of oligomers inside the neuron. (4) Neuron death leaving flame-shaped "ghost tangles". Adapted from [70, 72].

Pathological tau aggregates spread through the synapses of adjacent neurons [73] and also have a prion-like activity of altering healthy tau proteins [8, 49, 74]. Microglia may play a key role in spreading tau oligomers by phagocytosis and release [75, 76].

New findings show that these pathways may not be complete

though, as the presence of A $\beta$  plaques is necessary but not sufficient to trigger the pathogenesis [77, 78, 79]. Besides, the heterogeneity of the amyloid pathology is not fully understood yet: both conformation variants of A $\beta$  [80, 81] and different A $\beta$  depositions [52] have been described.

### 1.2.2. Metal dysregulation

Metals and ions are involved in a variety of neuro-physiological pathways. Regulation mechanisms enable a metal homeostasis — an equilibrium for all endogenous metals so to maintain all ionic forms at basal levels. It has been shown that patients with AD or animal models of AD present alterations of these pathways and an overall metal dysregulation, but little is known about the exact relationship between AD and metal dysregulation:

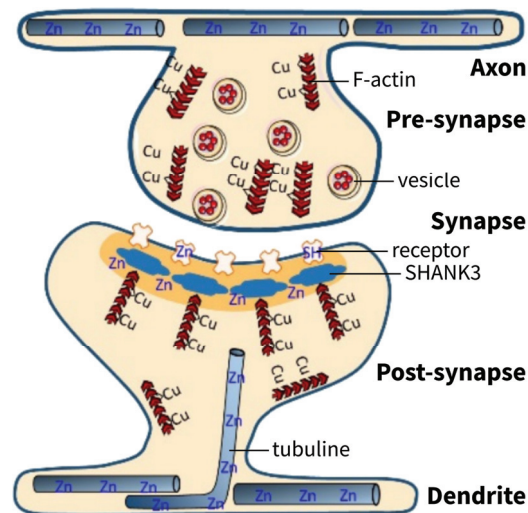
1. Is the amyloid cascade triggered by the disturbed metal homeostasis?
2. Is the metal dysregulation a consequence of deeper, unknown mechanisms?
3. Can therapies use or target metals to block AD progression?

This section will present a synthesis of literature about AD and metals, with a brief introduction to the physiological homeostasis around iron, zinc and copper. These endogenous metals are among the most present trace elements in the body and they have key roles in the brain metabolism.

In the whole body, iron (Fe) is present within the hemoglobin of circulating erythrocytes — red blood cells — for oxygen transportation (~ 60%), in the liver and heart where it is stored as ferritin (~ 20%) or in the myoglobin of muscles to locally store higher concentrations of oxygen (~ 10%). The remaining part serves different physiological processes such as enzymatic action and energy production [82]. Iron is mainly recycled from the aged erythrocytes; the minimal daily loss (1 to 2 mg) through sweating or small bleedings is compensated by the uptake (around 10% of the daily diet recommendations of 10 to 20 mg) [82]. In the brain, iron is required for the synthesis of myelin and neurotransmitters; an iron deficiency in infants impairs the neural development and causes intellectual disability [83].

Copper (Cu) is involved in biological processes as a cofactor of numerous metalloenzymes: for cellular respiration, disposal of free radicals and the biosynthesis of neurotransmitters (cf. Figure 1.7) and hormones [84]. It is essential for iron homeostasis with ceruloplasmin [85]. It also has an antimicrobial and antiviral activity and it is involved in the development of the immune system [84]. The human body contains 70 to 80 mg of copper, 10 % of which is in the blood and the rest in the tissues, mainly the skeleton, muscles, and organs like the liver — the major storage organ for copper —, the kidneys and the placenta [84]. The Menkes and Wilson diseases are both linked to an abnormal Cu metabolism and respectively cause neurological abnormalities or cirrhosis [85].

**Figure 1.7.:** Copper and zinc in the physiological brain. Cu interacts with actin filaments (F-actin) for the synapse formation and Zn contributes to the stability of the post-synaptic density (yellow area) through interaction with the SHANK3 proteins. Zn also acts as a neurotransmitter [86]. Adapted from [87].



Zinc (Zn) interacts with various ligands and takes part in many signalling mechanisms, thus modulating physiological processes at the cellular scale: neuronal communication (cf. Figure 1.7), immune response, cell proliferation [85]. It also regulates the action of insulin and has anti-inflammation and antioxidant properties — as redox-inactive  $Zn^{2+}$  is isostructural to redox-active iron and copper ions, it substitutes to them and blocks oxidative reactions e.g. the Fenton reaction [85]. The human body contains 2–3 mg of zinc [85]; within cells, only a small fraction of zinc is free ( $\sim 0.5$  nM) [88], the main part being trapped within vesicles named zincosomes.

In the pathological brain, the metal ion homeostasis is disrupted. First, the regional metal distribution is different in the AD brain compared to the ageing brain. Age-related changes have been observed in the non-AD brain, e.g. whole-brain

Zn depletion and Cu and Fe accumulations [89]; the Zn depletion was mapped to hippocampi and Fe accumulation to the corpus callosum [90]. In the AD brain, Leskovjan et al. [91] observed a 1.5-fold Fe increase in the cortex of PSAPP mice compared to same-age control, along with a Zn accumulation (vs. Zn depletion in control); they did not observe a Cu accumulation, although Wang et al. [92] did. The Fe increase was also observed in the brains of human AD patients [93]. Similar results were reported in other contributions [94, 95, 96, 97, 98].

Second, metals and  $A\beta$  interact, although it is not known whether this is the cause or a consequence of  $A\beta$  accumulation [99]. Lovell et al. [100] showed that there are accumulations in the AD neuropil (slight increase), senile plaque rim (intermediate increase) and senile plaque core (higher increase) compared to the control neuropil, for Fe, Zn and Cu; this has been confirmed by other studies [91, 92, 95, 96, 97, 99, 101, 102, 103, 104]. Through scanning transmission x-ray microscopy, Everett et al. [105] discovered that these entrapped metals can be in their metallic (non-ionic) form. Metals act as catalysts for the amyloid fibrillation process [106, 107, 108, 109, 110], paving the way to new therapeutic trials using chelatants [111, 112, 113, 114]. Studies at higher resolutions concur with these findings [115, 116, 117] and  $A\beta$ -metal complex formation may be responsible for the amyloid deposition and aggregation [118, 119, 120]. Another hypothesis identifies the metal accumulation as a cause for the impaired activity of  $A\beta$ -degrading enzymes [121]. Cu ions increase the neurotoxicity of  $A\beta$  oligomers [122] and they may also interact with tau [123].

Note that, despite the role of aluminium in AD being a widespread belief, interaction of  $A\beta$  with aluminium is not fully established [124, 125, 126, 127].

### 1.3. Diagnosis

As mentioned before, the diagnosis of AD is biomarker-based. These biomarkers have different spatiotemporal distributions (cf. Figure 1.8). This section will follow the chronology of AD diagnosis — rather than the chronology of biomarkers —, from screening to the *postmortem* confirmation.

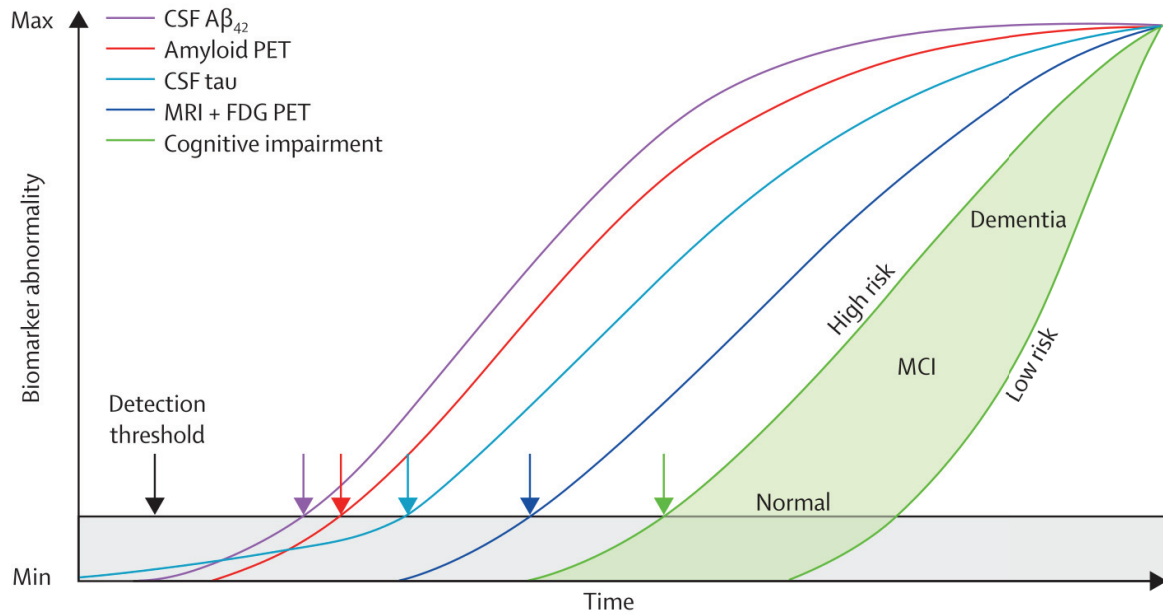


**Figure 1.8:** Chronology of the AD biomarkers. The threshold for biomarker detection of pathophysiological changes is denoted by the black horizontal line. The grey area denotes the zone in which abnormal pathophysiological changes lie below the biomarker detection threshold. In this figure, tau pathology precedes  $A\beta$  deposition in time, but only early on at a subthreshold biomarker detection level.  $A\beta$  deposition then occurs independently and rises above the biomarker detection threshold (purple and red arrows). This induces acceleration of tauopathy and CSF tau then rises above the detection threshold (light blue arrow). Later still, FDG PET and MRI (dark blue arrow) rise above the detection threshold. Finally, cognitive impairment becomes evident (green arrow), with a range of cognitive responses that depend on the individual's risk profile (light green-filled area). These pathophysiological changes can span over decades. CSF=cerebrospinal fluid. FDG=fluorodeoxyglucose. MCI=mild cognitive impairment. MRI=magnetic resonance imaging, PET=positron emission tomography. From [5].

### 1.3.1. Cognitive tests

Cognitive tests are the first means to detect AD, they will guide the diagnosis before any imaging or invasive technique.

#### 1.3.1.1. Simplistic tests

A few tests have been used for their simple design, which makes them effective for screening purposes.

**The 5-Word Test** The patient is told a list of 5 words (in French [128]: *musée, limonade, sauterelle, passoire, camion*) and is successively asked to ① tell them back through their semantic category (*What is the name of a vehicle? — Truck.*), then ② on their own, then again ③ with and ④ without the semantic

category hint after a 5-minute delay. The 4 sessions are scored with different weights into a final score.

**The Clock-Drawing Test (CDT)** The patient is scored on how they draw a clock (cf. Figure 1.9), including the clockface, the numbers from 1 to 12 and the hands pointing to 10 after 11. This test was first designed by Goodglass & Kaplan in 1972. The scoring table of this test was extended to take into account the different errors the patient could make, resulting in a better differentiation between healthy and AD subjects [129].

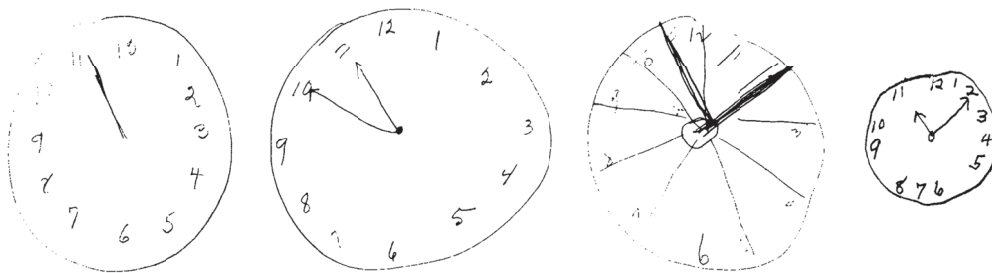


**Figure 1.9.:** Clock-Drawing Test results from 4 subjects at risk for dementia of Alzheimer type. From left to right: Conceptual error (the hands are not placed correctly); Stimulus-bound error (the hands point 10 and 11); Perseverative behavior (supplementary lines are drawn and hands are drawn in multiple strokes); Planning difficulties (the clockface is small and spaces between numbers are inconsistent). Adapted from [129].

### 1.3.1.2. Expert tests

These longer tests are also relevant for screening by a clinician.

**The Mini-Mental State Examination (MMSE)** The patient is asked to answer a 30-question test which assesses ① orientation (time and space); ② registration; ③ attention and calculation; ④ recall; ⑤ language and praxis. The first version of the test was proposed by Folstein, Folstein, and McHugh [130]; in the initial study, they could differentiate the patients with dementia from healthy people. For AD specifically, the test could differentiate healthy vs. mild AD vs. moderate AD [131]. However, tracking the progression of AD with annual MMSE lacked sensitivity because of the relatively high variability of the test [132]. A new version called Severe Mini-Mental State Examination (SMMSE) was proposed by Harrell et al. [133] to reliably discriminate between moderate and severe AD-caused impairment.

**The Montreal Cognitive Assessment (MoCA)** The patient is asked a series of 18 tasks about ① visuospatial/executive ability; ② naming; ③ short-term memory; ④ attention; ⑤ language; ⑥ abstraction; ⑦ delayed recall; ⑧ orientation. Nasreddine et al. [134] — the team who designed the test — found that it was better for MCI and AD detections (higher sensitivity) with a minor drop in specificity compared to MMSE, when setting the threshold at 26 points. Item ① includes the CDT test and items ③ and ⑦ are based on the 5-Word Test.

The MMSE and MoCA tests are currently used for inclusion in therapeutic trials [135] or to assess trial outcomes [136]. An MMSE score of 20 to 26 accounts for mild AD, 10 to 19 for moderate AD and lower scores for severe AD.

### 1.3.2. *In vivo* techniques

Following an AD suspicion based on cognitive impairments, multiple follow-up medical tests are considered. For patients with a family history of AD, the hypothesis of an inherited form of AD (cf. subsection 1.1.2) may be relevant and a DNA screening test for specific mutations can be appropriate [140, 141]. While radioimaging has been historically the most sensitive approach (compared to MRI and vascular disease imaging), fluid-derived biomarkers are becoming increasingly popular.

#### 1.3.2.1. Radioimaging

As a radiolabeled form of glucose, [<sup>18</sup>F]FDG (fluorodeoxyglucose) is a common radiotracer to study brain metabolism: a lower uptake means a decreased activity, which can indicate regions of neuronal dysfunction and degeneration. FDG positron emission tomography (PET) and perfusion single-photon emission computed tomography (SPECT) imaging were able to reveal patterns of hypometabolism and hypoperfusion in AD patients, first in the posterior cingulate cortex and precuneus, then in posterior temporo-parietal cortices, and later in frontal cortices [142]. Another radiotracer, [<sup>11</sup>C]UCB-J, targets the synaptic vesicle glycoprotein 2A, which is present in the synapses of all neurons, and thus proved efficient for imaging brain atrophy caused by

To get familiar with the human brain anatomy, one can refer to the [Human Brain Atlas](#) [137, 138, 139] on EBRAINS.

AD [143]. This accounts for the (N)<sup>+</sup> biomarker profile (cf. Table 1.1).

Multiple radiotracers target A $\beta$  for PET imaging of AD: [<sup>11</sup>C]PiB (cf. Figure 1.10) was first reported in 2003 by Klunk et al. [144] as a radiolabeled derivative of a benzothiazole, from the same family as the thioflavin T dye — commonly used for fluorescence imaging of A $\beta$ . A fluorine-18-labeled variant of PiB, flutemetamol — a.k.a. [<sup>18</sup>F]GE067 and [<sup>18</sup>F]3'F-PiB — was created to bring A $\beta$  imaging to centers that do not have a cyclotron on-site (as <sup>18</sup>F has a half-life of 110 min compared to 20 min for <sup>11</sup>C). Flortbetapir and flortbetaben are two other clinically approved amyloid PET tracers based on <sup>18</sup>F [145]. These modalities account for the A<sup>+</sup> biomarker profile (cf. Table 1.1).

Chien et al. [147] reported [<sup>18</sup>F]T807 (flortaucipir) as the first successful tau-specific PET tracer, which was approved by the FDA in 2020 (cf. Figure 1.11). The second-generation tau-specific PET tracers, like [<sup>18</sup>F]MK-6240 or [<sup>18</sup>F]PI-2620, have a broader dynamic range [146]. Tau PET tracers preferentially bind in AD-relevant areas of the temporal lobes [146]. They account for the T<sup>+</sup> biomarker profile (cf. Table 1.1).

Finally, PET imaging of neuroinflammation is of interest for AD. The microglial cells are the main drivers of the inflammatory process in the brain. Thus, monitoring the microglial activity thanks to the overexpression of Translocator Protein 18kDa (TSPO) can reflect AD pathology [148].

### 1.3.2.2. Fluid biomarkers

Wang et al. [149] recently reported that quantifying A $\beta$ <sub>1-42</sub> and P-tau in the cerebrospinal fluid (CSF) correlate with the amyloid & tau PET outcomes, and even with autopsy (cf. subsection 1.3.3). Hence, these fluid biomarkers, along with CSF A $\beta$ <sub>1-42</sub> / A $\beta$ <sub>1-40</sub> ratio, give complementary information with respect to AD [150, 151] and account for the A<sup>+</sup> and T<sup>+</sup> biomarker profiles (cf. Table 1.1). Besides, CSF total tau can account for the (N)<sup>+</sup> biomarker profile [152]. These techniques are now sufficiently reliable in clinical practice to determine an AD diagnosis and initiate therapy trials [153]; they are also less expensive than imaging sessions.

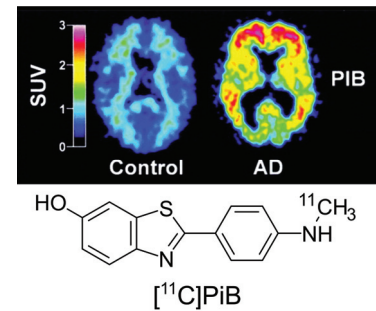


**Figure 1.10.** First A $\beta$  PET imaging with [<sup>11</sup>C]PiB along with the chemical structure of [<sup>11</sup>C]PiB. SUV: standardized uptake value. Adapted from [144].

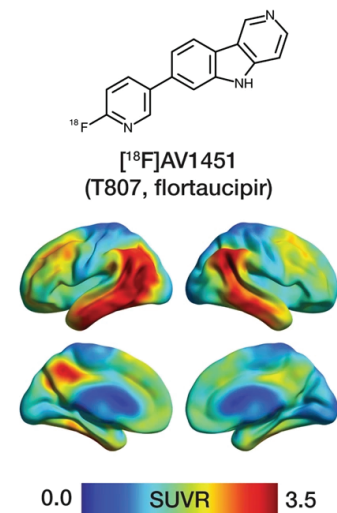


**Figure 1.11.** Chemical structure of flortaucipir and representative uptake images in an AD patient (74 years old, MMSE 14). SUVR: SUV ratio (cerebellar cortex as reference). Adapted from [146].

Plasma measurements are less invasive alternatives which had some promising results [154], but also received critics [155].

### 1.3.2.3. Magnetic resonance imaging (MRI)

Structural MRI can reveal hippocampal atrophy [156, 157] which accounts for the (N)<sup>+</sup> biomarker profile (cf. Table 1.1); this is also an indirect biomarker of the tau progression in AD [5]. Besides, structural-MRI-assessed atrophy correlates well with Braak stages (cf. Figure 1.19 and the corresponding section) to assess the progression of the disease by volume reduction [158]. Structural MRI also reveals white matter hyperintensities (WMH), another common observation in AD [159] — although they are also present in vascular diseases [158]. Both atrophy and WMH can predict the evolution from mild cognitive impairment to AD [160, 161] or differentiate AD from PD with dementia [161, 162].

Diffusion tensor imaging (DTI) is an MRI sequence that measures water diffusion (quantified as diffusivity), enabling the detection of white matter fibers. It outputs 3D parametric maps and tractographies — which follow the fibers and reveals the brain connectome. Among the 3D maps, some features are relevant to AD: fractional anisotropy (FA) is decreased in some regions (cingulum, corpus callosum, superior lateral fasciculus and uncinate fasciculus and throughout temporal, occipital and frontal white matter) and mean diffusivity (MD) is increased in a few concomitant regions (frontal, occipital, parietal, and temporal areas including the hippocampus) [158]; substantial differences in the parametric maps discriminate AD from MCI and FTDs [158].

MRI-derived cerebral blood flow (CBF) is also specifically altered for AD patients (decrease in occipital, parietal and temporal cortices, limited increase in anterior cingulate) [158, 163]. Arterial spin labelling (ASL) provides perfusion measurements which follow distinctive AD patterns too, excluding vascular diseases, LBDs and FTDs [158].

Other promising techniques, such as the BOLD functional-MRI sequence and magnetic resonance spectroscopy, give an insight into AD, respectively from functional connectivity and from metabolism [158].

### 1.3.2.4. Vascular disease imaging

As vascular dementia and cerebro-vascular diseases are comorbid pathologies of AD [165], their diagnosis through *in vivo* imaging can guide the diagnosis of AD. Hemosiderin deposits — foci of past hemorrhage containing iron — can be detected around blood vessels [166, 167]. They are superparamagnetic, hence they have a high magnetic susceptibility and they appear as slightly dilated (compared to their real size) black or hypointense spots in susceptibility-weighted MRI (cf. Figure 1.12), such as the  $T_2^*$ -weighted gradient-recalled echo sequence; higher sensitivity to these deposits requires either a higher magnetic field, a higher spatial resolution or an echo time within the 25–50 ms range [164]. Other confounding MRI signals can be calcium–iron deposits or partial-volume artifacts; a following CT scan is able to differentiate them from hemosiderin [164]. However, other origins of cerebral microbleeds are cavernous malformations, trauma-induced diffuse axonal injury or metastatic melanoma in the brain; the cerebral distribution and the medical history of the patient usually resolve this [164].

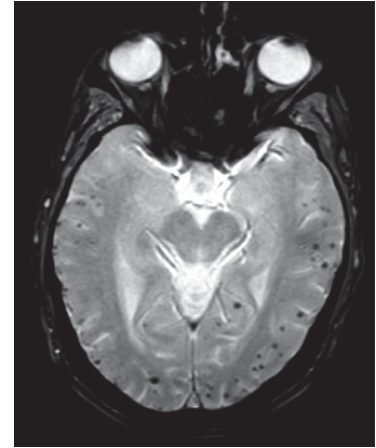


**Figure 1.12.:**  $T_2^*$ -weighted MRI of a 77-year-old female patient without hypertension. Microbleeds are present only in lobar brain regions, meeting criteria for probable CAA. From [164].

### 1.3.3. Postmortem diagnosis of certainty

AD usually develops with other neuropathologies, in a way that clinicians struggle to disentangle similar symptoms along with the effects of age-related cognitive decline. Besides, although the combination of amyloid and tau lesions is specific to AD, their independent spreading can be accelerated by other pathologies. AD encompasses multiple forms which may have different mechanisms. A precise diagnosis may be the key to innovative treatments that break the pathological pathways instead of minimizing the symptoms — the so-called disease-modifying drugs. However, current *in vivo* methods only conclude to a probability of AD dementia, requiring a *postmortem* diagnosis of certainty.

Diagnosis is confirmed upon autopsy by a clinician, usually a medical pathologist. The clinician can assess the brain atrophy after excision, sample regions of the brain — as shown in Figure 1.13 — and perform histology. Multiple complementary scorings have emerged based on histochemistry and immunohistology.

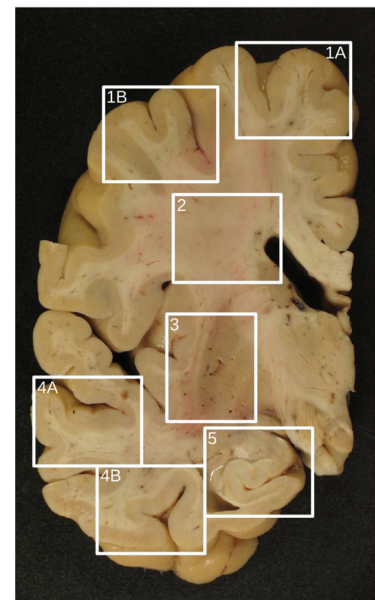


**Figure 1.13.:** Sampling of the brain hemisphere from a vertical-frontal plane parallel to the view of Charcot [168]. 1A&1B: frontal lobe; 2: white matter in the frontal lobe; 3: lenticular nucleus; 4A: superior temporal sulcus; 4B: inferior temporal sulcus; 5: hippocampus. Courtesy of Pr D. Meyronet.

### 1.3.3.1. Study of hippocampal lesions

The first assessment after histology is the examination of the hippocampus with the hematoxylin-eosin (H&E) stain. Indeed, multiple dementias can cause hippocampal lesions and hippocampal atrophy. Rauramaa et al. [169] proposed a standardization of these lesions into 6 groups, shown in Figure 1.14: type 0, type + and types 1 to 4.

To screen for neurodegenerative changes (★ in Figure 1.14), supplementary immunohistochemistries must be performed: p62 (an autophagy marker protein), P-tau, TDP-43 and/or  $\alpha$ -synuclein.

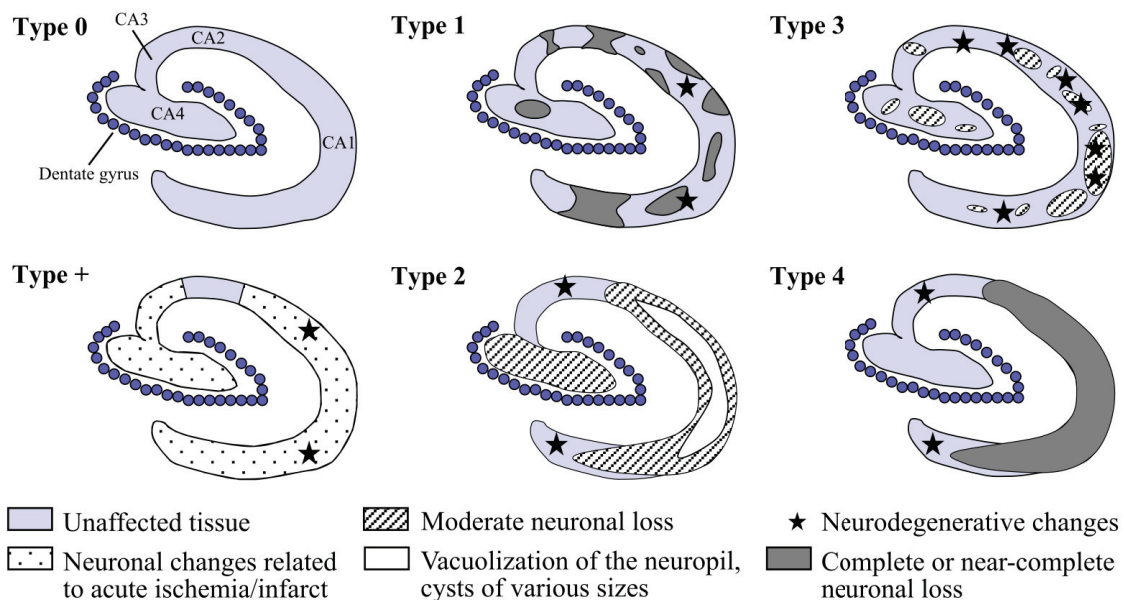


**Figure 1.14.:** Schematic representation of the categories of hippocampal pathology seen in the aged population, as defined by Rauramaa et al. [169]. Type + corresponds to recent diffuse hypoxic/ischemic degeneration of cornu ammonis (CA) neurons. Type 1 is characterized by small focal infarcts (single or multiple). Type 2 corresponds to an extensive infarction of the CA1 sector. Type 3 has patchy diffuse neuronal degeneration in CA sectors, mainly in CA1, with some vacuolization. Type 4 accounts for a complete neuronal loss in CA1 because of neurodegeneration, most frequently associated with NFT; moderate to severe gliosis and corpora amylacea may be seen in CA sectors. Adapted from the original article.

Lesions in types +, 1 and 2 primarily have a vascular origin. In Type 3 and 4, the hippocampal sclerosis is due to a defined neuronal degeneration lacking known neurodegenerative markers.

### 1.3.3.2. Histopathology of AD

Histology of  $A\beta$  plaques differentiates multiple types (cf. Figure 1.15):

- ▶ Pathological plaques:
  - Senile plaques, which can be either cored plaques with a rim or compact plaques without any peripheral rim;
  - Neuritic plaques, where dystrophic neurites containing neurofibrillary material are present.
- ▶ Diffuse plaques, which can be either lake-like, subpial band-like or fleecy.

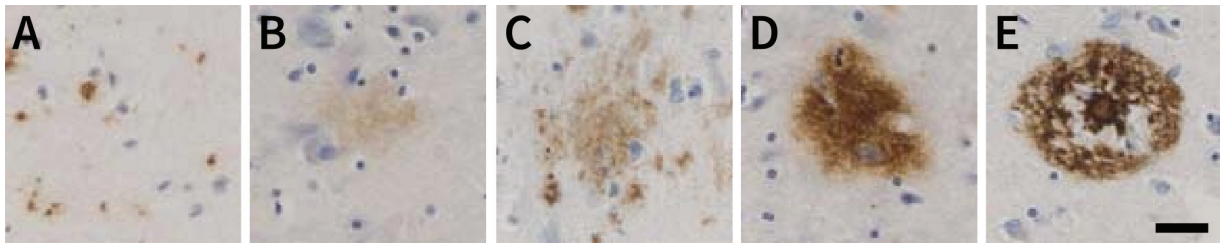


**Figure 1.15.:** Types of A $\beta$  deposits. (A) A $\beta$ -positive cells and small plaques; (B–D) Multiple diffuse A $\beta$  plaques; (E) Senile (cored) A $\beta$  plaque. Immunohistochemistry with 6F3D clone of anti-A $\beta$  antibody, dilution 1 : 100. Adapted from [170].

Multiple staining agents are suitable for the detection of amyloid deposits and P-tau tangles (cf. Figure 1.16). Congo red was first used for neuropathology in 1927 by Divry [171] then it was widely used in the years 1920 to 1970 [172, 173, 174, 175]; under a polarized-light microscope, amyloid stained with congo red gets an “apple green birefringence”. Thioflavin S [175] and thioflavin T [176] are fluorescent probes from the benzothiazole family which activate inside fibrils, present within neuritic plaques and neurofibrillary tangles. Two silver stains are used for the histology of AD: the Gallyas stain [177] and the Bielschowsky stain [178]; they also reveal fibrils [179].

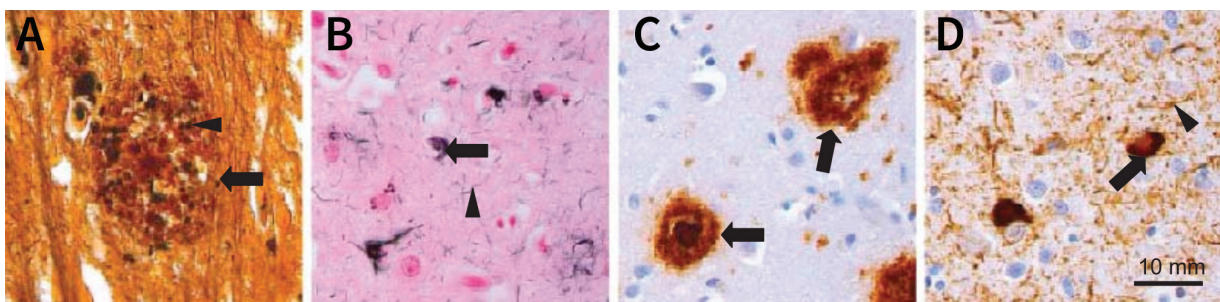


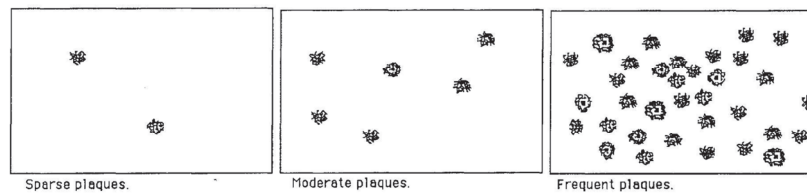
**Figure 1.16.:** Different stainings and revealed features. (A) Bielschowsky staining with neuritic plaques (arrow) where the dark thickened neurites (arrowhead) are seen; (B) Gallyas staining with black NFTs (arrow) and neuropil threads or neurites (arrowhead); (C) Immunohistochemical (IHC) staining of A $\beta$ -labeled protein aggregates, i.e. plaques (arrow); (D) IHC of P-tau-labeled NFTs (arrow) and neuropil threads/neurites (arrowhead). Adapted from [180].

Extensive lists of antibodies for AD are available on AlzForum: [anti-amyloid](#) and [anti-tau](#); on May 10, 2023, they contained respectively 619 and 572 results.

Nowadays, immunohistochemistry (IHC) is broadly used because of its higher specificity. Anti-amyloid antibodies all target fractions of the amyloid- $\beta_{1-42}$  peptide: 4G8 clones bind to amino acids 17–24, 6E10 clones bind to amino acids 1–16 and 6F3D clones bind to amino acids 9–14 of A $\beta$ . Thus, 4G8 antibodies are better to reveal diffuse plaques, while 6F3D and 6E10 mainly reveal pathological plaques. The AT-8 antibody targets neurofibrillary tangles as it binds to intracellular and extracellular phosphorylated tau proteins.

*Postmortem* neuropathological scorings of AD are now based on IHC. The CERAD (Consortium to Establish a Registry for Alzheimer's Disease) [181] designed a semiquantitative assessment of the density of the plaques (cf. Figure 1.17); during their examination, the neuropathologists need to also assess the proportion of the plaques with a core and the overall degree of vascular amyloid deposition. From this assessment — considering the highest density out of 3 regions: temporal gyri, middle frontal gyrus and inferior parietal lobule — and using the patient's age at death and their clinical history — whether they had dementia or not —, the CERAD had proposed a neuropathological diagnosis of "definite" / "probable" / "possible", which was supplanted by the NIA-RI and NIA-AA criteria (detailed below).

**Figure 1.17.:** Cartoon for semi-quantitative assessment of the density of senile and neuritic plaques under a  $\times 100$  magnification after histochemistry or IHC. Adapted from [181].



Thal et al. [182] classified the affected regions from a 51-patient cohort to propose a progression of the A $\beta$  spreading within the brain; the corresponding Thal–Braak phases are illustrated in Figure 1.18:

**Phase 1** is characterized by exclusively neocortical (frontal, parietal, temporal and occipital cortexes) A $\beta$  deposits.

**Phase 2** exhibits additional A $\beta$  deposits in one of: the molecular layer of the dentate gyrus, cornu ammonis, entorhinal area, gyrus singuli, and eventually in the insular cortex;

**Phase 3** shows additional A $\beta$  deposits in one of: the basal forebrain (hippocampus, amygdaloid nuclei, nucleus

basalis of Meynert) and in the striatum (including insular cortex);

**Phase 4** shows additional A $\beta$  deposits in the brainstem (substantia nigra and central grey);

**Phase 5** shows additional A $\beta$  deposits in the cerebellum and other brainstem nuclei (pontine nuclei, locus coeruleus, parabrachial nuclei, reticulo-tegmental nucleus, dorsal tegmental nucleus, and oral and central raphe nuclei).

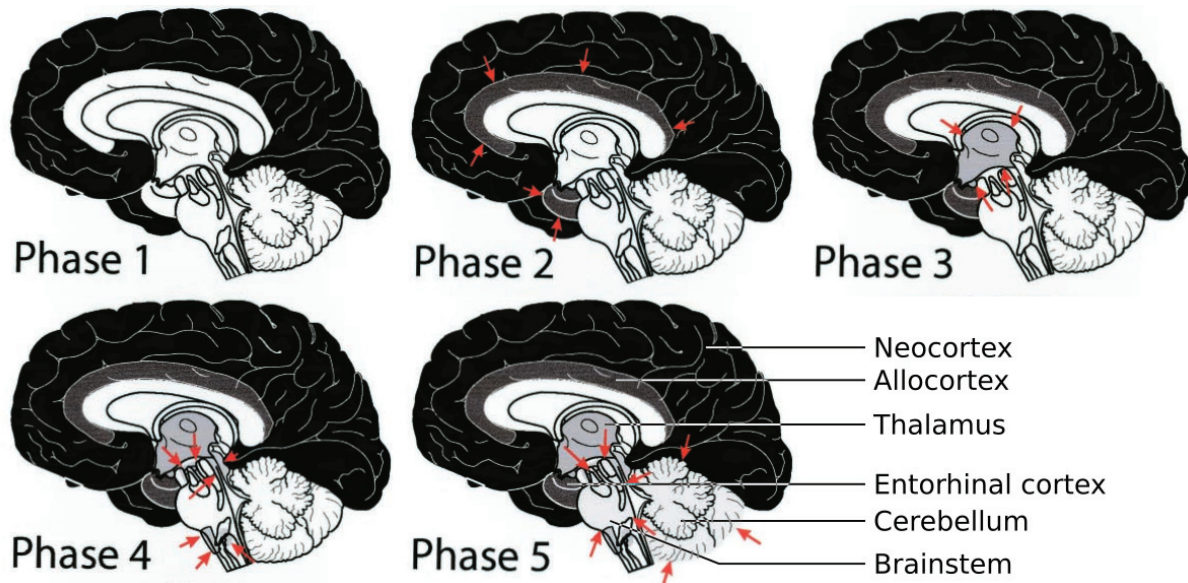


**Figure 1.18.:** Phases of  $\beta$ -amyloidosis. Regions which exhibit A $\beta$  plaques are shown in black and gray shades. Arrows show the development towards new regions. Adapted from [182].

The same team had previously introduced the Braak stages for NFTs, which they slightly revised later [183, 184], as detailed in Figure 1.19.

Two different works pooled the results from these individual assessments into complete descriptors:

- ▶ The NIA-RI Working Group [185] included the CERAD A $\beta$  score and the Braak stages (from the 1991 version);
- ▶ The NIA-AA Research Framework [26] included the CERAD A $\beta$  score, the Braak stages and the Thal-Braak phases.

The NIA-AA "ABC" score and the associated descriptors shown in Table 1.2 are the most up-to-date tools for the neuropathological diagnosis.

For the record, this process is based upon the sampling of a few brain areas that are then sliced. These slices are then stained for a semi-quantitative assessment with a microscope.

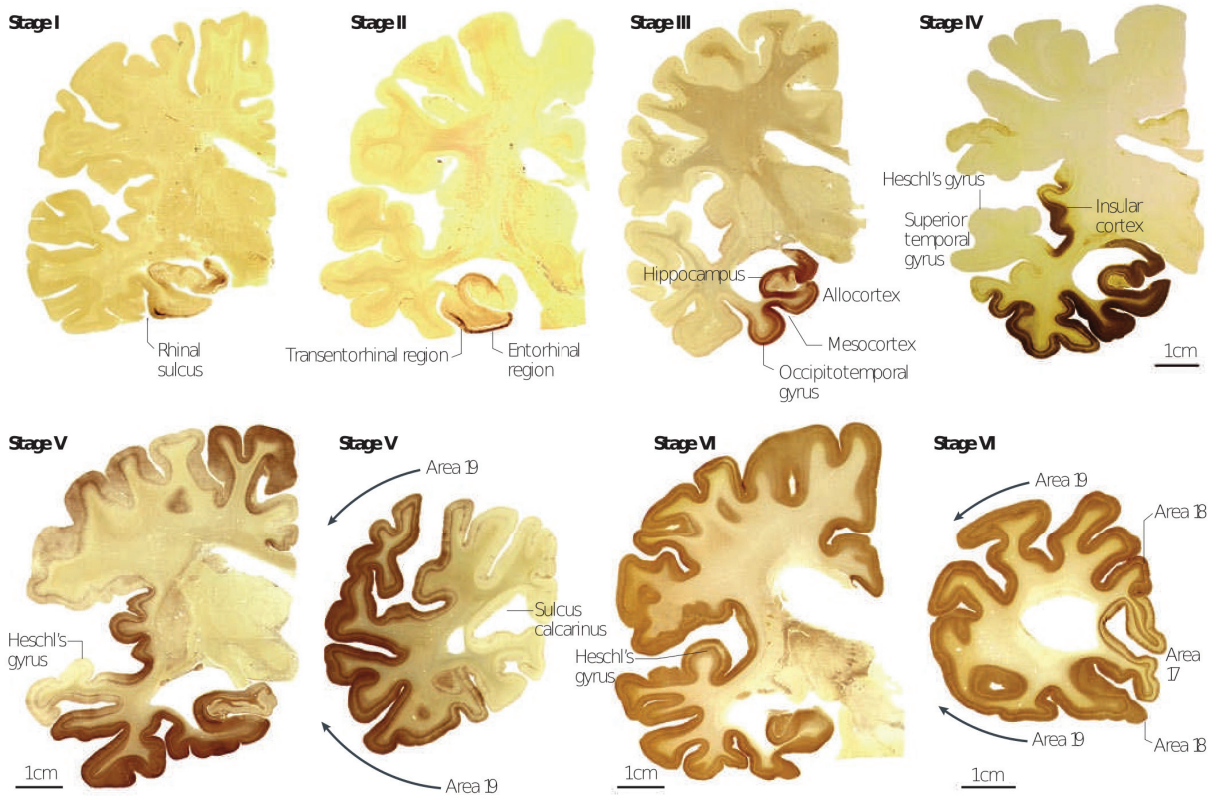


**Figure 1.19.:** Stages I–VI of cortical neurofibrillary pathology in 100 μm polyethylene glycol-embedded hemisphere sections immunostained for hyperphosphorylated tau (AT-8, Innogenetics). From [184].

**Table 1.2.:** Level of AD neuropathological change. \*: particular cases apply, please refer to the original article. From [26].

| A: Aβ/amyloid plaque score (Thal phases) | C: Neuritic plaque score (CERAD) | B: NFT score (Braak stage) |              |               |
|--|----------------------------------|----------------------------|--------------|---------------|
|  |                                  | B0 or B1 (None or I/II)    | B2 (III/IV)  | B3 (V/VI)     |
| A0 (0)                                   | C0 (none)                        | Not*                       | Not*         | Not*          |
| A1 (1/2)                                 | C0 or C1 (none to sparse)        | Low                        | Low          | Low           |
|  | C2 or C3 (mod. to freq.)*        | Low                        | Intermediate | Intermediate* |
| A2 (3)                                   | Any C                            | Low*                       | Intermediate | Intermediate* |
| A3 (4/5)                                 | C0 or C1 (none to sparse)        | Low*                       | Intermediate | Intermediate* |
|  | C2 or C3 (mod. to freq.)         | Low*                       | Intermediate | High          |

The multiple scorings have now been pooled together to account for the majority of pathological changes but they mainly rank the severity of these changes — whether these changes are mild, moderate or severe — and correlate them with the observation of cognitive decline.

## 1.4. Recent developments in A $\beta$ imaging in animal models and human tissue

### Context of the thesis

The thesis focused on x-ray phase-contrast tomography (XPCT; see Chapter 2) as a *postmortem* A $\beta$  imaging technique, for which the samples were whole excised brains (rodents) or cortical samples (deceased human donors). Indeed, the technique is not suitable for *in vivo* imaging at the moment, because of essentially 3 limits:

**Motion:** The brain is subject to motion and deformation because of heartbeat and respiration [186, 187] — motion effects can be reduced with gated acquisitions (cf. subsection 2.4.2);

**Skull:** The highly-attenuating skull creates artifacts during phase-contrast retrieval — this has been tackled in preliminary work by Croton et al. [188];

**Dose:** The radiation dose during acquisitions is well above the 2 Gy threshold for acute radiation syndrome [189] (we estimated a range of 60 to 150 000 Gy per scan, depending on the setup [190]).

Thus, the section below will first properly introduce the rodent research models, followed by an overview of pre-clinical developments in *in vivo* and *postmortem* imaging techniques.

### 1.4.1. Research models for AD

Although most of this chapter focused on clinical research, pre-clinical research on animal models — or smaller scales down to cells and proteins — is driving new discoveries. Animal models can reproduce aspects of the disease — amyloidosis or tauopathy. The most common method is to create transgenic strains [195] (cf. Figure 1.20 for a few examples) from the pool of identified genes for inherited AD (ADAD) (cf. subsection 1.1.2); or, on the contrary, to alter gene expression in "knock-out" models [195].

To get familiar with the rodent brain anatomy, one can refer to the [Mouse Brain Atlas](#) [191] or [Rat Brain Atlas](#) [192, 193, 194] on EBRAINS.

On July 4, 2023, 214 rodent models were listed: 197 mouse models and 27 rat models.

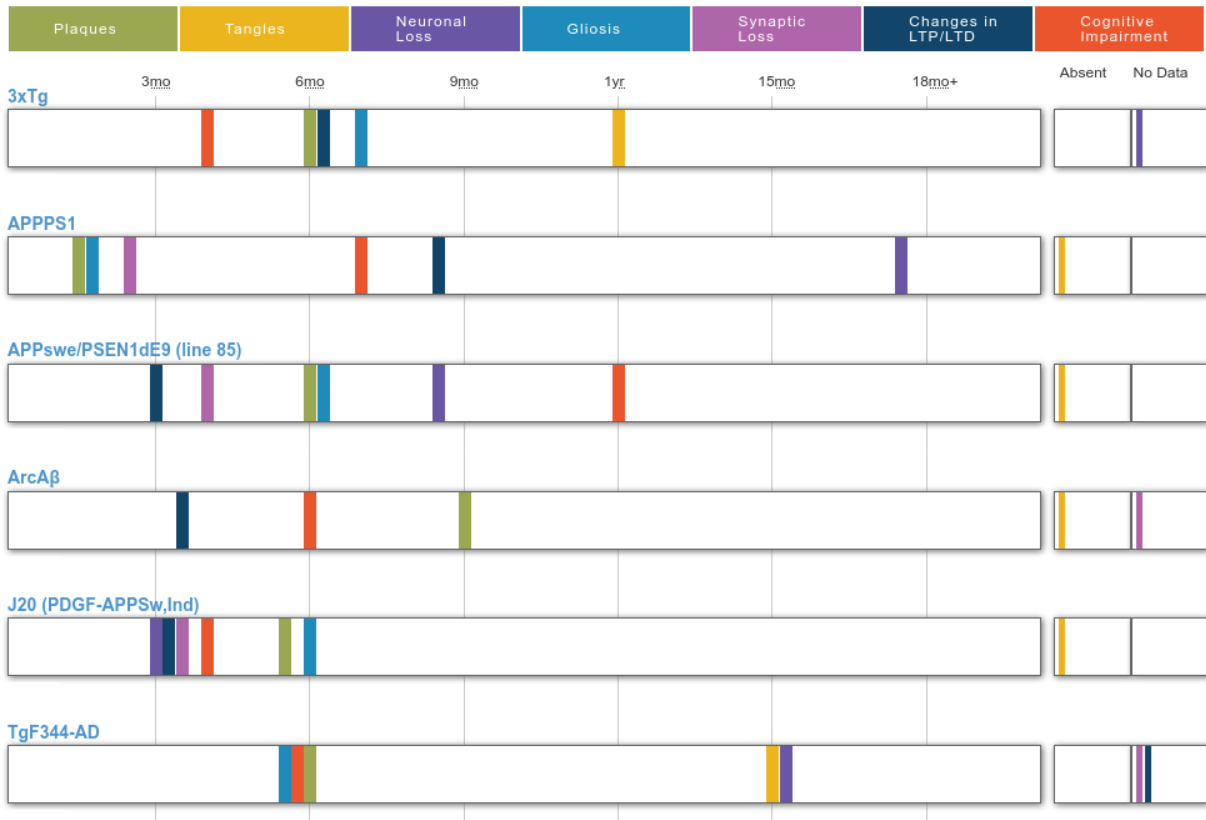


**Figure 1.20.:** Comparison of a selection of research models of AD with a timeline of observed pathophysiological changes. 3xTg, APPPS1, APPswe/PSEN1dE9 (line 85), ArcA $\beta$  and J20 are mouse models while TgF344-AD is a rat model. J20 and ArcA $\beta$  are mono-transgenic models (J20 with 2 mutations on the same gene), APPPS1, APPswe/PSEN1dE9 (line 85) and TgF344-AD are double-transgenic models and 3xTg is a triple-transgenic model with a tau co-pathology. Generated from [195].

### Context of the thesis

The models shown in Figure 1.20 were studied in the articles from the thesis:

- ▶ 3xTg, APPswe/PSEN1dE9 (line 85) — a.k.a. AP-P/PS1 — and J20 in Chapter 4,
- ▶ APPPS1, J20, ArcA $\beta$ , and TgF344-AD in Chapter 5.

In these articles, animals were sacrificed at 12 or 18 months old (see respective Methods), an age when they have all developed a massive amyloid burden in the brain, notably in the hippocampus and in the cortex.

Still, AD transgenic rodents do not have the same pathological phenotype as human AD patients [196, 197]; for instance, amyloidosis first appears in the mouse hippocampus then spreads to the cortex (centrifugal), while it starts in the human cortex then spreads to the deeper areas (centripetal). Other methods rely on the injection of CSF, brain extracts or isolated

A $\beta$  oligomers from AD patients.

### 1.4.2. *In vivo* imaging

A few *in vivo* techniques are emerging; among them, we will discuss new MRI protocols and fluorescence imaging. Both techniques are able to image plaques individually instead of depicting an overall A $\beta$  load.

New non-toxic fluorescent probes enable the detection of A $\beta$  plaques *in vivo* with two-photon imaging [198, 199, 200] but it is limited by its low penetration in the brain — which is even lower through the skull. In a pioneer multimodal study by Ni et al. [201], transcranial fluorescence imaging and volumetric multispectral optoacoustic tomography (vMSOT) were combined *in vivo* and validated with *postmortem* light-sheet microscopy (see below); the first technique was able to image the cortical A $\beta$  plaques at a resolution of 8  $\mu\text{m}$  — using the HS-169 probe and large-field multifocal illumination microscopy — while the second technique could image A $\beta$  in the whole mouse brain at a resolution of 113 to 157  $\mu\text{m}$  — with a targeted oxazine-derivative AOI987 dye.

A $\beta$ -targeted nanoparticles (NP) improve the signal-to-noise ratio of MRI, such as curcumin-conjugated NPs [202] or GdF<sub>3</sub> NPs [203] (the latter are also a contrast agent for x-ray imaging); the main challenge for NPs is to cross the blood-brain barrier [204].

Finally, retinal imaging is promising for AD diagnosis [205]: using a hyperspectral ophthalmoscope, this team was able to separate the 5xFAD mice (an AD model) and wild-type littermates solely based on retinal images. A 550 nm hump was detected in images from the 17-month-old transgenic mice, which the team linked to A $\beta$  deposition. At younger ages, a hump in shorter wavelengths around 450 nm could indicate the presence of A $\beta$  oligomers. This ophthalmoscope is cheaper than other diagnosis devices, thus it could help the spread of screening campaigns in low-income populations. Optical coherence tomography (OCT) is a similar technique which has been thoroughly studied and may be able to differentiate AD based on “AD-specific patterns of retinal structural and microvascular changes” [206]. However, both techniques suffer from the potential drawbacks of indirect imaging.

### 1.4.3. *Postmortem* imaging of individual plaques

As for *postmortem* techniques, two main approaches are developing concomitantly: 2D tissue characterisation and 3D virtual histology at the micrometric scale. They are also able to image plaques individually instead of depicting an overall A $\beta$  load.

Fourier-transform infrared spectrometry (FTIR, cf. subsection 2.5.2) and X-ray fluorescence spectrometry (XRF, cf. subsection 2.5.1) are two complementary techniques for 2D tissue characterisation. FTIR analyzes the molecular structure of the tissue to reveal the fibril composition that is specific of proteinopathies [207]. XRF, like other techniques such as induced coupled plasma mass spectrometry (ICP-MS), identifies the trace elements in the tissue [208]; most results from subsection 1.2.2 come from these modalities. Compared to other techniques, FTIR and XRF are less destructive and they are both available at synchrotron facilities (cf. subsection 2.1.1); thus, they have already been associated several times for the study of A $\beta$  plaques [103, 104, 196, 209].

Virtual histology of the brain has been developed in the last two decades to preserve the 3D structure of A $\beta$  plaques [210] or other anatomical landmarks [211]. Its concept is simple: to optimize the sample contrast with a non-destructive preparation and to scan it in 3D at a high resolution for 3D digital analysis. Three major methods have arisen: *ex vivo* MRI [212], light-sheet microscopy (LSM) on cleared samples [213] and x-ray imaging [211].

$T_2^*$ -weighted MRI [93, 212, 214] and susceptibility-weighted MRI [93, 215] are sensitive to the higher iron content of AD brains; thus, they are a mean of indirect detection for AD. Still, they could not detect individual plaques. However, Dhenain et al. [216] were able to detect large A $\beta$  plaques *in vivo* thanks to their iron load. The same group used Gd-enhanced MRI to detect insoluble A $\beta$  plaques as hyposignals [217].

A variety of clearing methods exist [218, 219]; they both make the tissue transparent to improve light penetration and ease the diffusion of targeted dyes and antibodies. This has enabled the whole-brain 3D study of A $\beta$  deposits [220, 221, 222, 223]. Besides, LSM is well suited for the analysis of the brain vasculature [222, 224, 225], including its alterations in

AD [222, 226]. They greatly alter the form of the sample, either by swelling or by shrinkage, in an anisotropic manner.

Sarri et al. [227] have demonstrated the ability of stimulated Raman scattering to obtain an equivalent histology colormap based on molecular composition on 3D samples, through a correlative approach with standard H&E staining; this technique bridges the gap between 2D molecular imaging and 3D imaging and it may rapidly be available for clinical applications.

For x-ray imaging, the development of new dyes for contrast-enhanced computed tomography is a lead towards the clinical application of this technique [228, 229]; Kavkova et al. [228] designed an iodine-based contrasting protocol that would stain the brain tissue but not the plaques because of their dense nature, resulting in an hyposignal for the plaques. Phase-contrast x-ray imaging is able to detect  $A\beta$  plaques in AD models [210, 230, 231, 232, 233, 234, 235, 236, 237, 238] and in AD patients [236]; this has enabled the study of their morphology and distribution [232, 235, 238].



# X-ray phase-contrast tomography 2.

## Context of the thesis

The imaging technique which was extensively used during the thesis is known as x-ray phase-contrast tomography (XPCT). Currently, it is easily performed at synchrotron facilities (cf. subsection 2.1.1). Once the sample is scanned in 3D with XPCT, one can perform virtual histology, i.e. browse through the 3D image and analyze 3D features.

## 2.1. Physics

### 2.1.1. Synchrotron radiation

The synchrotron is a circular particule accelerator which produces electromagnetic (EM) waves from electrons. These EM waves have an array of specific properties, hence they are referred to as synchrotron light or synchrotron radiation (SR) [239]:

1. The flux or emitted power is high — e.g. each electron in a 2 GeV-synchrotron emits  $\sim 0.42 \mu\text{W}$  in each bending magnet and there are  $\sim 10^{12}$  circulating electrons [239];
2. Their brightness\* is more than 1 000 000 the brightness of x-ray tubes and even higher than the brightness of the sun (cf. Figure 2.1);
3. The spectrum of radiated energies is wide — ranging from 0.01 keV (infrared) to 1 MeV (X rays) (cf. Figure 2.1);
4. The SR source is highly coherent — as this is a key notion, it is further detailed on page 39;
5. The SR beam is very stable — because the electrons circulate in a near-vacuum that is free of collision events;
6. SRs have a pulsed time structure — electrons are grouped into "bunches" of 10–100 ps separated by a few nanoseconds;
7. SRs are linearly polarized — because the electric and magnetic fields in the SR sources do not rotate and the trajectory of the electrons is planar.

|       |  |    |
|-------|--|----|
| 2.1   | Physics . . . . .  | 35 |
| 2.1.1 | Synchrotron radiation . . . . .                          | 35 |
| 2.1.2 | X-ray interaction with matter . . . . .                  | 40 |
| 2.2   | Reconstruction . . . . .                                 | 44 |
| 2.3   | Phase retrieval . . . . .                                | 46 |
| 2.4   | Current biomedical applications . . . . .                | 48 |
| 2.4.1 | Benefits of the technique . . . . .                      | 48 |
| 2.4.2 | Applications on soft-tissue imaging . . . . .            | 49 |
| 2.4.3 | Other applications . . . . .                             | 51 |
| 2.5   | Other synchrotron-based techniques . . . . .             | 51 |
| 2.5.1 | X-ray fluorescence (XRF) . . . . .                       | 52 |
| 2.5.2 | Fourier-transform infrared spectroscopy (FTIR) . . . . . | 53 |

\*: Brightness is defined as [240]:

$$b \propto \frac{F}{\Sigma\Omega}$$

where  $F$  is the flux,  $\Sigma$  the area of the source and  $\Omega$  the solid angular divergence of the emission; the unit of  $b$  is photons/s/mm<sup>2</sup>/mrad/0.1%BW (BW: spectral bandwidth).

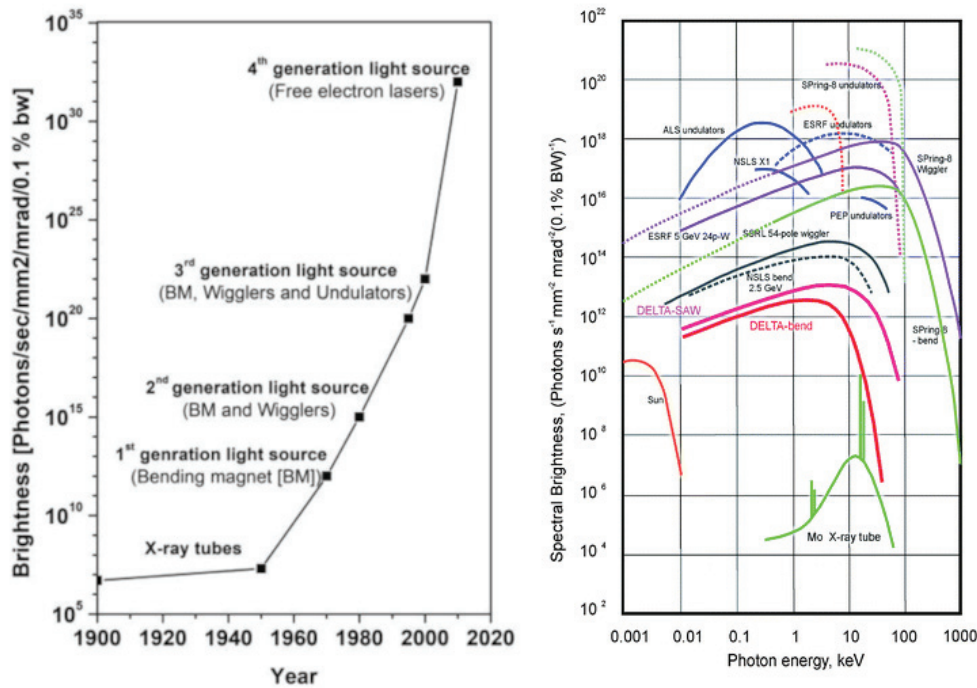


**Figure 2.1.:** Evolution of the average brightness of x-ray and synchrotron-radiation sources throughout the years (left) and relationship between photon energy and brightness of a few facilities (right). From [241] (left) and [242] (right).

Properties 6 and 7 are not relevant for XPCT, thus they will not be discussed below.

The synchrotron radiation facilities use this synchrotron radiation to conduct experiments on matter, e.g. non-destructive material study and biochemical characterization. There are currently about 50 facilities around the world, according to [lightsources.org](https://lightsources.org) (visited on June 22, 2023). Different energies and scales enable a variety of techniques.

### Context of the thesis

During the PhD project, experiments were performed at two facilities: SOLEIL (Gif-sur-Yvette, near Paris, France) and ESRF (European Synchrotron Radiation Facility; Grenoble, France). They have respective energies of 2.75 GeV and 6 GeV, along with circumferences of 354 m and 844 m.

The accelerator is composed of 4 elements (cf. Figure 2.2):

- ▶ A particle source, usually an electron gun;
- ▶ A linear accelerator, to speed up the ejected electrons;
- ▶ A circular booster accelerator to further speed up the

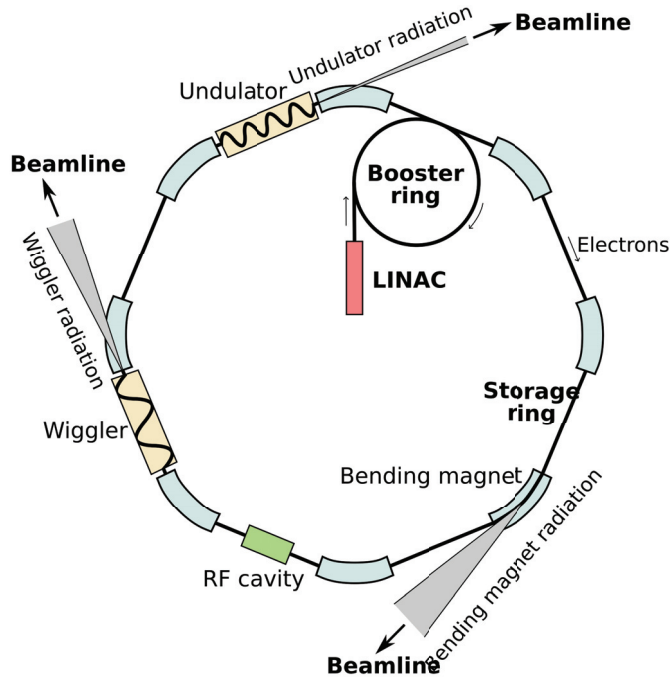


**Figure 2.2.:** Schematic of a synchrotron showing the linac, booster and storage rings, and the magnetic devices that produce the synchrotron radiation. Adapted from [243].

electrons — the final velocity is very close to  $c$ , the speed of light in the vacuum;

- ▶ A storage ring where the electrons will loop close to the nominal energy — systems along the path of the electrons serve different purposes:
  - bending magnets (BM) which curve the trajectory of the electrons within the ring — they are the first-generation synchrotron-radiation sources (cf. Figure 2.1);
  - insertion devices (ID) — wigglers or undulators — in the linear sections, which are the second- and third-generation synchrotron-radiation sources (cf. Figure 2.1);
  - radiofrequency (RF) cavities also in the linear sections, to maintain the speed/energy of the electrons and group them into bunches.

When a force is applied to an electron to follow a curved trajectory, the speed of the electron decreases in the tangent direction. At relativistic speed — i.e.  $v/c \approx 1$  — like in the storage ring, this depleted energy is radiated into a tangent beam of EM waves (cf. Figure 2.3). The half-angle  $\psi$  of the beam is given by  $\psi \approx \gamma^{-1}$  [239] with the Lorentz factor  $\gamma = \frac{1}{\sqrt{1-v^2/c^2}}$ , which determines the impact of relativistic effects ( $\gamma$  can also be seen as the ratio between the relativistic energy and the energy at rest). Hence, bending magnets

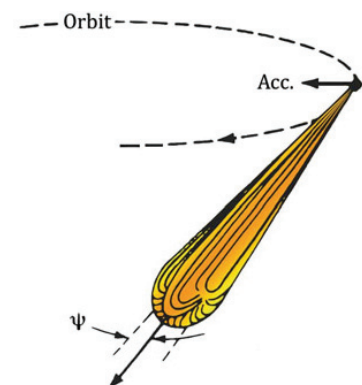


**Figure 2.3.:** At relativistic speed, an electron radiates a tangent beam within a cone of half-angle  $\psi$ . From [239].

are the most intuitive way to produce synchrotron radiation from electrons, which are sensitive to the Lorentz force of an electromagnetic field [244]:

$$\frac{d\mathbf{p}}{dt} = q(\mathbf{E} + \mathbf{v} \times \mathbf{B}) \quad (2.1)$$

where  $\mathbf{p}$ ,  $q$  and  $\mathbf{v}$  are the momentum, charge and velocity of the electron, and  $\mathbf{E}$  and  $\mathbf{B}$  are the electric and magnetic fields. Considering a sole electron at 1 GeV,  $\psi \approx 0.5$  mrad: the SR beam is highly collimated; however, electrons circulate by bunches (with a small non-negligible cross-section) in the storage ring so the collimation of the SR beam is slightly diminished [245]. Besides, the radiation emission is a stochastic event, which does not occur at the exact same time for all the electrons in the bunch. The SR beam is collected into a so-called beamline. The energy loss by radiation needs to be compensated by one or more RF cavities in the storage ring.

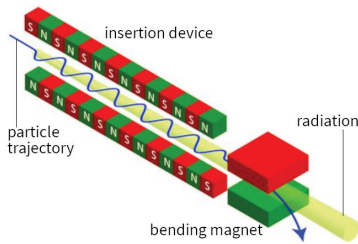


**Figure 2.4.:** Insertion device on the storage ring. From [246].

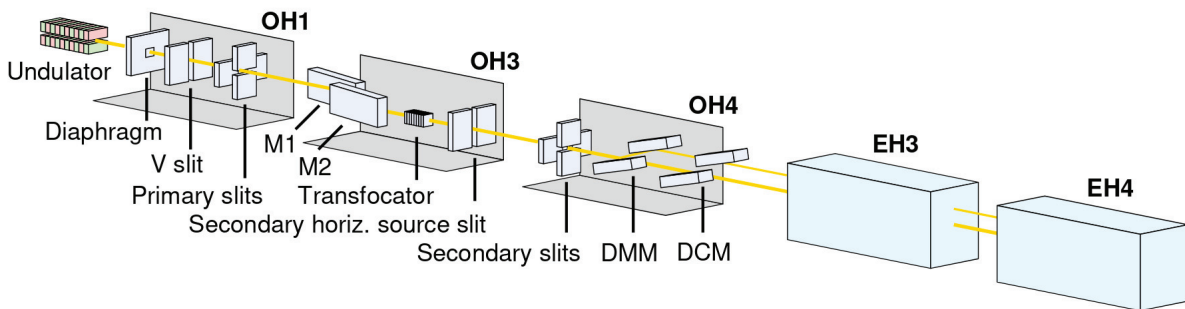
However, the angle of the SR beam generated by bending magnets is too wide for applications which require a high spatial coherence and the intensity of the beam is not sufficient (cf. Figure 2.1). This is why wigglers and undulators have been developed [247, 248]. Both IDs have a common setup (cf. Figure 2.4): they are made of dipoles, i.e. opposite magnetic poles, which are successively upside-down. The succession of vertically flipped dipoles creates a wavy trajectory and multiple tangent SR beams are generated. They interfere in constructive and destructive ways. The wigglers generate a series of short SR pulses with a continuous spectrum (they act as a series of small bending magnets) and the undulators generate a longer pseudo-monochromatic SR pulse with a better collimation [249].

Beamlines are built in front of most synchrotron-radiation sources (either BM or ID). These beamlines act as independent laboratories, where the setup is optimized for a specific scientific application. They are usually composed of 3 different sections:

1. An “optical hutch” where the SR beam is re-collimated and its spectrum is narrowed to the appropriate bandwidth;
2. An “experiment hutch” or “sample hutch” with the final equipment, such as the imaging devices;
3. The “control hutch” with the monitoring stations.

The optical hutch is usually not accessible to the end user, unless the beamline or the whole facility is under maintenance.

As stated above, a bunch of electrons in a BM or ID acts as an SR source for the beamline. This source is *spatially* highly coherent because the transverse cross-section of the bunch of electrons is small and the synchrotron radiation is highly collimated. Still, the horizontal collimation of BMs is not sufficient so that beamlines often require to have horizontal slits at the beginning of the "optical hutch". The generated synchrotron radiation is also *temporally* highly coherent because of the pulsed structure of the bunch, although the phase drifts within a multi-energy radiation. Hence, the temporal coherence deteriorates with the distance from the SR source. Where needed, this is corrected with a monochromator within the optical hutch, which narrows the bandwidth of the spectrum.



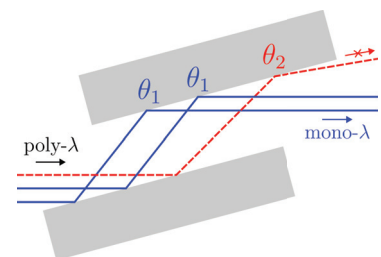
**Figure 2.5.:** The ANATOMIX beamline (SOLEIL, Gif-sur-Yvette, France) as an example of beamline for phase-contrast imaging. The translocator is a set of refractive lenses which collimate the beam. The M1–M2 mirror pair acts as a secondary source. The DMM and DCM are two different monochromators. EH3 is for propagation-based XPCT and EH4 for grating-interferometer XPCT. From [250].

Figure 2.5 shows an example of a beamline for x-ray phase-contrast tomography. The monochromators such as the double-crystal monochromator (DCM) or the double-multilayer monochromator (DMM) use the Braag's law [251]:

$$n\lambda = 2d \sin \theta \quad (2.2)$$

to diffract the different wavelengths twice and select one of them, obtaining a monochromatic beam — or a narrower spectrum bandwidth (cf. Figure 2.6).

The synchrotron radiation sources have evolved from bending magnets to wigglers and undulators (cf. Figure 2.1). The facilities have started to upgrade their storage ring technology [252], like the ESRF-EBS upgrade [253]. Free-electron



**Figure 2.6.:** The principle of a monochromator.

lasers [254] like the European XFEL (Schenefeld / Hamburg, Germany; <https://www.xfel.eu/>) [255] are even brighter than insertion devices and reach higher rates of x-ray pulses per second. They do not require a synchrotron storage ring but they have a lower numbers of beamlines (from 3 to 6).

### 2.1.2. X-ray interaction with matter

When a high-energy photon in the X-ray spectrum interacts with matter, multiple phenomena are in competition, depending on the exact path of the photon and its energy. They are shown in Figure 2.7 and detailed thereafter [256]:

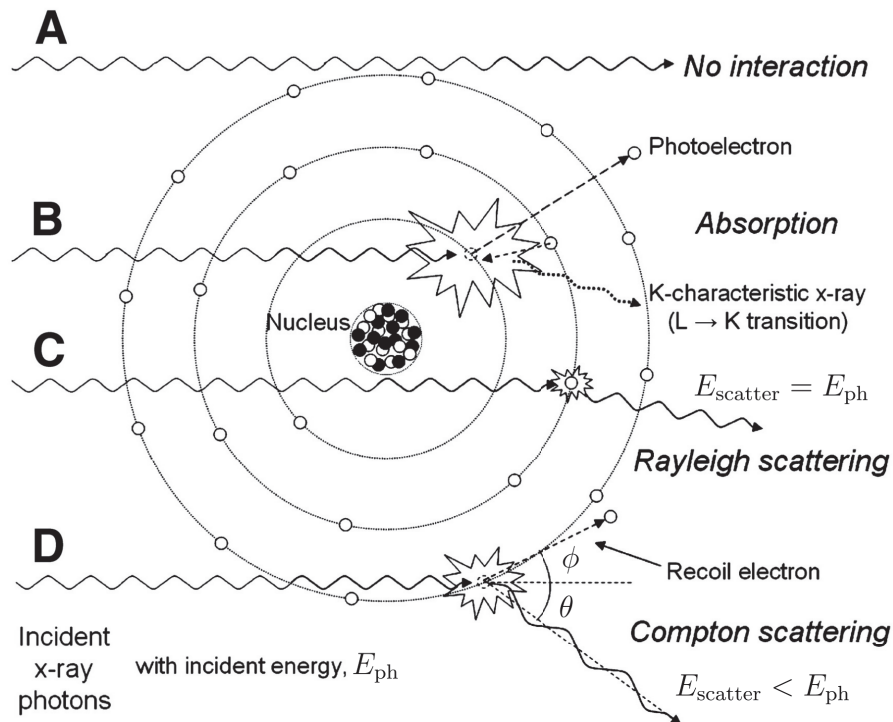


**Figure 2.7.:** The interaction of X rays with matter. (A) Primary, unattenuated beam does not interact with material. (B) Photoelectric absorption results in total removal of incident x-ray photon with an energy greater than the binding energy of an electron in its shell, with excess energy distributed to kinetic energy of photo-electron. (C) Rayleigh scattering is an interaction with an electron (or whole atom) in which no energy is exchanged and the incident x-ray energy equals the scattered x-ray energy with a small angular change in direction. (D) Compton scattering interactions occur with essentially unbound electrons, with transfer of energy shared between recoil electron and scattered photon, with energy exchange described by Klein–Nishina formula. From [256].

**Photoelectric absorption:** When an incident x-ray photon (of energy  $E_{\text{ph}}$ ) interacts with an inner shell electron, the x-ray photon transfers its energy to the electron, which is ejected. For this effect to occur, the binding energy  $E_{\text{bind}}$  of the electron must be inferior than — and

close to  $-E_{\text{ph}}$ ; the ejected electron will have a kinetic energy  $E_{\text{eject}} = E_{\text{ph}} - E_{\text{bind}}$ . Instead, if  $E_{\text{bind}} > E_{\text{ph}}$ , the photoelectric absorption cannot occur: this is why there are discontinuities for the binding energy of each shell. The vacated inner electron shell is filled by a cascade of electron transitions, each of them emits characteristic photons with an energy equal to the difference between the two binding energies of the shells — e.g., for a transition from L to K,  $E_{\text{L} \rightarrow \text{K}} = E_{\text{bind,K}} - E_{\text{bind,L}}$ . The ejected electron can contribute to more effects.

**Rayleigh (elastic) scattering:** The incident x-ray photon of energy  $E_{\text{ph}}$  can temporarily transfer all its energy to a bound atom, which will emit a new photon with the same energy  $E_{\text{scatter}} = E_{\text{ph}}$  but in a slightly different direction. This process occurs rarely in soft tissues, because it is dependent on the atomic number  $Z$  of the elements. Rayleigh scattering requires the particle to be smaller than the wavelength of the photon, which is the case for x-ray photon–electron interactions; Rayleigh scattering is a specific application of an effect known as Mie scattering.

**Compton (inelastic) scattering:** When an incident x-ray photon (of energy  $E_{\text{ph}}$ ) interacts with an outer shell electron of binding energy  $E_{\text{bind}} \ll E_{\text{ph}}$  — or an unbound electron —, the photon partially transfers its energy to the electron, which is ejected with an angle  $\phi$  ( $0 < \phi \leq \pi/2\text{rad}$ ); the remaining energy  $E_{\text{scatter}}$  is transferred to a scattered x-ray photon with an angle  $\theta$  which follows the Klein–Nishina equation,

$$\frac{E_{\text{scatter}}}{E_{\text{ph}}} = \frac{1}{1 + \frac{E_{\text{ph}}}{m_e c^2} (1 - \cos \theta)} \quad (2.3)$$

where  $m_e c^2 = 511 \text{ keV}$  is the rest energy of an electron.

**Pair production:** For high-energy incident photons ( $E_{\text{ph}} > 1.02 \text{ MeV}$ ), the photon interacts with the nucleus of the atom and its energy is converted into a pair of particles, an electron and a positron; they are ejected and the positron subsequently annihilates with an electron into two photons of energy  $511 \text{ keV}$  (the rest energy of an electron). This process occurs more frequently for higher atomic numbers  $Z$  and higher photon energies.

Note that although the particle definition of the x-ray radiation was used here, the scattering and photo-absorption

interaction processes can also be easily determined using the wave equations [257].

The probabilities of each event are often referred to as energy-dependent cross-sections — the higher the cross-section, the higher the chances. For instance, Figure 2.8 shows the cross-sections for carbon (an element that is abundant in biological samples) and iodine (as an example of a higher-Z element which is used in contrast agents): scattering and photo-absorption are the prominent effects in the energy range of synchrotron radiations. The mass interaction coefficient in  $\text{cm}^2 \text{g}^{-1}$  is another measure of these probabilities.

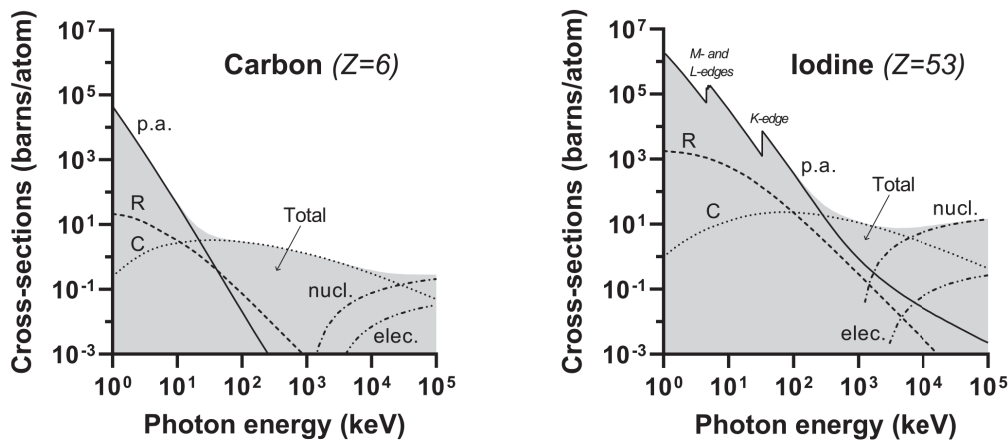


**Figure 2.8.:** Cross-sections of the different interactions of X rays with matter for two elements: carbon (left) and iodine (right). p.a.: photoelectric absorption; R: Rayleigh scattering; C: Compton scattering; nucl.: nuclear pair production; elec.: electron pair production. The gray area is the summed cross-section. Note that the photoelectric absorption cross-section of iodine has discontinuities; the K-edge of carbon is at a lower energy, 282 eV [258]. 1 barn =  $1 \times 10^{-24} \text{ cm}^2$ . Redrawn from [259].

### The complex refractive index

Using the wave definition of x-ray radiation, the complex refractive index describes the propagation of X rays through the different media and how they are affected by the medium interfaces.

When an EM wave propagates in the vacuum, its velocity is  $c = 299\,792\,458 \text{ m s}^{-1}$ . In any medium, the phase velocity becomes  $v = \frac{c}{n}$  with  $n$  the refractive index of the medium, which is a function of the wavelength (because the medium disperses the radiation). But this refractive index does not account for the photoelectric absorption. Besides, the refractive index can drop below 1 for X rays, this is the anomalous dispersion; the scattered wave is then phase-shifted by  $\pi$  rad

with a dispersion angle that is smaller than the incident angle. Hence, a complex index of refraction was introduced [257, 260]:

$$\underline{n} = n + i\beta \quad (2.4)$$

where  $\beta$  is the absorption index. Besides,  $n \lesssim 1$ : we can introduce the refractive-index decrement from unity,  $\delta$ , so that  $n = 1 - \delta$ . Equation 2.4 can then be written as [260]:

$$\underline{n} = 1 - \delta + i\beta \quad (2.5)$$

### Context of the thesis

This notion was extensively used in the articles from the thesis, as a key parameter of the phase-contrast retrieval algorithms which were used in these articles builds upon the assumption of a homogeneous material of fixed  $\delta/\beta$  ratio [261] (cf. section 2.3).

Far from absorption discontinuities,

$$\delta = \frac{\rho_e r_e \lambda^2}{2\pi} \quad (2.6)$$

with  $r_e = 2.82 \times 10^{-15}$  m the classical radius of a free electron and  $\rho_e$  the average electron density [260]. Note that, for a material of known mass density  $\rho$  and known composition  $\{(w_i, A_i, Z_i) \mid \forall i \text{ element}\}$  [263],  $\rho_e = \rho N_A \frac{\sum w_i Z_i}{\sum w_i A_i}$  with Avogadro's number  $N_A$ .

When X rays are transmitted through a material, the intensity follows the Beer–Lambert law:

$$I = I_0 \exp(-(\mu/\rho) \rho z) \quad (2.7)$$

and the absorption index  $\beta$  is linked to linear attenuation coefficient  $\mu$  by [260]:

$$\mu = \frac{4\pi\beta}{\lambda} \quad (2.8)$$

The (energy-dependent)  $(\delta, \beta)$  pair for a material fully characterizes the interactions of X rays with this material. The  $\frac{\delta}{\beta}$  ratio is an energy-dependent function which is also specific to each material. The U.S. National Institute of Standards and Technology (NIST) has published a complete dataset [265]; rather than  $\delta$  and  $\beta$ , they report the real ( $f_1$ ) and imaginary

The literal expression of  $r_e$  is:

$$r_e = \frac{e^2}{4\pi\epsilon_0 m_e c^2}$$

with  $e$  the elementary charge,  $m_e$  the mass of an electron and  $\epsilon_0$  the permittivity of free space [262].

$(\mu/\rho)$  is easier to tabulate [264] than  $\mu$  because it is absolute for every element, whereas  $\mu$  may vary (e.g. for carbon between graphite and diamond).

( $f_2$ ) parts of the form factor which relate respectively to  $\delta$  and  $\beta$ , as detailed in the article by Chantler [264].

## 2.2. Reconstruction

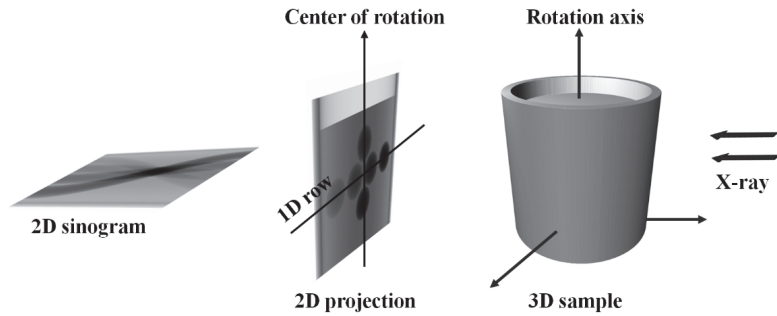


**Figure 2.9.:** Schematics of parallel-beam x-ray tomography. From [266].

Tomography consists into reconstructing a volume from a set of projections (cf. Figure 2.9). At a synchrotron radiation facility, the parallel beam approximation is very accurate because the x-ray primary or secondary source is quite far from the sample and collimators are often set up in the optical hutches (cf. Figure 2.5). This approximation greatly simplifies the reconstruction approach.

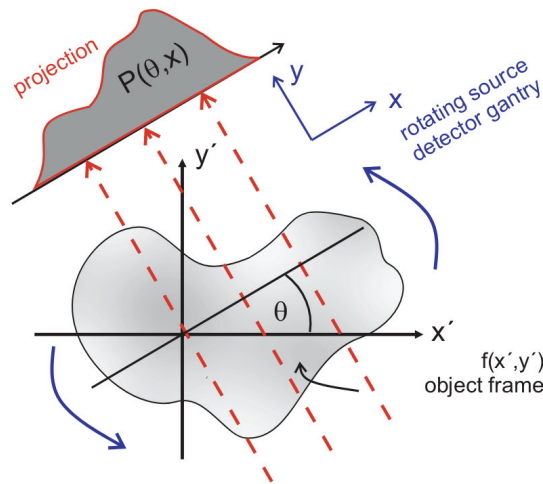


**Figure 2.10.:** The projection geometry in 2D based on line integrals, with the source detector gantry  $(x, y)$  rotated with respect to the Cartesian object frame  $(x', y')$  by  $\theta$ . From [267].

Formally, let's assume the source is rotating around the sample (although it is the opposite at a synchrotron facility), as shown in Figure 2.10: the object system  $(x', y', z')$  is fixed and the source system  $(x, y, z)$  rotates around  $z' = z$  with  $\theta$  the angle between  $x$  and  $x'$ . The beam propagates in the  $y$  direction. Each detector pixel in  $(x, z) := (x, y = y_{\text{detector}}, z)$  records a line integral of  $f(x, y, z)$  over  $y$ . Let

$P(\theta, x)$  be a projection, each plane normal to  $z$  can be treated independently [267]:

$$P(\theta, x) = \sum_z P_z(\theta, x) \quad (2.9)$$

so that the 2D function  $f_z(x, y) := f(x, y, z)$  yields a 1D curve when integrated over  $y$  for each detector pixel [267]:

$$\begin{cases} P_z(\theta = 0, x) = \int_{-\infty}^{\infty} f_z(x, y) dy \\ P_z(\theta, x) = \int_{-\infty}^{\infty} f_z(x \cos \theta - y \sin \theta, x \sin \theta + y \cos \theta) dy \end{cases} \quad (2.10)$$

One can introduce  $\mathcal{R}$  so that  $P_z(\theta, x) = \mathcal{R} f_z$ :  $\mathcal{R}$  is called the Radon transform [268]. Hence, the goal of reconstruction is to determine a 2D inverse operator  $\mathcal{R}^{-1}$  to apply:

$$f_z = \mathcal{R}^{-1} P_z \quad (2.11)$$

**Theorem 2.2.1** (Fourier slice theorem [269]) *With  $\tilde{P}_z(\theta, k)$  and  $\tilde{f}_z$  the Fourier transforms of  $P_z(\theta, x)$  and  $f_z$ ,*

$$\tilde{P}_z(\theta, k) = \sqrt{2\pi} \tilde{f}_z(k \cos \theta, k \sin \theta)$$

The Fourier slice theorem in Theorem 2.2.1 (illustrated in Figure 2.11) implies that angular sampling must satisfy [267]:

$$k_{max} \Delta \theta \leq \Delta k \quad (2.12)$$

$$\Leftrightarrow N_\theta := \frac{\pi}{\Delta \theta} \geq N \frac{\pi}{2} \quad (2.13)$$

Or that the number of projections  $N_\theta$  must be greater than the number of pixels  $N$  along a given direction, times a  $\pi/2$  factor. Hence, the number of acquired projections is critical to have a well-posed problem.

The sole Radon transform however induces a blur while doing simple back projection [270]. Indeed, the lower frequencies are oversampled compared to the higher frequencies, as shown in the panel (c) of Figure 2.11. This is why a weight as a ramp proportional to the spatial frequency has been introduced in the so-called filtered-back-projection (FBP)

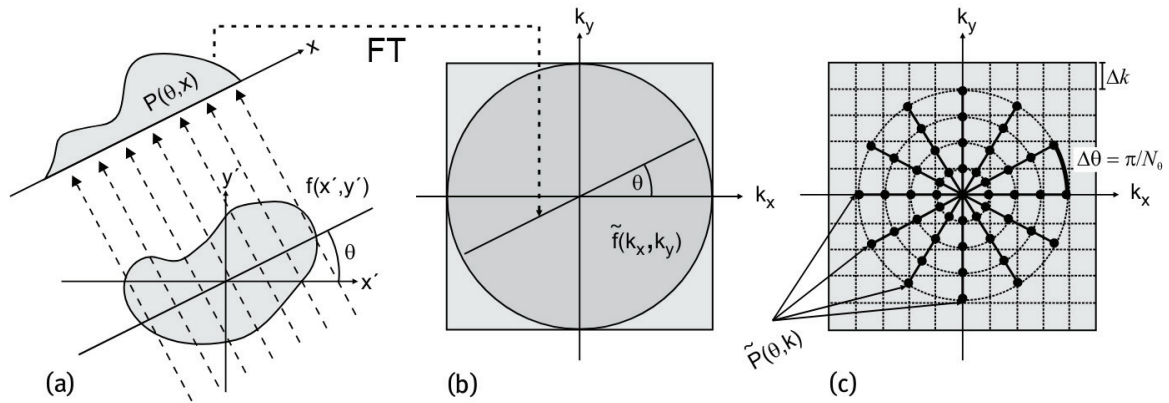


**Figure 2.11.:** Visualization of the Fourier slice theorem. The 1D Fourier transform  $\tilde{P}_z(\theta, k)$  of a projection  $P_z(\theta, x)$  obtained as shown in (a) corresponds to a line cut in the 2D Fourier transform  $\tilde{f}_z(k \cos \theta, k \sin \theta)$  of the object plane  $f_z(x', y')$ , as sketched in (b). (c) The density of (discrete) data points falls off as  $1/k$ , posing a challenge to sample the high spatial frequencies. Provided there is sufficient number of projections and suitable regridding, 2D fast Fourier transform (FFT) algorithms can be used to reconstruct  $f_z(x', y')$  in each plane. From [267].

algorithm for reconstruction [270]. The FBP algorithm is implemented in the PyHST2 software [271], currently in use at ANATOMIX. ASTRA is another toolbox for reconstruction [272] which implements another algorithm named the SIRT-filter reconstruction [273]; this algorithm uses a pseudo-iterative approach combined with FBP.

### 2.3. Phase retrieval

Phase objects — which have a low absorption profile — can be detected and resolved with phase-sensitive techniques like x-ray phase-contrast tomography (XPCT), using refraction in addition to attenuation.

To retrieve the phase, a variety of methods are available for coherent sources. Two main methods are detailed below: the propagation-based phase retrieval and the grating-interferometry phase retrieval. They require different phase-contrast imaging setups. The plane x-ray wavefront which hits the sample is both absorbed and slightly refracted depending of the complex refractive index of the sample (cf. section 2.1.2).

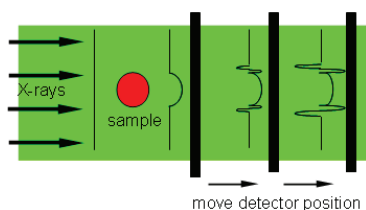


**Figure 2.12.:** The principle of propagation-based XPCT. From Wikipedia, CC BY-SA 3.0.

**Propagation-based XPCT [274]:** By moving the detector further away from the sample, these refracted rays interfere together before reaching the detector and create interference fringes on the detector, around the

projected edges of the sample (cf. Figure 2.12). This pattern creates intensity variations in the projections which are proportional to the Laplacian of the phase [275]. The Paganin method [261] assumes the sample is homogeneous (constant  $\delta$  and  $\beta$ ) so that  $\Phi = \delta t$  (the phase is proportional to the thickness with  $\delta$  as a factor); hence, one can retrieve the phase map in the plane of the slice before reconstruction [276]:

$$\Phi(x, y) = \frac{1}{2} \frac{\delta}{\beta} \ln \left( \mathcal{F}^{-1} \left\{ \frac{\mathcal{F}\{I_s(x, y)/I_r(x, y)\}(f)}{1 + \lambda D \pi \frac{\delta}{\beta} \|f\|^2} \right\} (x, y) \right) \quad (2.14)$$

where  $I_s(x, y)$  and  $I_r(x, y)$  are the images acquired with and without the sample, at a distance  $D$ ; as all the variables can be determined, this computation based on Fourier transforms and a logarithm is trivial to implement in order to obtain  $\Phi(x, y)$ .

**Grating-interferometry XPCT [277]:** By placing a grating (a *phase* grating with a low absorption but a high phase shift) right after the sample, the diffracted beam generates interference fringes that are slightly displaced by the phase of the sample; these displacements are however inferior to the pixel size, hence another grating right in front of the detector acts as a transmission mask and the phase  $\varphi(x, y)$  of the signal intensity oscillations is proportional to the gradient of the phase  $\Phi(x, y)$  (cf. Figure 2.13):

$$\varphi = \frac{\lambda d}{g_2} \frac{\partial \Phi}{\partial x} \quad (2.15)$$

and  $d$ , the distance between the two gratings, should satisfy the criterion for Talbot effect:

$$\exists m \in \mathbb{N}^* \quad \left( m - \frac{1}{2} \right) \frac{g_1^2}{4\lambda} \quad (2.16)$$

where  $g_1$  and  $g_2$  are the periods of the gratings — for an incident plane wave,  $g_2 = g_1/2$ . To reconstruct the phase, multiple images at multiple positions  $x_g$  (blue arrow) of the second grating are required — 4 to 8 is usually suitable — to integrate  $\varphi$  and obtain  $\Phi$ . Note that this method only retrieves the phase in one of the directions in the projection plane.

The propagation-based setup is the most simple, although the possibility of a mobile detector over a few meters must

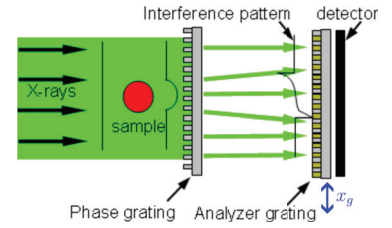


**Figure 2.13.:** The principle of grating-interferometry XPCT. From Wikipedia, CC BY-SA 3.0.

be taken into account during the design of the experiment hutch.

The transition of XPCT towards smaller devices is already possible [275]. Liquid-metal-jet sources provide a sufficient spatial coherence for phase contrast and cone-beam geometry has the asset of magnification [278]. Analyzer-based phase-contrast techniques do not require as much coherence and they can be transferred to lab devices [275]. Speckle imaging only requires a simple setup modification on standard CT devices; post-processing can retrieve phase-contrast information [279]. An XPCT setup at a synchrotron radiation facility can be considered as an ideal workbench from which one can determine the critical elements for proper characterization of biological tissues (optimized energies, preparation, etc.) to bootstrap a new biomedical application. For instance, dark-field imaging [280] is now mature enough for imaging human-scale phantoms [281] and it may soon be available on clinically-approved devices.

## 2.4. Current biomedical applications

X-ray phase-contrast tomography is a technique that is very versatile for biomedical imaging. Multiple setups, such as the aforementioned propagation-based and grating-interferometry setups, are available [282]. Although they have first been confined to synchrotron facilities, efforts have been put into the development of new sources and setups that can achieve similar results on benchtop devices [275].

### 2.4.1. Benefits of the technique

We will discuss thereafter two benefits of the technique: its non-destructive aspect (with respect to sample preparation and scanning procedure) and its higher sensitivity — which led to a variety of applications.

#### 2.4.1.1. Non-destructive technique

Sample preparation by dehydration [283, 284] is mostly reversible in comparison with other techniques such as tissue clearing or the paraffin-embedding process [219, 285, 286].

Besides, macroscopic anatomical landmarks are essentially preserved: one can identify them with gold-standard techniques such as MRI, CT and microscopy.

XPCT is mainly non-destructive as whole samples are imaged though one 360° rotation while preserving their 3D structure. However, some caution is required to reduce the radiation dose which can locally heat the samples; this is especially true when working at higher resolutions because of optical focusing and longer exposure times.

#### Context of the thesis

In the articles from the thesis, imaging was performed with pixel sizes of 6 μm or 3.09 μm and no damage was observed.

#### 2.4.1.2. Higher sensitivity

Phase contrast enables a label-free higher sensitivity compared to standard absorption-based devices — which often require contrast agents. Figure 2.14 shows how the regime for phase-contrast predominance is influenced by the sample-detector distance  $D$  in propagation-based XPCT; in particular, although this regime requires a free-propagation distance, this is limited by the near-field condition  $D \ll \frac{d^2}{\lambda}$  where  $d$  is “the characteristic size of the smallest discernible features in the object” [287] — a critical distance  $D_{crit}$  can be estimated from Figure 2.15.

### 2.4.2. Applications on soft-tissue imaging

Soft-tissue imaging benefits from the higher sensitivity of XPCT. Brain imaging with XPCT is limited to *ex vivo* sessions for rodents and bigger animals or human samples, because of the high absorption of the skull. Other organs can also be imaged and virtually browsed: the spinal cord [288], the lungs [278, 289], the liver [290], the heart [291, 292] and the muscles [293] have been studied *postmortem*; the lungs have also been studied *in vivo* with respiratory gating, i.e. by synchronizing acquisition with breathing of the live (usually anaesthetized) animal [294, 295, 296, 297]. An ongoing project, the Human Organ Atlas (<https://human-organ-atlas.esrf.eu/>), is

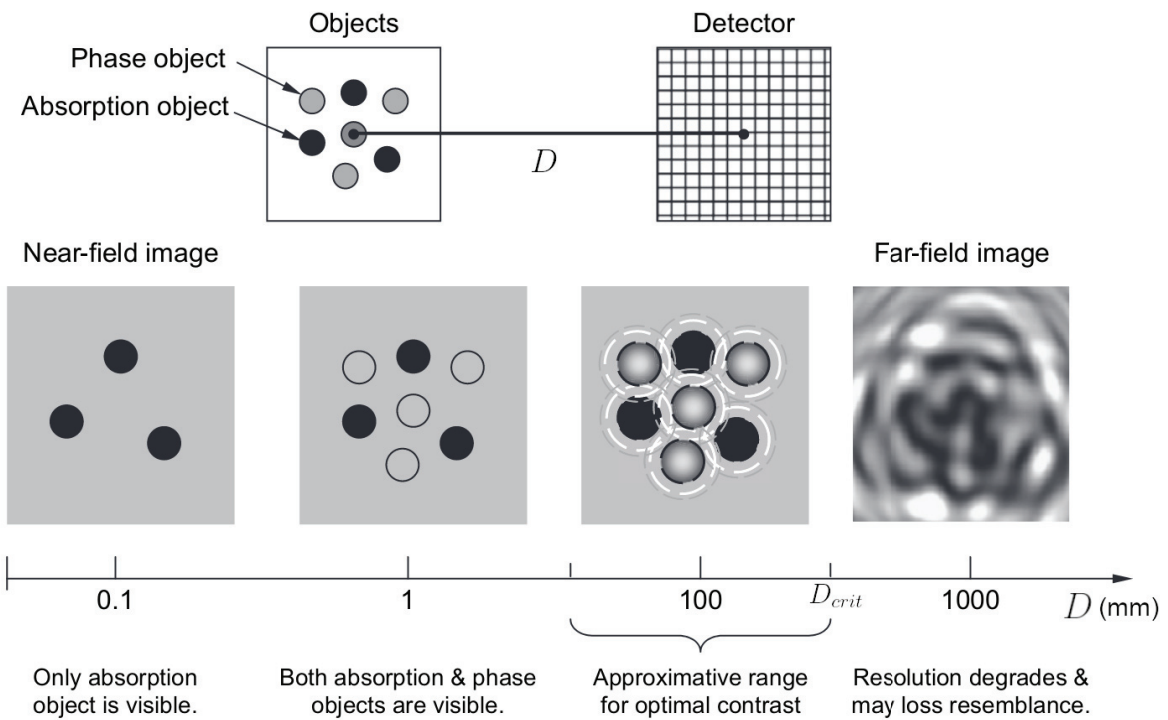
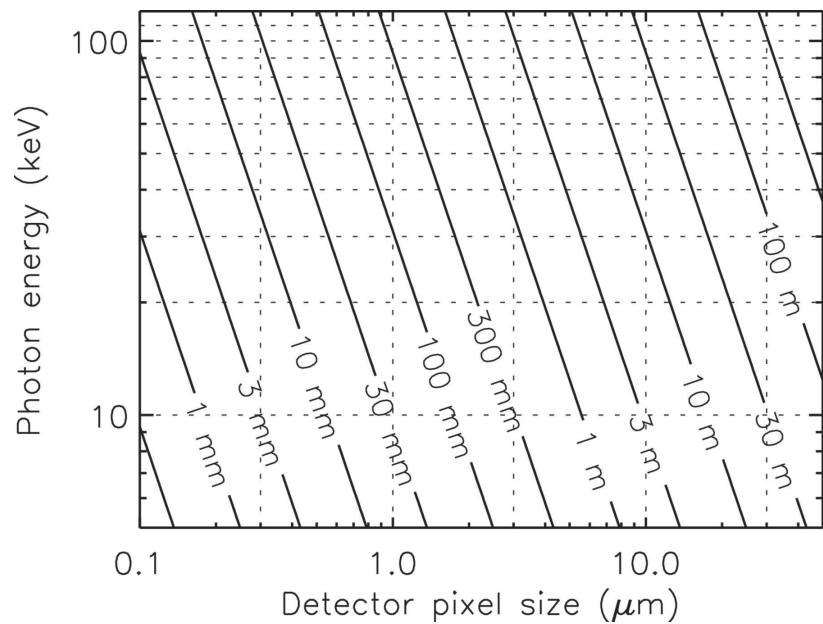


**Figure 2.14.:** Dependence of in-line phase-contrast images on the distance between object and detector. Here, given numerical data for  $D$  are only illustrative, which, in practice, will depend on the specific system setup. Adapted from [282].

**Figure 2.15.:** Contour plot of the critical propagation distance  $D_{crit} = (2\Delta)/\lambda$  to fulfill the near-field condition, for pixel sizes  $\Delta$  ranging between 0.1 and 50 mm and photon energies from 5 to 120 keV. The actual sample-detector distance  $D$  should be chosen well below  $D_{crit}$  to fulfill the near-field condition even for the smallest features that the detector can resolve. From [287].



planning to scan and analyze whole human organs [298] — both healthy and in pathological conditions.

### 2.4.3. Other applications

With XPCT, multiple groups have worked on bone and cartilage alteration in osteoarthritis [276, 299, 300, 301, 302, 303]; these alterations are detected with XPCT while they were not with MRI or micro-CT (cf. Figure 2.16) because XPCT is able to image both soft and hard tissue at the same time, with a better resolution than MRI and a resolution similar to micro-CT.

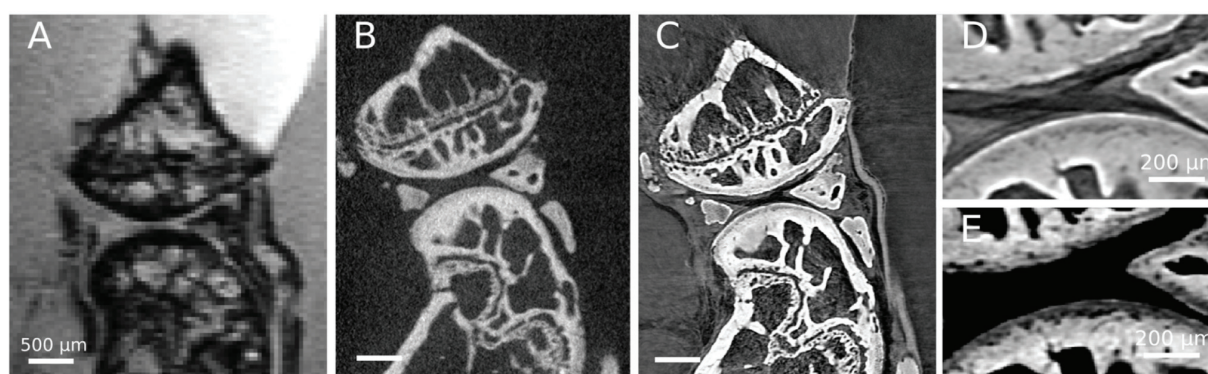


**Figure 2.16.:** Representative images of one osteoarthritis knee sample observed by each imaging technique. (A) MRI with an ultra-short echo time sequence (echo time = 0.008 13 ms; repetition time = 4.0 ms; flip angle = 5°; voxel size =  $50 \times 50 \times 50 \mu\text{m}^3$ ). (B) Conventional x-ray micro-tomography image (source voltage = 60 kVp; voxel size =  $6.06 \times 6.06 \times 6.06 \mu\text{m}^3$ ). (C) Synchrotron x-ray phase-contrast image (source energy = 52 keV; voxel size =  $6.1 \times 6.1 \times 6.1 \mu\text{m}^3$ ). (D,E) Phase-contrast image magnification with a soft (D) and hard (E) tissue contrast window. From [302].

Other applications of interest for life sciences include entomology [304], plant study [305, 306, 307] and archaeology — including work on mummies [308, 309] or burnt writings [310].

## 2.5. Other synchrotron-based techniques

### Context of the thesis

X-ray fluorescence spectrometry and Fourier-transform infrared spectroscopy have been used during the thesis because of the complementary information they convey on biological tissue. They are briefly introduced below.

### 2.5.1. X-ray fluorescence (XRF)

XRF is a spectroscopy technique to map the elemental composition of a material.

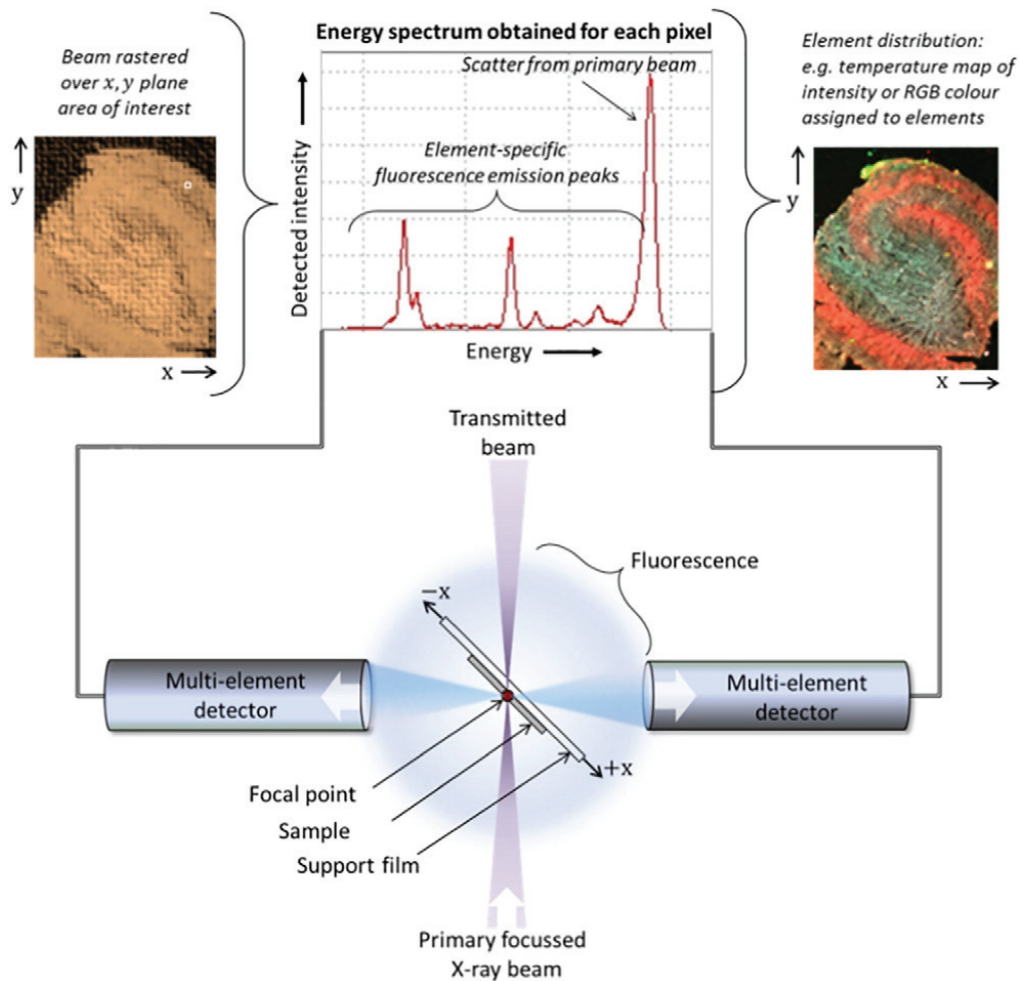


**Figure 2.17.:** The principle of XRF. The incident x-ray beam creates 2D hyperspectra which can be converted into 2D elemental maps of the sample. From [208].

As mentioned in subsection 2.1.2, when an x-ray photon causes a photoelectric absorption, a characteristic radiation is emitted because of a transitioning electron which fills the vacated shell. By collecting this radiation with an energy-resolving detector (cf. Figure 2.17), one can determine the element corresponding to the atom through spectrum fitting [311] with tabulated energies (cf. Table 2.1).

**Table 2.1.** A few characteristic energies of a few elements, with their symbols and atomic numbers  $Z$ . The binding energies of each shell indicate the incident energy that is required for a photoelectric absorption to occur, which in turn emits a new x-ray radiation that is detected in x-ray fluorescence. Iron, copper and zinc are extensively studied for their physiological involvement in subsection 1.2.2 and in Chapter 5; carbon and iodine cross-sections were shown in Figure 2.8; K-L<sub>2</sub> and K-L<sub>3</sub> spectral lines of argon are frequently used to normalize spectra. The IUPAC notations [312] K-L<sub>2</sub> through K-M<sub>3</sub> correspond to the former Siegbahn notations [313] K $\alpha_2$ , K $\alpha_1$ , K $\beta_3$  and K $\beta_1$ , respectively. Values were retrieved from PyMca [311].

| Element                    | K x-ray emission energies (keV) |                  |                  |     | Binding energies (keV) |                |                |                |     |
|----------------------------|---------------------------------|------------------|------------------|-----|------------------------|----------------|----------------|----------------|-----|
|                            | K-L <sub>2</sub>                | K-L <sub>3</sub> | K-M <sub>2</sub> | ... | K                      | L <sub>1</sub> | L <sub>2</sub> | L <sub>3</sub> | ... |
| Carbon ( <sub>6</sub> C)   | 0.28                            | 0.28             | N/A              | N/A | 0.28                   | 0.02           | 0.01           | 0.01           | N/A |
| Argon ( <sub>18</sub> Ar)  | 2.96                            | 2.96             | 3.19             | ... | 3.21                   | 0.33           | 0.25           | 0.25           | ... |
| Iron ( <sub>26</sub> Fe)   | 6.39                            | 6.40             | 7.06             | ... | 7.11                   | 0.85           | 0.72           | 0.71           | ... |
| Copper ( <sub>29</sub> Cu) | 8.03                            | 8.05             | 8.91             | ... | 8.98                   | 1.10           | 0.95           | 0.93           | ... |
| Zinc ( <sub>30</sub> Zn)   | 8.62                            | 8.64             | 9.57             | ... | 9.66                   | 1.19           | 1.04           | 1.02           | ... |
| Iodine ( <sub>53</sub> I)  | 28.32                           | 28.61            | 32.24            | ... | 33.17                  | 5.19           | 4.85           | 4.56           | ... |

### 2.5.2. Fourier-transform infrared spectroscopy (FTIR)

FTIR is a spectroscopy technique to map the molecular distribution within a material.

When an infrared (IR) radiation goes through a material, it is partially absorbed. At some wavelengths, the molecules vibrate due to the incident energy they absorb; these wavelengths form a signature spectrum for each functional group in the molecule (cf. Figure 2.18). Spectra can either represent the transmittance  $T = \frac{I}{I_0}$  of the absorbance  $A = -\log T$  (both  $T$  and  $A$  are unitless) on the y-axis, with the wavenumber in  $\text{cm}^{-1}$  on the x-axis (cf. Figure 2.19). Devices scan the sample for excitation and collection to retrieve hyperspectral maps of the material and analyse the distribution.

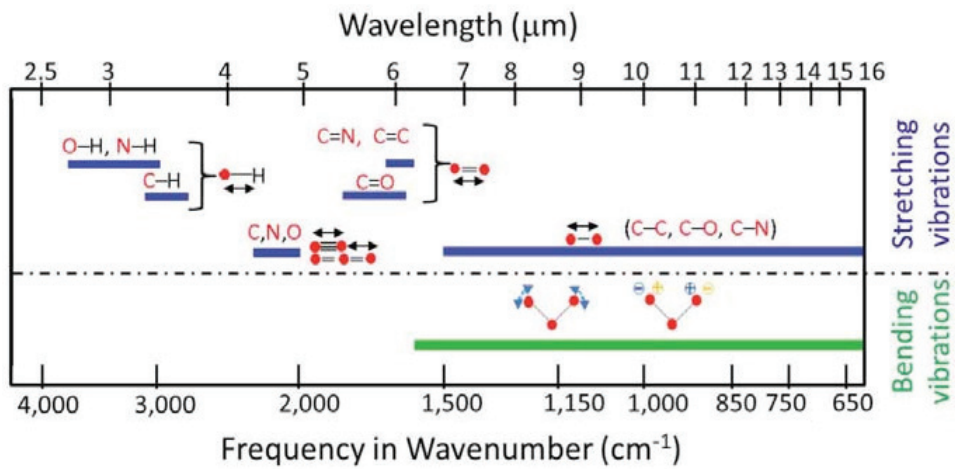


**Figure 2.18.:** Vibrational modes of common biomolecular bonds. Inherent vibrational motion of molecules gives rise to distinct, fingerprint-like absorption bands in the mid-infrared region. Different stretching or bending vibrational bands commonly encountered in biological samples are shown. Infrared spectroscopy is sensitive to the presence of many chemical functional groups (structural fragments) in molecules, and taken together the set of vibration modes are unique for every molecular configuration. From [314].

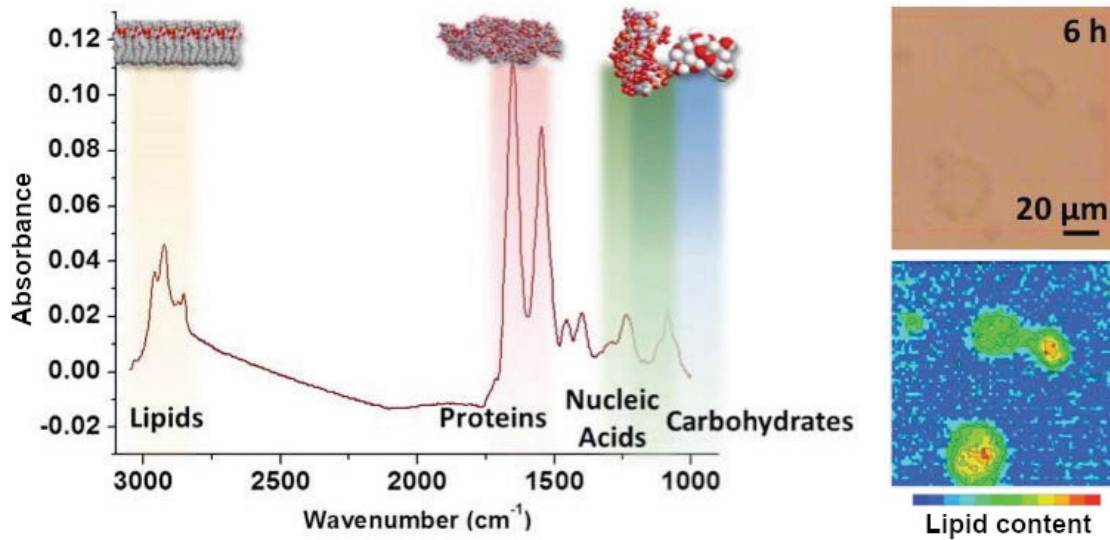


**Figure 2.19.:** Infrared spectrum of a single human cell with color bands highlighting absorption peaks associated with constituent macromolecules (left) and lipid distribution within MCF-7 living cells — chemical changes can be monitored in time (right). From [314] (left) and [315] (right).

# PHD PROJECT



# Browsing brain structures with XPCT

# 3.

## 3.1. Introduction

The first study reported in this PhD thesis focused on non-AD animal models: ischemic stroke, multiple sclerosis and neonatal hypoxia. These models had in common an alteration of white matter. White matter refers to the bright areas in brain tissue samples because of myelin, a lipidic sheath that protects one or several axons and speeds up the neuronal signals. Multiple brains from each model were collected *postmortem* for imaging with XPCT: ischemic stroke models (by middle cerebral artery occlusion) were acquired from the CarMeN laboratory, neonatal hypoxia models were acquired from the SBRI laboratory and multiple sclerosis models (by lysolecithin injection) were made in-house. The sample preparation — fixation in formaldehyde and dehydration in ethanol — gave us the best contrast after optimization. We could conclude that the high-density signal in XPCT was due to myelin with histology and comparative clearing for validation. Two major quantification strategies were applied to our images: a fiber segmentation in the striatum (where fibers are thin and separated) and a diffusion-tensor-like computation of the fiber orientations for the study of the corpus callosum (where the fibers are grouped into a major tract).

While this work is not related to Alzheimer’s Disease, this was a milestone towards the characterization of 3D features in the mouse and human brains, thanks to the sample preparation protocols and to the software which required a learning phase — both were used during the whole PhD project.

3.1 Introduction . . . . . 57

3.2 Associated published  
work . . . . . 58

3.3 Discussion . . . . . 85

To get familiar with the rodent brain anatomy, one can refer to the [Mouse Brain Atlas \[191\]](#) or [Rat Brain Atlas \[192, 193, 194\]](#) on EBRAINS.

## 3.2. Associated published work

---

Reproduced from Biomed Opt Express.

Chourrout M, Rositi H, Ong E, Hubert V, Paccalet A, Foucault L, Autret A, Fayard B, Olivier C, Bolbos R, Peyrin F, Crola-da-Silva C, Meyronet D, Raineteau O, Elleaume H, Brun E, Chauveau F, and Wiart M. Brain Virtual Histology with X-ray Phase-Contrast Tomography Part I: Whole-Brain Myelin Mapping in White-Matter Injury Models. *Biomed Opt Express*. 2022 Mar 1; 13

[Open Access – Version of Record]

---



# Brain virtual histology with X-ray phase-contrast tomography Part I: whole-brain myelin mapping in white-matter injury models

MATTHIEU CHOURROUT,<sup>1,11</sup> HUGO ROSITI,<sup>2,11</sup> ELODIE ONG,<sup>3,4</sup> VIOLAINE HUBERT,<sup>3</sup> ALEXANDRE PACCALET,<sup>3</sup> LOUIS FOUCAULT,<sup>5</sup> AWEN AUTRET,<sup>6</sup> BARBARA FAYARD,<sup>6</sup> CÉCILE OLIVIER,<sup>7</sup> RADU BOLBOS,<sup>8</sup> FRANÇOISE PEYRIN,<sup>7</sup> CLAIRE CROLA-DA-SILVA,<sup>3</sup> DAVID MEYRONET,<sup>4</sup> OLIVIER RAINETEAU,<sup>5</sup> HÉLÈNE ELLEAUME,<sup>9</sup> EMMANUEL BRUN,<sup>9</sup> FABIEN CHAUVEAU,<sup>1,10,12</sup> AND MARLENE WIART<sup>3,10,12,\*</sup>

<sup>1</sup>Univ-Lyon, Lyon Neuroscience Research Center, CNRS UMR5292, Inserm U1028, Université Claude Bernard Lyon 1, Lyon, France

<sup>2</sup>Univ-Clermont Auvergne; CNRS; SIGMA Clermont; Institut Pascal, Clermont-Ferrand, France

<sup>3</sup>Univ-Lyon, CarMeN laboratory, Inserm U1060, INRA U1397, Université Claude Bernard Lyon 1, INSA Lyon, Charles Mérieux Medical School, F-69600, Oullins, France

<sup>4</sup>Univ-Lyon, Hospices Civils de Lyon, Lyon, France

<sup>5</sup>Univ-Lyon, Université Claude Bernard Lyon 1, Inserm, Stem Cell and Brain Research Institute U1208, 69500 Bron, France

<sup>6</sup>NOVITOM, Grenoble, France

<sup>7</sup>Univ-Lyon, INSA-Lyon, Université Claude Bernard Lyon 1, CNRS, Inserm, CREATIS UMR5220, U1206, F-69621, France

<sup>8</sup>Cermep, Lyon, France

<sup>9</sup>Université Grenoble Alpes, Inserm UA7 Strobe, Grenoble, France

<sup>10</sup>CNRS, Lyon, France

<sup>11</sup>Co-first authors

<sup>12</sup>Co-last authors

\*marlene.wiart@univ-lyon1.fr

**Abstract:** White-matter injury leads to severe functional loss in many neurological diseases. Myelin staining on histological samples is the most common technique to investigate white-matter fibers. However, tissue processing and sectioning may affect the reliability of 3D volumetric assessments. The purpose of this study was to propose an approach that enables myelin fibers to be mapped in the whole rodent brain with microscopic resolution and without the need for strenuous staining. With this aim, we coupled in-line (propagation-based) X-ray phase-contrast tomography (XPCT) to ethanol-induced brain sample dehydration. We here provide the proof-of-concept that this approach enhances myelinated axons in rodent and human brain tissue. In addition, we demonstrated that white-matter injuries could be detected and quantified with this approach, using three animal models: ischemic stroke, premature birth and multiple sclerosis. Furthermore, in analogy to diffusion tensor imaging (DTI), we retrieved fiber directions and DTI-like diffusion metrics from our XPCT data to quantitatively characterize white-matter microstructure. Finally, we showed that this non-destructive approach was compatible with subsequent complementary brain sample analysis by conventional histology. In-line XPCT might thus become a novel gold-standard for investigating white-matter injury in the intact brain. This is Part I of a series of two articles reporting the value of in-line XPCT for virtual histology of the brain; Part II shows how in-line XPCT enables the whole-brain 3D morphometric analysis of amyloid- $\beta$  (A $\beta$ ) plaques.

© 2022 Optical Society of America under the terms of the [OSA Open Access Publishing Agreement](#)

## 1. Introduction

White-matter injury leads to severe functional loss in many neurological diseases. Diagnosis and monitoring of white-matter damage and repair is therefore paramount in order to limit the handicap resulting from these conditions. Magnetic resonance imaging techniques such as diffusion tensor imaging (DTI) and its variants (q-balls, kurtosis imaging) are now instrumental for the assessment of white-matter abnormalities [1]. Beside displaying fiber tract orientation maps, these approaches provide quantitative metrics such as fractional anisotropy (FA), axial diffusivity (AD) and radial diffusivity (RD), which in combination serve as biomarkers of axonal and myelin damage [2]. However, these techniques still present limitations, notably due to partial volume effects, the difficulty of resolving crossed fibers, and the delicate interpretation of DTI metrics that may be influenced by factors other than axonal degeneration and myelin degradation, such as inflammation and astrogliosis [3]. In addition, for post-mortem samples, acquisition times are very long (several hours to days) to achieve spatial resolution in the 10  $\mu\text{m}$  – 100  $\mu\text{m}$  range, thus preventing high-throughput imaging of high-resolution 3D datasets. There is thus a crucial need to develop novel whole-brain imaging approaches to study white-matter tracts at the microscopic level [4], especially for the investigation of animal models of white-matter injury.

Myelin staining on histological samples is a fundamental technique employed in many areas of neuroscience to study white-matter fibers. However, tissue processing and sectioning affect the reliability of 3-dimensional (3D) volumetric assessments. Recently, brain-clearing approaches coupled to the use of antibodies, for example targeting myelin basic protein (MBP) to visualize myelinated axons [5], have been proposed to overcome these limitations. Unfortunately, these techniques are laborious and time-consuming. In addition, tissue immunostaining is dependent on antibody penetration into the optically cleared brain, while light-sheet microscopy (the companion imaging tool for imaging cleared tissues) has limited through-plane resolution, thus introducing bias when retrieving 3D information [6].

X-ray based virtual histology is emerging as a new discipline, virtually slicing 3D datasets in any direction at microscopic level [7]. X-ray phase-contrast tomography (XPCT) using synchrotron radiation is particularly promising to image microstructures in excised biological tissues that have weak X-ray absorption. XPCT achieves a high signal-to-noise ratio without the need to add staining agents. It offers micrometric spatial resolution and isotropic reconstruction in a 1  $\text{cm}^3$  field of view (FOV), thus providing the ideal prerequisites for imaging white-matter fibers in the entire and intact (unsliced, unstained) rodent brain. To meet this challenge, however, certain improvements are required, notably to obtain sufficient contrast-to-noise in axons without labor-intensive contrast-enhancing steps [8].

We previously developed an imaging technique relying on in-line XPCT that identifies mouse brain anatomy as clearly as histology, with acquisition time in the range of minutes [9–11]. We here propose an optimized approach to map myelin fibers in the whole mouse brain with microscopic resolution without the need for strenuous staining. We provide the proof-of-concept that this approach enhances myelinated fibers in rodent and human brain tissue. In addition, we demonstrated that the technique detected and quantified white-matter injuries using three animal models: ischemic stroke, premature birth and multiple sclerosis. Furthermore, analogously to diffusion tensor imaging (DTI), we retrieved fiber directions and DTI-like diffusion metrics from our XPCT data to quantitatively characterize white-matter microstructures. Finally, we here show that this non-destructive approach is compatible with subsequent complementary brain sample analysis by conventional histology. In-line XPCT might thus become a novel gold-standard for investigating white-matter injury in the intact brain *ex vivo*. This is Part I of a series of two articles reporting the value of in-line XPCT for virtual histology of the brain; Part II shows how in-line XPCT enables whole-brain 3D morphometric analysis of amyloid- $\beta$  ( $A\beta$ ) plaques [12].

## 2. Materials and methods

Table 1 summarizes the samples and imaging techniques used in the study.

**Table 1. Summary of 19 samples used for XPCT, with concurrent testing of different ethanol titrations for sample preparation, DTI, histology and CLARITY evaluations.**

| Species | Age      | Disease / Animal model          | XPCT | DTI | Histology | CLARITY | Ethanol gradient |
|---------|----------|---------------------------------|------|-----|-----------|---------|------------------|
|         |          | None                            | 8    | 1   | 1         | 1       | 5                |
| Mouse   | 8 weeks  | Ischemic stroke                 | 2    |     | 1         |         |                  |
|         |          | Multiple sclerosis              | 2    |     |           |         |                  |
|         | 11 days  | Premature birth <i>Normoxia</i> | 2    |     | 2         |         |                  |
|         |          | <i>Hypoxia</i>                  | 2    |     | 2         |         |                  |
| Rat     | 10 weeks | Multiple sclerosis              | 1    | 1   |           |         |                  |
| Human   | 70 y.o.  | Frontotemporal dementia         | 2    |     |           | 1       |                  |

### 2.1. Animals

All experimental procedures involving animals and their care were carried out in accordance with European regulations for animal use (EEC Council Directive 2010/63/EU, OJ L 276, Oct. 20, 2010). The study was approved by our local review board "Comité d'éthique pour l'Expérimentation Animale Neurosciences Lyon" (CELYNE - CNREEA number: C2EA – 42, APAFIS#7457-2016110414498389, 5892-2016063014207327, 187-2015011615386357). Sixteen rodents (Janvier, France) were used (Table 1). Animals were housed in a temperature- and humidity-controlled environment ( $21 \pm 3^\circ\text{C}$ ), with 12 : 12 h light-dark cycle, with free access to standard chow and tap water. For surgeries, animals were anesthetized with isoflurane (induction: 3.5 %; surgery: 2 %; ISO-VET, Piramal Healthcare, Morpeth, UK). Pain was alleviated by subcutaneous injection of buprenorphine at 0.05 mg/kg prior to surgery. During surgery, body temperature was monitored with a rectal probe and maintained at  $37^\circ\text{C}$  using a feedback-regulated heating pad. At end of surgery, wounds were treated with lidocaine (lidocaine/prilocaine 5 %, Pierre Fabre, France).

### 2.2. Animal models of white-matter injury

Three animal models of white-matter injury that lead to myelin damage were used; the number of animals per model is specified in Table 1. Firstly, focal cerebral ischemia, a model of ischemic stroke encompassing the sensorimotor cortex and adjacent corpus callosum, was induced by permanent occlusion of the distal middle cerebral artery (pMCAO), as previously described [13]. Briefly, the right MCA was exposed by subtemporal craniectomy and occluded by electrocoagulating the distal part for 10 minutes. The animals were then allowed to recover from anesthesia and sacrificed at day 9 post-surgery. Secondly, chronic hypoxia was used as a model of very premature birth. This model consists in placing newborn mice in chronic hypoxia —10 %  $\text{O}_2$  for 8 days— during the early postnatal period —from post-natal day #3 (P3) to post-natal

day #11 (P11)—, corresponding to the late prenatal period of brain development in humans. This model reproduces all histopathological features observed in very preterm infants, including diffuse white-matter injuries [14]. Mice were sacrificed at the end of the hypoxic period: i.e., P11. Thirdly, focal demyelinating lesions, a model of multiple sclerosis, were induced by stereotaxic injection of lysophosphatidylcholine (LPC) (Sigma-Aldrich, ref. L4129) at 1 % in saline solution into the corpus callosum as previously described [15,16]. After bilateral craniotomy, LPC and saline were slowly infused (0.1  $\mu\text{L}/\text{min}$ ) with 30-gauge needles via tubing connected to syringes installed in injection pumps. In one mouse, 1- $\mu\text{L}$  was injected at AP 0.0 mm; ML  $\pm 2.5$  mm; DV -2.0 mm, with contralateral injection of 1  $\mu\text{L}$  saline. In the other mouse, 2  $\mu\text{L}$  was injected at the same ipsilateral site, without contralateral injection. In the rat, 5  $\mu\text{L}$  was injected: AP -0.3 mm; ML  $\pm 3.3$  mm; DV -2.8 mm / -3.5 mm; 2.5  $\mu\text{L}$  each, from depth to superficial, with contralateral injection of 5  $\mu\text{L}$  saline. The animals were then allowed to recover from anesthesia and sacrificed at day 7–9 post-surgery.

### 2.3. *In vivo MRI*

For *in vivo* MRI, the animals were placed in a temperature-controlled cradle and anesthetized by isoflurane as for surgery. The respiratory rhythm was monitored by a pressure sensor linked to a monitoring system (ECG Trigger Unit HR V2.0, RAPID Biomedical, Rimpac, Germany). MRI was performed on a horizontal 7 T Bruker BioSpec MRI system (Bruker Biospin MRI GmbH, Bruker, Germany) equipped with a set of gradients of 440mT/m and controlled via a Bruker ParaVision 5.1 workstation. A Bruker birdcage volume coil (inner diameter = 72 mm, outer diameter = 112 mm) was used for transmission, and a Bruker single loop surface coil (15 mm diameter) was used for reception. T2-weighted imaging and DTI were obtained; Table S1 summarizes the acquisition parameters.

### 2.4. *Rodent and human brain sample preparation*

All animals were euthanized by intracardiac perfusion with phosphate-buffered saline (PBS) and their brains were harvested. For XPCT, the impact of dehydration was examined in healthy brains fixed by formaldehyde 4 % and dehydrated in ethanol baths (25 %; 50 %; 75 % and 96 %). All subsequent (rodent and human) brains were fixed in formaldehyde 4 % and then dehydrated in successive ethanol baths until a titration of 96 % was reached. The total time for sample preparation was below 30 minutes. Some of the mouse brains were re-hydrated for histology and immunohistology. In addition to the rodent brains, cortex tissue (2 adjacent blocks of approx. 1  $\text{cm}^3$ ) from one patient with frontotemporal dementia was imaged; it was obtained from the local brain bank in Lyon: Tissue Tumorotheque Est, CRB-HCL (national authorizations DC2008-72 & AC2015-2576). One healthy mouse and one human brain sample were cleared with the CLARITY system to achieve brain clearing [17] after formaldehyde fixation and before ethanol dehydration: brains were incubated in a polymerization solution composed of PBS buffer 1X, with the addition of VA-044 concentrated at 0.25 % and acrylamide 4 %. Brains were kept in the solution for 12 hours at 4°C. After infusion, the gel was polymerized at 37°C under gentle agitation for 3 hours. Brains were then placed in the Logos electrophoretic tissue clearing solution for one day and cleared using the electrophoretic chamber of the X-Clarity system. Brains were cleared at 1.5 A in 6 (mouse) or 8 (human) hours. The total time for sample clearing was 2 days.

### 2.5. *X-ray phase-contrast computed tomography (XPCT)*

Imaging was performed at the ID17 and ID19 beamlines of the ESRF, the European Synchrotron (ESRF, Grenoble, France). The samples (whole mouse brains, rat hemispheres) were conditioned in 1 cm diameter plastic tubes filled with ethanol 96 %. We used the propagation-based imaging technique, which exploits free-space propagation in order to have detectable interference fringes. An example of the experimental set-up is shown in Fig. S1. A summary of experimental and

reconstruction parameters is given in Table S2. Briefly, the tomographic images were recorded at a single sample-detector distance where the camera was positioned away from the sample to obtain phase contrast. The experiments were performed with a "pink" incident X-ray beam generated by the undulator on ID19 (energy: 19 keV–35 keV according to the experiment setting, Table S2). When the sample exceeded the beam size in Z-direction, two stacks were acquired with  $\sim 100$  slices overlap and stitched afterwards. Tomographic reconstructions were performed after using the Paganin single distance phase-retrieval approach of the PyHST2 software using standard unsharp masking [18]. For all scans, the  $\delta/\beta$  ratio was set in the range [600;1000] on an image-to-image basis depending on the brain structures present in the image, in order to provide optimal contrast without blurring the image too much [10,11] (Table S2). Of note, in a preliminary work, we have already shown that fiber detectability reached a plateau in this range [11].

### 2.6. Data processing and quantitative analysis

The mouse brain library was used for labeling white-matter fiber tracks (<http://www.mbl.org/mbl.main/atlas.html>). Maximum intensity projections were generated using ImageJ software (<https://imagej.nih.gov/ij/index.html>). Segmentation, analysis and volume rendering were performed with Amira Software (<https://thermofisher.com/amira-avizo>). For fiber density quantification, XPCT hyperintense signals of the caudate putamen were segmented using a home-made pipeline made with Amira Software. This pipeline relied on a structure-enhancement filter (Frangi filter for rod-like elements [19]), then processed with the TEASAR tree-structure extraction algorithm [20] to segment the white-matter network. Fiber density was then evaluated as the ratio of the number of segmented voxels over the total number of voxels within 3D ROIs. For mice with pMCAO, ROIs encompassing 100 axial slices at the level of the ischemic lesion were placed in the peri-lesional caudate putamen. For mice with chronic hypoxia, ROIs encompassing 60 slices were placed in the center of the caudate putamen. The DTI parametric maps (FA, RD, AD) were reconstructed from MRI data using DSI studio software (<http://dsi-studio.labsolver.org>). The DTI-like parametric maps were computed from XPCT images using a dedicated tool developed by NOVITOM (<https://www.novitom.com/en/>) specifically for the current study. The algorithm was developed based on image gradient analysis to detect fibers orientation. The basic idea is that image gradient should be minimal along the fibers direction. The first step is the computation of the image intensity gradient along the 3 spatial axes, giving a gradient vector for each voxel:

$$\vec{\nabla}I = \begin{pmatrix} \frac{\partial I}{\partial x} \\ \frac{\partial I}{\partial y} \\ \frac{\partial I}{\partial z} \end{pmatrix} = \begin{pmatrix} g_x \\ g_y \\ g_z \end{pmatrix} \quad (1)$$

The gradient orientation tensor (or covariance matrix) is then built using the tensor product:

$$T_g = \vec{\nabla}I \otimes \vec{\nabla}I = \begin{pmatrix} g_x g_x & g_x g_y & g_x g_z \\ g_y g_x & g_y g_y & g_y g_z \\ g_z g_x & g_z g_y & g_z g_z \end{pmatrix} \quad (2)$$

The tensor components are locally correlated using a convolution by a Gaussian kernel  $k_g$  with a standard deviation  $\sigma_g$ :

$$(T_g * k_g)(x, y) = \int_u \int_v T_g(u, v) \frac{1}{\sigma_g \sqrt{2\pi}} \exp\left(-\frac{(x-u)^2 + (y-v)^2}{2\sigma_g^2}\right) du dv \quad (3)$$

Then the gradient orientation tensor is diagonalized to extract the local orientation axes:

$$D^{-1}T_gD = \begin{pmatrix} \eta_1 & 0 & 0 \\ 0 & \eta_2 & 0 \\ 0 & 0 & \eta_3 \end{pmatrix}, \text{ with } D = (\vec{a}_1 \vec{a}_2 \vec{a}_3) \quad (4)$$

The eigen vectors  $\vec{a}_i$  ( $i \in [1; 3]$ ) are associated with the eigen values  $\eta_i$ . The eigen vector  $\vec{a}_n$  associated with the smallest eigen value is aligned with the direction in which the gradient is weakest, which should be locally aligned with the fiber direction. The fiber orientation  $\vec{v}_f$  is defined as:

$$\vec{v}_f = \frac{\vec{a}_n}{\|\vec{a}_n\|} \quad (5)$$

The fiber orientation tensor is constructed as the tensor product of this vector by itself:

$$T_f = \vec{v}_f \otimes \vec{v}_f \quad (6)$$

The components of the tensor are locally correlated by applying a convolution by a Gaussian kernel  $k_f$  with a standard deviation  $\sigma_f$ :

$$(T_f * k_f)(x, y) = \int_u \int_v T_f(u, v) \frac{1}{\sigma_f \sqrt{2\pi}} \exp\left(-\frac{(x-u)^2 + (y-v)^2}{2\sigma_f^2}\right) du dv \quad (7)$$

Finally, the fiber orientation tensor is diagonalized to obtain the eigenvalues  $\lambda_j$  ( $j \in [1; 3]$ ), used to compute the DTI parametric maps:

$$AD = \lambda_1 \quad (8a)$$

$$RD = \frac{\lambda_2 + \lambda_3}{2} \quad (8b)$$

$$FA = \sqrt{\frac{3}{2} \frac{\sqrt{(\lambda_1 - \bar{\lambda})^2 + (\lambda_2 - \bar{\lambda})^2 + (\lambda_3 - \bar{\lambda})^2}}{\sqrt{\lambda_1^2 + \lambda_2^2 + \lambda_3^2}}} \quad \text{where } \bar{\lambda} = \frac{\lambda_1 + \lambda_2 + \lambda_3}{3} \quad (8c)$$

### 2.7. Histology and immunohistology

Brain samples were frozen at  $-80^\circ\text{C}$ . For GFAP and collagen IV staining, rehydrated frozen brains were cut into  $12 \mu\text{m}$  axial sections using a cryostat. Brain slices were rehydrated 10 minutes in 0.1 M PBS, fixed for 20 minutes in 4 % PFA, and rinsed 3 times with PBS. They were then blocked and permeabilized in PBS (Sigma-Aldrich, Saint Louis, MO, USA) with 5 % BSA (bovine serum albumin, Sigma-Aldrich, Saint Louis, MO, USA) and 0.5 % Triton X-100 (PBST) for 30 minutes at room temperature. Slides were then incubated overnight at  $4^\circ\text{C}$  with primary polyclonal anti-GFAP rabbit antibody (1:1000; Z0334, DAKO, Golstrup, Denmark) or anti-collagen IV rabbit antibody (1:200, AB6586, AbCam, Cambridge, UK) dissolved in 0.5 % PBST. They were then washed 3 times in PBS and incubated with a secondary anti-rabbit GFP antibody dissolved in PBST (1:1000, AF546, ThermoFisher, Waltham, MA, USA) for 1 hour at room temperature. Finally, slides were rinsed 3 times in PBS and mounted in aqueous medium containing DAPI (Roti-Mount, Carl Roth, Karlsruhe, Germany). For Sudan Black B staining, brain slices were post-fixed with 4 % formaldehyde in PBS, briefly dehydrated in 70 % ethanol and then incubated in 0.1 % Sudan Black B solution (Sigma-Aldrich, ref. 199664, Saint Louis, MO, USA) at room temperature for 10 minutes. They were then washed in 70 % ethanol for 10–30 minutes and moved into distilled water to be mounted in aqueous medium

(Roti-Mount, Carl Roth, Karlsruhe, Germany). For MBP staining, brains were first rehydrated in 0.1 M PBS, then cut into 50  $\mu\text{m}$  axial sections using a vibratome. Free-floating sections were blocked in TNB buffer (0.1 M PB; 0.5 % Casein; 0.25 % BSA; 0.25 % TopBlock) with 0.4 % triton-X (TNB-Tx), then incubated overnight at 4°C with a rabbit anti-MBP primary antibody (1:1000; AbCam, Cambridge, UK), under constant gentle shaking. Following extensive washing in 0.1 M PBS with 4°C triton-X (PB-Tx), sections were incubated with appropriate secondary antibodies conjugated with Alexafluor 488 (1:500; Life Technologies, Carlsbad, Germany) for 4 hours at room temperature. Sections were washed and counterstained with DAPI (300 nM; D1306; Life Technologies, Carlsbad, Germany). Images were acquired using an Axio Scope A.1 fluorescence microscope (4 filters, Carl Zeiss, Oberkochen, Germany) equipped with a  $\times 0.63$  AxioCam MRc (Carl Zeiss, Oberkochen, Germany).

### 2.8. Data and code availability statement

The XPCT raw data cannot be shared at this time due to the large size of the datasets, but can be made available on reasonable request. The DTI-like algorithm is the property of NOVITOM.

## 3. Results

### 3.1. XPCT enables visualization of myelinated white-matter fibers in the whole mouse brain

We first aimed to evaluate the impact of dehydration on XPCT brain contrast. As reported earlier by ourselves and others [9,21–24], formaldehyde fixation resulted in faint hypointense contrast of white-matter fiber tracts (Fig. 1, 0 %). Successive baths of ethanol resulted in appearance of hyperintense signal in myelinated white-matter fibers, with dose effect (Fig. 1, 25%–96%). Because ethanol 96 % dehydration produced the best visual contrast, we adopted this brain processing technique for the rest of the study. XPCT of dehydrated brain samples provided 3D mapping of all myelinated white-matter tracts, enabling accurate labeling despite tissue shrinkage (Fig. 2). Dynamic visualization of virtual slicing ([Visualization 1](#) for coronal incidence and [Visualization 2](#) for sagittal incidence) and static visualization of maximum intensity projections (Fig. 2(C-D-E-H-I)) revealed the complexity of fiber orientations and entanglement in the whole brain (see for example stria medullaris and fasciculus retroflexus in Fig. 2(E)).

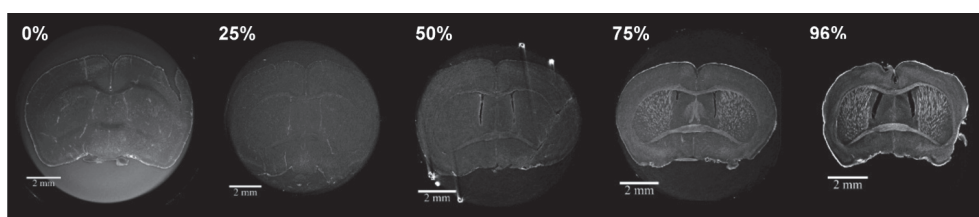


**Fig. 1.** Ethanol dehydration enhances myelin contrast on images obtained with in-line XPCT. Axial section (Bregma 0) through brains prepared using PFA 4 % and a gradient of ethanol baths [25%–96%].

Importantly, XPCT contrast enhancement of white matter was also observed in human brain tissue after dehydration (Fig. 3(A), arrows).

Brain anatomy was exquisitely revealed by XPCT, with many relevant neurological features (overall vasculature, neuronal bodies of the barrel cortex and hippocampus layers, choroid plexus, cerebellum, etc.) being clearly identifiable (Fig. S5).

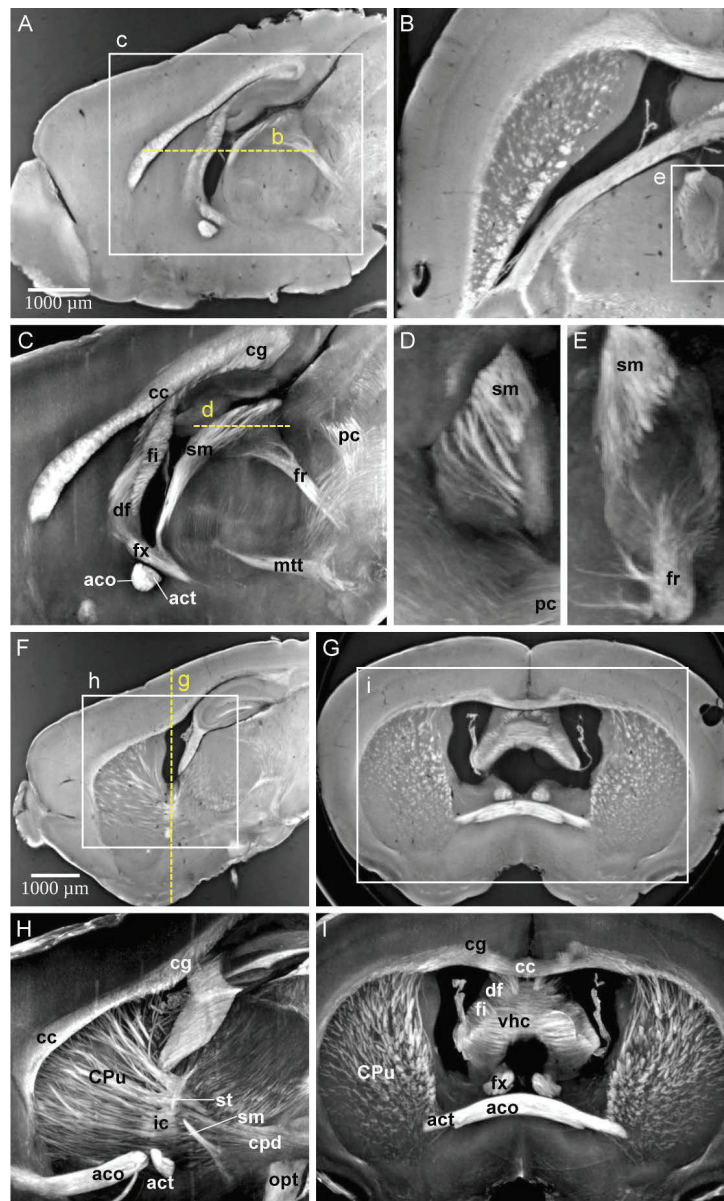


**Fig. 2.** White matter fiber tracts are revealed by XPCT in a mouse brain. The same brain sample is shown in all panels from a mouse with LPC administration with a focus on normal-appearing white matter. (A) Sagittal view of single slice; (B) Corresponding axial view of single slice; (C) Maximum intensity projection (MIP) of sagittal view over 35 slices (262  $\mu\text{m}$ ), with white matter fiber tracts annotations; (D) MIP showing the entanglement between stria medullaris (sm) and the posterior commissure (pc); (E) MIP showing the entanglement between stria medullaris (sm) and the fornix (fr); (F) Sagittal view of single slice; (G) Corresponding coronal view; (H) Maximum intensity projection (MIP) of sagittal view over 35 slices (750  $\mu\text{m}$ ), with white matter fiber tract annotations; (I) MIP of coronal view over 35 slices (750  $\mu\text{m}$ ), with white matter fiber tract annotations; Labels: aco anterior commissure, olfactory limb; act anterior commissure, temporal limb; cc corpus callosum; cg cingulum; cpd cerebral peduncle; CPu caudate putamen; df dorsal fornix; fi fimbria; fr fasciculus retroflexus; fx columns of the fornix; mtt mammillothalamic tract; sm stria medullaris; st stria terminalis; opt optical tract; pc posterior commissure.; vhc ventral hippocampal commissure.

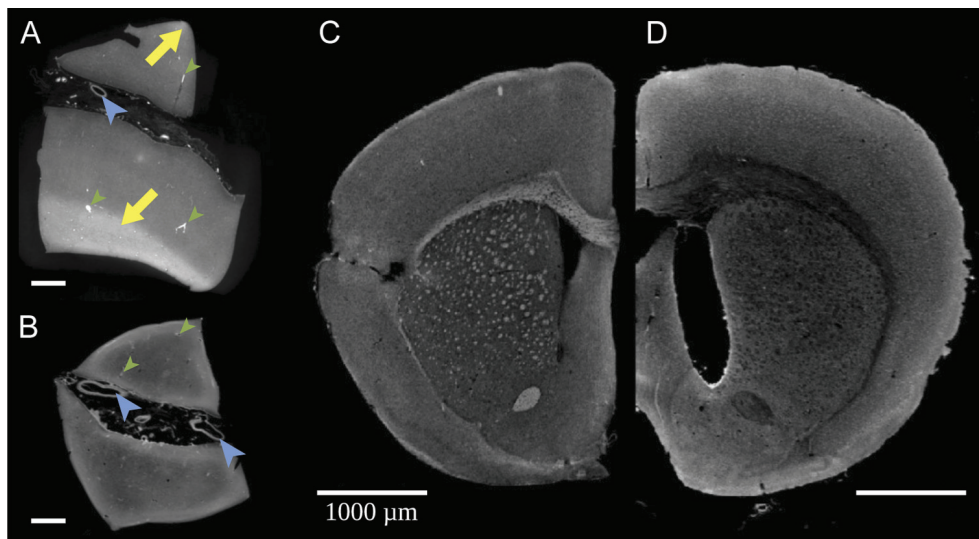


**Fig. 3.** White matter fiber tracts are revealed by XPCT in a human brain and disappear upon demyelination brain clearing. **(A-B)** Single XPCT slice of a human brain sample from 2 distinct but adjacent blocks. **(A)** Ethanol dehydration reveals white matter as hyperintense areas (arrows); **(B)** White matter hyperintense signal is lost after demyelination by brain clearing. Other anatomical landmarks such as large vessels are clearly seen (large blue arrowheads). Because the sample was not perfused, there is also contrast from small vessels (smaller green arrowheads); **(C-D)** Single XPCT slice through a rodent brain **(C)** without and **(D)** with demyelination by brain clearing: note the disappearance of white matter hyperintense signal. Clearing procedure induced brain expansion and ethanol dehydration induced brain shrinkage, hence the slight difference in sample size.

### 3.2. XPCT white-matter enhancement in dehydrated brain samples is related to myelin

We hypothesized that the white-matter contrast seen with our approach was related to a mismatch of refractive indices between myelin and surrounding tissue, occurring after the removal of water by ethanol. Myelin has a much higher lipid content than gray matter [25] and might thus be less affected by dehydration than other brain tissues. To investigate this possibility, we used brain clearing, a technique that removes lipids (and hence the myelin sheath) to render the brain translucent to light before ethanol dehydration [26–28]. We observed a loss of white-matter tract contrast after lipid removal in both human (Fig. 3(B)) and mouse brains (Fig. 3(D)), suggesting a role of myelin in contrast generation.

### 3.3. XPCT detects and quantifies white-matter injuries in a range of animal models

We then aimed to evaluate the value of XPCT as a virtual histology tool for the diagnosis and characterization of white-matter injuries. For this, we used 3 different small animal models:

1. ischemic stroke (pMCAO),
2. premature birth (neonatal chronic hypoxia) and
3. multiple sclerosis (intracerebral LPC administration).

Firstly, the pMCAO model induced a focal lesion in the sensorimotor cortex, as seen on the *in vivo* ADC map (Fig. 4(A), white dotted lines) and T2-weighted MRI (Fig. 4(B), white dotted lines). Subcortical white-matter loss, as can be seen in Fig. 4(C) (yellow dashed lines), may occur

in this model; it is not detectable on conventional MRI and difficult to quantify on histology; with XPCT, 3D segmentation of white matter in the caudate putamen and subsequent quantification of fiber density enabled white-matter loss to be assessed in one individual (Fig. 4(D)) and white-matter integrity in the other (Table 2).

**Table 2. XPCT quantifications (ROI: region of interest; SD: standard deviation)**

| Animal model       | Parameter  |               |                                |               |                              |
|--------------------|--|---------------|--------------------------------|---------------|------------------------------|
| Ischemic stroke    | <b>Fiber density (%)</b>   |               |                                |               |                              |
|                    | Mouse #1   |               | Mouse #2                       |               |                              |
|                    | Ipsilateral  | Contralateral | Ipsilateral                    | Contralateral |                              |
|                    | 6%   | 11%           | 11%                            | 13%           |                              |
| Premature birth    | <b>Fiber density, mean of left and right ROI <math>\pm</math> SD</b> |               |                                |               |                              |
| <i>Normoxia</i>    | Mouse #3   |               | Mouse #4                       |               |                              |
|                    | 11% $\pm$ 2%   |               | 9% $\pm$ 2%                    |               |                              |
| <i>Hypoxia</i>     | Mouse #5   |               | Mouse #6                       |               |                              |
|                    | 0% $\pm$ 0%  |               | 0% $\pm$ 2%                    |               |                              |
| Multiple sclerosis | <b>Lesion volumes (<math>10^8 \times \mu\text{m}^3</math>)</b>       |               |                                |               |                              |
|                    | Mouse #7 (2 $\mu\text{L}$ LPC)                                       |               | Mouse #8 (1 $\mu\text{L}$ LPC) |               | Rat #1 (5 $\mu\text{L}$ LPC) |
|                    | 4.4  |               | 1.2 & 1.8                      |               | 8.7                          |
|                    | <b>DTI-like parameters (% of mirror ROI)</b>                         |               |                                |               |                              |
|                    | Rat #1 (5 $\mu\text{L}$ LPC)   |               |                                |               |                              |
|                    | FA: 72%  |               | AD: 79%                        |               | RD: 146%                     |

Secondly, normoxic mouse neonates showed normal white matter aspect (Fig. 4(E)) while their hypoxic littermates exhibited very faint white-matter contrast (Fig. 4(F)). This difference in white-matter content was quantified in the striatum on an individual basis (Table 2).

Thirdly, areas of focal demyelination were clearly observed in LPC-injected animals (Fig. 5(A-B), arrow: internal capsule and caudate putamen). Focal lesions remote from the injection site were also seen in one animal, including collapse of the ipsilateral lateral ventricle (Fig. 5(A), arrowhead) and demyelination of the olfactory limb of the anterior commissure (Fig. 5(C), arrowhead). Disorganization of the stria terminalis was also observed in this mouse, despite the very small size of this fiber tract (Fig. 5(D), dashed lines). Segmentation of white-matter abnormalities gave ready access to the volume of demyelinated areas in the individual animals (Fig. 5(E), Table 2).

### 3.4. Fiber directions and diffusion metrics can be retrieved from XPCT data

To go further in the analysis of XPCT data, we explored reconstructing the orientation of brain fibers to shed light on brain structural connectivity. A DTI-like algorithm was developed, based on digital gradient analysis to detect fiber orientation [29]. Some of the brain samples (1 normal

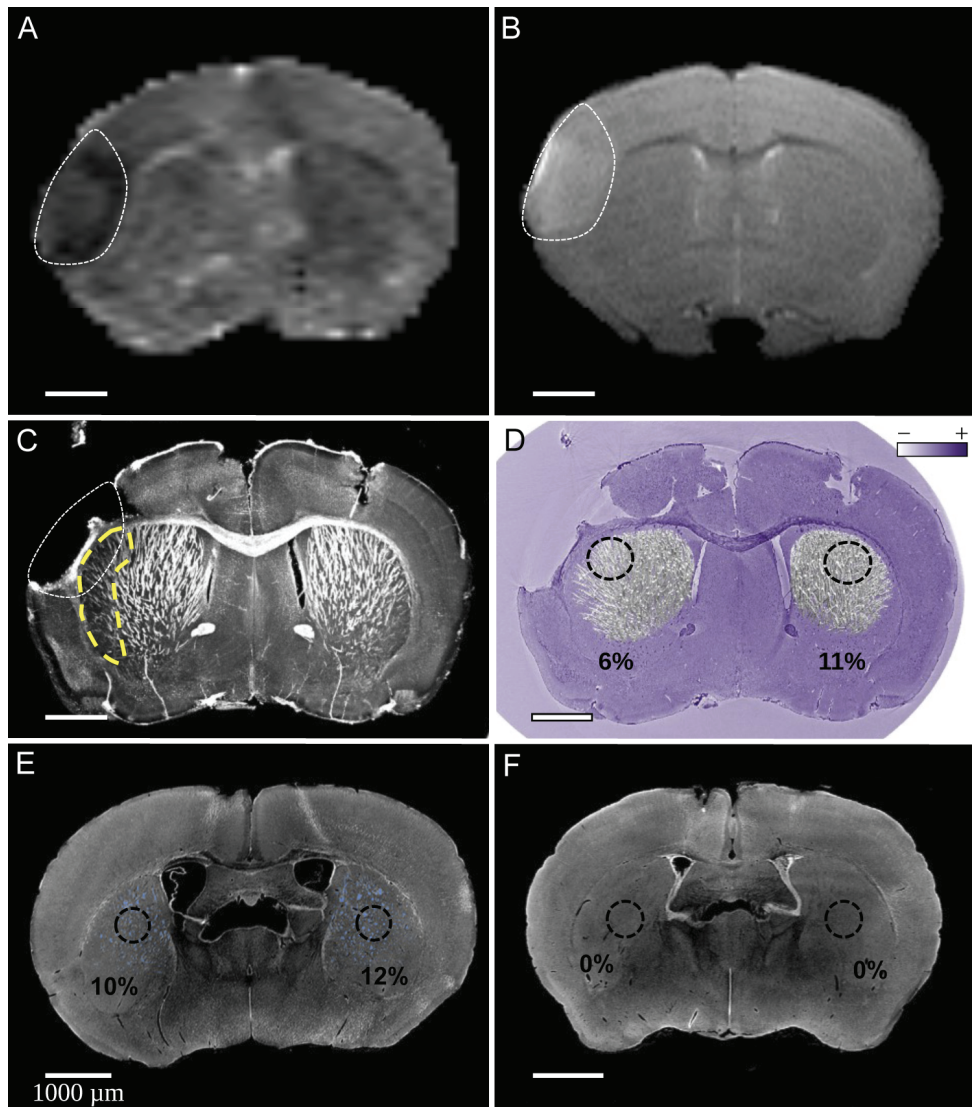


**Fig. 4.** XPCT identifies subcortical white matter loss in mouse models of ischemic stroke and preterm birth. (A-D) MRI and XPCT data in a mouse model of ischemic stroke (mouse #1 of Table 2). (A) In vivo MRI data of mouse brain with pMCAO (single slice with 800  $\mu\text{m}$  thickness) imaged at 6 hours post-ischemia. The ischemic lesion (white dotted line) appears hypointense on apparent diffusion coefficient map (A) and hyperintense on T2-weighted image (B); (C) MIP over 107 slices (807  $\mu\text{m}$ ) of XPCT data obtained at the same slice level in the same mouse after sacrifice at day 9 post-ischemia. At this stage, the infarcted cortex tended to come off along the perfusion, extraction and dehydration steps of the brain. White matter loss is clearly seen in the subcortical peri-lesional area in this animal (yellow dashed line); (D) Segmentation of caudate putamen white-matter fibers and quantification of fiber density in symmetrical regions (percentage calculated in 3D ROIs over 100 slices). The background XPCT native image is represented in false colors to provide a cresyl violet-like contrast using a home-made colormap. (E-F) XPCT data in a mouse model of preterm birth: native (single axial slice) XPCT images in (E) normoxic and (F) hypoxic mice at post-natal day #11. White-matter fiber tracts were segmented and quantified in the striatum as shown in blue in normoxic animal (mouse #3 of Table 2) (E) but barely detectable in the animals that underwent neonatal chronic hypoxia (mouse #5 of Table 2) (F).

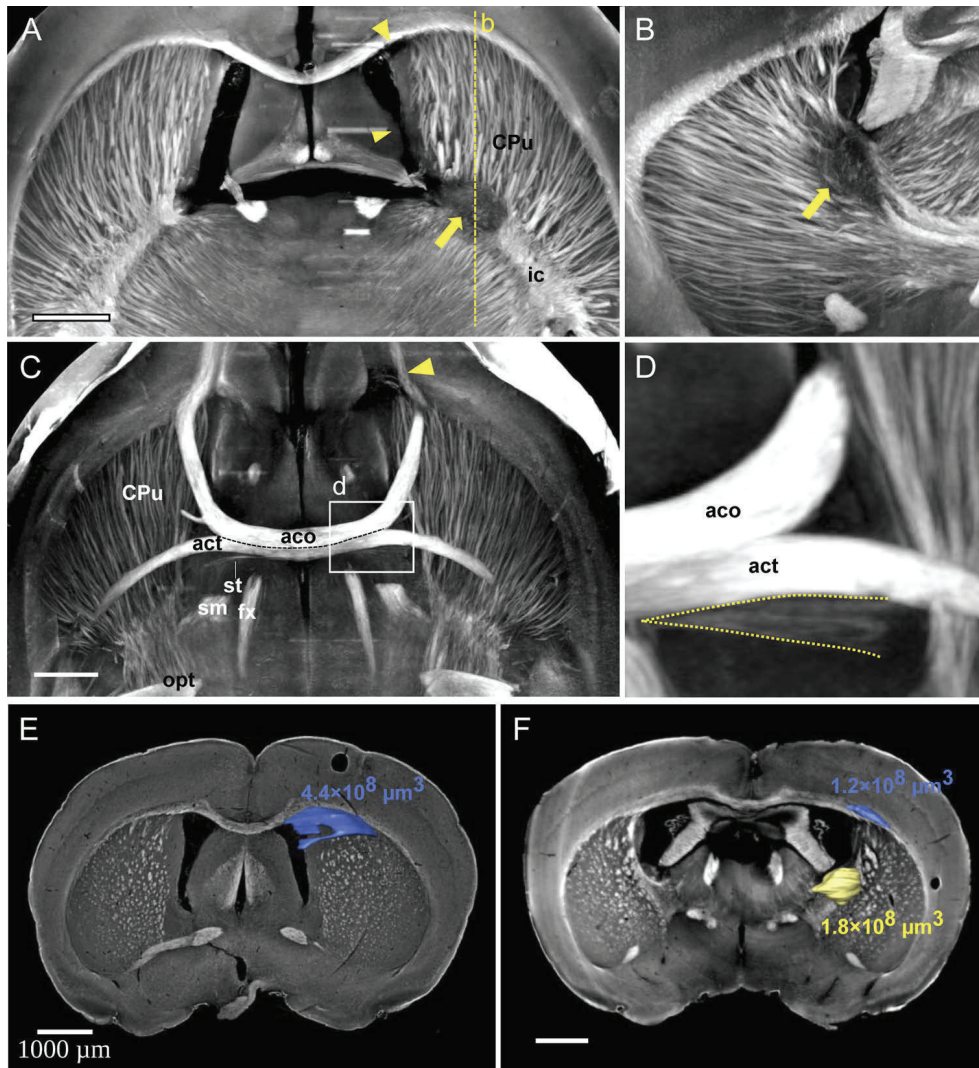


**Fig. 5.** XPCT detects white-matter fiber tract damage in a mouse model of focal demyelination. (A) MIP of axial views over 100 slices (750  $\mu\text{m}$ ) at the level of the lateral ventricles. Focal demyelination is clearly seen in the internal capsule (arrow). Other focal lesions are shown in the ipsilateral (right) side with an arrow head such as lateral ventricle collapse; (B) MIP of sagittal views at the level of the lateral ventricle over 100 slices (750  $\mu\text{m}$ ); Again, focal demyelination is clearly seen in the internal capsule (arrow); (C) MIP of axial views over 100 slices (750  $\mu\text{m}$ ) at the level of the anterior commissure; degeneration of white-matter fiber tracts can be seen in the ipsilateral anterior part of the anterior commissure (arrowhead); (D) Disorganization of the ipsilateral stria terminalis is also seen compared to the contralateral stria, despite the small size of this fiber tract (dashed lines). (E-F) Segmentation and quantification of lesion volumes in two separate mice where demyelinated lesions were induced with the LPC model.

mouse, and 1 LPC-injected rat) were imaged back-to-back with in vivo DTI (Table 1). Visual examination of brain-wide connectivity maps showed good agreement between the 2 techniques (Fig. 6(A-C)). LPC-induced demyelination of the corpus callosum was clearly depicted on XPCT fiber-orientation maps (Fig. 6(D-E)), whereas on DTI maps it was less clear (Fig. 6(F)). Fig. 6(G-H) shows examples of diffusion metrics maps obtained with in vivo DTI and XPCT respectively in the same animal. Examples of direction maps obtained in ischemic stroke and hypoxia is shown in Fig. S4. To compare FA values in the same regions of interest we have

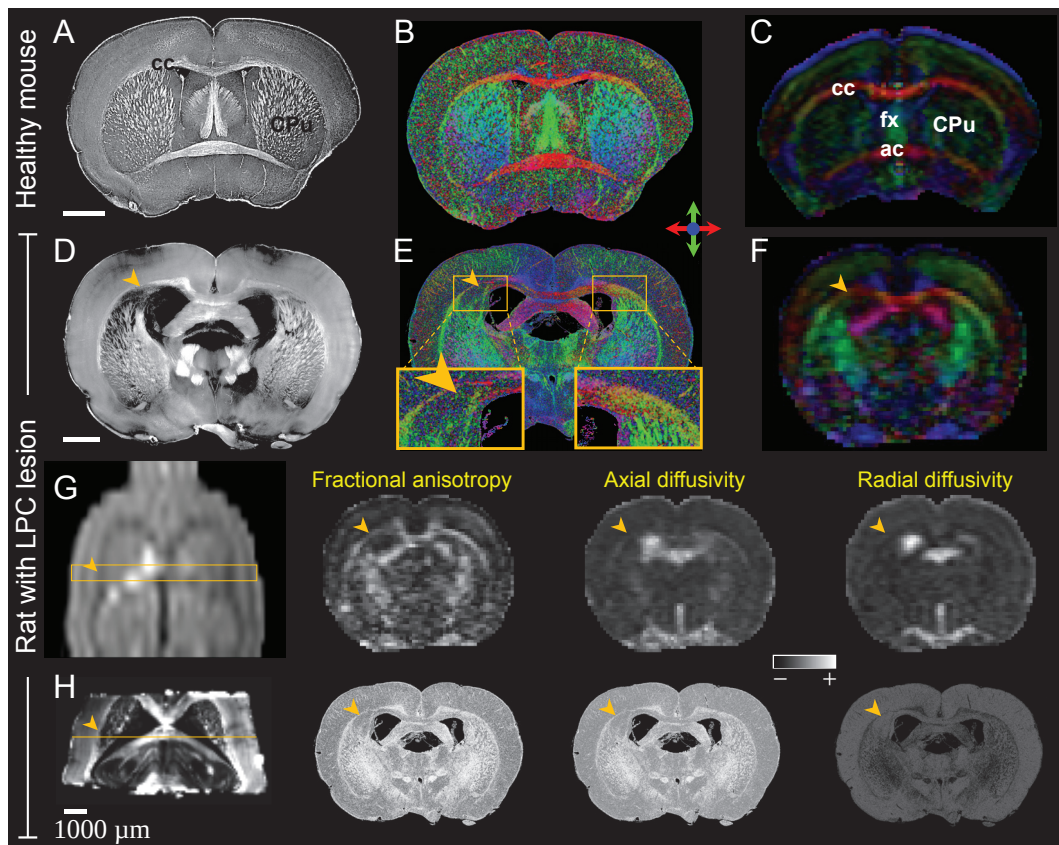


**Fig. 6.** XPCT retrieves brain-wide structural connectivity in a DTI-like manner. (A) MIP over 5 slices (37.5  $\mu\text{m}$ ) of a healthy mouse brain (coronal view); (B) Color-coded direction map extracted from XPCT from the same data set (cf. Fig. S3); (C) Color-coded direction map from in vivo DTI obtained in the same mouse at the corresponding slice level. White-matter tract directions are identical between the two techniques within major white-matter tracts such as corpus callosum (cc), fornix (fx), anterior commissure (ac) and caudate putamen (CPu); (D) MIP over 10 slices (65  $\mu\text{m}$ ) of a rat brain with an LPC-induced lesion in the corpus callosum (coronal view, arrowhead); (E) Color-coded direction map extracted from XPCT from the same dataset. The loss in right-left directionality is clearly seen in the demyelinated area compared to the contralateral side (inserts); (F) Color-coded direction map from in vivo DTI obtained in the same rat at the corresponding slice level; (G) Native DTI data ( $b_0$ ) for a rat with an LPC lesion (coronal view). The box indicates DTI slice thickness (1000  $\mu\text{m}$ ) and the arrow points to the area of demyelination. DTI metrics maps of this slice are shown in axial incidence. (H) MIP over 5 slices (65  $\mu\text{m}$ ) of XPCT image and DTI-like metrics maps corresponding to the slice indicated on the MIP (slice thickness: 6.5  $\mu\text{m}$ ).

registered the DTI volume with affine transformation over the XPCT volume and oversampled to the XPCT voxel size with nearest neighbor interpolation. The mean FA value was compared in 16 regions sampled in major white matter fiber tracts. There was a fair correlation between the two approaches (Fig. S2).

Quantification of these metrics in the injured corpus callosum further confirmed the ability of XPCT to quantitatively assess microstructural white-matter abnormalities, with a marked increase in DTI-like RD and a smaller decrease in DTI-like FA and AD compared to the symmetrically contralateral region (Table 2), as expected in demyelinated areas with limited axonal damage [2].

### 3.5. XPCT is compatible with subsequent conventional histology of brain samples

Finally, we aimed to ascertain that brain imaging with XPCT did not prevent complementary analysis with on standard approaches such as histological staining and immunohistochemistry. After XPCT imaging, 3 brain samples were rehydrated and processed using our conventional 2D histology protocols. GFAP (Fig. 7(A)), collagen type IV (Fig. 7(B)), Sudan Black B (Fig. 7(C)) and myelin basic protein (MBP) (Fig. 7(D)) immunostaining was readily achievable, with no noticeable impact of prior processing and imaging on staining quality.

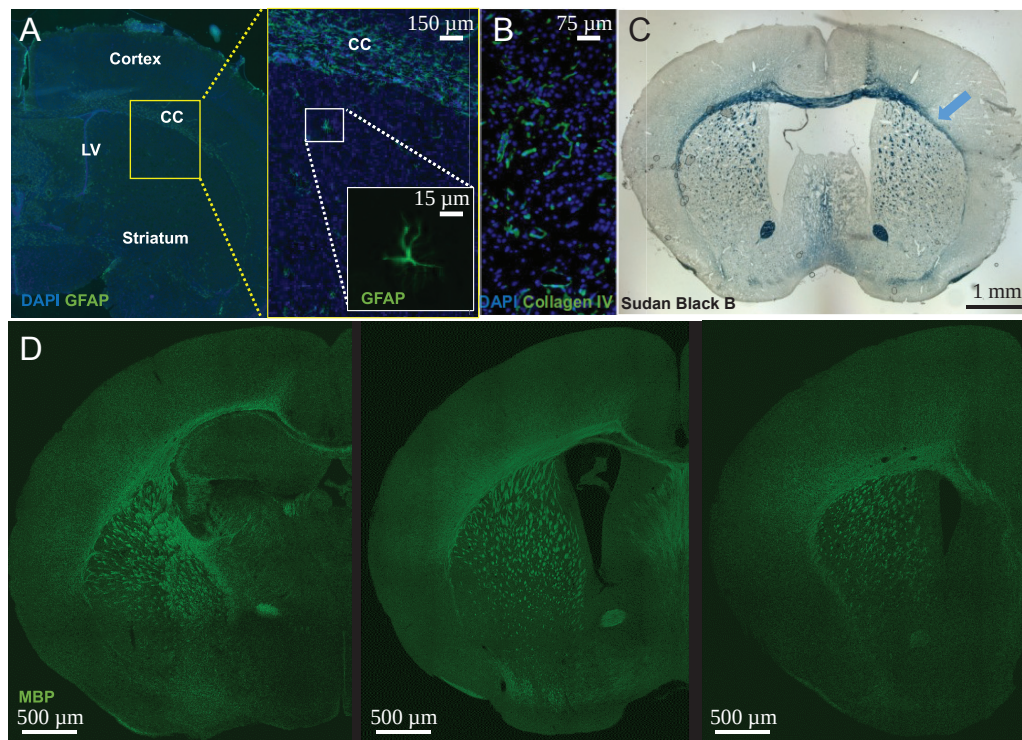


**Fig. 7.** Brain preparation for XPCT does not prevent further brain evaluation with immunohistochemistry. (A) Constitutive expression of astrocytes GFAP in healthy mouse (CC: corpus callosum, LV: lateral ventricle); (B) Collagen IV overexpression in the ischemic lesion of a pMCAO mouse; (C) Sudan Black B staining (myelin marker) of a pMCAO mouse with demyelination of the corpus callosum (blue arrow) and (D) Myelin basic protein (MBP) staining in neonatal mice (P11); three slice levels are shown.

#### 4. Discussion

This paper describes a novel label-free method based on in-line XPCT for mapping myelin in the whole mouse brain. XPCT offers many advantages over other intact-brain approaches such as electron microscopy [30,31], brain clearing [5], small angle X-ray scattering (SAXS) CT [6,32,33] or dark field CT [34]. Firstly, the FOV-to-resolution ratio is optimal for imaging the whole rodent brain at microscopic level. Secondly, isotropic resolution enables straightforward analysis of the 3D imaging data. Thirdly, acquisition and reconstruction times remain within a range of minutes. And last but not least, phase sensitivity offers an alternative to staining, as contrast between tissues is based on changes in X-ray phase rather than on absorption. Consequently, sample preparation is simple and fast. Taken together, this should enable high-throughput whole-brain studies in small laboratory animals and 3D evaluation of human brain samples.

However, phase contrast alone is not sufficient to enhance white-matter tracts, probably because the differences in refractive index between axons and surrounding tissue are minimal. The originality of our approach was to obtain myelin specificity simply by modulating the refractive indices through dehydration of brain samples with ethanol. Ethanol dehydration is the first step before paraffin embedment for histological analysis and is therefore a way of preparing brain samples that is already well-accepted by the neuroscientific community. Ethanol fixation has already been used for virtual XPCT histology of whole organs: vocal folds [35], lung [36], heart [36,37], and kidney [36,38,39]. A few brain studies also mentioned using ethanol dehydration to prepare their sample; however, they focused on displaying the angio- and/or cyto-architecture of the brain, or neuropathological features such as amyloid plaques, and did not report specific enhancement of myelinated axons [22,23,40–43]. Therefore, to the best of our knowledge, we are the first to specifically investigate and demonstrate the value of combining in-line XPCT with ethanol dehydration for 3D visualization of white-matter fiber tracts in the whole mouse brain, to relate the enhanced signal to myelin, and to provide a comprehensive framework for applications in neurological diseases.

Beside its well-known vital role in conducting signals along the nerves, myelin has many other indispensable functions in the central nervous system: providing metabolic support to axons, regulating ion and water homeostasis, and finely tuning neuronal signaling [44]. Consequently, disruption of myelin has significant neurological impact. Investigation of myelin disruption and loss in animal models is relevant not only for pathophysiology but also for lesion repair and drug discovery. We here showed, in three different animal models, that XPCT is a powerful tool to probe white-matter injury at organ scale. 3D regions of myelin loss were accurately quantified, and lesions remote from the primary injury site were straightforwardly identified. These intact-brain analyses are a major improvement over classical histology, which involves slicing the brain tissue: i.e., disrupting the structural integrity of axonal tracts.

The technique of directional diffusion is widely used to study white-matter microstructural connections [45]. However, DTI has limited in-plane and through-plane spatial resolution, and provides indirect observation of white-matter fibers. Moreover, even when performed *ex vivo* at high resolution, partial volume effects may impair DTI metrics accuracy, and the very long scanning time (typically overnight) is prone to vibration artefacts and tissue heating. We here show that XPCT can be used to obtain an estimate of whole-brain axonal tract orientations in microscopic voxels. This information can then be combined with a directional algorithm to reconstruct structural connections. Classical diffusion metrics (fractional anisotropy, axial, and radial diffusivities) can also be extracted from the diffusion tensor obtained with this algorithm. Thus, XPCT can detect subtle changes in white-matter microstructure in the course of a neuropathology, as illustrated by our results in the LPC rat model of focal demyelination. This method also seems ideally suited for future phenotype screening of myelin abnormalities in transgenic animals. Another potential application of connectome mapping by XPCT is the need for new imaging tools to cross-validate DTI [46,47]. In particular, XPCT might provide a

reference in regions of crossing fibers, which are typically difficult to resolve on DTI. Additionally, interpretation of DTI metrics in terms of neuronal and non-neuronal cell types might benefit from XPCT solely depiction of myelinated axons.

Another advantage is that XPCT is non-destructive, and dehydration by ethanol is reversible; thus, brain samples remain available for further analysis. After rehydration, we were able to perform our usual histological and immunohistological analyses. Importantly, brain slices did not show overt signs of radiation damage. In addition, ethanol dehydration/rehydration induces less volume variation and brain sample distortion than brain-clearing techniques. Because XPCT gives access to anatomic landmarks, co-registration of X-ray and optical images may be readily obtained. For instance (relevant to our discussion of DTI validation), affine or non-linear co-registration between DTI, XPCT and brain slices immunolabeled for activated glial cells could help decipher the contribution of inflammation to DTI metrics. Ultimately, such pipelines would pave the way to atlas-based analyses of XPCT datasets [48].

Like any technique, XPCT is not devoid of limitations. Propagation-based imaging set-up employed here has some limitations on the quantitativity of the reconstructed phase. Other techniques that can reconstruct quantitatively phase at this resolution [49] emerged only a few years ago (before the imaging campaign) and might even give better contrast between the different tissues. Imaging live brains at such high spatial resolution is not currently an option, because of dosimetry [50] and because the skull interferes with X-ray coherence hence having a high contrast with the brain in situ remains a challenge. Nevertheless, there is no obstacle to imaging postmortem human brains [6,22] or other human tissue [51], which has important implications for anatomopathological studies [42,52]. In addition, a synchrotron X-ray source is currently needed to produce high coherence for phase-contrast imaging, which may be a concern in terms of accessibility. However, producing phase contrast with laboratory and clinical sources is an active field of research that might solve the problem in the near future [53–56]. Finally, XPCT produces large datasets that are not easy to handle and necessitate the development of automatic post-processing tools and pipelines. This was achieved in the current project through a public-private partnership. Here, 3D analyses were performed only locally where animal models exhibited white matter loss, while information was available for the whole brain: in future work, exploitation of whole brain 3D rendering of myelin might provide new insight into white matter injury diseases. In part II of this series of articles, we develop and share a pipeline designed with open-source tools (<https://zenodo.org/record/4584753>) to segment amyloid- $\beta$  plaques and extract 3D morphometric parameters in different animal models of Alzheimer's disease [12]. The development of such end-user-friendly workflows is crucial to allow widespread use of XPCT in the neuroscience community. Collaborative efforts by multidisciplinary teams will be crucial to boosting innovation in the field of novel X-ray imaging techniques and to fostering discoveries that will ultimately benefit patients with white-matter injuries.

## 5. Conclusion

The proposed XPCT approach enables brain-wide studies of myelinated fiber tracts and of their microstructural changes in neurological diseases. Fiber directions and anisotropy metrics were retrieved from XPCT data. This is achieved with conventional animals (i.e., no need for fluorescent reporter mice), minimal sample preparation, and fast acquisition, thus allowing high throughput analysis. Furthermore, XPCT was compatible with subsequent conventional histology of brain samples. To date, the main limitation is represented by synchrotron accessibility; however, transfer of this technology to conventional X-ray sources accessible to standard laboratories is under active development [57]. In the future, combining different imaging techniques with different resolution levels and complementary information will push the frontiers of our understanding of brain structure and function.

**Funding.** Labex PRIMES (ANR-11-IDEX-0007, ANR-11-LABX-0063); European Synchrotron Radiation Facility

(LS2292, MD1018, MD1094, MD1106, MD1125); Agence Nationale de la Recherche (Breakthru (ANR-18-CE19-0003), NanoBrain (ANR15-CE18-0026), NeoRepair (ANR-17-CE16-0009)).

**Acknowledgments.** This work was performed within the framework of LABEX PRIMES (ANR-11-LABX-0063) of Université de Lyon, within the "Investissements d'Avenir" program (ANR-11-IDEX-0007) operated by the French National Research Agency (ANR). The MRI part of the study was performed on CERMEP imaging facilities (<http://www.cermep.fr>, Lyon, France). The authors would like to thank Jean-Baptiste Langlois from CERMEP for animal preparation and MRI acquisition and Corinne Perrin from the Tumorothèque Est tissue bank, CRB-HCL (Lyon, France), for managing human brain samples. We thank Clément Tavakoli for designing Fig. S1. The authors would like to thank our local ESRF contacts Lukas Helfen and Vincent Fernandez, as well as Max Langer, Loriane Weber and David Rousseau for participating in XPCT data acquisition at ESRF. This work was supported by the ESRF by allocation of beam time (LS2292, MD1018, MD1094, MD1106, MD1125). The research was funded by the French national research agency (ANR) NanoBrain (ANR15-CE18-0026), and Breakthru (ANR-18-CE19-0003). LF is supported by ANR NeoRepair (ANR-17-CE16-0009).

#### Authors' contributions (according to Contributor Role Taxonomy (CRediT))

- Conceptualization: MW, FC
- Data curation: MC, EB, HR, MW, FC
- Formal analysis: MC, AA
- Funding acquisition: EB, FP, MW, FC
- Investigation: HR, EO, VH, AP, CCdS, LF, OR, RB, EB, CO, FP, FC, MW
- Methodology: EB, HR, MW, FC
- Project administration: MW, FC
- Resources: BF, DM
- Software: AA, BF
- Supervision: EB, FC, MW
- Validation: MC, HE, FP, FC, MW
- Visualization: MC
- Writing – original draft: MW
- Writing – review & editing: MC, FP, HE, HR, MW, FC

**Disclosures.** The authors declare no conflicts of interest.

**Data availability.** The XPCT raw data cannot be shared at this time due to the large size of the datasets, but can be made available on reasonable request. The DTI-like algorithm is the property of NOVITOM.

**Supplemental document.** See [Supplement 1](#) for supporting content.

#### References

1. W. S. Tae, B. J. Ham, S. B. Pyun, S. H. Kang, and B. J. Kim, "Current clinical applications of diffusion-tensor imaging in neurological disorders," *J. Clin. Neurol.* **14**, 129–140 (2018).
2. W. Y. Aung, S. Mar, and T. L. Benzinger, "Diffusion tensor MRI as a biomarker in axonal and myelin damage," *Imaging in Medicine* **5**, 427–440 (2013).
3. J. Zhuo, S. Xu, J. L. Proctor, R. J. Mullins, J. Z. Simon, G. Fiskum, and R. P. Gullapalli, "Diffusion kurtosis as an in vivo imaging marker for reactive astrogliosis in traumatic brain injury," *NeuroImage* **59**, 467–477 (2012).
4. M. Aswendt, M. Schwarz, W. M. Abdelmoula, J. Dijkstra, and S. Dedeurwaerdere, "Whole-brain microscopy meets in vivo neuroimaging: techniques, benefits, and limitations," *Mol. Imaging Biol.* **19**, 1–9 (2017).
5. E. H. Chang, M. Argyelan, M. Aggarwal, T.-S. S. Chandon, K. H. Karlsgodt, S. Mori, and A. K. Malhotra, "The role of myelination in measures of white matter integrity: Combination of diffusion tensor imaging and two-photon microscopy of CLARITY intact brains," *NeuroImage* **147**, 253–261 (2017).
6. M. Georgiadis, A. Schroeter, Z. Gao, M. Guizar-Sicairos, D. S. Novikov, E. Fieremans, and M. Rudin, "Retrieving neuronal orientations using 3D scanning SAXS and comparison with diffusion MRI," *NeuroImage* **204**, 116214 (2020).
7. J. Albers, S. Pacilé, M. A. Markus, M. Wiart, G. Vande Velde, G. Tromba, and C. Dullin, "X-ray-based 3D virtual histology-adding the next dimension to histological analysis," *Mol. Imaging Biol.* **20**, 732–741 (2018).
8. Y. Hwu, G. Margaritondo, and A.-S. Chiang, "Q&A: Why use synchrotron x-ray tomography for multi-scale connectome mapping?" *BMC Biol.* **15**, 122 (2017). Number: 1.
9. M. Marinescu, M. Langer, A. Durand, C. Olivier, A. Chabrol, H. Rositi, F. Chauveau, T. H. Cho, N. Nighoghossian, Y. Berthezène, F. Peyrin, and M. Wiart, "Synchrotron radiation X-ray phase micro-computed tomography as a new method to detect iron oxide nanoparticles in the brain," *Mol. Imaging Biol.* **15**, 552–559 (2013). Number: 5.

10. H. Rositi, C. Frindel, M. Langer, M. Wiart, C. Olivier, F. Peyrin, and D. Rousseau, "Information-based analysis of X-ray in-line phase tomography with application to the detection of iron oxide nanoparticles in the brain," *Opt. Express* **21**, 27185–27196 (2013).
11. H. Rositi, C. Frindel, M. Wiart, M. Langer, C. Olivier, F. Peyrin, and D. Rousseau, "Computer vision tools to optimize reconstruction parameters in x-ray in-line phase tomography," *Phys. Med. Biol.* **59**, 7767–7775 (2014).
12. M. Chourrou, M. Roux, C. Boisvert, C. Gislard, D. Legland, I. Arganda-Carreras, C. Olivier, F. Peyrin, H. Boutin, N. Rama, T. Baron, D. Meyronet, E. Brun, H. Rositi, M. Wiart, and F. Chauveau, "Brain virtual histology with X-ray phase-contrast tomography Part II: 3D morphologies of amyloid- $\beta$  plaques in Alzheimer's disease models," *Biomed. Opt. Express* **13**, 1640–1653 (2022).
13. F. Chauveau, S. Moucharrafié, M. Wiart, J.-C. Brisset, Y. Berthezène, N. Nighoghossian, and T.-H. Cho, "In vivo MRI assessment of permanent middle cerebral artery occlusion by electrocoagulation: pitfalls of procedure," *Exp & Trans Stroke Med* **2**, 4 (2010).
14. J. Scafidi, T. R. Hammond, S. Scafidi, J. Ritter, B. Jablonska, M. Roncal, K. Szigeti-Buck, D. Coman, Y. Huang, R. J. McCarter, F. Hyder, T. L. Horvath, and V. Gallo, "Intranasal epidermal growth factor treatment rescues neonatal brain injury," *Nature* **506**, 230–234 (2014).
15. M. Zhang, G. Hugon, C. Bouillot, R. Bolbos, J.-B. Langlois, T. Billard, F. Bonnefoi, B. Li, L. Zimmer, and F. Chauveau, "Evaluation of myelin radiotracers in the lysocleithin rat model of focal demyelination: beware of pitfalls!" *Contrast Media & Molecular Imaging* **2019**, 9294586 (2019).
16. B. Nait-Oumesmar, L. Decker, F. Lachapelle, V. Avellana-Adalid, C. Bachelin, and A. B.-. Van Evercooren, "Progenitor cells of the adult mouse subventricular zone proliferate, migrate and differentiate into oligodendrocytes after demyelination: Oligodendrocyte differentiation in adult SVZ," *European Journal of Neuroscience* **11**, 4357–4366 (1999).
17. K. Chung, J. Wallace, S.-Y. Kim, S. Kalyanasundaram, A. S. Andalman, T. J. Davidson, J. J. Mirzabekov, K. A. Zalocusky, J. Mattis, A. K. Denisin, S. Pak, H. Bernstein, C. Ramakrishnan, L. Grose, V. Gradinaru, and K. Deisseroth, "Structural and molecular interrogation of intact biological systems," *Nature* **497**, 332–337 (2013). Number: 7449.
18. D. Paganin, S. C. Mayo, T. E. Gureyev, P. R. Miller, and S. W. Wilkins, "Simultaneous phase and amplitude extraction from a single defocused image of a homogeneous object," *J Microsc* **206**, 33–40 (2002). Number: Pt 1.
19. A. F. Frangi, W. J. Niessen, K. L. Vincken, and M. A. Viergever, "Multiscale vessel enhancement filtering," in *Medical Image Computing and Computer-Assisted Intervention—MICCAI'98*, vol. 1496, W. M. Wells, A. Colchester, and S. Delp, eds. (Springer Berlin Heidelberg, 1998), pp. 130–137. Series Title: Lecture Notes in Computer Science.
20. M. Sato, I. Bitter, M. Bender, A. Kaufman, and M. Nakajima, "TEASAR: tree-structure extraction algorithm for accurate and robust skeletons," in *Proceedings the Eighth Pacific Conference on Computer Graphics and Applications* (IEEE Comput. Soc, 2000), pp. 281–449.
21. G. E. Barbone, A. Bravin, P. Romanelli, A. Mittone, D. Bucci, T. Gaaß, G. Le Duc, S. Auweter, M. F. Reiser, M. J. Kraiger, M. Hrabe de Angelis, G. Battaglia, and P. Coan, "Micro-imaging of brain cancer radiation therapy using phase-contrast computed tomography," *International Journal of Radiation Oncology, Biology, Physics* **101**, 965–984 (2018). Number: 4.
22. M. Töpferwien, M. Krenkel, D. Vincenz, F. Stöber, A. M. Oelschlegel, J. Goldschmidt, and T. Salditt, "Three-dimensional mouse brain cytoarchitecture revealed by laboratory-based x-ray phase-contrast tomography," *Sci Rep* **7**, 42847 (2017).
23. M. Saccomano, J. Albers, G. Tromba, M. Dobrivojevic Radmilovic, S. Gajovic, F. Alves, and C. Dullin, "Synchrotron inline phase contrast  $\mu$ CT enables detailed virtual histology of embedded soft-tissue samples with and without staining," *J Synchrotron Rad* **25**, 1153–1161 (2018).
24. Y. Ren, Y. Wang, G. Zhou, Y. He, H. Xie, G. Du, B. Deng, X. Lin, G.-y. Yang, and T. Xiao, "X-ray propagation-based equally sloped tomography for mouse brain," *Journal of X-Ray Science and Technology* **24**, 79–86 (2016).
25. J. S. O'Brien and E. L. Sampson, "Lipid composition of the normal human brain: gray matter, white matter, and myelin," *XST* **6**, 537–544 (1965).
26. L.-Y. Zhang, P. Lin, J. Pan, Y. Ma, Z. Wei, L. Jiang, L. Wang, Y. Song, Y. Wang, Z. Zhang, K. Jin, Q. Wang, and G.-Y. Yang, "CLARITY for High-resolution Imaging and Quantification of Vasculature in the Whole Mouse Brain," *Aging and disease* **9**, 262 (2018).
27. C. Leuze, M. Goubran, M. Barakovic, M. Aswendt, Q. Tian, B. Hsueh, A. Crow, E. Weber, G. Steinberg, M. Zeineh, E. Plowey, A. Daducci, G. Innocenti, J.-P. Thiran, K. Deisseroth, and J. McNab, "Comparison of diffusion MRI and CLARITY fiber orientation estimates in both gray and white matter regions of human and primate brain," *NeuroImage* **228**, 117692 (2021).
28. M. Morawski, E. Kirilina, N. Scherf, C. Jäger, K. Reimann, R. Trampel, F. Gavriilidis, S. Geyer, B. Biedermann, T. Arendt, and N. Weiskopf, "Developing 3D microscopy with CLARITY on human brain tissue: towards a tool for informing and validating MRI-based histology," *NeuroImage* **182**, 417–428 (2018).
29. M. Krause, J. M. Hausherr, B. Burgeth, C. Herrmann, and W. Krenkel, "Determination of the fibre orientation in composites using the structure tensor and local X-ray transform," *J Mater Sci* **45**, 888–896 (2010).
30. S. Mikula, J. Binding, and W. Denk, "Staining and embedding the whole mouse brain for electron microscopy," *Nat Methods* **9**, 1198–1201 (2012). Number: 12.

31. R. A. Salo, I. Belevich, E. Manninen, E. Jokitalo, O. Gröhn, and A. Sierra, "Quantification of anisotropy and orientation in 3D electron microscopy and diffusion tensor imaging in injured rat brain," *NeuroImage* **172**, 404–414 (2018).
32. T. Jensen, M. Bech, O. Bunk, A. Menzel, A. Bouchet, G. Le Duc, R. Feidenhans'l, and F. Pfeiffer, "Molecular X-ray computed tomography of myelin in a rat brain," *NeuroImage* **57**, 124–129 (2011). Number: 1.
33. M. Georgiadis, A. Schroeter, Z. Gao, M. Guizar-Sicairos, M. Liebi, C. Leuze, J. A. McNab, A. Balolia, J. Veraart, B. Ades-Aron, S. Kim, T. Shepherd, C. H. Lee, P. Walczak, S. Chodankar, P. DiGiacomo, G. David, M. Augath, V. Zerbi, S. Sommer, I. Rajkovic, T. Weiss, O. Bunk, L. Yang, J. Zhang, D. S. Novikov, M. Zeineh, E. Fieremans, and M. Rudin, "Nanostructure-specific X-ray tomography reveals myelin levels, integrity and axon orientations in mouse and human nervous tissue," *Nat Commun* **12**, 2941 (2021).
34. M. Wiczorek, F. Schaff, C. Jud, D. Pfeiffer, F. Pfeiffer, and T. Lasser, "Brain connectivity exposed by anisotropic X-ray dark-field tomography," *Sci Rep* **8**, 14345 (2018). Number: 1.
35. L. Bailly, T. Cochereau, L. Orgéas, N. Henrich Bernardoni, S. Rolland du Roscoat, A. McLeer-Florin, Y. Robert, X. Laval, T. Laurencin, P. Chaffanjon, B. Fayard, and E. Boller, "3D multiscale imaging of human vocal folds using synchrotron X-ray microtomography in phase retrieval mode," *Sci Rep* **8**, 14003 (2018).
36. J. Dudak, J. Zemlicka, J. Karch, M. Patzelt, J. Mrzilkova, P. Zach, Z. Hermanova, J. Kvacsek, and F. Krejci, "High-contrast X-ray micro-radiography and micro-CT of ex-vivo soft tissue murine organs utilizing ethanol fixation and large area photon-counting detector," *Sci Rep* **6**, 30385 (2016). Number: 1.
37. M. Reichardt, J. Frohn, A. Khan, F. Alves, and T. Salditt, "Multi-scale X-ray phase-contrast tomography of murine heart tissue," *Biomed. Opt. Express* **11**, 2633–2651 (2020).
38. R. Shirai, T. Kunii, A. Yoneyama, T. Oozumi, H. Maruyama, T.-T. Lwin, K. Hyodo, and T. Takeda, "Enhanced renal image contrast by ethanol fixation in phase-contrast X-ray computed tomography," *J Synchrotron Rad* **21**, 795–800 (2014). Number: 4.
39. J. Missbach-Guentner, D. Pinkert-Leetsch, C. Dullin, R. Ufartes, D. Hornung, B. Tampe, M. Zeisberg, and F. Alves, "3D virtual histology of murine kidneys—high resolution visualization of pathological alterations by micro computed tomography," *Sci Rep* **8**, 1407 (2018). Number: 1.
40. M. Töpperwien, A. Markus, F. Alves, and T. Salditt, "Contrast enhancement for visualizing neuronal cytoarchitecture by propagation-based x-ray phase-contrast tomography," *NeuroImage* **199**, 70–80 (2019).
41. M.-Q. Zhang, L. Zhou, Q.-F. Deng, Y.-Y. Xie, T.-Q. Xiao, Y.-Z. Cao, J.-W. Zhang, X.-M. Chen, X.-Z. Yin, and B. Xiao, "Ultra-high-resolution 3D digitalized imaging of the cerebral angioarchitecture in rats using synchrotron radiation," *Sci Rep* **5**, 14982 (2015). Number: 1.
42. L. Massimi, I. Bukreeva, G. Santamaria, M. Fratini, A. Corbelli, F. Brun, S. Fumagalli, L. Maugeri, A. Pacureanu, P. Cloetens, N. Pieroni, F. Fiordaliso, G. Forloni, A. Uccelli, N. Kerlero de Rosbo, C. Balducci, and A. Cedola, "Exploring Alzheimer's disease mouse brain through X-ray phase contrast tomography: From the cell to the organ," *NeuroImage* **184**, 490–495 (2019).
43. L. Massimi, N. Pieroni, L. Maugeri, M. Fratini, F. Brun, I. Bukreeva, G. Santamaria, V. Medici, T. E. Poloni, C. Balducci, and A. Cedola, "Assessment of plaque morphology in Alzheimer's mouse cerebellum using three-dimensional X-ray phase-based virtual histology," *Sci Rep* **10**, 11233 (2020). Number: 1.
44. M. A. Marin and S. T. Carmichael, "Mechanisms of demyelination and remyelination in the young and aged brain following white matter stroke," *Neurobiology of Disease* **126**, 5–12 (2019).
45. H. Chen, T. Liu, Y. Zhao, T. Zhang, Y. Li, M. Li, H. Zhang, H. Kuang, L. Guo, J. Z. Tsien, and T. Liu, "Optimization of large-scale mouse brain connectome via joint evaluation of DTI and neuron tracing data," *NeuroImage* **115**, 202–213 (2015).
46. T. B. Dyrby, G. M. Innocenti, M. Bech, and H. Lundell, "Validation strategies for the interpretation of microstructure imaging using diffusion MRI," *NeuroImage* **182**, 62–79 (2018).
47. M. Andersson, H. M. Kjer, J. Rafael-Patino, A. Pacureanu, B. Pakkenberg, J.-P. Thiran, M. Ptito, M. Bech, A. Bjorholm Dahl, V. Andersen Dahl, and T. B. Dyrby, "Axon morphology is modulated by the local environment and impacts the noninvasive investigation of its structure–function relationship," *Proc Natl Acad Sci USA* **117**, 33649–33659 (2020).
48. C. J. Niedworok, A. P. Y. Brown, M. Jorge Cardoso, P. Osten, S. Ourselin, M. Modat, and T. W. Margrie, "aMAP is a validated pipeline for registration and segmentation of high-resolution mouse brain data," *Nat Commun* **7**, 11879 (2016). Number: 1.
49. M.-C. Zdora, P. Thibault, W. Kuo, V. Fernandez, H. Deyhle, J. Vila-Comamala, M. P. Olbinado, A. Rack, P. M. Lackie, O. L. Katsamenis, M. J. Lawson, V. Kurtcuoglu, C. Rau, F. Pfeiffer, and I. Zanette, "X-ray phase tomography with near-field speckles for three-dimensional virtual histology," *Optica* **7**, 1221 (2020).
50. Y. Prezado, M. Vautrin, I. Martínez-Rovira, A. Bravin, F. Estève, H. Elleaume, P. Berkvens, and J. F. Adam, "Dosimetry protocol for the forthcoming clinical trials in synchrotron stereotactic radiation therapy (SSRT): dosimetry protocol for the clinical trials in SSRT," *Med. Phys.* **38**, 1709–1717 (2011).
51. H. Rougé-Labriet, S. Berujon, H. Mathieu, S. Bohic, B. Fayard, J.-N. Ravey, Y. Robert, P. Gaudin, and E. Brun, "X-ray phase contrast osteo-articular imaging: a pilot study on cadaveric human hands," *Sci. Rep.* **10**, 1911 (2020).
52. A. Cedola, A. Bravin, I. Bukreeva, M. Fratini, A. Pacureanu, A. Mittone, L. Massimi, P. Cloetens, P. Coan, G. Campi, R. Spanò, F. Brun, V. Grigoryev, V. Petrosino, C. Venturi, M. Mastrogiacomo, N. Kerlero de Rosbo, and A. Uccelli,

- “X-ray phase contrast tomography reveals early vascular alterations and neuronal loss in a multiple sclerosis model,” *Sci Rep* **7**, 5890 (2017). Number: 1.
53. L. Birnbacher, M. Willner, A. Velroyen, M. Marschner, A. Hipp, J. Meiser, F. Koch, T. Schröter, D. Kunka, J. Mohr, F. Pfeiffer, and J. Herzen, “Experimental realisation of high-sensitivity laboratory x-ray grating-based phase-contrast computed tomography,” *Sci Rep* **6**, 24022 (2016).
54. H. Rougé-Labriet, L. Quenot, S. Bohic, B. Fayard, D. M. Paganin, E. Brun, and S. Berujon, “Comparison of X-ray speckle based imaging deflection retrieval algorithms for the optimization of radiation dose,” *Phys. Medicine & Biol.* **66**, 065005 (2020).
55. D. H. Larsson, W. Vågberg, A. Yaroshenko, A. O. Yildirim, and H. M. Hertz, “High-resolution short-exposure small-animal laboratory x-ray phase-contrast tomography,” *Sci Rep* **6**, 39074 (2016).
56. T. Zhou, U. Lundström, T. Thüring, S. Rutishauser, D. H. Larsson, M. Stampanoni, C. David, H. M. Hertz, and A. Burvall, “Comparison of two x-ray phase-contrast imaging methods with a microfocus source,” *Opt. Express* **21**, 30183 (2013).
57. L. Quenot, H. Rougé-Labriet, S. Bohic, S. Berujon, and E. Brun, “Implicit tracking approach for X-ray phase-contrast imaging with a random mask and a conventional system,” *Optica* **8**, 1412–1415 (2021).

Supplemental Document

Biomedical Optics EXPRESS

## Brain virtual histology with X-ray phase-contrast tomography Part I: whole-brain myelin mapping in white-matter injury models: supplement

**MATTHIEU CHOURROUT**<sup>1,11</sup>  **HUGO ROSITI**<sup>2,11</sup> **ELODIE ONG**<sup>3,4</sup> **VIOLAINE HUBERT**<sup>3</sup> **ALEXANDRE PACCALET**<sup>3</sup> **LOUIS FOUCAULT**<sup>5</sup> **AWEN AUTRET**<sup>6</sup> **BARBARA FAYARD**<sup>6</sup> **CÉCILE OLIVIER**<sup>7</sup> **RADU BOLBOS**<sup>8</sup> **FRANÇOISE PEYRIN**<sup>7</sup> **CLAIRE CROLA-DA-SILVA**<sup>3</sup> **DAVID MEYRONET**<sup>4</sup> **OLIVIER RAINETEAU**<sup>5</sup> **HÉLÈNE ELLEAUME**<sup>9</sup> **EMMANUEL BRUN**<sup>9</sup>  **FABIEN CHAUVEAU**<sup>1,10,12</sup>  **AND MARLENE WIART**<sup>3,10,12,\*</sup> 

<sup>1</sup>Univ-Lyon, Lyon Neuroscience Research Center, CNRS UMR5292, Inserm U1028, Université Claude Bernard Lyon 1, Lyon, France

<sup>2</sup>Univ-Clermont Auvergne; CNRS; SIGMA Clermont; Institut Pascal, Clermont-Ferrand, France

<sup>3</sup>Univ-Lyon, CarMeN laboratory, Inserm U1060, INRA U1397, Université Claude Bernard Lyon 1, INSA Lyon, Charles Mérieux Medical School, F-69600, Oullins, France

<sup>4</sup>Univ-Lyon, Hospices Civils de Lyon, Lyon, France

<sup>5</sup>Univ-Lyon, Université Claude Bernard Lyon 1, Inserm, Stem Cell and Brain Research Institute U1208, 69500 Bron, France

<sup>6</sup>NOVITOM, Grenoble, France

<sup>7</sup>Univ-Lyon, INSA-Lyon, Université Claude Bernard Lyon 1, CNRS, Inserm, CREATIS UMR5220, U1206, F-69621, France

<sup>8</sup>Cermep, Lyon, France

<sup>9</sup>Université Grenoble Alpes, Inserm UA7 Strobe, Grenoble, France

<sup>10</sup>CNRS, Lyon, France

<sup>11</sup>Co-first authors

<sup>12</sup>Co-last authors

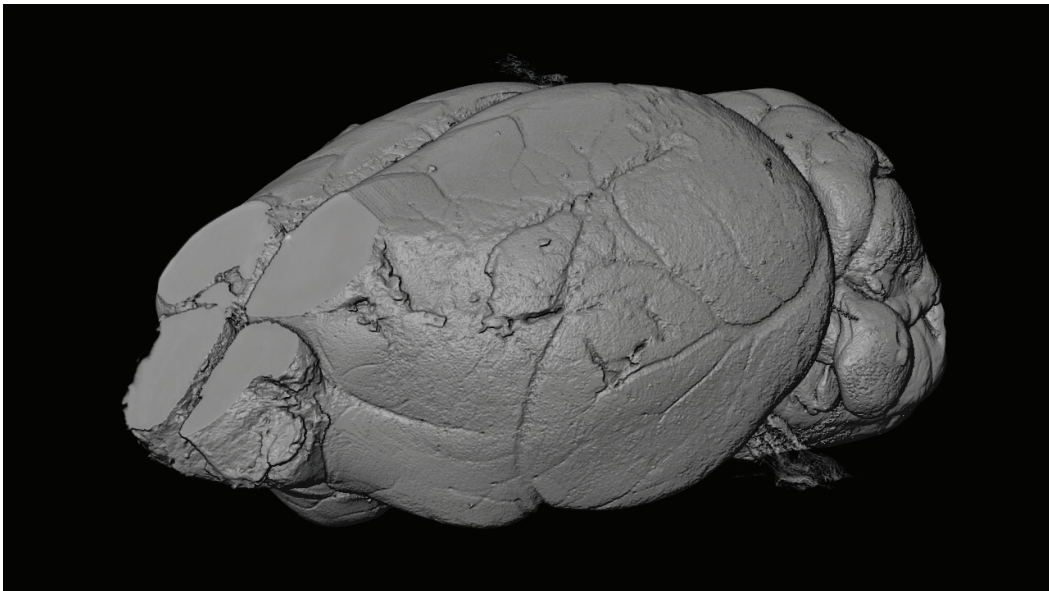
\*marlene.wiart@univ-lyon1.fr

This supplement published with Optica Publishing Group on 23 February 2022 by The Authors under the terms of the [Creative Commons Attribution 4.0 License](https://creativecommons.org/licenses/by/4.0/) in the format provided by the authors and unedited. Further distribution of this work must maintain attribution to the author(s) and the published article's title, journal citation, and DOI.

Supplement DOI: <https://doi.org/10.6084/m9.figshare.16941094>

Parent Article DOI: <https://doi.org/10.1364/BOE.438832>

# Brain virtual histology with X-ray phase-contrast tomography — Part I: whole-brain myelin mapping in white-matter injury models — Supplemental document



**Visualization 1.** 3D rendering of a whole mouse brain and virtual histology in coronal view.  
URL: <https://osapublishing.figshare.com/s/8b5ff8dc95b502237a09>

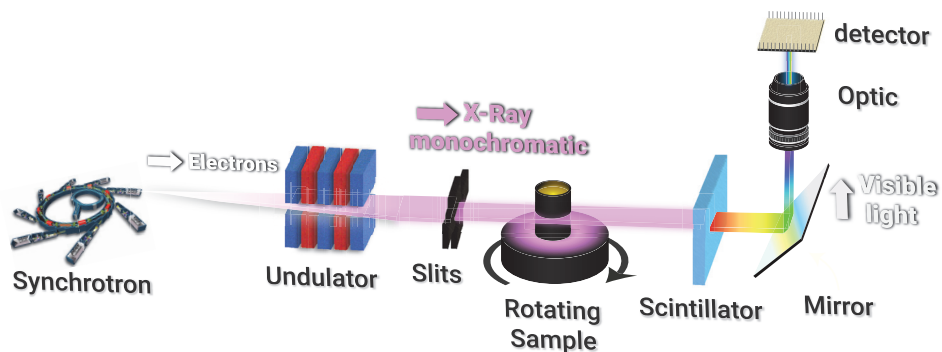


**Fig. S1.** Principle of in-line phase contrast tomography: experimental set-up

**Table S1.** Experimental MRI parameters. TE: echo time; TR: repetition time; T2WI: T2-weighted MRI; DTI: diffusion tensor imaging; N/A: non-applicable.

| MR imaging parameter               | T2WI             | DTI                       |
|------------------------------------|------------------|---------------------------|
| Spatial acquisition dimension      | 2D               | 3D                        |
| Measuring method                   | SpinEcho         | DtiEpi                    |
| TE [ms]                            | 69.1             | 25.1                      |
| TR [ms]                            | 4000             | 650                       |
| Number of diffusion directions     | N/A              | 30                        |
| Number of A0 images                | N/A              | 5                         |
| Max. B value [ $s/mm^2$ ]          | N/A              | 1600                      |
| Number of segments                 | N/A              | 2                         |
| Number of averages                 | 2                | 1                         |
| Bandwidth [kHz]                    | 25               | 300                       |
| Field of view [ $mm^2$   $mm^3$ ]  | $20 \times 20$   | $20 \times 10 \times 17$  |
| Slice thickness or interslice [mm] | 1                | 0.5                       |
| Number of slices                   | 10               | 36                        |
| Matrix size [pixels]               | $256 \times 256$ | $192 \times 96 \times 36$ |
| In-plane resolution [ $\mu m^2$ ]  | $78 \times 78$   | $104 \times 104$          |
| Acquisition time [s]               | 192              | 1638                      |

**Table S2.** Experimental XPCT parameters

|  | Figures<br>1, 2, 4C-D,<br>5, 6A-B, 7B                     | 3C-D, 4E-F,<br>6D-E, 6G-H    | 3A-B                        |
|--|---|------------------------------|-----------------------------|
| <b>Supplemental Figures</b>                        | 4, 5E-F   | 5C-D                         | 5A                          |
| <b>Setup</b>                                       | ID19  | ID19                         | ID17                        |
| <b>Detector</b>                                    | FReLoN  | sCMOS<br>(PCO edge)          | sCMOS<br>(PCO edge)         |
| <b>Scintillator</b>                                | LuAg (500 $\mu m$ )                                       | LuAg (500 $\mu m$ )          | LuAg (500 $\mu m$ )         |
| <b>Energy [keV] (<math>\Delta E</math> [eV])</b>   | 19 (600)  | 26 (600)                     | 35 (35)                     |
| <b>Sample-detector distance [m]</b>                | 1   | 1.3–3                        | 11                          |
| <b>Field-of-view [<math>cm^3</math>]</b>           | $1.5 \times 1.5 \times 1.5$                               | $1.3 \times 1.3 \times 1.23$ | $1.5 \times 1.5 \times 1.5$ |
| <b>Matrix</b>                                      | $2048 \times 2048$  | $2048 \times 2048$           | $2560 \times 2160$          |
| <b>Total number of slices</b>                      | 2000  | 2000                         | 3200                        |
| <b>Voxel size (isotropic) [<math>\mu m</math>]</b> | 7.5   | 6.5                          | 6.13                        |
| <b>Exposure time [s]</b>                           | 0.15  | 0.05                         | 0.05                        |
| <b>Number of projections</b>                       | 2000 (180°)   | 2499 (180°)                  | 2800 (360°)                 |
| <b>Estimated dose [Gy]</b>                         | 150 000   | 35 000                       | 60                          |
| <b>Acquisition time [min]</b>                      |   | < 10                         |                             |
| <b>Reconstruction algorithm</b>                    | PyHST 2 (Paganin filter, $\delta/\beta \in [600; 1000]$ ) |                              |                             |

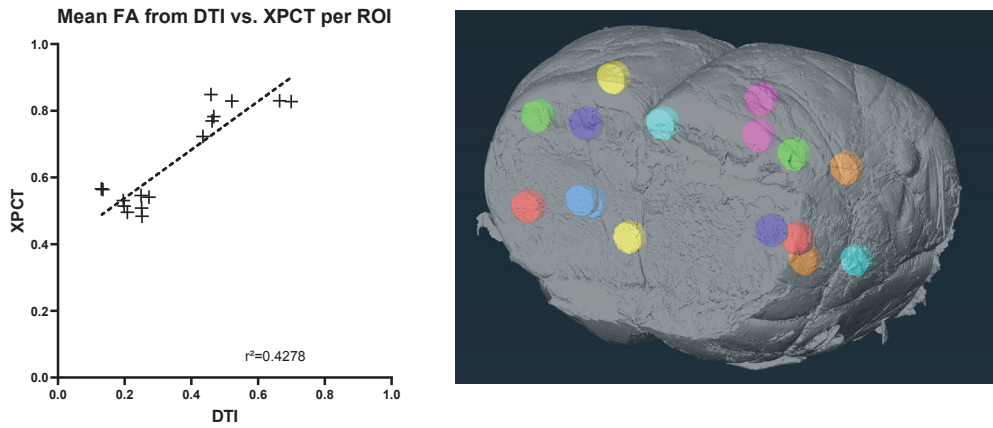


**Fig. S2.** Comparison of mean FA between in vivo DTI and ex vivo XPCT

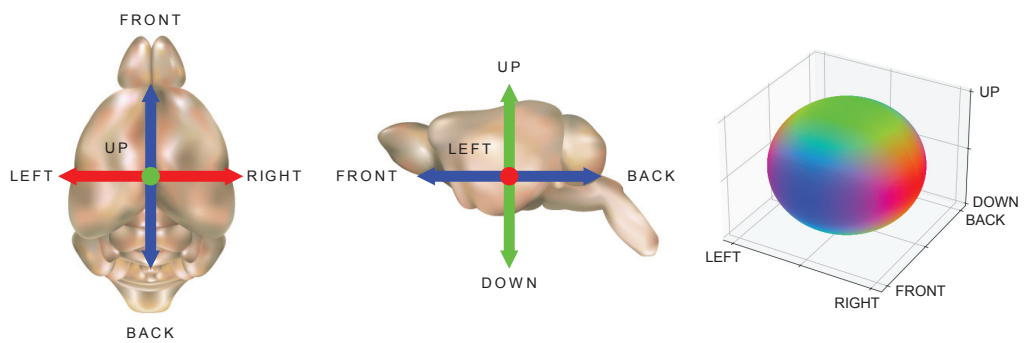


**Fig. S3.** Color-code convention for fiber orientation from the diffusion MRI community. It is replicated in the NOVITOM software.



**Visualization 2.** Virtual histology of a whole mouse brain in sagittal view. URL: <https://osapublishing.figshare.com/s/b3288191f556cfd27b99>

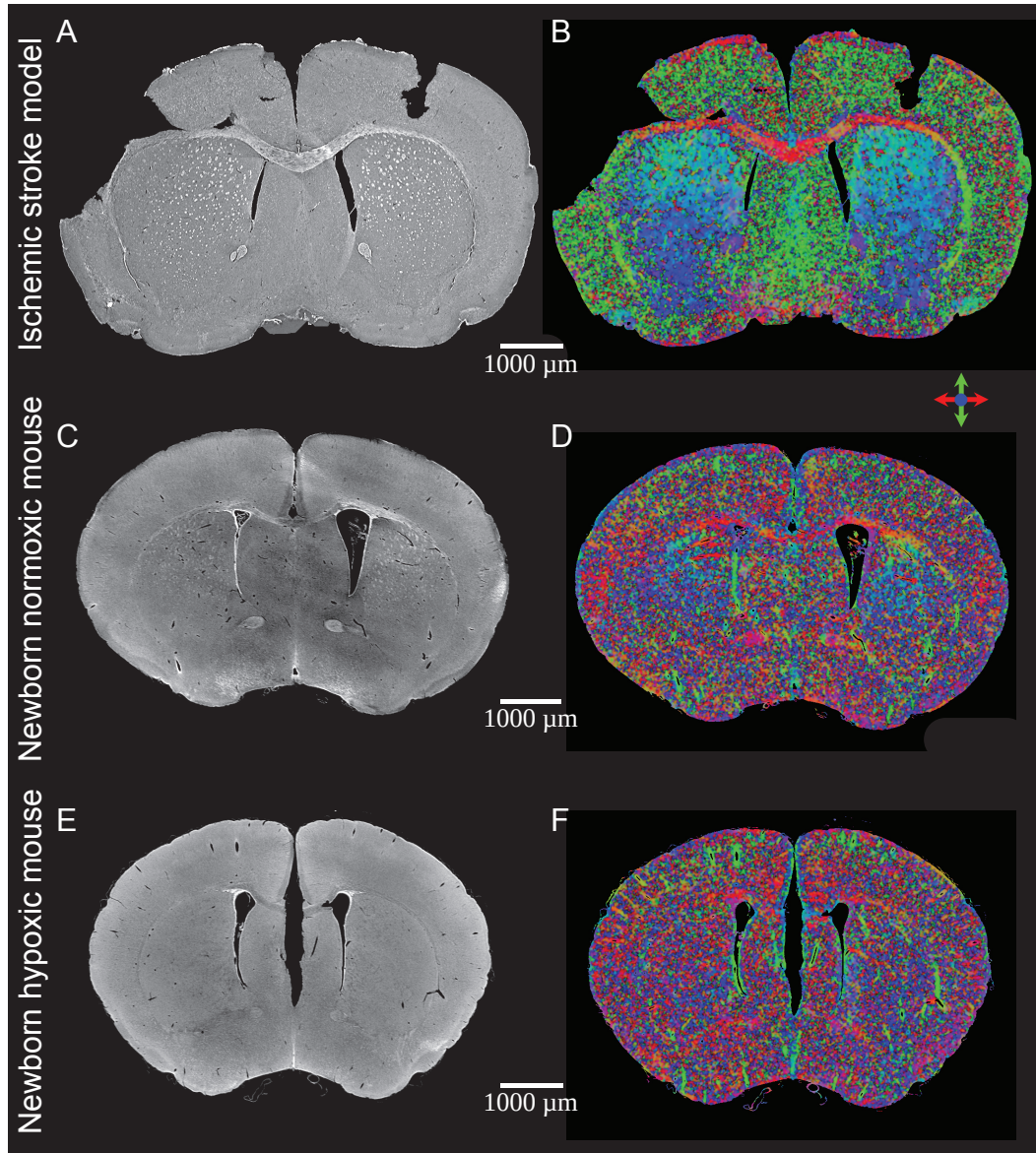


**Fig. S4.** XPCT retrieves brain-wide structural connectivity in a DTI-like manner. **(A)** Native (single coronal slice) XPCT image of mouse #1 (ischemic stroke model, from Table 2); **(B)** Color-coded direction maps extracted from the same dataset (cf. Fig. S3); **(C)** Native (single coronal slice) XPCT image of mouse #4 (normoxic mouse); **(D)** Color-coded direction maps extracted from the same dataset; **(E)** Native (single coronal slice) XPCT image of mouse #6 (hypoxic mouse); **(F)** Color-coded direction maps extracted from the same dataset. As expected, the newborn normoxic brain is not completely myelinated yet but some of the major fiber tracts are visible (corpus callosum and anterior commissure), whereas they are not observed in the newborn mouse that underwent hypoxia.

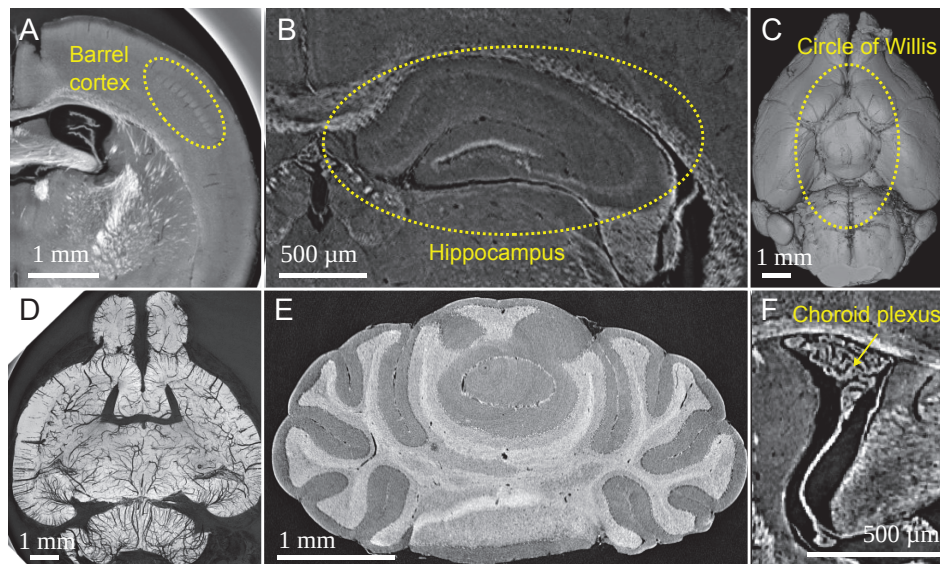


**Fig. S5.** Virtual histology with XPCT displays major brain anatomic features in the whole mouse brain taken from different samples. (A) Barrel cortex; (B) Hippocampus; (C) Circle of Willis obtained by surface rendering of the whole brain (rostral side); (D) Angiography obtained by minimum intensity projection over 100 slices; (E) Cerebellum; (F) Choroid plexus.

### 3.3. Discussion

In this article, we demonstrated that propagation-based XPCT can yield (pre-)clinically-relevant results for the study of white-matter tracts in a few animal models and in autopsy-derived human samples. We also reported how XPCT enables the non-destructive exploration of the healthy and diseased brains without any contrast agent, which was a milestone for the subsequent work within the scope of the PhD project.

We demonstrated that the XPCT high-density signal — i.e. bright in our images — of white-matter tracts can be attributed to myelin: tracts turned dark when imaged after the clearing process which removes myelin; this was confirmed with ulterior histology. Other groups have tried different preparations for the samples, such as paraffin-embedding [286, 316] which is widely adopted to process clinical samples for histology. However, during the process of paraffin-embedding, myelin and other lipids are washed out; myelin can be protected thanks to osmium tetroxide or chromic acid [317]. To distinguish the smaller myelin sheaths ( $\varnothing \approx 0.4 \mu\text{m}$  [318]) and assess the myelin content, one would need an effective resolution close to  $0.1 \mu\text{m}$ ; this has been reached with holotomography [319] — and applied to isolated mouse nerves in the same work — or with cryo-CT setups [320].

Imaging healthy brain and neuronal system with XPCT has been reported in small-cohort studies for a decade [233, 284, 319, 321, 322, 323, 324, 325]. Thus, we targeted animal models for ischemic stroke and multiple sclerosis with a local alteration. The use of models with local alterations complied with our team's 3R commitment concerning research ethics for animal studies ([www.fc3r.com/en/](http://www.fc3r.com/en/)): the ipsilateral lesions were characterized with respect to a contralateral "control" region. The high resolution of XPCT proved relevant to study these small-size lesions. Partial-volume effects — i.e. when multiple types of tissue are contained in a single voxel — are inherent in MRI because of its low resolution [326] — which is even reduced in the axial direction of the device. Contrary to MRI, XPCT has an isotropic resolution. In our work, virtual histology with XPCT has achieved precise localization and a range of quantitative studies for three different animal models.

We individually segmented the tracts in the striatum by

combining a gray-level thresholding on raw images with a fiber-enhancement filter (3D Frangi [327]). The detected demyelination in the ischemic stroke model was broader than the necrotic zone. Young mice from a premature birth model had no detectable myelin in the striatum whereas the control littermates had a fairly complete white-matter network in the same region.

Following a private–public partnership, a proprietary software was developed to generate DTI-like parametric maps; the software was closed source but the methods were thoroughly described in our article. The software relied on image gradient analysis to construct a structure tensor. *In vivo* DTI acquisitions were performed before sacrifice. The values between DTI and XPCT were quite different: this can be imputed to partial-volume effects, the very different process for the generation of the metrics and the fact that DTI data was acquired *in vivo* while XPCT data was acquired *ex vivo*; however, the diminished fractional anisotropy (FA) and the increased radial diffusivity (RD), with respect to the contralateral region, were consistent between the two imaging techniques. Following this work, we have been contacted for a collaboration which has already resulted in a joint article[229]. The algorithm was implemented recently (in Python) in a common project with Joshua Gobé, the PhD student who will further develop the biomedical applications of XPCT in our group. A first strategy identified TrackVis (Ruopeng Wang, Van J. Wedeen, TrackVis.org, Martinos Center for Biomedical Imaging, Massachusetts General Hospital; [trackvis.org](http://trackvis.org)) [328], a closed-source software which could generate the tractography from our pre-processed XPCT data; first results were encouraging (cf. Figure 3.1) but TrackVis development was stopped in 2017 and we encountered software limitations. The current strategy is to rely on Dipy [329], an open-source software with a large community and active developers; the Python ecosystem seems more accurate nowadays and the open-source integration of our contribution into Dipy is foreseen.

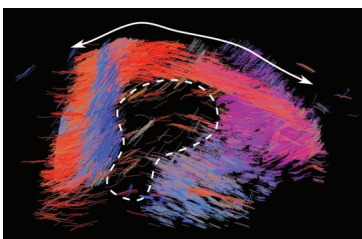


**Figure 3.1.:** Tractography of the corpus callosum from an XPCT image in a multiple sclerosis model (LPC injection) using our pipeline and TrackVis. The corpus callosum contains long fibers (along the plain arrow); the empty region corresponds to the white-matter injury (dashed area). Unpublished results.

Exact correlation between different modalities along with histology (for validation) has been reported before [236, 330, 331] and after [332, 333] the publication of our work. Depending on the technique one wants to combine with XPCT, sample preparation methods might have to be adapted; a recent protocol review highlighted this challenge [334]. The

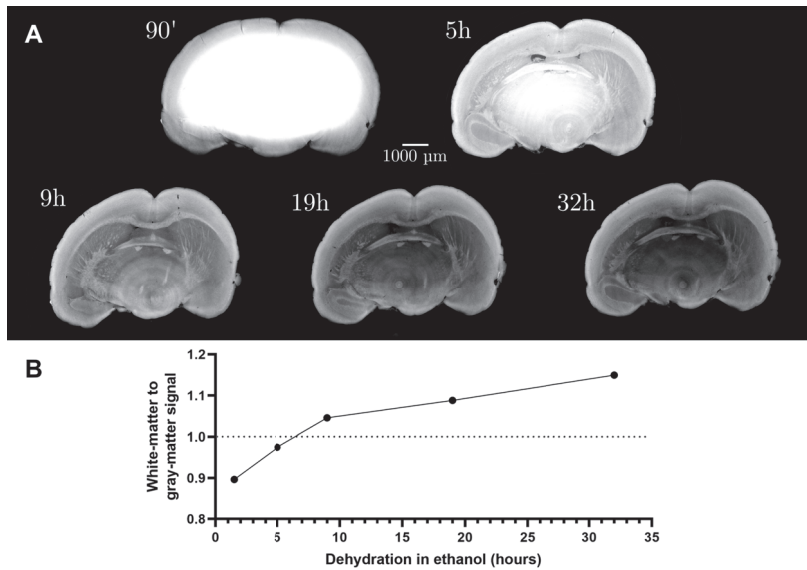


**Figure 3.2.:** Dehydration kinetics of a full mouse brain immersed in 96% ethanol. (A) Snapshots of the same mouse brain imaged at different time-points during dehydration. (B) Ratio of signal intensities between the anterior commissure and the thalamus. Unpublished results.

sample preparation we used in our study was well-known (formaldehyde-fixation and ethanol-dehydration) [283, 335, 336, 337], but we adjusted the protocol (progressive dehydration and final ethanol concentration) for optimal contrast; recently, we showed this contrast appears after more than 10 h (cf. Figure 3.2). In our study, we used anatomical landmarks from the 2D MRI plane or from the 2D histology slices to fine-tune the position and orientation of our virtual XPCT slice; we performed minimal rigid registration. A thorough study [286, 338] measured the anisotropic shrinkage and contrast changes of paraffin embedding at multiple stages of the process, including after fixation and dehydration in ethanol; their work highlighted the importance of non-rigid registration for future applications. The registration has two purposes: to easily compare multiple modalities and to automatically retrieve labeled regions from a reference atlas like the Allen Reference Atlas – Adult Mouse Brain ([atlas.brain-map.org](https://atlas.brain-map.org)) [339] or the rat brain atlas by Paxinos and Watson [340].



# Morphological study of amyloid- $\beta$ plaques with XPCT

# 4.

## 4.1. Introduction

The second study reported in this PhD thesis focused on AD transgenic mouse models: one mono-transgenic strain (J20) we acquired from collaborators at the Cancer Research Center of Lyon, one double-transgenic strain (APPPS1) we acquired from the French Agency for Food, Environmental and Occupational Health & Safety (ANSES) and one triple-transgenic strain (3xTg) from Manchester University. They all develop A $\beta$  plaques, mainly in the hippocampus (cf. subsection 1.4.1). Previous works have already reported that these plaques appear in label-free XPCT images. Multiple brains from each strain were collected *postmortem* for imaging with XPCT. The sample preparation was the same as in the first study. We designed a versatile segmentation pipeline that we shared online; it uses open-source software. We identified a set of 8 relevant 3D metrics and compared them for the three transgenic strains.

|   |     |
|---|-----|
| 4.1 Introduction . . . . .              | 89  |
| 4.2 Associated published work . . . . . | 89  |
| 4.3 Discussion . . . . .                | 108 |

To get familiar with the rodent brain anatomy, one can refer to the [Mouse Brain Atlas \[191\]](#) or [Rat Brain Atlas \[192, 193, 194\]](#) on EBRAINS.

## 4.2. Associated published work

---

Reproduced from Biomed Opt Express.

Chourrout M, Roux M, Boisvert C, Gislard C, Legland D, Arganda-Carreras I, Olivier C, Peyrin F, Boutin H, Rama N, Baron T, Meyronet D, Brun E, Rositi H, Wiart M, and Chauveau F. Brain Virtual Histology with X-ray Phase-Contrast Tomography Part II: 3D Morphologies of Amyloid- $\beta$  Plaques in Alzheimer’s Disease Models. *Biomed Opt Express*. 2022 Mar 1; 13

[Open Access – Version of Record]

---



# Brain virtual histology with X-ray phase-contrast tomography Part II: 3D morphologies of amyloid- $\beta$ plaques in Alzheimer's disease models

MATTHIEU CHOURROUT,<sup>1</sup>  MARGAUX ROUX,<sup>1</sup> CARLIE BOISVERT,<sup>1,15</sup> CORALIE GISLARD,<sup>1</sup> DAVID LEGLAND,<sup>2</sup> IGNACIO ARGANDA-CARRERAS,<sup>3,4,5</sup> CÉCILE OLIVIER,<sup>6</sup> FRANÇOISE PEYRIN,<sup>6</sup> HERVÉ BOUTIN,<sup>7</sup> NICOLAS RAMA,<sup>8</sup> THIERRY BARON,<sup>9</sup> DAVID MEYRONET,<sup>10</sup> EMMANUEL BRUN,<sup>11</sup>  HUGO ROSITI,<sup>12</sup> MARLÈNE WIART,<sup>13,14,16</sup>  AND FABIEN CHAUVEAU<sup>1,14,16,\*</sup> 

<sup>1</sup>Univ. Lyon, Lyon Neuroscience Research Center, CNRS UMR5292, Inserm U1028, Université Claude Bernard Lyon 1, Lyon, France

<sup>2</sup>UR BIA; BIBS Facility, INRAE, Nantes, France

<sup>3</sup>University of the Basque Country (UPV/EHU), San Sebastian, Spain

<sup>4</sup>Ikerbasque, Basque Foundation for Science, Bilbao, Spain

<sup>5</sup>Donostia International Physics Center (DIPC), San Sebastian, Spain

<sup>6</sup>Univ. Lyon, CREATIS; CNRS UMR5220; INSERM U1044; INSA-Lyon; Univ. Lyon 1, Lyon, France

<sup>7</sup>Univ. Manchester, Faculty of Biology Medicine and Health, Wolfson Molecular Imaging Centre, Manchester, UK

<sup>8</sup>Univ. Lyon, CRCL; INSERM U1052; CNRS UMR5286; Univ. Lyon 1; Centre Léon Bérard, Lyon, France

<sup>9</sup>Univ. Lyon, ANSES, Lyon, France

<sup>10</sup>Univ. Lyon, Hospices Civils de Lyon, Lyon, France

<sup>11</sup>Univ. Grenoble Alpes, Inserm UA07 Strobe Grenoble, France

<sup>12</sup>Univ. Clermont Auvergne, Institut Pascal; CNRS UMR 6602; SIGMA Clermont, Clermont-Ferrand, France

<sup>13</sup>Univ. Lyon, CarMeN Laboratory; INSERM U1060; INRA U1397; Hospices Civils de Lyon, Lyon, France

<sup>14</sup>CNRS, Lyon, France

<sup>15</sup>Current affiliation: Faculty of Medicine, The Ottawa Hospital and University of Ottawa, Ottawa, Ontario, Canada

<sup>16</sup>These authors contributed equally to this work

\*[chauveau@cermep.fr](mailto:chauveau@cermep.fr)

**Abstract:** While numerous transgenic mouse strains have been produced to model the formation of amyloid- $\beta$  (A $\beta$ ) plaques in the brain, efficient methods for whole-brain 3D analysis of A $\beta$  deposits have to be validated and standardized. Moreover, routine immunohistochemistry performed on brain slices precludes any shape analysis of A $\beta$  plaques, or require complex procedures for serial acquisition and reconstruction. The present study shows how in-line (propagation-based) X-ray phase-contrast tomography (XPCT) combined with ethanol-induced brain sample dehydration enables hippocampus-wide detection and morphometric analysis of A $\beta$  plaques. Performed in three distinct Alzheimer mouse strains, the proposed workflow identified differences in signal intensity and 3D shape parameters: 3xTg displayed a different type of A $\beta$  plaques, with a larger volume and area, greater elongation, flatness and mean breadth, and more intense average signal than J20 and APP/PS1. As a label-free non-destructive technique, XPCT can be combined with standard immunohistochemistry. XPCT virtual histology could thus become instrumental in quantifying the 3D spreading and the morphological impact of seeding when studying prion-like properties of A $\beta$  aggregates in animal models of Alzheimer's disease. This is Part II of a series of two articles reporting the value of in-line XPCT for virtual histology of the brain; Part I shows how in-line XPCT enables 3D myelin mapping in the whole

rodent brain and in human autopsy brain tissue.

© 2022 Optical Society of America under the terms of the [OSA Open Access Publishing Agreement](#)

## 1. Introduction

The amyloid cascade is considered pivotal in the development of Alzheimer's disease. In the last 20 years, numerous transgenic mouse strains have been produced to model the accumulation of amyloid- $\beta$  ( $A\beta$ ) peptides and formation of  $A\beta$  plaques in the brain. Most are knock-in animals, obtained by insertion of human genes, which usually include mutations observed in familial cases: presenilins (PSEN1/2), amyloid precursor protein (APP), microtubule associated protein tau (MAPT), triggering receptor expressed on myeloid cells 2 (TREM2), etc. The Alzforum database currently lists 126 mouse models with 1 transgene, and 62 multi-transgene mouse models (<https://www.alzforum.org/research-models>; last access on October 14, 2021). Fast methods for whole-brain analysis are thus of great value for characterizing and comparing phenotypes among the variety of strains available. Several recent developments have been proposed to enable individual  $A\beta$  plaque detection through the entire brain in 3D. These include two-photon serial imaging [1], ultramicroscopy [2], or optical projection tomography [3], which all belong to the field of optical mesoscopy.

X-ray-based virtual histology is a new field of research mainly aimed at 3D datasets of biological tissue virtually sliced in any direction [4]. X-ray phase-contrast tomography (XPCT) using synchrotron radiation allows imaging of excised biological tissues or organs with weak X-ray absorption (like the brain) at microscopic level [5]. XPCT achieves a high signal-to-noise ratio without the need to add staining agents, by probing small changes in refractive indices in the tissue microstructure. It provides micrometric spatial resolution and isotropic reconstruction in a  $\sim 1 \text{ cm}^3$  field of view (FOV), thus offering ideal prerequisites for imaging protein aggregates of  $\sim 10 \mu\text{m}$  in the entire and intact (unsliced, unstained) mouse brain [6].

Several pioneer studies already reported detection of  $A\beta$  plaques with various X-ray phase-contrast techniques [7–9]. However, these first developments required long acquisition times (30 min–180 min) and/or provided limited anatomical contrast. Recently, free space propagation between object and detector has been shown to be a simple, fast and efficient technique for detecting  $A\beta$  plaques with good contrast [10,11]. In addition, anatomic contrast can be greatly enhanced by dehydrating the brain prior to imaging, which increases small local differences between the refractive indices of the different brain structures [5,6]. In terms of analysis and quantification, most previous studies reported only qualitative results, or quantification restricted to parameters accessible to standard 2D histology (e.g., number of plaques, diameter, volume). Only one recent report used XPCT to extract sphericity of  $A\beta$  plaques inside the cerebellum [12]. The present study aimed to realize the full potential of XPCT by combining:

1. optimal brain tissue preparation through dehydration in ethanol,
2. fast acquisition in three different (mono, double and triple) transgenic mouse strains displaying  $A\beta$  pathology,
3. semi-automatic segmentation of  $A\beta$  plaques inside the hippocampus using open-source tools (combination of Fiji plugins),
4. and full characterization of their 3D morphology.

This is Part II of a series of two articles reporting the value of in-line XPCT for virtual histology of the brain; Part I shows how in-line XPCT enables myelin mapping of the whole brain [13].

## 2. Methods

### 2.1. Samples

All experimental procedures were carried out in accordance with European regulations for animal use (EEC Council Directive 2010/63/EU). The present study was performed on excised brains. Three transgenic lines were used, for a total of 8 brains:

1. mono-transgene line J20 ( $n=2$  animals, 2 y.o.), with mutant APP [14];
2. double-transgene line APP<sup>swe</sup>/PSEN1<sup>dE9</sup> or APP/PS1 ( $n=3$  animals, 1 y.o.), with mutant APP and mutant PSEN1 [15];
3. triple-transgene line 3xTg ( $n=3$  animals, 1 y.o.), with mutant APP, mutant PSEN1 and mutant MAPT [16].

One additional brain, from a wild-type mouse of C57BL6/129sv background, was used as a control.

### 2.2. Preparation

On the day before imaging, formaldehyde-fixed brains were dehydrated in baths of ascending ethanol concentrations (25, 50, 75, 96%, at least 5 min per bath), and conditioned in plastic tubes (1 cm diameter) filled with ethanol.

### 2.3. Acquisition

Imaging was performed at the ID19 beamline of the European Synchrotron Research Facility (ESRF, Grenoble, France). Acquisition parameters and data characteristics are summarized in Table 1. Briefly, the tomographic images were recorded within 3 minutes at a single sample-detector distance where the camera was positioned away from the sample (3 m) to obtain phase contrast. The experiments were performed with a polychromatic "pink" incident X-ray beam of 26 keV energy. Tomographic reconstructions were performed using the single-distance phase-retrieval approach ("Paganin" method [17]) with PyHST2 software [18], the  $\delta/\beta$  ratio being set to 1000.

### 2.4. Segmentation

Semi-automated detection of A $\beta$  plaques used Fiji software [19]. A pipeline was built with the following plugins: segmentation editor (to isolate hippocampus; [https://imagej.net/Segmentation\\_Editor](https://imagej.net/Segmentation_Editor)), Trainable Weka Segmentation 3D (to identify plaques) [20], and MorphoLibJ [21] and 3D ImageJ suite [22] (to label objects and extract relevant parameters). Image features used for trainable segmentation were "Difference of Gaussian", "Variance", and "Maximum" for J20 and 3xTg. For APP/PS1, "Minimum" was used instead of "Maximum" after the application of a 3D Laplacian-of-Gaussian (Mexican Hat) filter [23], as suggested by Astolfo et al. [10]. A step-by-step guide to perform all image processing, "Amyloid- $\beta$  XPCT Workflow", is publicly available (DOI: 10.5281/zenodo.4584752) [24].

### 2.5. 3D parameters

Sphericity, elongation, flatness, sparseness and distance to nearest object were outputs from 3D ImageJ Suite. Surface area, volume, mean breadth and mean signal intensity (here normalized by background intensity) were outputs from MorphoLibJ. Definitions of these parameters are reported in Table 2.

**Table 1. Acquisition parameters and data characteristics.**

|  |  |
|--|--|
| <b>Setup</b>   | ID19   |
| <b>Detector</b>  | sCMOS (PCO edge)                                 |
| <b>Scintillator</b>                                      | LuAg (500 $\mu\text{m}$ )                        |
| <b>Energy [keV]</b>                                      | 26   |
| <b>Sample-detector distance [m]</b>                      | 3  |
| <b>Exposure time [s]</b>                                 | 0.04   |
| <b>Number of projections</b>                             | 3000   |
| <b>Sample rotation [°]</b>                               | 360  |
| <b>Acquisition time [min]</b>                            | 3  |
| <b>Reconstruction algorithm</b>                          | PyHST 2 (Paganin filter, $\delta/\beta = 1000$ ) |
| <b>Field-of-view [<math>\text{cm}^3</math>]</b>          | $1.3 \times 1.3 \times 0.9$                      |
| <b>Matrix</b>  | $2048 \times 2048$                               |
| <b>Number of slices</b>                                  | 1400   |
| <b>Voxel size (isotropic) [<math>\mu\text{m}</math>]</b> | 6.5  |
| <b>Image size [GB]</b>                                   | 11.7 (as 16-bit data)                            |
| <b>Estimated dose [Gy]</b>                               | 35000  |

## 2.6. Analysis and statistics

Prism 8 (GraphPad) was used for violin plots and statistics. The Welch version of one-way ANOVA (gaussian populations, unequal variances) was used to compare the above-cited parameter values of individual A $\beta$  plaques across the three transgenic groups, with additional Games-Howell tests (recommended for  $n > 50$ ) for pairwise comparisons. Linear correlations between parameters were quantified on Pearson correlation coefficient. MIPAV (v10.0.0, CIT, NIH [26]) was used for 2D visualization of semi-transparent overlay of plaque labels onto native images. Amira Software 6 (ThermoFisher) was used for all 3D renderings.

## 2.7. Immunohistochemistry

One sample of each transgenic strain underwent paraffin embedding, 7  $\mu\text{m}$ -thick microtome slicing (Leica RM2245) and standard A $\beta$  immunofluorescence or histological staining. A $\beta$  immunofluorescence was performed after i) standard dewaxing, ii) antigen retrieval with 100% formic acid for 15–20 minutes at room temperature (RT), and iii) blocking with 5% Bovine Serum Albumin (BSA) and 0.5% Triton-X in Phosphate Buffer Saline (PBS, Sigma-Aldrich ref. P4417) for 30 minutes at RT, by incubating the anti-A $\beta$  monoclonal antibody 4G8 (Covance, ref. SIG-39220, dilution 1 : 1000 in 5% BSA) on each microscope slide overnight, in a humid chamber at 4°C. After three 5 min washes in PBS at RT, secondary antibody (anti-mouse AlexaFluor 488 or 546, ThermoFisher, dilution 1 : 500 in 5% BSA) was incubated on each microscope slide for 60 minutes, in a humid chamber at RT. After three 5 min washes in PBS at RT, slides were mounted with DAPI-containing medium (Roti-Mount FluorCare DAPI, Carl Roth), and stored at 4°C. Thioflavin S staining (ThS, Sigma-Aldrich ref. T1892) (0.05% in ethanol 70%) was performed for 10 min at RT after dewaxing, and slides were mounted with DAPI-containing medium, after two 1 min washes in ethanol 70%. Fluorescence images were captured on a microscope (AxioScope A1, Zeiss) equipped with a digital camera interfaced with image-analysis software (ZEN 2 lite, Zeiss).

**Table 2. Morphometric parameters. More details are available at <https://imagej.net/MorphoLibJ.html#Documentation> and in [25].**

| Name                                 | Definition   | Formula  |
|--------------------------------------|--|--|
| <b>Compactness</b><br>(not reported) | Ratio ( $C$ ) between volume ( $V$ ) and surface area ( $A$ ); "3D ImageJ Suite" implements a 'discrete' compactness, described by Bribiesca (2008), estimated from the number of voxels ( $N_{\text{voxels}}$ ); spheres have a compactness of 1. | $C = \frac{36\pi V^2}{A^3} \approx \frac{N_{\text{voxels}} - \frac{A}{6}}{N_{\text{voxels}} - (N_{\text{voxels}})^{2/3}}$        |
| <b>Sphericity</b>                    | Ratio ( $S$ ) between volume ( $V$ ) and surface area ( $A$ ); linked to compactness (or discrete compactness); spheres have a sphericity of 1.  | $S = C^{1/3} \approx \left( \frac{N_{\text{voxels}} - \frac{A}{6}}{N_{\text{voxels}} - (N_{\text{voxels}})^{2/3}} \right)^{1/3}$ |
| <b>Elongation</b>                    | Elongation of the equivalent ellipsoid, where $R_1 > R_2 > R_3$ are the lengths of the semi-axes of the ellipsoid with same inertia tensor as the object   | $\text{Elongation} = \frac{R_1}{R_2}$  |
| <b>Flatness</b>                      | Flatness of the equivalent ellipsoid, where $R_1 > R_2 > R_3$ are the lengths of the semi-axes of the ellipsoid with same inertia tensor as the object   | $\text{Flatness} = \frac{R_2}{R_3}$  |
| <b>Sparseness</b>                    | Ratio between the volume of the equivalent ellipsoid ( $V_{\text{ell}}$ ) and the volume of the object ( $V_{\text{obj}}$ )  | $\text{Sparseness} = \frac{V_{\text{ell}}}{V_{\text{obj}}}$  |
| <b>Mean Signal Intensity (SI)</b>    | Mean intensity from the raw image; here reported as a mean signal-to-background ratio  |  |
| <b>Volume</b>                        | Volume in the given unit ( $\mu\text{m}^3$ )   |  |
| <b>Surface Area</b>                  | Surface area in the given unit ( $\mu\text{m}^2$ )   |  |
| <b>Mean Breadth</b>                  | Average of the Feret diameter of convex objects measured over a selected number of orientations ( $\mu\text{m}$ )  |  |
| <b>Distance</b>                      | Distance between two closest segmented objects ( $\mu\text{m}$ )   |  |

### 3. Results

#### 3.1. Qualitative analysis

After ethanol dehydration, brain anatomy, and specifically white matter tracts, was uniquely displayed on XPCT images (Fig. 1), as reported in Part I of this series of articles [13].

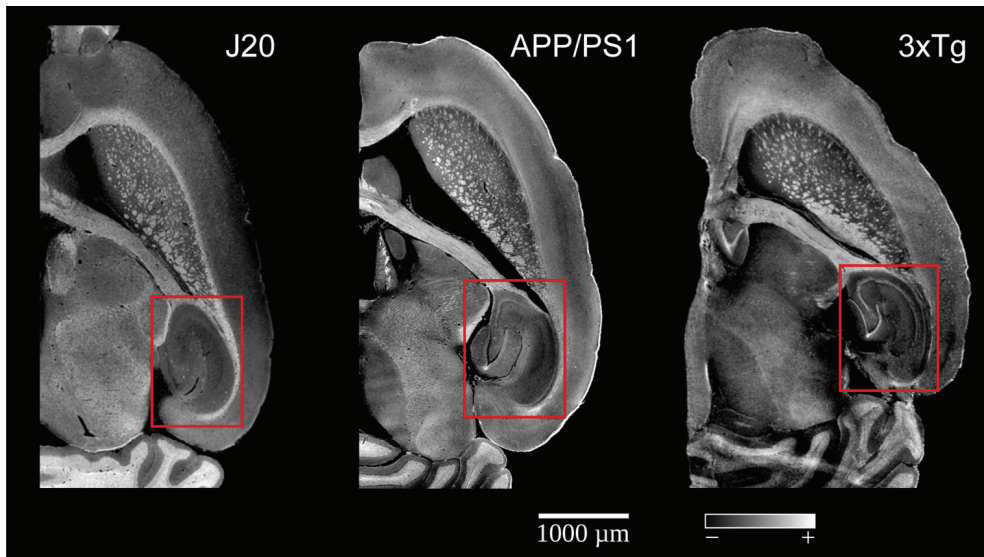


**Fig. 1.** Whole-brain anatomy of ethanol-dehydrated brains from the three mouse strains (XPCT single slices). The plaques from the three strains are visible mainly in the hippocampi (in red).

One additional formaldehyde-fixed sample of the J20 strain was scanned in PBS using the same set-up and reconstruction algorithm (Fig. S1): though some  $A\beta$  plaques were visible, surrounding brain tissue exhibited low overall signal intensity, strongly contaminated by ring artefacts. Thus, imaging in ethanol was required for region-specific segmentation. In this proof-of-concept study, we chose to focus on the hippocampus, in which all three mouse strains exhibited  $A\beta$  plaques. However, these plaques displayed strikingly different appearances (Fig. 2): i) J20 exhibited numerous small intense spots, sometimes very close to each other and seemingly

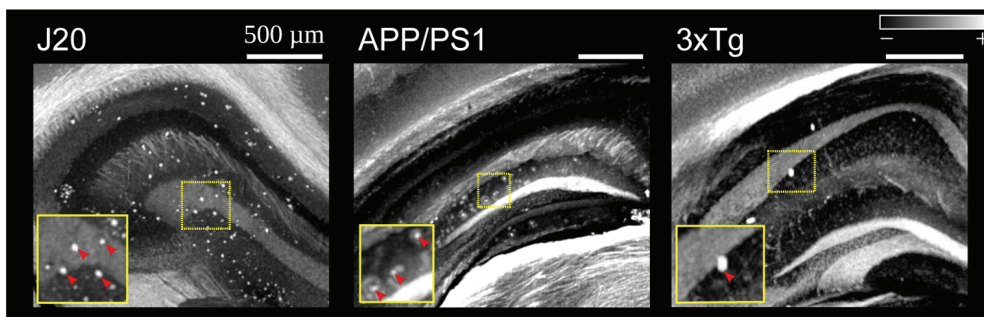


**Fig. 2.** XPCT images (maximum intensity projections over 50 slices) obtained at the level of the dorsal hippocampus, showing the density and appearance of  $A\beta$  plaques in the three mouse strains.

coalescing; ii) APP/PS1 displayed intense spots, often surrounded by a diffuse rim, resembling typical human dense-core plaques; iii) 3xTg showed few but large and highly intense deposits.

These 3D signals obtained without labeling matched the 2D fluorescence of corresponding brain slices after thioflavin S staining or A $\beta$ -peptide immunohistochemistry (Fig. 3), although some of the stained plaques seemed not to produce hyperintense contrast on XPCT.

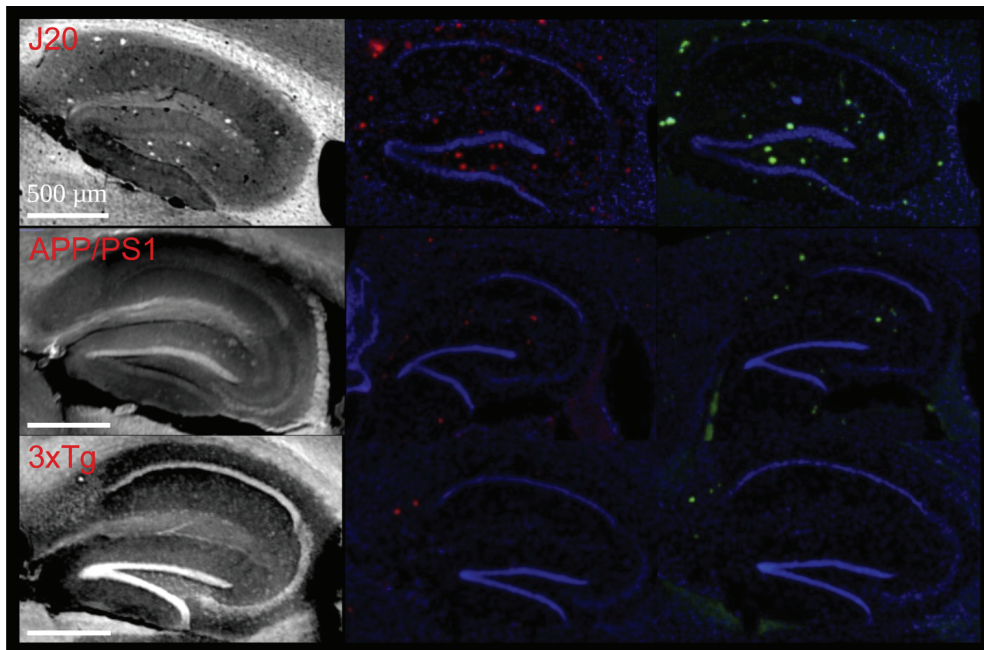


**Fig. 3.** Corresponding XPCT image (left row), amyloid staining with 4G8 antibody (red filter, exc 550 nm, em 605 nm), and Thioflavin S staining (right row, green filter, exc 485 nm, em 515 nm), for the three transgenic mouse strains. DAPI staining was obtained with a blue fluorescence filter (exc 365 nm, em 445 nm).

### 3.2. Morphological quantification

Following hippocampus extraction (steps 2–3 in the Amyloid- $\beta$  XPCT Workflow), machine learning was used to perform A $\beta$  plaque recognition: Trainable Weka Segmentation 3D used a strain-selective classifier that was built from 5 consecutive slices and then applied to the whole hippocampus (>200 slices) to produce a probability map that was thresholded by visual inspection (steps 4–5 in the Amyloid- $\beta$  XPCT Workflow). This strategy proved versatile and accommodated the different types and numbers of plaques imaged in this study (Fig. 4).

After automatic labeling and size filtering of segmented objects (step 6 in the Amyloid- $\beta$  XPCT Workflow), a few manual cleaning steps were performed under expert supervision (author FC). False-positive objects were, in most cases, located in the myelinated tracts of the perforant pathway (Fig. S2). On rare occasions, neurons or blood clots remaining in vessels were also detected as plaques. In 3xTg brains, a few false-positive labels were easily identified and removed, out of a dozen correctly segmented plaques (6–16 per hemisphere). In J20, which in contrast had several hundreds of plaques (774–916 per hemisphere), expert screening showed that the false-positive detection rate was below 5%. Importantly, not all J20 plaques could be individually separated; hence some segmented objects were "twin" plaques, in close contact, which were manually removed from analysis. In the case of APP/PS1, plaques were of lower signal intensity, and could not be unambiguously distinguished from perforant pathway signals. APP/PS1 volumes

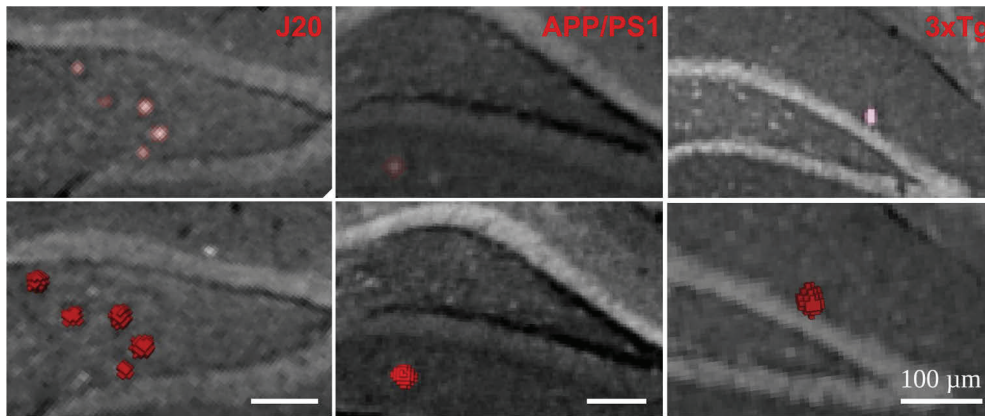


**Fig. 4.** Representative 2D overlay and 3D orthographic rendering (AMIRA) of segmented plaques for each strain.

were thus screened to manually select a hundred representative plaques outside the perforant tracts, which were used to calculate morphological parameters. Finally, as a specificity control, the 3 classifiers were applied to the hippocampus of a wild-type mouse, and, after similar

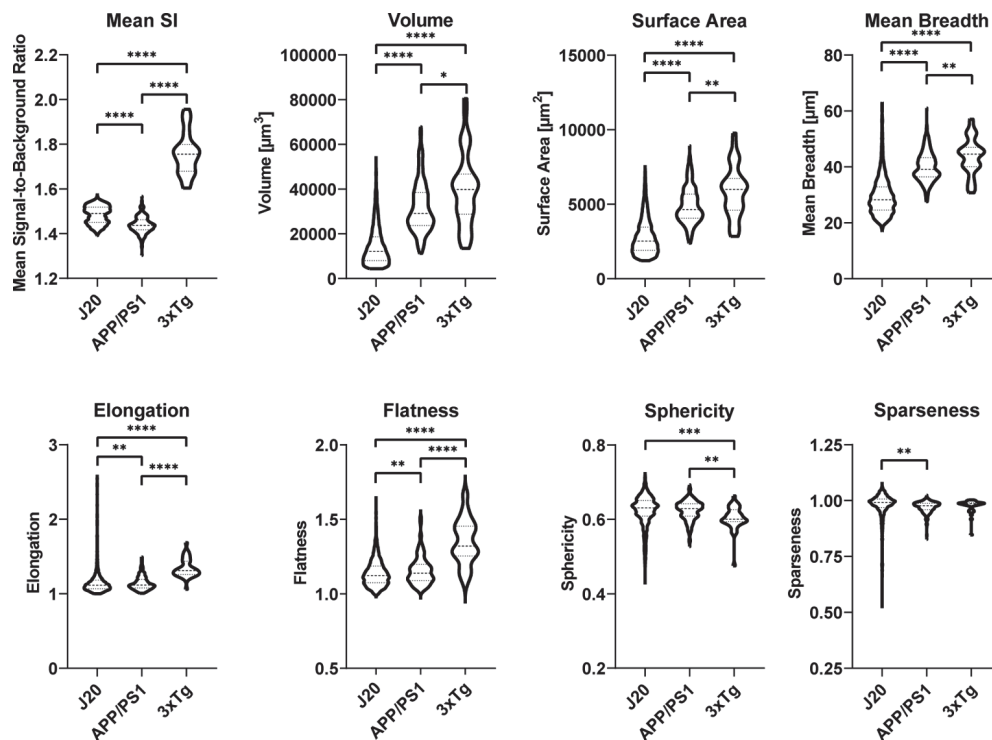


**Fig. 5.** Violin plots of morphological parameters extracted from the population of A $\beta$  plaques. Definitions of the parameters are reported in Table 2; Significance levels of pairwise Games-Howell comparisons are indicated (\*  $p < 0.05$ ; \*\*  $p < 0.01$ ; \*\*\*  $p < 0.001$ ; \*\*\*\*  $p < 0.0001$ ); Mean (interquartile range) are represented as dashed lines.

thresholding and size filtering, yielded no other detection than the same type of false-positive objects described above (Fig. S2).

Both the MorphoLibJ and 3D ImageJ Suite plugins were able to extract morphological parameters (step 7 in the Amyloid- $\beta$  XPCT Workflow), and we here report a combination of the shape parameters available for each strain (Fig. 5).

As expected from visual assessment, 3xTg displayed the highest plaque signal intensity after normalization to background ( $3xTg > J20 > APP/PS1$ ,  $p < 0.0001$ ), while J20 had the smallest volume ( $J20 < APP/PS1 < 3xTg$ ,  $p < 0.0001$ ) and surface area ( $J20 < APP/PS1 < 3xTg$ ,  $p < 0.0001$ ) per plaque. Mean breadth, a parameter proportional to the integral of the mean curvature, was also significantly less in J20 ( $< APP/PS1 < 3xTg$ ,  $p < 0.0001$ ). Shape differences were more pronounced for 3xTg, which had greater elongation and flatness ( $3xTg > APP/PS1 \approx J20$ , both  $p < 0.0001$ ), and lower sphericity ( $3xTg < APP/PS1 \approx J20$ ,  $p = 0.0002$ ) compared to J20 and APP/PS1. Finally, it was possible to compute nearest-neighbor distances (Fig. S3), the mean value of which was 4-fold greater in 3xTg than J20. These parameters are not mutually independent, and correlation matrices were computed to highlight strain differences in correlation coefficients (Fig. 6).

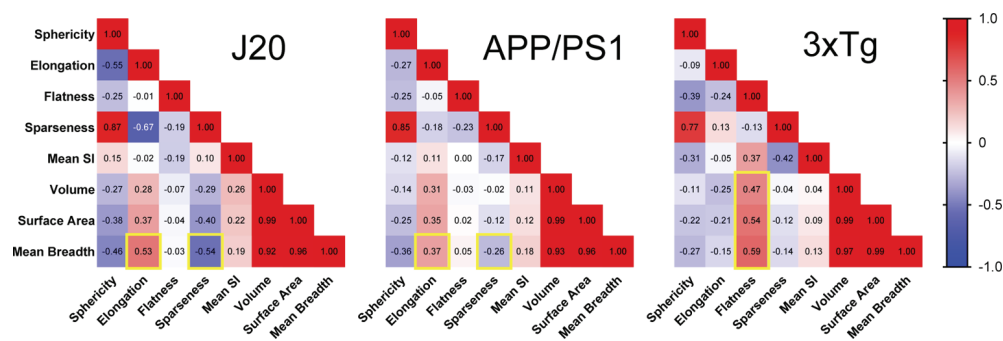


**Fig. 6.** Pearson  $r$  correlation coefficients (color-coded from  $-1 =$  blue to  $1 =$  red) between the 8 parameters. Correlation coefficients highlighted with yellow boxes refer to comments in the text.

While sphericity and sparseness were highly correlated in all three strains, mean breadth was positively correlated with elongation, and negatively with sparseness, both in J20 and APP/PS1 (Fig. 6, yellow boxes), but not in 3xTg. In contrast, flatness was correlated with surface area, volume and mean breadth in 3xTg only (Fig. 6, yellow boxes).

#### 4. Discussion

The present study went beyond previous pioneer reports of A $\beta$  detection with XPCT by:

1. studying a complete experimental group (10 brains in total vs 1–2 samples);
2. comparing 3 different strains (vs. a single one);
3. and providing access to multiple morphometric parameters (while previous reports were confined to plaque number, volume and sphericity).

An additional contribution consisted in building and sharing a "biologist-friendly" analysis workflow, by assembling multiple Fiji plugins: segmentation editor, Trainable Weka Segmentation, 3D, MorphoLibJ, 3D ImageJ Suite. We were especially interested in the ability of the workflow to correctly detect a significant proportion of A $\beta$  plaques with very different appearances and morphologies. Hence versatility rather than completeness of the segmentation was the primary

goal of the method. We were able to successfully segment numerous A $\beta$  plaques, even when their refractive indices (and subsequent XPCT signals) were barely different from surrounding tissue, as in the case of APP/PS1. In future studies in a dedicated mouse strain, segmentation may be improved, by building a dedicated Weka classifier combining a few slices from different animals, and/or by using several classes of objects to better discriminate A $\beta$  plaques from neuronal tracts, and/or by using wild-type littermate brains to avoid false-positive detections and thus avoid human intervention to threshold probability maps and exclude false positives.

Tested on three different transgenic mouse strains, the analysis workflow yielded an entirely new class of 3D parameters, with distribution easily measured on multiple plaques. We provide basic examples of how to handle this set of parameters: e.g., building correlation matrices (Fig. 6) or searching for spatial patterns (Visualization 1 showing the distribution of mean breadth values on APP/PS1 hippocampus). Hence, the present work leveraged 3D analysis to extract multiple morphological parameters of A $\beta$  plaques which otherwise require extended serial microscopy acquisitions with 3D reconstruction [1]. The development of such quantification pipelines is a necessary step for popularizing XPCT in neuroscience laboratories which need to phenotype transgenic animal cohorts. Moreover, this imaging modality could be instrumental in studying the prion-like properties of A $\beta$  fibrillar aggregates. Typical experiments involve exogenously inoculated A $\beta$  seeds (prion-like agents) which template and accelerate A $\beta$  deposition in the host brain [27,28]. Hence non-destructive 3D imaging would be a great advantage in identifying the spreading routes of inoculated seeds [29]. Moreover, it was suggested that seed morphology influences the final morphology of disseminated A $\beta$  deposits; but the existence of these "morphotypes" was inferred from 2D immunohistochemistry [30] and awaits 3D confirmation.

In this proof-of-concept report, 3xTg displayed a different type of A $\beta$  plaque, with larger volume and area, greater elongation and flatness, and much higher signal intensity than J20 and APP/PS1. A $\beta$  aggregation has been shown to start intracellularly in hippocampal neurons of the 3xTg strain, and it is interesting to note that neuronal bodies in the hippocampus showed high signal intensity in comparison to other strains (Fig. 1). Thus, the distinct aggregation cascade in this strain might translate into different extracellular morphotypes of A $\beta$  plaque. While the mechanisms leading to these particularities remain elusive, these observations illustrate how XPCT can probe the pathophysiological microenvironment of brain tissue. In terms of morphometry, the study identified mean breadth as an original and discriminating parameter. Mean breadth is a quantity proportional to the integral of mean curvature over area (>0 for convex objects such as A $\beta$  plaques). In this case, mean breadth can be defined as the average of the Feret diameter measured over a selected number of orientations. It correlated strongly with area and volume (all related to the size of the plaque), but exhibited radically different correlation patterns with other parameters in 3xTg (Fig. 6). This shows that the analysis of 3D geometry can benefit from other parameters in addition to the often-reported sphericity and volume. Ultimately, the combination of all parameters results in "morphological signatures" that allows discriminating the strains. The interpretation of the associations between the morphological parameters could however complexify when the number of parameters increases. In that case, exploratory data analysis such as dimensionality reduction or clustering could help reveal which parameters correlate, and which ones carry complementary information [31,32]

Though the pathophysiological relevance of A $\beta$  shape remains unknown, the morphology of A $\beta$  plaques gained interest with the recent development of brain clearing techniques [2,3,33,34]. In comparison, XPCT has the following advantages: i) ultra-fast sample preparation (around 1 hour, whereas 3D immunofluorescence typically requires several days' incubation with anti-amyloid antibodies), ii) variation in size through sole ethanol dehydration (up to 40% decrease in the brain [35]) whereas most clearing techniques drastically change brain size, leading to shrinkage or expansion, through multiple and successive chemical treatments [36], and iii)

whole-brain acquisition (whereas light-sheet imaging usually requires multiple acquisitions and fastidious stitching procedures). Therefore, XPCT can be positioned as a forefront technique, allowing high-throughput brain screening, and guidance for subsequent brain clearing and 3D immunohistochemistry on selected samples. XPCT is therefore unique as a whole-brain, label-free method for ex vivo amyloid imaging. The current limitations of XPCT are the following.

1. The sensitivity of detection of A $\beta$  plaques likely depends on size and location in the brain; this point could be addressed by more precisely adjusting tissue dehydration (by varying the percentage of ethanol) so as to get minimal anatomical contrast while preserving A $\beta$  detectability.
2. Not all A $\beta$  plaques seem detectable and the source of the XPCT contrast from A $\beta$  plaques is not currently fully understood, though it is likely to arise from a local change in refractive index due to insoluble fibrillar A $\beta$  [37], along with a possible contribution of endogenous metals entrapped in the plaque [38]. Indeed, there are scarce reports of calcium accumulation in transgenic mice and in Alzheimer patients [39,40]. Furthermore, using various methods, metals like iron, copper or zinc have been shown to accumulate in amyloid plaques, although contrasting results have been reported according plaque types (mouse or human, senile or diffuse) [38,40–43].
3. The availability of synchrotron sources with XPCT capacity is restricted to 20–30 sites in the world; but several methods have been proposed to obtain phase-contrast images from a laboratory X-ray source [40,44–46].

## 5. Conclusion

In summary, we presented a complete workflow for ex vivo whole-brain imaging and quantification of A $\beta$  pathology. Sample preparation was limited to reversible dehydration of tissue, which remained available for standard immunohistochemistry. Propagation-based XPCT produced unequalled image quality (Fig. S4), with various concurrent types of anatomical information (white matter, vessels, neuronal organization). New 3D parameters, not attainable on routine immunohistochemistry, were successfully extracted from 3 transgenic Alzheimer's disease models.

**Funding.** European Synchrotron Research Facility (ESRF) (LS2292, MD1018, IN1041); Labex (ANR-11-LABX-0063); Agence Nationale de la Recherche (ANR-11-IDEX-0007, NanoBrain (ANR15-CE18-0026)); Mitacs (Globalink [travel grant for Carlie Boisvert]).

**Acknowledgments.** This study was performed within the framework of LABEX PRIMES (ANR-11-LABX-0063) of Université de Lyon, within the "Investissements d'Avenir" program (ANR-11-IDEX-0007) operated by the French National Research Agency (ANR). The research was in part funded by the French ANR project NanoBrain (ANR15-CE18-0026). The study was supported by the European Synchrotron Research Facility (ESRF) by allocation of beam time (LS2292, MD1018, IN1041), and the authors would like to thank ESRF local contact Lukas Helfen. Carlie Boisvert was supported by Mitacs Globalink Canada (travel grant). 3xTg and WT brains were kindly provided by Dr Catherine Lawrence of the University of Manchester. Paraffin embedding and microtome slicing were performed at the CIQLE Imaging Platform, University of Lyon, with the help of Annabelle Bouchardon and Batoule Smatti.

**Authors' contributions (according to Contributor Role Taxonomy (<https://casrai.org/credit/>)) CRediT**

- Conceptualization: MW, FC
- Data curation: MC, MR, CG, CO, EB, HR
- Formal analysis: MC, MR
- Funding acquisition: FP, HR, MW, FC
- Investigation: MC, MR, CB, CG, CO
- Methodology: EB, HR, MW, FC
- Project administration: MW, FC
- Resources: DL, IAC, HB, NR, TB, DM

- Supervision: EB, HR, MW, FC
- Validation: MC, FC
- Visualization: MC, MR, CB, CG
- Writing — original draft: FC
- Writing — review & editing: MC, MR, CB, EB, HR, MW, FC

**Disclosures.** The authors declare no conflicts of interest.

**Data availability.** The raw data required to reproduce these findings cannot be shared at this time due to the large size of the XPCT datafile, but are available on request. The image processing workflow is available on Zenodo [24].

**Supplemental document.** See [Supplement 1](#) for supporting content.

## References

1. J. D. Whitesell, A. R. Buckley, J. E. Knox, L. Kuan, N. Graddis, A. Pelos, A. Mukora, W. Wakeman, P. Bohn, A. Ho, K. E. Hirokawa, and J. A. Harris, "Whole brain imaging reveals distinct spatial patterns of amyloid beta deposition in three mouse models of Alzheimer's disease," *J. Comp. Neurol.* **527**(13), 2122–2145 (2019).
2. N. Jähring, K. Becker, B. M. Wegenast-Braun, S. A. Grathwohl, M. Jucker, and H.-U. Dodt, "Cerebral  $\beta$ -amyloidosis in mice investigated by ultramicroscopy," *PLoS One* **10**(5), e0125418 (2015).
3. D. Nguyen, P. J. Marchand, A. L. Planchette, J. Nilsson, M. Sison, J. Extermann, A. Lopez, M. Sylwestrzak, J. Sordet-Dessimoz, A. Schmidt-Christensen, D. Holmberg, D. Van De Ville, and T. Lasser, "Optical projection tomography for rapid whole mouse brain imaging," *Biomed. Opt. Express* **8**(12), 5637–5650 (2017).
4. J. Albers, S. Pacilé, M. A. Markus, M. Wiart, G. Vande Velde, G. Tromba, and C. Dullin, "X-ray-based 3D virtual histology-adding the next dimension to histological analysis," *Mol. Imaging Biol.* **20**(5), 732–741 (2018). Number: 5.
5. G. E. Barbone, A. Bravin, P. Romanelli, A. Mittone, D. Bucci, T. Gaaß, G. Le Duc, S. Auweter, M. F. Reiser, M. J. Kraiger, M. Hrabe de Angelis, G. Battaglia, and P. Coan, "Micro-imaging of brain cancer radiation therapy using phase-contrast computed tomography," *Int. J. Radiat. Oncol., Biol., Phys.* **101**(4), 965–984 (2018). Number: 4.
6. M. Marinescu, M. Langer, A. Durand, C. Olivier, A. Chabrol, H. Rositi, F. Chauveau, T. H. Cho, N. Nighoghossian, Y. Berthezène, F. Peyrin, and M. Wiart, "Synchrotron radiation X-ray phase micro-computed tomography as a new method to detect iron oxide nanoparticles in the brain," *Mol. Imaging Biol.* **15**(5), 552–559 (2013). Number: 5.
7. K. Noda-Saita, A. Yoneyama, Y. Shitaka, Y. Hirai, K. Terai, J. Wu, T. Takeda, K. Hyodo, N. Osakabe, T. Yamaguchi, and M. Okada, "Quantitative analysis of amyloid plaques in a mouse model of Alzheimer's disease by phase-contrast X-ray computed tomography," *Neuroscience* **138**(4), 1205–1213 (2006).
8. D. M. Connor, H. Benveniste, F. A. Dilmanian, M. F. Kritzer, L. M. Miller, and Z. Zhong, "Computed tomography of amyloid plaques in a mouse model of Alzheimer's disease using diffraction enhanced imaging," *NeuroImage* **46**(4), 908–914 (2009).
9. B. Pinzer, M. Cacquevel, P. Modregger, S. McDonald, J. Bensadoun, T. Thuering, P. Aebischer, and M. Stampanoni, "Imaging brain amyloid deposition using grating-based differential phase contrast tomography," *NeuroImage* **61**(4), 1336–1346 (2012).
10. A. Astolfo, A. Lathuilière, V. Laversenne, B. Schneider, and M. Stampanoni, "Amyloid- $\beta$  plaque deposition measured using propagation-based X-ray phase contrast CT imaging," *J. Synchrotron Radiat.* **23**(3), 813–819 (2016).
11. L. Massimi, N. Pieroni, L. Maugeri, M. Fratini, F. Brun, I. Bukreeva, G. Santamaria, V. Medici, T. E. Poloni, C. Balducci, and A. Cedola, "Assessment of plaque morphology in Alzheimer's mouse cerebellum using three-dimensional X-ray phase-based virtual histology," *Sci. Rep.* **10**(1), 11233 (2020). Number: 1.
12. L. Massimi, I. Bukreeva, G. Santamaria, M. Fratini, A. Corbelli, F. Brun, S. Fumagalli, L. Maugeri, A. Pacureanu, P. Cloetens, N. Pieroni, F. Fiordaliso, G. Forloni, A. Uccelli, N. Kerlero de Rosbo, C. Balducci, and A. Cedola, "Exploring Alzheimer's disease mouse brain through X-ray phase contrast tomography: From the cell to the organ," *NeuroImage* **184**, 490–495 (2019).
13. M. Chourrout, H. Rositi, E. Ong, V. Hubert, A. Paccalet, L. Foucault, A. Autret, B. Fayard, C. Olivier, R. Bolbos, F. Peyrin, C. Crola-da Silva, D. Meyronet, O. Raineteau, H. Elleaume, E. Brun, F. Chauveau, and M. Wiart, "Brain virtual histology with X-ray phase-contrast tomography Part I: whole-brain myelin mapping in white-matter injury models," *Biomed. Opt. Express* **13**, 1620–1639 (2022).
14. L. Mucke, E. Masliah, G.-Q. Yu, M. Mallory, E. M. Rockenstein, G. Tatsuno, K. Hu, D. Kholodenko, K. Johnson-Wood, and L. McConlogue, "High-level neuronal expression of  $\text{A}\beta$ 1-42 in wild-type human amyloid protein precursor transgenic mice: synaptotoxicity without plaque formation," *J. Neurosci.* **20**(11), 4050–4058 (2000). Number: 11.
15. J. L. Jankowsky, D. J. Fadale, J. Anderson, G. M. Xu, V. Gonzales, N. A. Jenkins, N. G. Copeland, M. K. Lee, L. H. Younkin, S. L. Wagner, S. G. Younkin, and D. R. Borchelt, "Mutant presenilins specifically elevate the levels of the 42 residue  $\beta$ -amyloid peptide in vivo: evidence for augmentation of a 42-specific  $\beta$  secretase," *Hum. Mol. Genet.* **13**(2), 159–170 (2004). Number: 2.
16. S. Oddo, A. Caccamo, J. D. Shepherd, M. Murphy, T. E. Golde, R. Kaye, R. Metherate, M. P. Mattson, Y. Akbari, and F. M. LaFerla, "Triple-transgenic model of Alzheimer's disease with plaques and tangles," *Neuron* **39**(3), 409–421 (2003). Number: 3.

17. D. Paganin, S. C. Mayo, T. E. Gureyev, P. R. Miller, and S. W. Wilkins, "Simultaneous phase and amplitude extraction from a single defocused image of a homogeneous object," *J. Microsc.* **206**(1), 33–40 (2002). Number: Pt 1.
18. A. Mirone, E. Brun, E. Gouillart, P. Tafforeau, and J. Kieffer, "The PyHST2 hybrid distributed code for high speed tomographic reconstruction with iterative reconstruction and a priori knowledge capabilities," *Nucl. Instruments Methods Phys. Res. Sect. B: Beam Interactions with Mater. Atoms* **324**, 41–48 (2014).
19. J. Schindelin, I. Arganda-Carreras, E. Frise, V. Kaynig, M. Longair, T. Pietzsch, S. Preibisch, C. Rueden, S. Saalfeld, B. Schmid, J.-Y. Tinevez, D. J. White, V. Hartenstein, K. Eliceiri, P. Tomancak, and A. Cardona, "Fiji: an open-source platform for biological-image analysis," *Nat. Methods* **9**(7), 676–682 (2012).
20. I. Arganda-Carreras, V. Kaynig, C. Rueden, K. W. Eliceiri, J. Schindelin, A. Cardona, and H. Sebastian Seung, "Trainable Weka Segmentation: a machine learning tool for microscopy pixel classification," *Bioinformatics* **33**(15), 2424–2426 (2017).
21. D. Legland, I. Arganda-Carreras, and P. Andrey, "MorphoLibJ: integrated library and plugins for mathematical morphology with ImageJ," *Bioinformatics* **32**, 3532–3534 (2016).
22. J. Ollion, J. Cochenne, F. Loll, C. Escudé, and T. Boudier, "TANGO: a generic tool for high-throughput 3D image analysis for studying nuclear organization," *Bioinformatics* **29**(14), 1840–1841 (2013).
23. D. Sage, F. Neumann, F. Hediger, S. Gasser, and M. Unser, "Automatic tracking of individual fluorescence particles: application to the study of chromosome dynamics," *IEEE Trans. on Image Process.* **14**(9), 1372–1383 (2005).
24. M. Chourrout, M. Roux, C. Gislard, I. Arganda-Carreras, D. Legland, H. Rositi, M. Wiart, and F. Chauveau, "A Fiji pipeline to segment 3D objects and retrieve shape parameters in biomedical images," Zenodo 2021, <http://10.5281/zenodo.4584752>.
25. E. Bribiesca, "An easy measure of compactness for 2D and 3D shapes," *Pattern Recognit.* **41**(2), 543–554 (2008).
26. M. McAuliffe, F. Lalonde, D. McGarry, W. Gandler, K. Csaky, and B. Trus, "Medical image processing, analysis and visualization in clinical research," in *Proceedings 14th IEEE Symposium on Computer-Based Medical Systems. CBMS 2001*, (IEEE Comput. Soc, 2001), pp. 381–386.
27. M. Meyer-Luehmann, "Exogenous induction of cerebral -amyloidogenesis is governed by agent and host," *Science* **313**(5794), 1781–1784 (2006).
28. M. Friesen and M. Meyer-Luehmann, "A $\beta$  seeding as a tool to study cerebral amyloidosis and associated pathology," *Front. Mol. Neurosci.* **12**, 233 (2019).
29. Y. S. Eisele, T. Bolmont, M. Heikenwalder, F. Langer, L. H. Jacobson, Z.-X. Yan, K. Roth, A. Aguzzi, M. Staufenbiel, L. C. Walker, and M. Jucker, "Induction of cerebral -amyloidosis: Intracerebral versus systemic A inoculation," *Proc. Natl. Acad. Sci.* **106**(31), 12926–12931 (2009).
30. J. C. Watts, C. Condello, J. Stohr, A. Oehler, J. Lee, S. J. DeArmond, L. Lannfelt, M. Ingelsson, K. Giles, and S. B. Prusiner, "Serial propagation of distinct strains of A prions from Alzheimer's disease patients," *Proc. Natl. Acad. Sci.* **111**(28), 10323–10328 (2014).
31. D. Legland and J. Beaugrand, "Automated clustering of lignocellulosic fibres based on morphometric features and using clustering of variables," *Ind. Crop. Prod.* **45**, 253–261 (2013).
32. P. J. Strzelecki, A. Swierczewska, K. Kopczewska, A. Fheed, J. Tarasiuk, and S. Wronski, "Decoding rocks: an assessment of geomaterial microstructure using X-ray microtomography, image analysis and multivariate statistics," *Materials* **14**(12), 3266 (2021).
33. K. Ando, Q. Laborde, A. Lazar, D. Godefroy, I. Youssef, M. Amar, A. Pooler, M.-C. Potier, B. Delatour, and C. Duyckaerts, "Inside Alzheimer brain with CLARITY: senile plaques, neurofibrillary tangles and axons in 3-D," *Acta Neuropathol.* **128**(3), 457–459 (2014).
34. T. Liebmann, N. Renier, K. Bettayeb, P. Greengard, M. Tessier-Lavigne, and M. Flajolet, "Three-dimensional study of Alzheimer's disease hallmarks using the iDISCO clearing method," *Cell Rep.* **16**(4), 1138–1152 (2016).
35. G. Rodgers, W. Kuo, G. Schulz, M. Scheel, A. Migga, C. Bikis, C. Tanner, V. Kurtcuoglu, T. Weitkamp, and B. Müller, "Virtual histology of an entire mouse brain from formalin fixation to paraffin embedding. Part 1: Data acquisition, anatomical feature segmentation, tracking global volume and density changes," *J. Neurosci. Methods* **364**, 109354 (2021).
36. Y. Qi, T. Yu, J. Xu, P. Wan, Y. Ma, J. Zhu, Y. Li, H. Gong, Q. Luo, and D. Zhu, "FDISCO: Advanced solvent-based clearing method for imaging whole organs," *Sci. Adv.* **5**(1), eaau8355 (2019).
37. M. Rak, M. R. Del Bigio, S. Mai, D. Westaway, and K. Gough, "Dense-core and diffuse A $\beta$  plaques in TgCRND8 mice studied with synchrotron FTIR microspectroscopy," *Biopolymers* **87**(4), 207–217 (2007).
38. A. C. Leskova, A. Lanzirotti, and L. M. Miller, "Amyloid plaques in PSAPP mice bind less metal than plaques in human Alzheimer's disease," *NeuroImage* **47**(4), 1215–1220 (2009).
39. M. Dhenain, N. El Tannir El Tayara, T.-D. Wu, M. Guégan, A. Volk, C. Quintana, and B. Delatour, "Characterization of in vivo MRI detectable thalamic amyloid plaques from APP/PS1 mice," *Neurobiol. Aging* **30**(1), 41–53 (2009).
40. M. Töpperwien, F. van der Meer, C. Stadelmann, and T. Salditt, "Correlative x-ray phase-contrast tomography and histology of human brain tissue affected by Alzheimer's disease," *NeuroImage* **210**, 116523 (2020).
41. M. Bulk, W. M. Abdelmoula, R. J. A. Nabuurs, L. M. van der Graaf, C. W. H. Mulders, A. A. Mulder, C. R. Jost, A. J. Koster, M. A. van Buchem, R. Natté, J. Dijkstra, and L. van der Weerd, "Postmortem MRI and histology demonstrate differential iron accumulation and cortical myelin organization in early- and late-onset Alzheimer's disease," *Neurobiol. Aging* **62**, 231–242 (2018).

42. F. Lermyte, J. Everett, J. Brooks, F. Bellingeri, K. Billimoria, P. J. Sadler, P. B. O'Connor, N. D. Telling, and J. F. Collingwood, "Emerging approaches to investigate the influence of transition metals in the proteinopathies," *Cells* **8**(10), 1231 (2019).
43. E. Álvarez Marimon, H. Castillo-Michel, J. Reyes-Herrera, J. Seira, E. Aso, M. Carmona, I. Ferrer, J. Cladera, and N. Benseny-Cases, "Synchrotron X-ray fluorescence and FTIR signatures for amyloid fibrillary and nonfibrillary plaques," *ACS Chem. Neurosci.* **12**(11), 1961–1971 (2021).
44. M. Töpperwien, M. Krenkel, D. Vincenz, F. Stöber, A. M. Oelschlegel, J. Goldschmidt, and T. Salditt, "Three-dimensional mouse brain cytoarchitecture revealed by laboratory-based x-ray phase-contrast tomography," *Sci. Rep.* **7**(1), 42847 (2017).
45. D. M. Paganin, H. Labriet, E. Brun, and S. Berujon, "Single-image geometric-flow X-ray speckle tracking," *Phys. Rev. A* **98**(5), 053813 (2018).
46. M.-C. Zdora, P. Thibault, W. Kuo, V. Fernandez, H. Deyhle, J. Vila-Comamala, M. P. Olbinado, A. Rack, P. M. Lackie, O. L. Katsamenis, M. J. Lawson, V. Kurtcuoglu, C. Rau, F. Pfeiffer, and I. Zanette, "X-ray phase tomography with near-field speckles for three-dimensional virtual histology," *Optica* **7**(9), 1221 (2020).

Supplemental Document

Biomedical Optics EXPRESS

## Brain virtual histology with X-ray phase-contrast tomography Part II:3D morphologies of amyloid- $\beta$ plaques in Alzheimer's disease models: supplement

**MATTHIEU CHOURROUT,<sup>1</sup>  MARGAUX ROUX,<sup>1</sup> CARLIE BOISVERT,<sup>1,15</sup> CORALIE GISLARD,<sup>1</sup> DAVID LEGLAND,<sup>2</sup> IGNACIO ARGANDA-CARRERAS,<sup>3,4,5</sup> CÉCILE OLIVIER,<sup>6</sup> FRANÇOISE PEYRIN,<sup>6</sup> HERVÉ BOUTIN,<sup>7</sup> NICOLAS RAMA,<sup>8</sup> THIERRY BARON,<sup>9</sup> DAVID MEYRONET,<sup>10</sup> EMMANUEL BRUN,<sup>11</sup>  HUGO ROSITI,<sup>12</sup> MARLÈNE WIART,<sup>13,14,16</sup>  AND FABIEN CHAUVEAU<sup>1,14,16,\*</sup> **

<sup>1</sup>Univ. Lyon, Lyon Neuroscience Research Center, CNRS UMR5292, Inserm U1028, Université Claude Bernard Lyon 1, Lyon, France

<sup>2</sup>UR BIA; BIBS Facility, INRAE, Nantes, France

<sup>3</sup>University of the Basque Country (UPV/EHU), San Sebastian, Spain

<sup>4</sup>Ikerbasque, Basque Foundation for Science, Bilbao, Spain

<sup>5</sup>Donostia International Physics Center (DIPC), San Sebastian, Spain

<sup>6</sup>Univ. Lyon, CREATIS; CNRS UMR5220; INSERM U1044; INSA-Lyon; Univ. Lyon 1, Lyon, France

<sup>7</sup>Univ. Manchester, Faculty of Biology Medicine and Health, Wolfson Molecular Imaging Centre, Manchester, UK

<sup>8</sup>Univ. Lyon, CRCL; INSERM U1052; CNRS UMR5286; Univ. Lyon 1; Centre Léon Bérard, Lyon, France

<sup>9</sup>Univ. Lyon, ANSES, Lyon, France

<sup>10</sup>Univ. Lyon, Hospices Civils de Lyon, Lyon, France

<sup>11</sup>Univ. Grenoble Alpes, Inserm UA07 Strobe Grenoble, France

<sup>12</sup>Univ. Clermont Auvergne, Institut Pascal; CNRS UMR 6602; SIGMA Clermont, Clermont-Ferrand, France

<sup>13</sup>Univ. Lyon, CarMeN Laboratory; INSERM U1060; INRA U1397; Hospices Civils de Lyon, Lyon, France

<sup>14</sup>CNRS, Lyon, France

<sup>15</sup>Current affiliation: Faculty of Medicine, The Ottawa Hospital and University of Ottawa, Ottawa, Ontario, Canada

<sup>16</sup>These authors contributed equally to this work

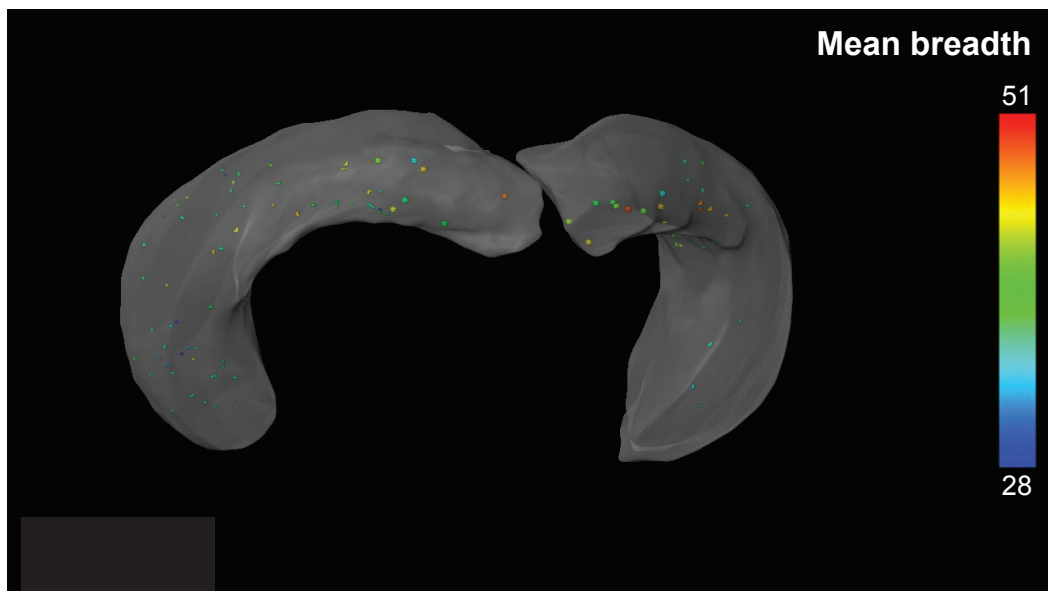
\*[chauveau@cermep.fr](mailto:chauveau@cermep.fr)

This supplement published with Optica Publishing Group on 23 February 2022 by The Authors under the terms of the [Creative Commons Attribution 4.0 License](https://creativecommons.org/licenses/by/4.0/) in the format provided by the authors and unedited. Further distribution of this work must maintain attribution to the author(s) and the published article's title, journal citation, and DOI.

Supplement DOI: <https://doi.org/10.6084/m9.figshare.16826065>

Parent Article DOI: <https://doi.org/10.1364/BOE.438890>

## Brain virtual histology with X-ray phase-contrast tomography — Part II: 3D morphologies of amyloid- $\beta$ plaques in Alzheimer's disease models — Supplemental document



**Visualization 1.** 3D rendering of whole brain, hippocampi and A $\beta$  plaques (with mean breadth value visualization) segmented from transgenic APP/PS1 mouse brain. URL: <https://osapublishing.figshare.com/s/b67dc8e839059e885974>

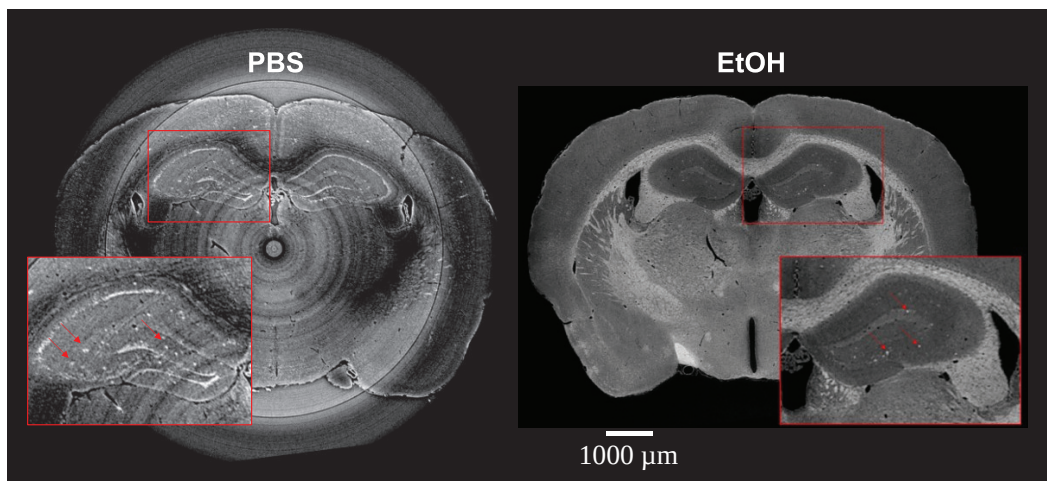


**Fig. S1.** Single-slice XPCT images from J20 brains with (right) and without (left) dehydration in ethanol.

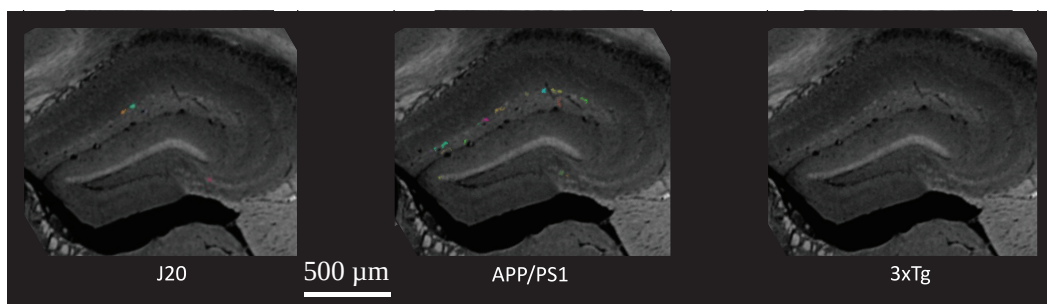


**Fig. S2.** Results of trainable WEKA segmentation using a strain-specific classifier applied on the same non-transgenic C57/Bl6 brain. Colored labels represent false positive detections of plaque-like signals.

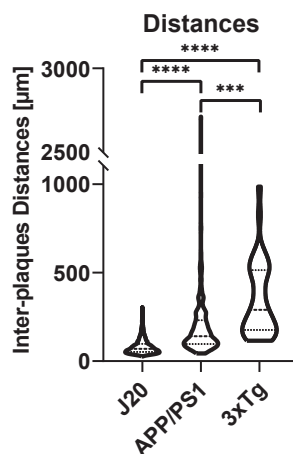


**Fig. S3.** Violin plots of nearest-neighbour distances extracted from the population of segmented  $A\beta$  plaques. The present results are reported to highlight feasibility but may be biased because only a subset of individual plaques was selected in APP/PS1, and closest pairs of J20 plaques couldn't be resolved.

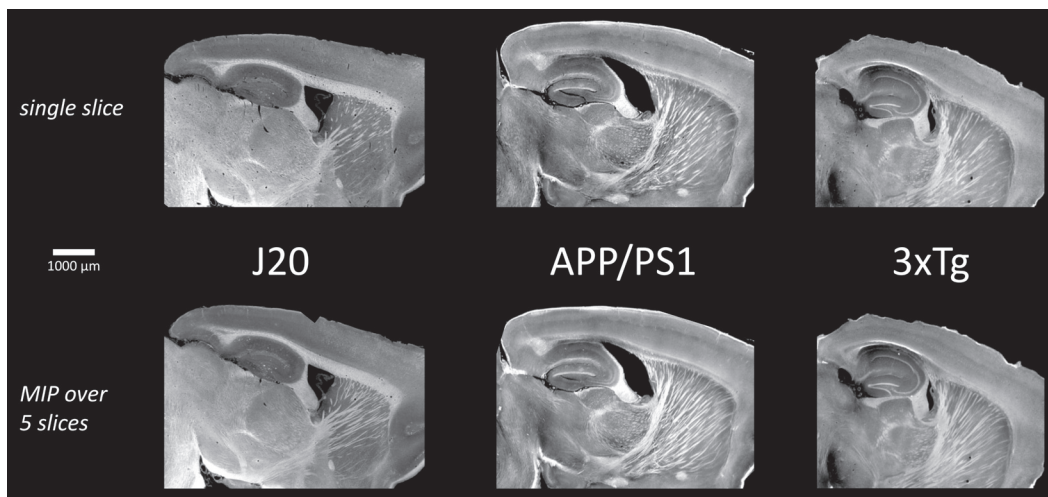


**Fig. S4.** XPCT images (single slices and maximum intensity projections over 5 slices) of the three mouse strains.

### 4.3. Discussion

In this article, we analyzed amyloid- $\beta$  plaques, which can be seen with propagation-based XPCT. These plaques were mainly detected in the hippocampus. Eventually, the anatomical contrast can be enhanced with a dehydration protocol but it is not necessary to see the plaques, as they are already detectable in PBS-immersed brains (cf. Fig. S1 in the supplement of the article).

Since 2006, amyloid- $\beta$  plaques have been studied with x-ray phase-contrast imaging, both in AD models [210, 230, 231, 232, 233, 234, 235, 236, 237] and in AD patients [236]. With the propagation-based XPCT setup at the ID-19 and ID-17 beamlines of ESRF instead of grating interferometry, the acquisition time was greatly reduced — while it took 80 min per sample in the study by Pinzer et al. [231], our scans with a pixel size of 6  $\mu\text{m}$  required 5 min for one whole mouse brain. The 6  $\mu\text{m}$  pixel size was a good compromise because it resolved most of the individual A $\beta$  plaques. A measurement of the effective resolution was not performed; this could be implemented using the half-bit threshold intersection with the Fourier shell correlation curve [341]. Other solutions require the use of a phantom, such as a resolution test chart [342]; one could conceive a biology-accurate phantom with micrometric high-density inclusions of known size, separated with varying distances — the assessment would consist into resolving individual inclusions.

Our study involved the segmentation of A $\beta$  plaques in 3 transgenic models of AD ( $n = 8$  animals in total) with open-source software: the Weka toolbox [343] and the Fiji/ImageJ software [344] (along with a few plugins: Trainable Weka Segmentation [345], MorpholibJ [346] and the 3D ImageJ Suite [347]). The segmentation pipeline we designed is fully detailed and illustrated in a separate document [348]. This pipeline is not limited to our application as it is relevant for the segmentation of any blob-like object with any 3D gray-scale technique. We reported an extensive set of volumetric measurements on images which were acquired in the same conditions, ensuring consistent contrasts. However, the segmentation was not exhaustive: false positives and false negatives (which we did not estimate) required a segmentation strategy and label-cleaning which were slightly different for each strain. The smaller objects were discarded under a

volume threshold (number of voxels) because of the ambiguity between small  $A\beta$  plaques and neuron heads. The spatial distribution of the mean breadth — shown in the supplemental movie; <https://opticapublishing.figshare.com/s/b67dc8e839059e885974> — revealed that plaques towards the cranial dorsal extremity of the hippocampi had lower mean breadths than plaques at the latero-ventral extremity. A different segmentation strategy would be required for a bigger cohort or for the study of more complex objects, such as blood vessels in Chapter 6. The strain-dependent distributions of our 8 metrics highlighted the well-known  $A\beta$  polymorphism [52, 349, 350]; future research about the structural  $A\beta$  polymorphism could for instance target the different  $A\beta$  conformations that develop upon injection of different  $A\beta$  prions [351]; or identify the interactions of co-pathologies with  $A\beta$  plaques in multiple-transgenic models such as an  $A\beta + \alpha$ -syn model by Baron et al. [352], just like we did with the  $A\beta + \tau$  model, 3xTg.

We performed correlative histology after XPCT: we confirmed with fluorescent dyes that the detected objects were  $A\beta$ -positive inclusions, e.g.  $A\beta$  plaques. However, Figure 3 in the article suggested that we could only detect a subset of the plaques with XPCT: it raises the question about the properties of  $A\beta$  that make the contrast-agent-free detection possible. This led to the design of a study which is described in Chapter 5 on page 111.



# The origin of the contrast of amyloid- $\beta$ plaques in XPCT

# 5.

## 5.1. Introduction

In the previous chapters, we detailed how XPCT can assess neuropathological changes in 3D in *postmortem* samples. Concerning A $\beta$  plaques, the question of their selective label-free detection with XPCT remains unanswered. In anterior articles [210, 230, 231, 232, 233, 234, 235, 236, 237], A $\beta$  plaques have been reported as high-density inclusions — appearing as bright spots in our images [238]. We hypothesized this local contrast variation was related to the entrapped metals or to the insoluble A $\beta_{1-42}$  fibrils of the A $\beta$  plaques. On one hand, the metal hypothesis was supported by MRI studies that could indirectly detect iron-loaded A $\beta$  plaques [93, 216]; A $\beta$  plaques are known to trap multiple metals, especially endogenous iron, zinc and copper [99, 100]. On the other hand, the fibril hypothesis was supported by our recent study about myelin in XPCT, which is also a non-soluble protein [190]. We also considered a mix of the metal and fibril hypotheses. We designed a study involving three different techniques: XPCT, X-ray fluorescence microscopy (XRF) and Fourier-transform infrared microspectroscopy (FTIR). XRF and FTIR are 2D modalities that can respectively quantify metal and fibril levels (cf. subsection 2.5.1 and subsection 2.5.2). We coupled XRF and FTIR with optical fluorescence microscopy to target the same A $\beta$  deposits and correlate these data. The combined results on AD samples — either from human patients or from animal models — emphasize the role of metals for XPCT detection.

5.1 Introduction . . . . . 111

5.2 Associated published work . . . . . 112

5.3 Discussion . . . . . 149

To get familiar with the human brain anatomy, one can refer to the [Human Brain Atlas](#) [137, 138, 139] on EBRAINS.

To get familiar with the rodent brain anatomy, one can refer to the [Mouse Brain Atlas](#) [191] or [Rat Brain Atlas](#) [192, 193, 194] on EBRAINS.

## 5.2. Associated published work

---

Reproduced from bioRxiv

Chourrout M, Sandt C, Weitkamp T, Dučić T, Meyronet D, Baron T, Klohs J, Rama N, Boutin H, Singh S, Olivier C, Wiart M, Brun E, Bohic S, and Chauveau F. Why Are Amyloid- $\beta$  Plaques Detected by X-ray Phase-Contrast Imaging? Role of Metals Revealed through Combined Synchrotron Infrared and X-ray Fluorescence Microscopies. 2023 Jan 1. preprint

[Now published in Acta Biomaterialia with doi:  
[10.1016/j.actbio.2023.07.046](https://doi.org/10.1016/j.actbio.2023.07.046)]

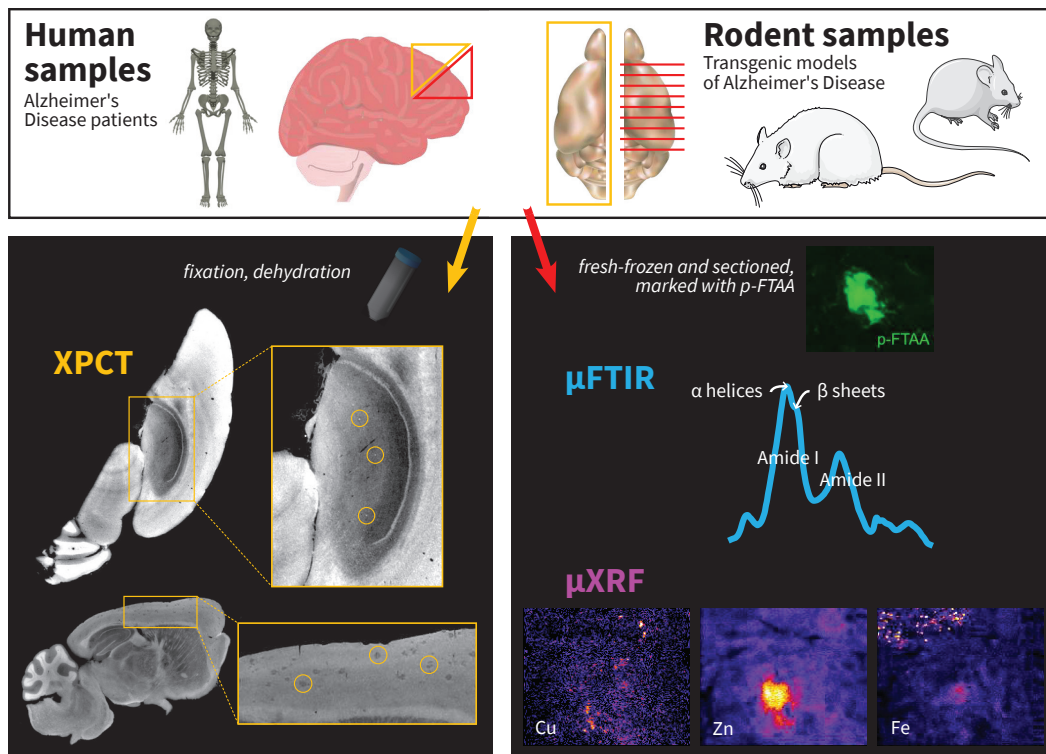
---

bioRxiv preprint doi: <https://doi.org/10.1101/2022.09.27.509706>; this version posted March 30, 2023. The copyright holder for this preprint (which was not certified by peer review) is the author/funder, who has granted bioRxiv a license to display the preprint in perpetuity. It is made available under aCC-BY-NC-ND 4.0 International license.

## 1 Graphical Abstract

### 2 Why are amyloid- $\beta$ plaques detected by X-ray phase-contrast imaging? Role of metals revealed through combined synchrotron infrared and X-ray fluorescence microscopies

3  
4  
5 Matthieu Chourrout, Christophe Sandt, Timm Weitkamp, Tanja Dučić, David  
6 Meyronet, Thierry Baron, Jan Klohs, Nicolas Rama, Hervé Boutin, Shifali  
7 Singh, Cécile Olivier, Marlène Wiart, Emmanuel Brun, Sylvain Bohic, Fabien  
8 Chauveau



## 9 Highlights

### 10 **Why are amyloid- $\beta$ plaques detected by X-ray phase-contrast imag-** 11 **ing? Role of metals revealed through combined synchrotron in-** 12 **frared and X-ray fluorescence microscopies**

13 Matthieu Chourrout, Christophe Sandt, Timm Weitkamp, Tanja Dučić, David  
14 Meyronet, Thierry Baron, Jan Klohs, Nicolas Rama, Hervé Boutin, Shifali  
15 Singh, Cécile Olivier, Marlène Wiart, Emmanuel Brun, Sylvain Bohic, Fabien  
16 Chauveau

- 17 • Amyloid- $\beta$  plaques in the different forms of Alzheimer's Disease have  
18 various contrasts in X-ray phase-contrast tomography
- 19 • In transgenic rodents, a core-restricted, positive contrast is driven by  
20 the level of metal entrapment within plaques
- 21 • In humans, greater and more diffuse metal accumulation lead to a  
22 positive contrast in a genetic case of AD

23 Why are amyloid- $\beta$  plaques detected by X-ray  
 24 phase-contrast imaging? Role of metals revealed  
 25 through combined synchrotron infrared and X-ray  
 26 fluorescence microscopies

27 Matthieu Chourrout<sup>a</sup>, Christophe Sandt<sup>b</sup>, Timm Weitkamp<sup>b</sup>, Tanja Dučić<sup>c</sup>,  
 28 David Meyronet<sup>d,e</sup>, Thierry Baron<sup>f</sup>, Jan Klohs<sup>g</sup>, Nicolas Rama<sup>e</sup>, Hervé  
 29 Boutin<sup>h</sup>, Shifali Singh<sup>i</sup>, Cécile Olivier<sup>i</sup>, Marlène Wiart<sup>j,k</sup>, Emmanuel Brun<sup>i</sup>,  
 30 Sylvain Bohic<sup>i</sup>, Fabien Chauveau<sup>a,k,\*</sup>

<sup>a</sup>Univ. Lyon, Lyon Neuroscience Research Center (CRNL); CNRS UMR5292; INSERM U1028; Univ. Lyon 1, Lyon, France

<sup>b</sup>Synchrotron SOLEIL, Saint-Aubin, France

<sup>c</sup>ALBA-CELLS Synchrotron, MIRAS Beamline, Cerdanyola del Vallès, Spain

<sup>d</sup>Hospices Civils de Lyon, Neuropathology department, Lyon, France

<sup>e</sup>Univ. Lyon, Cancer Research Center of Lyon (CRCL); INSERM U1052; CNRS UMR5286; Univ. Lyon 1; Centre Léon Bérard, Lyon, France

<sup>f</sup>Univ. Lyon, ANSES, Lyon, France

<sup>g</sup>ETH Zurich, Institute for Biomedical Engineering, Zurich, Switzerland

<sup>h</sup>Univ. Manchester, Faculty of Biology Medicine and Health, Wolfson Molecular Imaging Centre, Manchester, United Kingdom

<sup>i</sup>Univ. Grenoble Alpes, Synchrotron Radiation for Biomedicine (STROBE); Inserm UA7, Grenoble, France

<sup>j</sup>Univ. Lyon, CarMeN Laboratory; INSERM U1060, INRA U1397, INSA Lyon, Univ. Lyon 1, Lyon, France

<sup>k</sup>CNRS, France

31 **Abstract**

Amyloid- $\beta$  (A $\beta$ ) plaques from Alzheimer's Disease (AD) can be visualized *ex vivo* in label-free brain samples using synchrotron X-ray phase-contrast tomography (XPCT). However, for XPCT to be useful as a screening method for amyloid pathology, it is essential to understand which factors drive the detection of A $\beta$  plaques. The current study was designed to test the hypothesis that A $\beta$ -related contrast in XPCT could be caused by the A $\beta$  fibrils and/or by metals trapped in the plaques. This study probed the fibrillar and elemental compositions of A $\beta$  plaques in brain samples from different types of AD pa-

\*Corresponding author  
 Preprint submitted to *bioRxiv*

tients and AD models to establish a relationship between XPCT contrast and A $\beta$  plaque characteristics. XPCT, micro-Fourier-Transform Infrared spectroscopy and micro-X-Ray Fluorescence spectroscopy were conducted on human samples (genetic and sporadic cases) and on four transgenic rodent strains (mouse: APPPS1, ArcA $\beta$ , J20; rat: TgF344). A $\beta$  plaques from the genetic AD patient were visible using XPCT, and had higher  $\beta$ -sheet content and higher metal levels than the sporadic AD patient, which remained undetected by XPCT. A $\beta$  plaques in J20 mice and TgF344 rats appeared hyperintense on XPCT images, while they were hypointense with an hyperintense core in the case of APPPS1 and ArcA $\beta$  mice. In all four transgenic strains,  $\beta$ -sheet content was similar, while metal levels were highly variable: J20 (zinc and iron) and TgF344 (copper) strains showed greater metal accumulation than APPPS1 and ArcA $\beta$  mice. Hence, a positive contrast formation of A $\beta$  plaques in XPCT images appeared driven by biometal entrapment.

32 *Keywords:* Neurodegenerative diseases, Alzheimer’s disease, Amyloid- $\beta$   
33 plaques, X-ray phase-contrast tomography, Fourier-Transform Infrared  
34 spectroscopy, X-Ray Fluorescence spectroscopy

---

## 35 1. Introduction

36 Amyloid- $\beta$  (A $\beta$ ) plaques are an early hallmark of Alzheimer’s Disease  
37 (AD) in the human brain. A $\beta$  plaques are formed by the aggregation of  
38 amyloid- $\beta$  peptides with altered conformation into fibrils. Multiple tech-  
39 niques have arisen to assess the AD suspicion *in vivo*, especially A $\beta$  positron  
40 emission tomography (PET) [1]. However, definite AD diagnosis still requires  
41 the *postmortem* examination of brain tissue and neuropathological scorings  
42 like the CERAD scoring [2], which qualitatively assesses the density and dis-  
43 tribution within the brain, and Thal–Braak stages [3], which describe the  
44 progression of A $\beta$  plaques within the brain areas.

45 X-ray phase-contrast tomography (XPCT) refers to a family of techniques  
46 which uses the phase shift rather than the attenuation of X-rays to probe  
47 the microstructure in soft biological tissues. X-ray 3D imaging of A $\beta$  plaques  
48 has been described in transgenic rodent models that develop amyloidosis  
49 for the past decade, using propagation-based phase contrast (either with  
50 synchrotron radiation [4, 5, 6, 7] or with a laboratory source [8]) or us-  
51 ing grating-based phase contrast (with synchrotron radiation [9, 10, 11, 4]).  
52 These techniques generate 3D images with an isotropic resolution ranging

53 from 1  $\mu\text{m}$  to 10  $\mu\text{m}$ , thus providing a so-called “virtual histology” of the ex-  
54 cised brain [12, 13, 14] with minimal preparation (fixation, dehydration or  
55 paraffin embedding). Imaging AD samples with XPCT is particularly inter-  
56 esting because plaques stand out in the images without the need to add any  
57 staining agents. Previous studies highlighted the great potential of XPCT  
58 for the quantitative analysis of amyloid- $\beta$  plaques (overall burden [11, 4],  
59 spatial distribution [6], 3D morphometry [7]). These advances (which bring  
60 original information not available to standard immunohistochemistry), com-  
61 bined with increasingly faster acquisitions (less than 5 min per sample [7]),  
62 position XPCT as a potential screening tool for amyloid pathology. However,  
63 up to now, the substrate underlying contrast of A $\beta$  plaques in XPCT images  
64 remains unexplored. In other words, it is not known why A $\beta$  plaques are  
65 detected with XPCT.

66 Phase-contrast signal emerges from local changes of the X-ray refrac-  
67 tive index within the plaques — compared to that of the surrounding tissue  
68 —, which makes them stand out. Changes of the refractive index could  
69 be caused by the characteristics of the fibrils structured as  $\beta$ -sheet stacks  
70 of amyloid- $\beta$  peptides [15, 16, 17], which form dense and relatively insol-  
71 uble aggregates. Or they could be linked to the entrapment of endogenous  
72 metals within the plaques, as iron, copper and zinc have been observed as  
73 co-localized with A $\beta$  plaques, both in the human pathology [15, 18] and in  
74 rodent models [19, 20, 21]. We tested these two non-exclusive hypotheses  
75 to elucidate the origin of the phase-contrast signal of A $\beta$  plaques. To this  
76 end, we performed an examination of the same excised brains from a va-  
77 riety of transgenic rodents (four transgenic strains) and AD patients (one  
78 sporadic case and one familial case) with three different and complementary  
79 synchrotron techniques, namely:

- 80 *i)* XPCT to visualize the plaques and measure the contrast with sur-  
81 rounding tissue,
- 82 *ii)* Fourier-transform infrared microspectroscopy ( $\mu\text{FTIR}$ ) to quantify the  
83 proportion of  $\beta$  sheets in the plaques,
- 84 *iii)* X-ray fluorescence microspectroscopy ( $\mu\text{XRF}$ ) to assess metal quanti-  
85 ties in the plaques.

86 We here report new XPCT contrasts related to A $\beta$  plaques: in rodents,  
87 some strains displayed a hypointense (dark) contrast while others had the

88 already described hyperintense (bright) contrast. In humans, XPCT high-  
89 lighted parenchymal A $\beta$  plaques for the first time (in the genetic patient).  
90 Overall our results suggest that positive XPCT contrast is mainly driven by  
91 the level and spatial distribution of metal entrapment.

## 92 2. Material & Methods

### 93 2.1. Study design

94 Figure 1 summarizes study design, which intended to examine A $\beta$  plaques  
95 from the same brains with XPCT,  $\mu$ FTIR and  $\mu$ XRF. Tissue preparation was  
96 not compatible between the three techniques, thus the samples had to be cut:  
97 one half was processed for XPCT, the other half was processed for  $\mu$ FTIR  
98 followed by  $\mu$ XRF. The list of samples, and all measurements performed on  
99 individual A $\beta$  plaques ( $n = 9\text{--}23$  per strain), is available as a supplementary  
100 file.

### 101 2.2. Samples

#### 102 2.2.1. Human brain samples

103 Human brain samples (from parietal and frontal cortex) and associated  
104 data were obtained from Tissu-Tumorotheque Est Biobank (CRB-HCL Hos-  
105 pices Civils de Lyon) authorized by the French Ministry of Research (autho-  
106 rizations DC2008-72 & AC2015-2576):

- 107 • A 51-year-old male patient with genetic (APP duplication) AD (post-  
108 mortem delay 36 h);
- 109 • An 82-year-old female patient with sporadic AD (post-mortem delay  
110 11 h).

111 Both had pronounced A $\beta$  pathology (Thal–Braak stage V, CERAD score 3)  
112 [22], and had been previously diagnosed as free from prion disease.

113 Two snap-frozen samples were collected. One sample was kept frozen for  
114 sectioning, while the other was fixed with formaldehyde 4% (as described in  
115 the tissue preparation section below).

116 Paired formalin-fixed paraffin-embedded (FFPE) blocks were cut onto  
117 slides and stained with multiple agents:

- 118 • Anti-A $\beta$  A4 antibodies for A $\beta$  load;
- 119 • Anti-phosphorylated-tau antibodies for neurofibrillary tangles (NFTs);

bioRxiv preprint doi: <https://doi.org/10.1101/2022.09.27.509706>; this version posted March 30, 2023. The copyright holder for this preprint (which was not certified by peer review) is the author/funder, who has granted bioRxiv a license to display the preprint in perpetuity. It is made available under aCC-BY-NC-ND 4.0 International license.

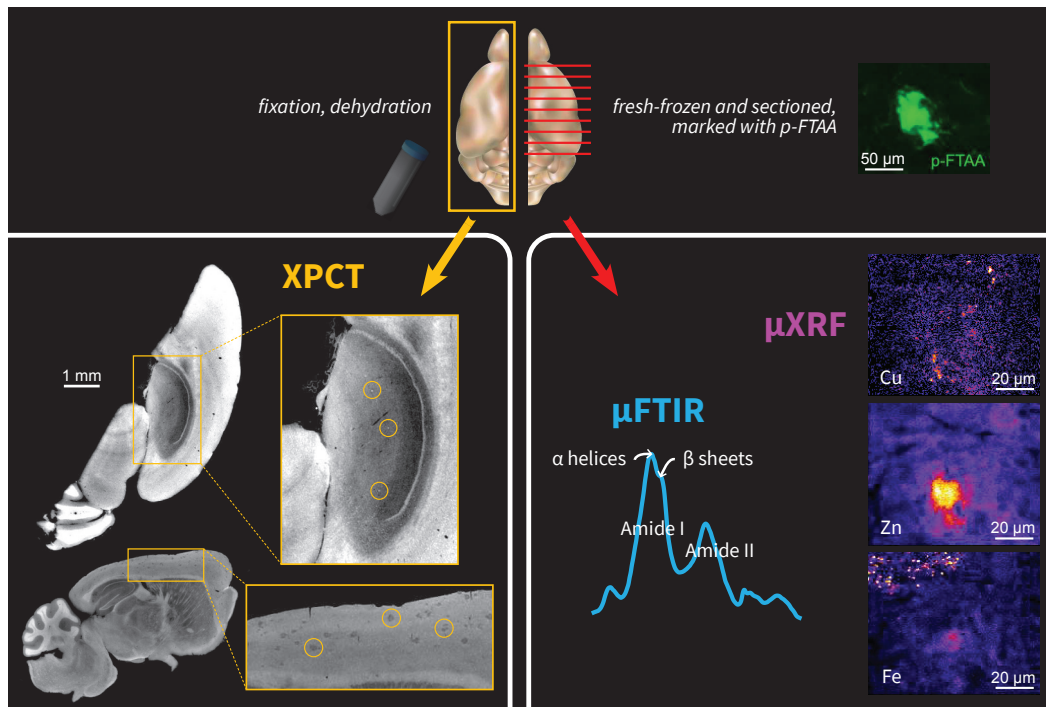


Figure 1: Experimental design, summarizing sample preparation and imaging techniques. A half of the sample was fixed and dehydrated then scanned in 3D with XPCT (left part). The other half was sectioned while frozen, fluorescently stained to locate A $\beta$  plaques, and analyzed in 2D using  $\mu$ FTIR (for  $\beta$ -sheet load) and  $\mu$ XRF (for metal level).

- 120 • Luxol fast blue and periodic acid-Schiff (PAS) stains for myelin and  
121 glycogen-rich bodies.

### 122 2.2.2. Transgenic rodent brain samples

123 Four transgenic rodent models that develop amyloidosis were studied:

- 124 • Mono-transgene line ArcA $\beta$  ( $n = 3$  mice, 15 months old), with mutant  
125 APP [23] (<https://www.alzforum.org/research-models/arcav>)
- 126 • Double-transgene line APPPS1 ( $n = 3$  mice, 12 months old), with mu-  
127 tant APP and PSEN1 [24] ([https://www.alzforum.org/research-models/](https://www.alzforum.org/research-models/appps1)  
128 [appps1](https://www.alzforum.org/research-models/appps1))
- 129 • Mono-transgene line J20 ( $n = 2$  mice, 13 months old), with mutant  
130 APP [25] (<https://www.alzforum.org/research-models/j20-pdgf-appswind>)

- 131 • Double-transgene line TgF344 ( $n = 3$  rats, 20 months old), with mutant  
132 APP and PSEN1 [26] ([https://www.alzforum.org/research-models/  
133 tgf344-ad](https://www.alzforum.org/research-models/tgf344-ad))

134 One wild-type (WT) rat (Fischer 344) and one WT mouse (C57Bl/6), re-  
135 spectively 20 and 15 months old, were used as controls.

136 Rodents were sacrificed with intracardiac PBS perfusion to clean blood  
137 vessels. Brains were excised and kept at  $-80^{\circ}\text{C}$ .

138 Mouse brains were cut in half along the hemisphere (Figure 1). One half  
139 was then fixed and dehydrated (for XPCT). The other half was immediately  
140 put back at  $-80^{\circ}\text{C}$  (for  $\mu\text{FTIR}$  and  $\mu\text{XRF}$ ).

141 Only one hemisphere was available per rat brain. The hemispheres were  
142 cut in the middle of the hippocampus. One half was then fixed and dehy-  
143 drated (for XPCT). The other half was immediately put back at  $-80^{\circ}\text{C}$  (for  
144  $\mu\text{FTIR}$  and  $\mu\text{XRF}$ ).

#### 145 2.2.3. Fixed tissue and dehydration

146 The unfrozen samples were fixed for 24 to 48 hours with 4% FA. Then  
147 they were dehydrated at RT in a series of 8 baths with a gradient of ethanol  
148 concentrations, diluted with PBS, for 5 minutes each: 25%, 25%, 50%, 50%,  
149 75%, 75%, 96%, 96%. Finally, they were put into plastic tubes filled with  
150 96% ethanol and kept at  $4^{\circ}\text{C}$ .

#### 151 2.2.4. Frozen tissue and preparation of SiRN membranes

152 The frozen samples were dissected into blocks in the hippocampus / upper  
153 cortex area, to ensure they would fit into an area of  $4 \times 4 \text{ mm}^2$ . Then they  
154 were sectioned using a Leica CM1850 cryostat at  $-20^{\circ}\text{C}$  with a thickness of  
155  $7 \mu\text{m}$ . PTFE-coated blades (DuraEdge™, TedPella, Inc., USA) were used to  
156 prevent metallic contamination. Brain sections were placed with a paintbrush  
157 on 200 nm-thick silicon-rich nitride (SiRN) membranes (Silson Ltd, UK) with  
158 an inner frame side of 4 millimeters. Sections were stained for 5 minutes with  
159 a pan-amyloid fluorescent agent, p-FTAA [27] ( $1 \mu\text{mol L}^{-1}$  in PBS with 0.01%  
160  $\text{NaN}_3$ ); membranes were then rinsed once with nanopure water. Fluorescence  
161 and bright-field transmission images were acquired with a ZEISS microscope  
162 (cf. Figure 2, A). Afterwards, membranes were kept in a desiccator with  
163 silica gel blue (2 mm–4 mm, Roth) until synchrotron experiments (1–4 weeks  
164 after).

bioRxiv preprint doi: <https://doi.org/10.1101/2022.09.27.509706>; this version posted March 30, 2023. The copyright holder for this preprint (which was not certified by peer review) is the author/funder, who has granted bioRxiv a license to display the preprint in perpetuity. It is made available under aCC-BY-NC-ND 4.0 International license.

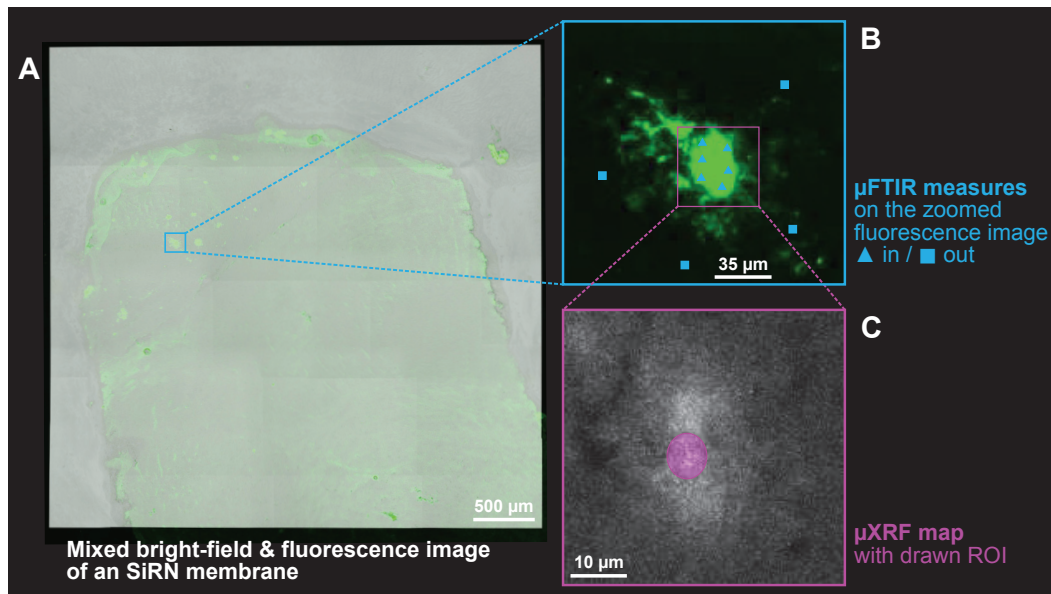


Figure 2: Silicon-nitride membrane overview and 2D imaging with  $\mu$ FTIR and  $\mu$ XRF. (A) Sectioned samples were placed on SiRN membranes, fluorescently stained and imaged with a microscope with 2 channels: bright-field and green fluorescence. (B) During the experiment at the SMIS beamline, the fluorescence was used to target  $A\beta$  plaques and multiple  $\mu$ FTIR spectra were acquired within individual plaques and in the surrounding tissue. (C) During the experiment at the NANOSCOPIUM beamline,  $\mu$ XRF hypermaps were acquired on the same  $A\beta$  plaques — here shown as the sum over the whole spectrum.

### 165 2.3. Synchrotron experiments

166 All experiments, unless explicitly stated, were conducted at the syn-  
167 chrotron radiation facility SOLEIL, within the scope of the proposal #20200258.

#### 168 2.3.1. X-ray phase-contrast tomography (XPCT)

169 Formaldehyde-fixed, ethanol-dehydrated samples were imaged with X-ray  
170 phase-contrast tomography (XPCT) at the ANATOMIX beamline [28] with  
171 a pink beam of mean energy 22 keV and a detector pixel size of 6.5  $\mu$ m. The  
172 detector system consisted of a lutetium aluminum garnet (LuAG,  $\text{Lu}_3\text{Al}_5\text{O}_{12}$ )  
173 single-crystal scintillator (600  $\mu$ m thick) coupled to a CMOS camera (Hama-  
174 matsu Orca Flash 4.0 V2, 2048  $\times$  2048 pixels) via a 1 : 1 lens system consist-  
175 ing of two Hasselblad photo objectives ( $f = 100$  mm) in tandem geometry.  
176 Complete acquisition parameters are reported in Supplemental Table 1.

177 For reconstruction using PyHST2 [29], we set the Paganin length param-  
178 eter to 552  $\mu$ m ( $\delta/\beta = 1525$ ). We used a motion blur correction algorithm

179 and an unsharp mask filter ( $c_{unsharp} = 0.5$ ,  $\sigma_{unsharp} = 2$  px).

180 Human samples were imaged at a higher resolution via a 1.45 : 1.45 lens  
181 system using a similar setup. The Paganin length was adapted to 216.65  $\mu\text{m}$   
182 ( $\delta/\beta = 1400$ ).

### 183 2.3.2. XPCT image analysis

184 Ring artifacts were removed using an in-house tool implemented by the  
185 company NOVITOM (France; <https://www.novitom.com/en/>) [14]. Sam-  
186 ples were isolated from the background (air, plastic tube and ethanol) and  
187 rotated within the AMIRA 3D software (release 2021.1, Thermo Fisher Sci-  
188 entific, USA). A $\beta$  plaques were segmented semi-automatically using a ran-  
189 dom forest algorithm from the IPSDK software (Reactiv'IP, France; <https://www.reactivip.com/>). The generated masks were screened for false pos-  
190 itive segmentations and  $\sim 20$  plaques were selected, along with ROIs of the  
191 background. Signal intensity measurements — as a ratio of the mean intensi-  
192 ties of the plaques and the mean intensities of the background ROIs — were  
193 retrieved with MorphoLibJ [30], an ImageJ plugin.

### 195 2.3.3. Fourier-transform infra-red microspectroscopy ( $\mu\text{FTIR}$ )

196 The brain cryosections on the membranes (cf. Figure 2, panel B) were an-  
197 alyzed by synchrotron-radiation FTIR microspectroscopy with a Continuum  
198 XL microscope and a Thermo Nicolet 6700 bench at the SMIS beamline. The  
199 microscope was equipped with a fluorescence imaging setup and an halogen  
200 mercury lamp for excitation of the p-FTAA fluorescent probe that binds A $\beta$   
201 plaques.

202 Spectra on and around the spots of interest (respectively referred as  
203 “In” and “Out”) were recorded between 650  $\text{cm}^{-1}$  and 4000  $\text{cm}^{-1}$  at 4  $\text{cm}^{-1}$   
204 in  $10 \times 10 \mu\text{m}^2$  dual-aperture mode, using a Schwarzschild 32 $\times$  (NA 0.65)  
205 objective and a matching condenser; zero-padding enhanced resolution to  
206 0.5  $\text{cm}^{-1}$ . All parameters are shown in Supplemental Table 2. Spectra were  
207 pre-processed with the atmospheric suppression algorithm from OMNIC 9.2  
208 (Thermo Fisher Scientific, USA) to remove water vapor contribution.

209 Besides, a few acquisitions were performed as evenly-spaced arrays (“maps”)  
210 with a lower co-addition to scan larger areas on a few samples, especially  
211 those devoid of A $\beta$  from the WT animals.

212 *2.3.4.  $\mu$ FTIR spectral analysis*

213 Spectra were processed using Quasar [31]. All the data were imported  
214 and processed with the same pipeline:

215 Cutting: The region from  $650\text{ cm}^{-1}$  to  $800\text{ cm}^{-1}$  was cut out because of high-  
216 frequency noise;

217 Quality assessment: Spectra were thoroughly screened for Mie scattering ar-  
218 tifacts — indeed, Mie scattering is responsible for the shifting of the  
219 Amide I peak towards lower wave numbers and for its distortion, which  
220 leads to measurements that are easily mistaken for higher  $\beta$ -sheet con-  
221 tent [32];

222 Absorbance thresholding: MCT detectors have a limited range for linearity  
223 between 0.2 and 1.4, so spectra with a peak-to-peak amplitude outside  
224 this range were discarded;

225 Baseline correction: A linear baseline correction was applied on the Amide I  
226 band, from  $1415\text{ cm}^{-1}$  to  $1770\text{ cm}^{-1}$ ;

227 Feature selection: Absorbance values closest to  $1655\text{ cm}^{-1}$  (non- $\beta$  sheets) and  
228  $1630\text{ cm}^{-1}$  ( $\beta$  sheets) [33] were used as features to compute a spectro-  
229 scopic ratio for amyloid  $\beta$ -sheet content:  $\frac{A_{1630\text{ cm}^{-1}}}{A_{1655\text{ cm}^{-1}}}$

230 *2.3.5. X-ray fluorescence microscopy ( $\mu$ XRF)*

231 The brain cryosections on the membranes (cf. Figure 2, panel C) were  
232 analyzed by x-ray fluorescence ( $\mu$ XRF) microscopy on the “CX3” custom  
233 bench at the NANOSCOPIUM beamline, using the “flyscan” mode with steps  
234 of  $0.3\text{ }\mu\text{m}$ . Measures were performed on the same locations on the membranes  
235 as for  $\mu$ FTIR acquisitions (cf. § 2.3.3), through the method described in ??.  
236 The inline optical bright-field microscope which is mounted on the beamline  
237 helped fine-tuning the position. All parameters are shown in Supplemental  
238 Table 3.

239 Three standard reference materials (SRMs) were also scanned: the SRM  
240 1577c “bovine liver” and SRM 1832 (NIST, USA), along with the “RF”  
241 standard thin film (AXO DRESDEN GmbH, Germany).

### 242 2.3.6. $\mu$ XRF elemental analysis

243 Spectra were processed using PyMca [34]. First, the raw spectral maps  
244 were summed to locate the plaques more precisely within the scanned field  
245 of view — from  $20 \times 20 \mu\text{m}^2$  to  $80 \times 80 \mu\text{m}^2$ . Regions of Interest (ROIs) were  
246 drawn at the location of each plaque.

247 Then, the measures on the three SRMs and on a blank SiRN membrane  
248 helped the calibration of the software — using the fundamental parame-  
249 ter method — and the batch-fitting tool computed the mass fraction maps  
250 for each element. Reported mass fractions in  $\mu\text{g g}^{-1}$  or “parts per million”  
251 (ppm) were obtained by averaging within the drawn ROI. One can easily  
252 retrieve an approximate surface concentration:  $10 \text{ ppm} \approx 1 \text{ ng cm}^{-2}$ ; because  
253  $e_{\text{dried tissue}} \approx 1 \mu\text{m}$  and  $\rho_{\text{dried tissue}} = 1.04 \text{ g cm}^{-3}$  (the density of dried brain  
254 tissue).

### 255 2.4. Statistics

256 Results are displayed as box plots which use the Tukey standards, i.e.  
257 the whiskers end at  $Q1 - 1.5 \times IQR$  and  $Q3 + 1.5 \times IQR$  ( $IQR$  is the inter-  
258 quartile range); values outside of  $[Q1 - 1.5 \times IQR; Q3 + 1.5 \times IQR]$  are  
259 represented as points; means are represented as crosses and medians as a  
260 wide line. Reported fold increases are computed between the means.

261 The normality and log-normality D’Agostino-Pearson tests failed for the  
262 whole data set. Kruskal-Wallis tests with post-hoc Dunn’s multiple com-  
263 parison tests were performed on XPCT intensities,  $\mu$ FTIR-derived data and  
264  $\mu$ XRF-derived data in rodents. A separate Kruskal-Wallis test with post-hoc  
265 Dunn’s multiple comparison tests was performed for human  $\mu$ FTIR-derived  
266 data. For human  $\mu$ XRF-derived data, a non-parametric Mann-Whitney test  
267 was performed per element (iron, zinc and copper levels were considered  
268 independent).

## 269 3. Results

### 270 3.1. Genetic and sporadic human AD samples exhibit different $A\beta$ contrasts 271 in XPCT

272 On XPCT images (Figure 3), the multiple  $A\beta$  plaques from the genetic  
273 AD patient were clearly visible in grey matter, exhibiting a typical neuritic  
274 aspect (Figure 3, A1-B1, yellow arrow heads) and diameter around  $50 \mu\text{m}$ .  
275 Anti- $A\beta$  staining of slides derived from paired FFPE block confirmed the

276 presence of numerous plaques with dense central core and less compact pe-  
277 ripheral halo (Figure 3, C1, yellow arrows). The central core of neuritic  
278 plaques and surrounding dystrophic neurites containing neurofibrillary ma-  
279 terial were also stained using anti-p-tau antibodies (Figure 3, D1, yellow  
280 arrows). The presence of multiple A $\beta$  plaques in this familial form of AD  
281 was especially striking when scrolling through the virtual sample (movie).  
282 In contrast, the numerous A $\beta$  diffuse plaques detected in A $\beta$ -stained slides  
283 from the sporadic AD patient could not be reliably visualized in XPCT (Fig-  
284 ure 3, red arrow heads). In both genetic and sporadic AD cases, smaller,  
285 round-shaped and highly hyperintense structures were observed in sub-pial  
286 layer of frontal sulcus. These structures were presumably corporea amy-  
287 lacea, as far as similarly shaped inclusions positive to periodic acid-Schiff  
288 (PAS) staining were found in similar location in slides from FFPE paired  
289 blocks for both genetic and sporadic AD (Figure 3, blue arrows). Additional  
290 triangle shaped structures disseminated across cortex layers were also seen.  
291 They were enhanced after Maximum Intensity Projection (MIP). Their shape  
292 and distribution across the cortex corresponded to p-tau-stained tangles in  
293 FFPE-derived slides (Figure 3, green arrows). Other variably hyperdense  
294 structures were neuronal bodies and vessel walls.

bioRxiv preprint doi: <https://doi.org/10.1101/2022.09.27.509706>; this version posted March 30, 2023. The copyright holder for this preprint (which was not certified by peer review) is the author/funder, who has granted bioRxiv a license to display the preprint in perpetuity. It is made available under aCC-BY-NC-ND 4.0 International license.

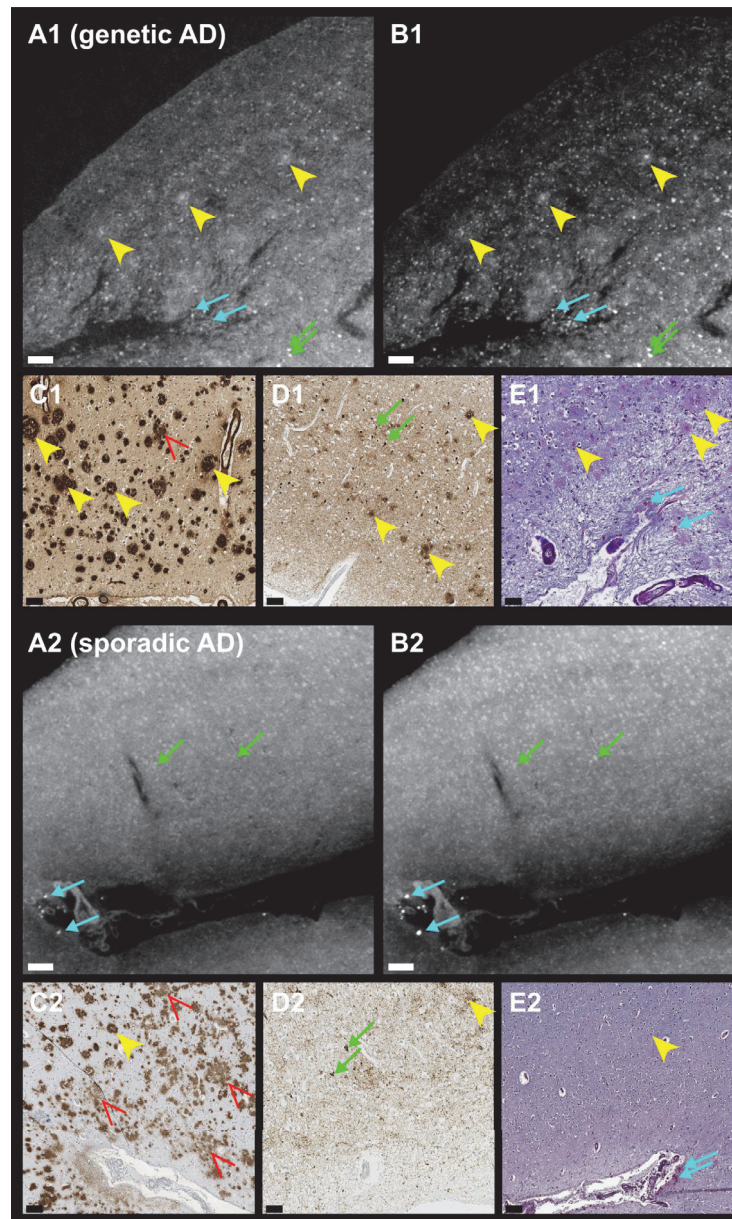


Figure 3: Representative XPCT images of brain tissue with A $\beta$  plaques from a genetic (A1-E1) and a sporadic (A2-E2) cases of Alzheimer's Disease. Insets A1&A2 are single slices while insets B1&B2 are maximum intensity projections (MIPs) of the same FOVs over 5 slices (16  $\mu$ m). Virtual slices are compared to (contralateral) FFPE slices: anti-A $\beta$  A4 immunostaining (C1&C2), anti-p-tau immunostaining (D1&D2) and LFB / PAS staining (E1&E2). Yellow arrow heads point at neuritic amyloid plaques while red arrow heads point at diffuse plaques. Other hyperdensities, smaller than A $\beta$  plaques, were p-tau stained tangles (green arrows) and corpora amylacea (blue arrows). Neuron soma and blood vessel walls were slightly hyperdense. Scale bars equal 100  $\mu$ m.

bioRxiv preprint doi: <https://doi.org/10.1101/2022.09.27.509706>; this version posted March 30, 2023. The copyright holder for this preprint (which was not certified by peer review) is the author/funder, who has granted bioRxiv a license to display the preprint in perpetuity. It is made available under aCC-BY-NC-ND 4.0 International license.

295 3.2.  $\beta$ -sheet content and metal entrapment are strikingly enhanced in the  
296 genetic case compared to the sporadic case

297 As expected, the  $\beta$ -sheet content in the fluorescence-labelled plaques (Fig-  
298 ure 4, panel A) was higher than in the surrounding tissue for both patients  
299 (genetic AD: +50 %; sporadic AD: +4 %). Besides, the  $\beta$ -sheet content sig-  
300 nificantly differentiated A $\beta$  plaques between the genetic and sporadic AD  
301 patients (genetic AD: +55 %;  $p = 0.0291$ ).

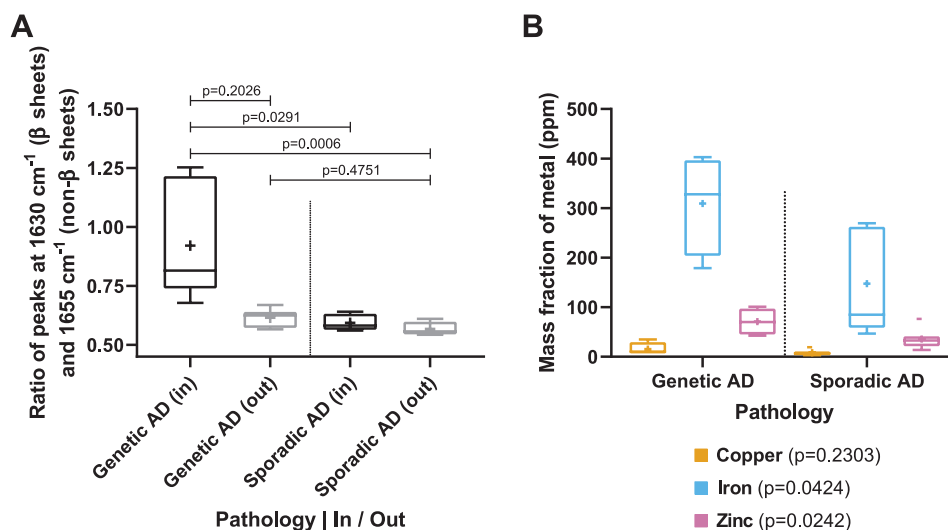


Figure 4: (A) Amyloid  $\beta$ -sheet content and (B) metal levels within A $\beta$  plaques from Alzheimer's Disease patients.  $\beta$ -sheet content is computed from peak ratios on  $\mu$ FTIR spectra and averaged per plaque ( $n = 6$  for each patient). Metal levels are obtained by peak fitting on  $\mu$ XRF hyperspectra and averaged within a ROI on a plaque ( $n = 4$  for the genetic AD,  $n = 7$  for the sporadic AD).

302 Levels of metals within A $\beta$  plaques (Figure 4, panel B) were higher (iron:  
303 +109 %; zinc: +97 %; copper: +88 %) for the genetic AD patient compared  
304 to the sporadic AD patient.

305 3.3. Transgenic AD models exhibit a variety of A $\beta$  contrasts in XPCT

306 To further investigate the relationship between XPCT A $\beta$  contrast and  
307 A $\beta$  composition, we used 4 different transgenic rodent strains (Figure 5A):  
308 the J20 mice and the TgF344 rats had small hyperintense plaques (typi-  
309 cally in the range  $\varnothing$ 25–30  $\mu$ m for J20; and  $\varnothing$ 15–20  $\mu$ m for TgF344) mostly

310 seen in the hippocampus (movies), while the APPPS1 and ArcA $\beta$  strains  
 311 had numerous and large hypointense plaques (APPPS1:  $\varnothing$ 40–45  $\mu$ m; Ar-  
 312 cA $\beta$ :  $\varnothing$ 45–60  $\mu$ m), which however frequently exhibited a hyperintense core  
 313 (APPPS1:  $\varnothing$ 10–15  $\mu$ m; ArcA $\beta$ :  $\varnothing$ 15–20  $\mu$ m), and were mainly located in the  
 314 cortex but also in the hippocampus. Signal intensity measurements from  
 315  $\sim$  20 segmented plaques per sample are shown in Figure 5 B.

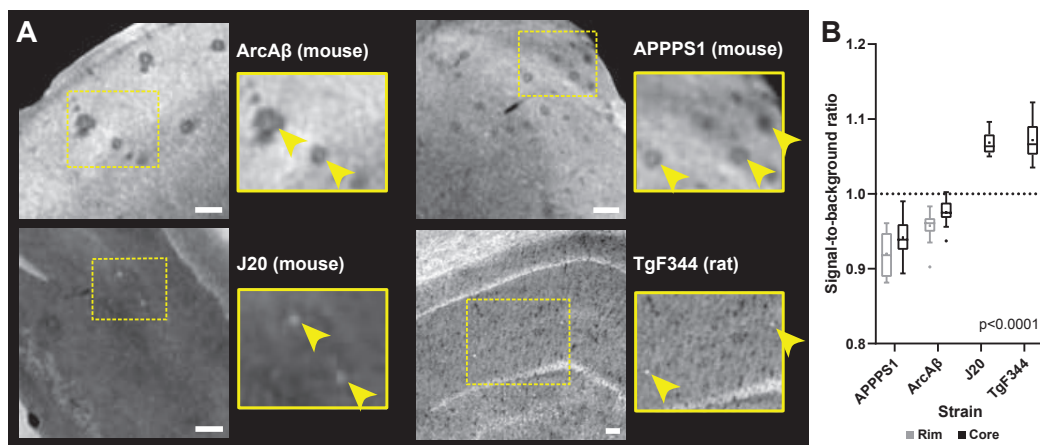


Figure 5: (A) XPCT slices of brain tissue with A $\beta$  plaques from transgenic rodents and (B) associated contrasts of A $\beta$  plaques. Insets are zoomed single-slice ROIs of the main views. Plaques from ArcA $\beta$  and APPPS1 mice are hypointense and mainly observed in the cortex. Plaques from J20 mice and TgF344 rats are hyperintense and mostly located in the hippocampus. Comparisons of signal-to-background ratio between hyperintense-plaque strains and hypointense-plaque strains yielded significant differences ( $p < 0.0001$ ). Scale bars equal 100  $\mu$ m.

### 316 3.4. $\beta$ -sheet content is constant across transgenic strains while metal entrap- 317 ment is highly variable

318 The contralateral hemispheres were used to study fibrillar and elemental  
 319 composition of these plaques. The  $\beta$ -sheet content (Figure 6, A) increased  
 320 in fluorescently-labelled spots in the rodent brain slices (measurements “In”  
 321 vs. “Out” of fluorescent A $\beta$  plaques: +37% for APPPS1, +36% for ArcA $\beta$ ,  
 322 +38% for J20, +47% for TgF344). The  $\beta$ -sheet content in the surrounding  
 323 tissue (“Out”) in transgenic animals was similar to the level in correspond-  
 324 ing wild-type animals (APPPS1: +6%; ArcA $\beta$ : +2%; J20: +9%; TgF344:  
 325 –6%).

326 All transgenic strains also had increased levels of iron, zinc and copper at  
 327 the analyzed A $\beta$  plaques compared to their wild-type counterparts. However,

bioRxiv preprint doi: <https://doi.org/10.1101/2022.09.27.509706>; this version posted March 30, 2023. The copyright holder for this preprint (which was not certified by peer review) is the author/funder, who has granted bioRxiv a license to display the preprint in perpetuity. It is made available under aCC-BY-NC-ND 4.0 International license.

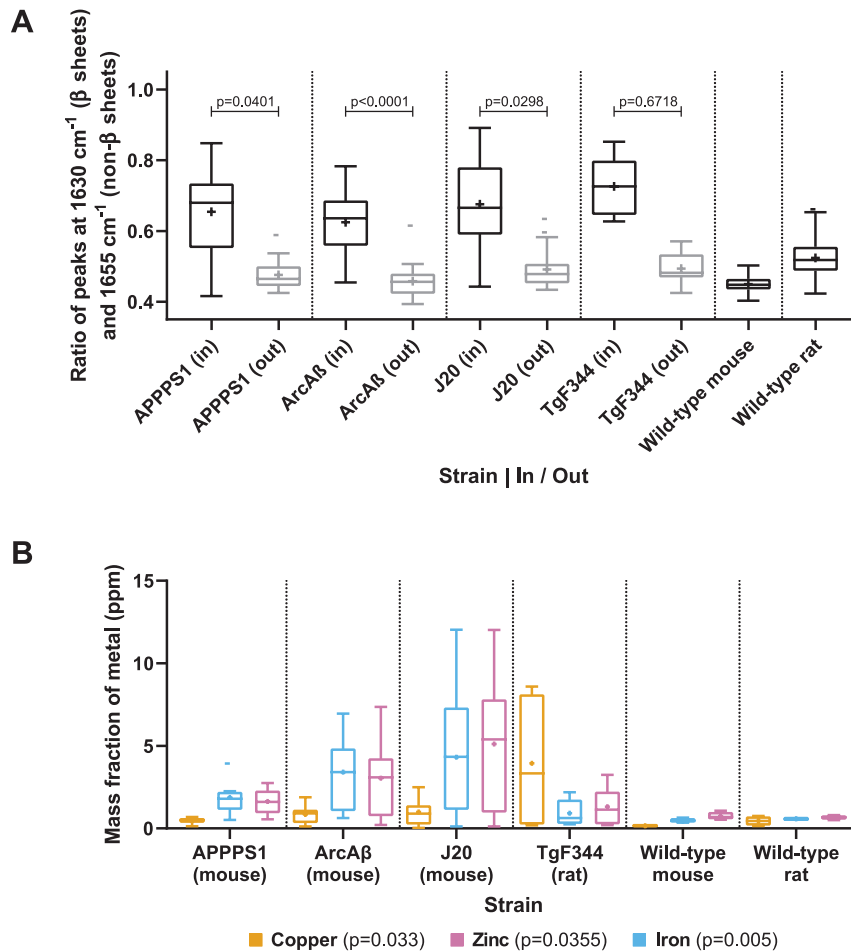


Figure 6: (A) Amyloid  $\beta$ -sheet content and (B) metal levels within  $A\beta$  plaques and in the surrounding tissue from transgenic rodents.  $\beta$ -sheet content is computed from peak ratios on  $\mu$ FTIR spectra and averaged per plaque ( $n = 9 - 20$  plaques per strain). Metal levels are obtained by peak fitting on  $\mu$ XRF hyperspectra and averaged within a ROI on a plaque ( $n=4-17$  plaques per strain).

328  $\mu$ XRF-measured metal composition of the  $A\beta$  plaques (Figure 6, B) varied  
 329 between the different strains. J20 mice had the highest levels of zinc and  
 330 iron compared to the other strains (zinc: +583 % vs. WT; iron: +803 % vs.  
 331 WT) and TgF344 rats had the highest level of copper (+770 % vs. WT).  
 332 Meanwhile, APPPS1 mice had the lowest mean levels and ArcA $\beta$  mice had

333 intermediate levels.

### 334 *3.5. Comparison between human and rodent datasets*

335 Figure 7 shows a qualitative comparison of the multimodal dataset ob-  
336 tained with XPCT,  $\mu$ FTIR and  $\mu$ XRF, between transgenic rodents and hu-  
337 mans. XPCT (left row) highlighted 3 distinct types of A $\beta$  plaques: small  
338 hyperintense plaques in J20 mice and TgF344; larger, hypointense plaques  
339 with a bright core in ArcA $\beta$  and APPPS1; and similarly large, but diffusely  
340 hyperintense plaques in the genetic case of AD. All types of plaques exhibited  
341 an increased level of  $\beta$ -sheet content which matched the fluorescence signal,  
342 as measured by  $\mu$ FTIR (central row), and which tended to be increased in  
343 the human case compared to animal models. The accumulation of endoge-  
344 nous metals (right row) was mainly restricted to the (hyperintense) core of  
345 the plaque in rodents, while it appeared consistently diffuse over the whole  
346  $\mu$ XRF FOV in the human plaques.

bioRxiv preprint doi: <https://doi.org/10.1101/2022.09.27.509706>; this version posted March 30, 2023. The copyright holder for this preprint (which was not certified by peer review) is the author/funder, who has granted bioRxiv a license to display the preprint in perpetuity. It is made available under aCC-BY-NC-ND 4.0 International license.

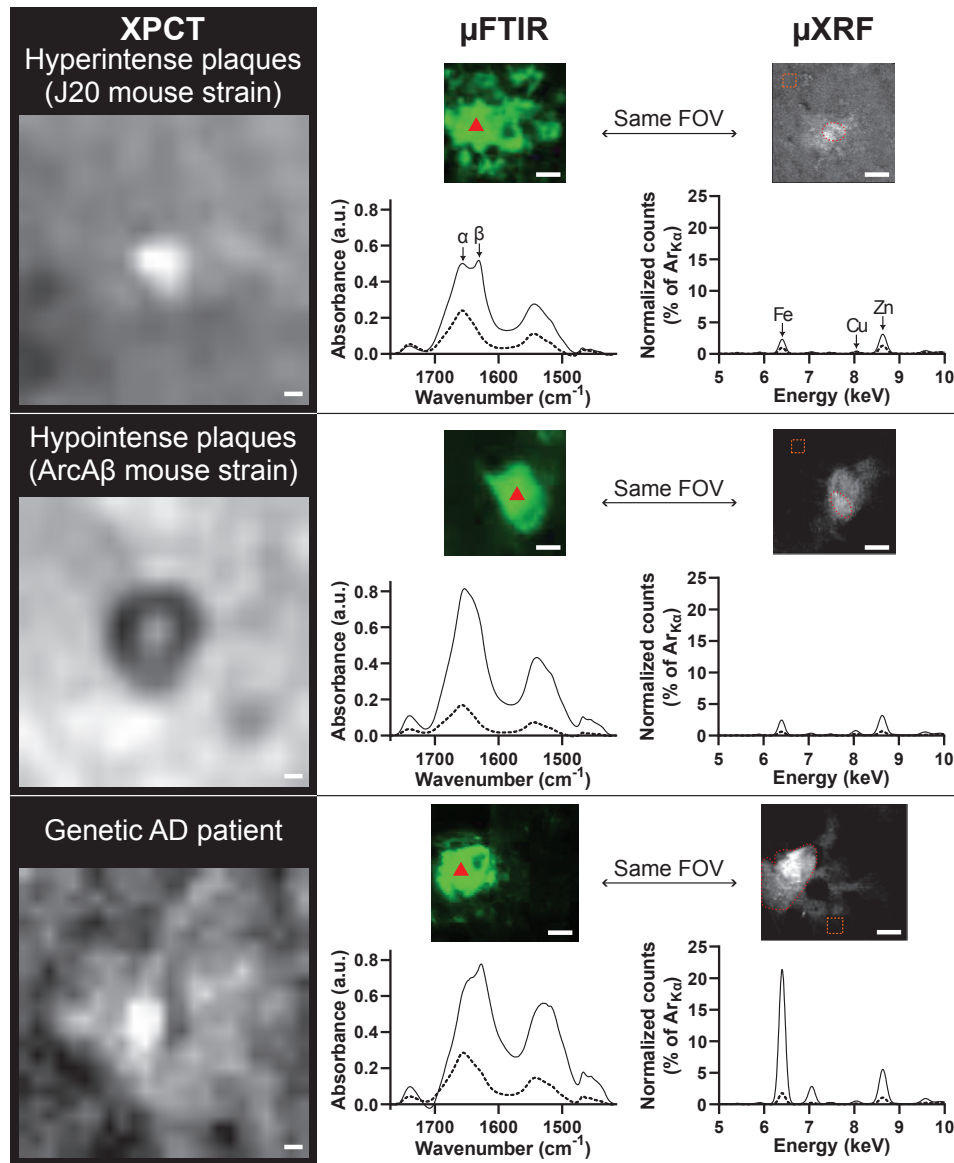


Figure 7: Multimodal dataset obtained with the three techniques on A $\beta$  plaques. XPCT scans (left column) were acquired on an unsectioned sample, while  $\mu$ FTIR (center) &  $\mu$ XRF (right) hyperspectra were acquired on a paired, sectioned, sample. Inline bright-field microscopy was used to match the fields of view (FOVs) between  $\mu$ FTIR and  $\mu$ XRF. Representative measurements in the plaques are indicated with a red arrowhead ( $\mu$ FTIR) and red outline ( $\mu$ XRF), and plotted as plain lines. Measurements outside the plaques ( $\mu$ FTIR: acquired in fluorescence-free regions outside the shown FOVs;  $\mu$ XRF: orange outline) are plotted as dotted lines. In the case of  $\mu$ FTIR, a linear baseline correction was applied on the Amide I band, from  $1415\text{ cm}^{-1}$  to  $1770\text{ cm}^{-1}$ . In the case of  $\mu$ XRF, maps show the summed  $\mu$ XRF signal and spectra were normalized with the  $K_{\alpha}$  peak of argon (Ar). Scale bars equal  $10\text{ }\mu\text{m}$ .

#### 347 4. Discussion

348 The present study sought to provide a rationale for the detection for A $\beta$   
349 plaques with synchrotron X-ray phase-contrast tomography, through a cor-  
350 relative approach between the local contrast — or signal intensity — and the  
351 fibrillar ( $\mu$ FTIR) and elemental ( $\mu$ XRF) compositions. The experimental de-  
352 sign relied on three imaging modalities, all available at synchrotron SOLEIL,  
353 and included brain samples from patients diagnosed with Alzheimer’s Disease  
354 (AD) and transgenic rodents which developed amyloidosis. 2D correlative ex-  
355 amination of A $\beta$  plaques through  $\mu$ FTIR and  $\mu$ XRF has been an active field  
356 of research for 15 years (e.g. [15, 19, 35, 36]), which constantly highlighted  
357 that local elevations of  $\beta$ -sheet content and metal trapping were concomitant  
358 features across a variety of AD specimens, including in cellular models [37].  
359 However this is the first time that the composition of A $\beta$  plaques is linked  
360 with a 3D imaging method such as XPCT.

361 Using propagation-based imaging, now the most widely employed XPCT  
362 method for virtual histology of label-free samples, we made original obser-  
363 vations. In animals, A $\beta$  plaques from the J20 mouse strain and the TgF344  
364 rat strain appeared as small bright (hyperintense) spots, as already reported  
365 for these and for other transgenic models such as 3xTg [7], APP/PS1 [6, 7],  
366 TauPS2APP [4] and B6C3-Tg [10]. But surprisingly, A $\beta$  plaques in the newly  
367 imaged APPPS1 and ArcA $\beta$  mouse strains appeared as dark (hypointense)  
368 spots, with the largest plaques frequently exhibiting an hyperintense core. In  
369 humans, we confirmed previous observations that parenchymal A $\beta$  plaques  
370 are usually not detected with XPCT, except rare deposits which were re-  
371 ported as calcified [13, 38]. However, we unveiled that A $\beta$  contrast in the  
372 human samples is more pronounced in an inherited case of AD — of which the  
373 first XPCT images are reported here — compared to sporadic AD. This vari-  
374 able appearance of A $\beta$  aggregates is reminiscent of A $\beta$  polymorphism, which  
375 describes, both in animal models and in humans, the existence of subtypes  
376 of A $\beta$  plaques [39, 40].

377 FTIR microspectroscopy can be used to quantify the  $\beta$ -sheet content in  
378 individual A $\beta$  plaques with exquisite sensitivity. Indeed, the ratio of the  $\beta$ -  
379 sheet over non- $\beta$ -sheet frequencies is used as a surrogate for fibrillar content.  
380 A $\beta$  plaques were localized with a pan-amyloid fluorescent stain, and we found  
381 a relatively similar level of fibrils in all transgenic models (interquartile ranges  
382 of ratio were: 0.55–0.73 for APPPS1; 0.56–0.69 for ArcA $\beta$ ; 0.59–0.78 for  
383 J20; 0.65–0.80 for TgF344). Not surprisingly, the genetic AD patient had

384 much higher levels of fibrils (interquartile ranges of ratio: 0.74–1.22) than the  
385 sporadic patient (0.54–0.60), probably due to the presence of more diffuse  
386 deposits in the sporadic case. Overall, these  $\mu$ FTIR results showed that the  
387 fibrillar content of A $\beta$  plaques is not the sole factor responsible for XPCT  
388 detection.

389 Multiple studies — based on X-ray fluorescence [20] or other methods like  
390 inductively coupled plasma mass spectrometry (ICP-MS) [41, 42] — have  
391 linked AD pathogenesis with a disruption of the metal homeostasis in the  
392 brain, and more specifically copper, iron and zinc. These endogenous met-  
393 als, whether in ionic or non-ionic forms [18], are locally trapped in A $\beta$  plaques  
394 at the expense of the surrounding tissue [15]. The metal concentrations we  
395 detected in the human A $\beta$  plaques matched those from the seminal study  
396 by Lovell et al. [43]. As already observed, animal models had much lower  
397 metal quantities associated with A $\beta$  plaques than humans [19, 44]. Import-  
398 tantly, copper, zinc and iron levels in the genetic patient were all significantly  
399 higher (2-fold increase) compared to the sporadic AD patient. In animals, A $\beta$   
400 plaques from each strain preferentially bound to different metals (elevated  
401 Zn and Fe in J20; elevated Cu in TgF344). It has already been reported that  
402 iron is dysregulated within the hippocampus of J20 mouse model of AD [45].  
403 And some differences between mouse and rat hippocampus — particularly  
404 on copper accumulation [46] — may explain our results on copper-enriched  
405 plaques in the rat model compared to mouse strain.

406 Overall, the combination of XPCT,  $\mu$ FTIR and  $\mu$ XRF (performed on the  
407 same brains with advanced amyloid pathology) allows us to propose the  
408 following interpretations. In mouse models, A $\beta$  plaques form numerous well-  
409 defined, and clearly visible deposits on XPCT images. Elevated levels of  
410 metals, mainly restricted to a small core area on XRF maps, are associ-  
411 ated with a positive signal (hyperintensity) detectable in all three strains on  
412 XPCT. Importantly, the brighter signals are detected in the strain with the  
413 highest level of metals (J20). However, a larger dark rim (hypointensity)  
414 extending this core is also detected in APPPS1 and ArcA $\beta$ , while absent in  
415 J20. A $\beta$  fibrils, which match the fluorescence area and exceed the core area,  
416 cannot explain this difference as similar levels of fibrils were measured with  
417  $\mu$ FTIR. Other factors, such as structural [40] or proteomic [47] differences  
418 between strains, might play a role.

419 In the transgenic rat, the pathology develops more slowly. Few plaques,  
420 representing only a subset of the global amyloid burden, are indeed detected  
421 with XPCT, as small hyperintense spots. In contrast, amyloid fluorescence

422 was widely detected in hippocampus, which pointed to a spatially widespread  
423 pathology (Supplemental Figure 1). In line with this, additional  $\mu$ FTIR  
424 mapping experiments performed at ALBA synchrotron (beamline MIRAS),  
425 showed a global and unimodal increase in fibrillar content (Supplemental Fig-  
426 ure 2), suggesting a diffuse accumulation of fibrils in the entire hippocampus.  
427 This implies that the few, large fluorescent areas that were targeted in our  
428  $\mu$ FTIR/ $\mu$ XRF experiments, are likely to be biased and maybe not be en-  
429 tirely representative of the pathology. Nevertheless, if we assume that the  
430 largest fluorescent plaques are the ones that give rise to XPCT detection, the  
431 high amounts of copper highlighted by  $\mu$ XRF specifically in this model, are  
432 consistent with the results from mouse models, and could explain the bright  
433 appearance, restricted to the core of A $\beta$  plaques in XPCT.

434 In humans, our data from two patients are obviously insufficient to dis-  
435 entangle the combined effect of  $\beta$ -sheet level and metal entrapment, which  
436 both drastically increased in the inherited case vs. sporadic one. However,  
437 the strikingly diffuse pattern of metal entrapment observed in XRF (in com-  
438 parison to rodent models, Figure 7) seems consistent with the detection of  
439 hyperintense plaques on XPCT images. More samples would be needed to un-  
440 derstand the local contrast in different types of A $\beta$  plaques (diffuse, neuritic)  
441 which could not be properly discriminated here. A direct comparison, at the  
442 individual plaque level, between 3D XPCT and subsequent 2D  $\mu$ FTIR/ $\mu$ XRF  
443 would be ideal for that purpose, but would require cryogenic XPCT to avoid  
444 the chemical fixation used here (incompatible with  $\mu$ XRF). Also, tau pathol-  
445 ogy, which is present in human samples in the form of neurofibrillary tangles  
446 (and potentially associated with microcalcifications [48]), but lacking in the  
447 rodent strains studied here, could contribute to the XPCT contrast, as it was  
448 recently shown in a triple-transgenic mouse model [49]. It is nevertheless re-  
449 markable that A $\beta$  plaques from the genetic case display a detectable XPCT  
450 contrast, and this observation deserves further confirmation in other familial  
451 cases of AD.

452 In conclusion, XPCT has attracted increasing interest in neuroscience  
453 these last years for its ability to provide valuable microstructural character-  
454 ization (myelin, vessels, neuron density, protein deposits) in excised, intact,  
455 brain samples. XPCT can now be acquired in a few minutes at various res-  
456 olutions, enabling a virtual dissection from the organ-level to the (sub-)cel-  
457 lular level. Indeed, high-resolution scans of whole organs are now possible  
458 as recently demonstrated by the particularly impressive 3D imaging of a full  
459 human brain [50]. The present report reinforces the potential of XPCT to

460 capture key aspects of the A $\beta$  pathology. However, if XPCT is envisioned as a  
461 potential screening method for A $\beta$  pathology in brain samples, it is crucial to  
462 understand which factors drive the detection of some and not all A $\beta$  plaques.  
463 This study was specifically designed to tackle this question, and highlighted  
464 sharp XPCT differences in A $\beta$  pathology, which were related to the different  
465 levels of metals locally bound to A $\beta$  plaques. This model-specific, dyshome-  
466 ostasis of endogenous metals might be a downstream consequence of the ge-  
467 netic alterations, and could be region-specific or depend on the disease stage  
468 of progression. Additional factors, other than the overall  $\beta$ -sheet content, are  
469 likely to contribute to the XPCT contrast and remain to be identified.

## 470 Acknowledgements

471 The authors acknowledge Synchrotron SOLEIL (Saint-Aubin, France)  
472 for allocation of beamtime within the scope of proposals #20200258 and  
473 #20220319 and we would like to thank the staff for assistance in using  
474 beamlines ANATOMIX (M. Scheel, J. Perrin), SMIS and NANOSCOPIUM  
475 (K. Medjoubi, A. Somogyi). ANATOMIX is an Equipment of Excellence  
476 (EQUIPEX) funded by the Investments for the Future program of the French  
477 National Research Agency (ANR), project NanoimagesX, grant no. ANR-  
478 11-EQPX-0031. We would like to thank Clément Tavakoli (STROBE, Univ.  
479 Grenoble-Alpes, Grenoble; Univ. Lyon 1, Lyon) for his help during the  
480 acquisitions at SOLEIL. The study was further supported by the ALBA  
481 Synchrotron Light Source (ALBA-CELLS, Barcelona, Spain; beamline MI-  
482 RAS; proposal 2018082957). This study was performed within the framework  
483 of LABEX PRIMES (ANR-11-LABX-0063) of Université de Lyon, within  
484 the “Investissements d’Avenir” program (ANR-11-IDEX-0007) of the French  
485 National Research Agency (ANR). We are grateful to Corinne Perrin from  
486 the Tumorothèque Est tissue bank, CRB-HCL (Lyon, France), for manag-  
487 ing human brain samples. We also thank Jérémy Verchère (ANSES, Lyon,  
488 France) for the management of APPPS1 brains. p-FTAA was a gift from the  
489 laboratory of chemistry at ENS-Lyon. S. Singh received support from the  
490 Auvergne-Rhône-Alpes region (FUI GigaQuant project).

491 **Authors' contributions (according to Contributor Role Taxonomy**  
492 **(CRediT))**

- 493 • Conceptualization: FC
- 494 • Methodology: EB, SB, FC
- 495 • Resources: CS, TW, TD, DM, TB (APPPS1), JK (ArcA $\beta$ ), NR (J20),  
496 HB (TgF344), CO, EB, SB
- 497 • Investigation: MC, CS, TW, TD, CO, MW, EB, SB
- 498 • Formal analysis: MC, CS, SS, SB
- 499 • Data curation: MC, CS, SB
- 500 • Software:
- 501 • Visualization: MC, DM, FC
- 502 • Validation: MC
- 503 • Supervision: CS, EB, SB, FC
- 504 • Project administration: FC
- 505 • Funding acquisition: FC
- 506 • Writing – original draft: MC, FC
- 507 • Writing – review & editing: MC, DM, CS, TW, TD, JK, MW, EB, FC

## 508 References

- 509 [1] M. A. Kolanko, Z. Win, F. Loreto, N. Patel, C. Carswell, A. Gontsarova,  
510 R. J. Perry, P. A. Malhotra, Amyloid PET imaging in clinical  
511 practice, *Practical Neurology* 20 (2020) 451–462. doi:10.1136/  
512 practneuro1-2019-002468.
- 513 [2] S. S. Mirra, A. Heyman, D. McKeel, S. M. Sumi, B. J. Crain, L. M.  
514 Brownlee, F. S. Vogel, J. P. Hughes, G. v. Belle, L. Berg, participating  
515 CERAD neuropathologists, The Consortium to Establish a Registry  
516 for Alzheimer’s Disease (CERAD): Part II. Standardization of the neu-  
517 ropathologic assessment of Alzheimer’s disease, *Neurology* 41 (1991)  
518 479–479. doi:10.1212/WNL.41.4.479.
- 519 [3] D. R. Thal, U. Rüb, M. Orantes, H. Braak, Phases of A beta-deposition  
520 in the human brain and its relevance for the development of AD, *Neu-  
521 rology* 58 (2002) 1791–1800. doi:10.1212/wnl.58.12.1791.
- 522 [4] A. Astolfo, A. Lathuilière, V. Laversenne, B. Schneider, M. Stampanoni,  
523 Amyloid- $\beta$  plaque deposition measured using propagation-based X-ray  
524 phase contrast CT imaging, *Journal of Synchrotron Radiation* 23 (2016)  
525 813–819. doi:10.1107/S1600577516004045.
- 526 [5] L. Massimi, I. Bukreeva, G. Santamaria, M. Fratini, A. Corbelli,  
527 F. Brun, S. Fumagalli, L. Maugeri, A. Pacureanu, P. Cloetens,  
528 N. Pieroni, F. Fiordaliso, G. Forloni, A. Uccelli, N. Kerlero de Rosbo,  
529 C. Balducci, A. Cedola, Exploring Alzheimer’s disease mouse brain  
530 through X-ray phase contrast tomography: From the cell to the organ,  
531 *NeuroImage* 184 (2019) 490–495. doi:10.1016/j.neuroimage.2018.09.  
532 044.
- 533 [6] L. Massimi, N. Pieroni, L. Maugeri, M. Fratini, F. Brun, I. Bukreeva,  
534 G. Santamaria, V. Medici, T. E. Poloni, C. Balducci, A. Cedola, As-  
535 sessment of plaque morphology in Alzheimer’s mouse cerebellum using  
536 three-dimensional X-ray phase-based virtual histology, *Scientific reports*  
537 10 (2020) 11233. doi:10.1038/s41598-020-68045-8.
- 538 [7] M. Chourrout, M. Roux, C. Boisvert, C. Gislard, D. Legland,  
539 I. Arganda-Carreras, C. Olivier, F. Peyrin, H. Boutin, N. Rama,  
540 T. Baron, D. Meyronet, E. Brun, H. Rositi, M. Wiart, F. Chauveau,

- 541 Brain virtual histology with X-ray phase-contrast tomography Part II:  
542 3D morphologies of amyloid- $\beta$  plaques in Alzheimer's disease models,  
543 *Biomedical Optics Express* 13 (2022) 1640. doi:10.1364/BOE.438890.
- 544 [8] M. Töpperwien, M. Krenkel, D. Vincenz, F. Stöber, A. M. Oelschlegel,  
545 J. Goldschmidt, T. Salditt, Three-dimensional mouse brain cytoarchi-  
546 tecture revealed by laboratory-based x-ray phase-contrast tomography,  
547 *Scientific Reports* 7 (2017) 42847. doi:10.1038/srep42847.
- 548 [9] K. Noda-Saita, A. Yoneyama, Y. Shitaka, Y. Hirai, K. Terai, J. Wu,  
549 T. Takeda, K. Hyodo, N. Osakabe, T. Yamaguchi, M. Okada, Quan-  
550 titative analysis of amyloid plaques in a mouse model of Alzheimer's  
551 disease by phase-contrast X-ray computed tomography, *Neuroscience*  
552 138 (2006) 1205–1213. doi:10.1016/j.neuroscience.2005.12.036.
- 553 [10] D. M. Connor, H. Benveniste, F. A. Dilmanian, M. F. Kritzer, L. M.  
554 Miller, Z. Zhong, Computed tomography of amyloid plaques in a mouse  
555 model of Alzheimer's disease using diffraction enhanced imaging, *Neu-  
556 roImage* 46 (2009) 908–914. doi:10.1016/j.neuroimage.2009.03.019.
- 557 [11] B. Pinzer, M. Cacquevel, P. Modregger, S. McDonald, J. Bensadoun,  
558 T. Thuering, P. Aebischer, M. Stampanoni, Imaging brain amyloid  
559 deposition using grating-based differential phase contrast tomography,  
560 *NeuroImage* 61 (2012) 1336–1346. doi:10.1016/j.neuroimage.2012.  
561 03.029.
- 562 [12] J. Albers, S. Pacilé, M. A. Markus, M. Wiart, G. Vande Velde,  
563 G. Tromba, C. Dullin, X-ray-Based 3D Virtual Histology-Adding the  
564 Next Dimension to Histological Analysis, *Molecular Imaging and Biol-  
565 ogy* 20 (2018) 732–741. doi:10.1007/s11307-018-1246-3.
- 566 [13] M. Eckermann, B. Schmitzer, F. van der Meer, J. Franz, O. Hansen,  
567 C. Stadelmann, T. Salditt, Three-dimensional virtual histology of  
568 the human hippocampus based on phase-contrast computed tomog-  
569 raphy, *Proceedings of the National Academy of Sciences* 118 (2021)  
570 e2113835118. doi:10.1073/pnas.2113835118.
- 571 [14] M. Chourrout, H. Rositi, E. Ong, V. Hubert, A. Paccalet, L. Foucault,  
572 A. Autret, B. Fayard, C. Olivier, R. Bolbos, F. Peyrin, C. Crola-da-  
573 Silva, D. Meyronet, O. Raineteau, H. Elleaume, E. Brun, F. Chauveau,

bioRxiv preprint doi: <https://doi.org/10.1101/2022.09.27.509706>; this version posted March 30, 2023. The copyright holder for this preprint (which was not certified by peer review) is the author/funder, who has granted bioRxiv a license to display the preprint in perpetuity. It is made available under aCC-BY-NC-ND 4.0 International license.

- 574 M. Wiart, Brain virtual histology with X-ray phase-contrast tomogra-  
575 phy Part I: Whole-brain myelin mapping in white-matter injury models,  
576 Biomedical Optics Express 13 (2022) 1620. doi:10.1364/BOE.438832.
- 577 [15] L. M. Miller, Q. Wang, T. P. Telivala, R. J. Smith, A. Lanzirotti, J. Mik-  
578 lossy, Synchrotron-based infrared and X-ray imaging shows focalized  
579 accumulation of Cu and Zn co-localized with  $\beta$ -amyloid deposits in  
580 Alzheimer's disease, Journal of Structural Biology 155 (2006) 30–37.  
581 doi:10.1016/j.jsb.2005.09.004.
- 582 [16] M. Rak, M. R. D. Bigio, S. Mai, D. Westaway, K. Gough, Dense-core and  
583 diffuse  $A\beta$  plaques in TgCRND8 mice studied with synchrotron FTIR  
584 microspectroscopy, Biopolymers 87 (2007) 207–217. doi:10.1002/bip.  
585 20820.
- 586 [17] C. R. Liao, M. Rak, J. Lund, M. Unger, E. Platt, B. C. Albensi, C. J.  
587 Hirschmugl, K. M. Gough, Synchrotron FTIR reveals lipid around and  
588 within amyloid plaques in transgenic mice and Alzheimer's disease brain,  
589 The Analyst 138 (2013) 3991. doi:10.1039/c3an00295k.
- 590 [18] J. Everett, F. Lermyte, J. Brooks, V. Tjendana-Tjhin, G. Plascencia-  
591 Villa, I. Hands-Portman, J. M. Donnelly, K. Billimoria, G. Perry,  
592 X. Zhu, P. J. Sadler, P. B. O'Connor, J. F. Collingwood, N. D. Telling,  
593 Biogenic metallic elements in the human brain?, Science Advances 7  
594 (2021) eabf6707. doi:10.1126/sciadv.abf6707.
- 595 [19] A. C. Leskovjan, A. Lanzirotti, L. M. Miller, Amyloid plaques in  
596 PSAPP mice bind less metal than plaques in human Alzheimer's dis-  
597 ease, NeuroImage 47(2009) 1215–1220. doi:10.1016/j.neuroimage.  
598 2009.05.063.
- 599 [20] S. A. James, Q. I. Churches, M. D. de Jonge, I. E. Birchall, V. Streltsov,  
600 G. McColl, P. A. Adlard, D. J. Hare, Iron, Copper, and Zinc Concen-  
601 tration in  $A\beta$  Plaques in the APP/PS1 Mouse Model of Alzheimer's  
602 Disease Correlates with Metal Levels in the Surrounding Neuropil, ACS  
603 Chemical Neuroscience 8 (2017) 629–637. doi:10.1021/acscchemneuro.  
604 6b00362.
- 605 [21] A. C. Leskovjan, A. Kretlow, A. Lanzirotti, R. Barrea, S. Vogt, L. M.  
606 Miller, Increased brain iron coincides with early plaque formation in

- 607 a mouse model of Alzheimer's disease, *NeuroImage* 55 (2011) 32–38.  
608 doi:10.1016/j.neuroimage.2010.11.073.
- 609 [22] I. Alafuzoff, D. R. Thal, T. Arzberger, N. Bogdanovic, S. Al-Sarraj,  
610 I. Bodi, S. Boluda, O. Bugiani, C. Duyckaerts, E. Gelpi, S. Gentle-  
611 man, G. Giaccone, M. Graeber, T. Hortobagyi, R. Höftberger, P. Ince,  
612 J. W. Ironside, N. Kavantzias, A. King, P. Korkolopoulou, G. G.  
613 Kovács, D. Meyronet, C. Monoranu, T. Nilsson, P. Parchi, E. Patsouris,  
614 M. Pikkarainen, T. Revesz, A. Rozemuller, D. Seilhean, W. Schulz-  
615 Schaeffer, N. Streichenberger, S. B. Wharton, H. Kretzschmar, Assess-  
616 ment of  $\beta$ -amyloid deposits in human brain: A study of the Brain-  
617 Net Europe Consortium, *Acta Neuropathologica* 117 (2009) 309–320.  
618 doi:10.1007/s00401-009-0485-4.
- 619 [23] M. Knobloch, U. Konietzko, D. C. Krebs, R. M. Nitsch, Intracellular  
620  $A\beta$  and cognitive deficits precede  $\beta$ -amyloid deposition in transgenic  
621 arcA $\beta$  mice, *Neurobiology of Aging* 28 (2007) 1297–1306. doi:10.1016/  
622 j.neurobiolaging.2006.06.019.
- 623 [24] R. Radde, T. Bolmont, S. A. Kaeser, J. Coomaraswamy, D. Lindau,  
624 L. Stoltze, M. E. Calhoun, F. Jäggi, H. Wolburg, S. Gengler, C. Haass,  
625 B. Ghetti, C. Czech, C. Hölscher, P. M. Mathews, M. Jucker,  $A\beta$ 42-  
626 driven cerebral amyloidosis in transgenic mice reveals early and robust  
627 pathology, *EMBO reports* 7 (2006) 940–946. doi:10.1038/sj.embor.  
628 7400784.
- 629 [25] L. Mucke, E. Masliah, G.-Q. Yu, M. Mallory, E. M. Rockenstein, G. Tat-  
630 suno, K. Hu, D. Kholodenko, K. Johnson-Wood, L. McConlogue, High-  
631 Level Neuronal Expression of  $A\beta$ 1-42 in Wild-Type Human Amyloid  
632 Protein Precursor Transgenic Mice: Synaptotoxicity without Plaque  
633 Formation, *The Journal of Neuroscience* 20 (2000) 4050–4058. doi:10.  
634 1523/JNEUROSCI.20-11-04050.2000.
- 635 [26] R. M. Cohen, K. Rezai-Zadeh, T. M. Weitz, A. Rentsendorj, D. Gate,  
636 I. Spivak, Y. Bholat, V. Vasilevko, C. G. Glabe, J. J. Breunig, P. Rakic,  
637 H. Davtayan, M. G. Agadjanyan, V. Kepe, J. R. Barrio, S. Bannykh,  
638 C. A. Szekely, R. N. Pechnick, T. Town, A Transgenic Alzheimer Rat  
639 with Plaques, Tau Pathology, Behavioral Impairment, Oligomeric  $A\beta$ ,  
640 and Frank Neuronal Loss, *Journal of Neuroscience* 33 (2013) 6245–6256.  
641 doi:10.1523/JNEUROSCI.3672-12.2013.

bioRxiv preprint doi: <https://doi.org/10.1101/2022.09.27.509706>; this version posted March 30, 2023. The copyright holder for this preprint (which was not certified by peer review) is the author/funder, who has granted bioRxiv a license to display the preprint in perpetuity. It is made available under aCC-BY-NC-ND 4.0 International license.

- 642 [27] A. Åslund, C. J. Sigurdson, T. Klingstedt, S. Grathwohl, T. Bolmont,  
643 D. L. Dickstein, E. Glimsdal, S. Prokop, M. Lindgren, P. Konrads-  
644 son, D. M. Holtzman, P. R. Hof, F. L. Heppner, S. Gandy, M. Jucker,  
645 A. Aguzzi, P. Hammarström, K. P. R. Nilsson, Novel Pentameric Thio-  
646 phene Derivatives for in Vitro and in Vivo Optical Imaging of a Plethora  
647 of Protein Aggregates in Cerebral Amyloidoses, *ACS Chemical Biology*  
648 4 (2009) 673–684. doi:10.1021/cb900112v.
- 649 [28] T. Weitkamp, M. Scheel, J. Perrin, G. Daniel, A. King, L. Roux, V, J.-L.  
650 Giorgetta, A. Carcy, F. Langlois, K. Desjardins, C. Menneglier, M. Cer-  
651 ato, C. Engblom, G. Cauchon, T. Moreno, C. Rivard, Y. Gohon, F. Po-  
652 lack, Microtomography on the ANATOMIX beamline at Synchrotron  
653 SOLEIL, 2022. arXiv:2002.03242.
- 654 [29] A. Mirone, E. Brun, E. Gouillart, P. Tafforeau, J. Kieffer, The  
655 PyHST2 hybrid distributed code for high speed tomographic recon-  
656 struction with iterative reconstruction and a priori knowledge capa-  
657 bilities, *Nuclear Instruments and Methods in Physics Research Sec-  
658 tion B: Beam Interactions with Materials and Atoms* 324 (2014) 41–48.  
659 doi:10.1016/j.nimb.2013.09.030.
- 660 [30] D. Legland, I. Arganda-Carreras, P. Andrey, MorphoLibJ: Integrated  
661 library and plugins for mathematical morphology with ImageJ, *Bioin-  
662 formatics* (2016) btw413. doi:10.1093/bioinformatics/btw413.
- 663 [31] M. Toplak, S. T. Read, C. Sandt, F. Borondics, Quasar: Easy Ma-  
664 chine Learning for Biospectroscopy, *Cells* 10 (2021) 2300. doi:10.3390/  
665 cells10092300.
- 666 [32] P. Bassan, H. J. Byrne, F. Bonnier, J. Lee, P. Dumas, P. Gardner,  
667 Resonant Mie scattering in infrared spectroscopy of biological materials  
668 – understanding the ‘dispersion artefact’, *The Analyst* 134 (2009) 1586.  
669 doi:10.1039/b904808a.
- 670 [33] D. Röhr, B. D. C. Boon, M. Schuler, K. Kremer, J. J. M. Hoozemans,  
671 F. H. Bouwman, S. F. El-Mashtoly, A. Nabers, F. Großerueschkamp,  
672 A. J. M. Rozemuller, K. Gerwert, Label-free vibrational imaging of dif-  
673 ferent  $A\beta$  plaque types in Alzheimer’s disease reveals sequential events in  
674 plaque development, *Acta Neuropathologica Communications* 8 (2020)  
675 222. doi:10.1186/s40478-020-01091-5.

- 676 [34] V. Solé, E. Papillon, M. Cotte, P. Walter, J. Susini, A multiplatform  
677 code for the analysis of energy-dispersive X-ray fluorescence spectra,  
678 *Spectrochimica Acta Part B: Atomic Spectroscopy* 62 (2007) 63–68.  
679 doi:10.1016/j.sab.2006.12.002.
- 680 [35] K. L. Summers, N. Fimognari, A. Hollings, M. Kiernan, V. Lam, R. J.  
681 Tidy, D. Paterson, M. J. Tobin, R. Takechi, G. N. George, I. J. Pickering,  
682 J. C. Mamo, H. H. Harris, M. J. Hackett, A Multimodal Spectroscopic  
683 Imaging Method To Characterize the Metal and Macromolecular Con-  
684 tent of Proteinaceous Aggregates (“Amyloid Plaques”), *Biochemistry*  
685 56 (2017) 4107–4116. doi:10.1021/acs.biochem.7b00262.
- 686 [36] A. D. Surowka, M. Czyzycki, A. Ziomber-Lisiak, A. Migliori,  
687 M. Szczerbowska-Boruchowska, On 2D-FTIR-XRF microscopy – A  
688 step forward correlative tissue studies by infrared and hard X-ray ra-  
689 diation, *Ultramicroscopy* 232 (2022) 113408. doi:10.1016/j.ultramic.  
690 2021.113408.
- 691 [37] N. Gustavsson, A. Paulus, I. Martinsson, A. Engdahl, K. Medjoubi,  
692 K. Klementiev, A. Somogyi, T. Deierborg, F. Borondics, G. K. Gouras,  
693 O. Klementieva, Correlative optical photothermal infrared and X-ray  
694 fluorescence for chemical imaging of trace elements and relevant molec-  
695 ular structures directly in neurons, *Light: Science & Applications* 10  
696 (2021) 151. doi:10.1038/s41377-021-00590-x.
- 697 [38] M. Töpferwien, F. van der Meer, C. Stadelmann, T. Salditt, Correlative  
698 x-ray phase-contrast tomography and histology of human brain tissue  
699 affected by Alzheimer’s disease, *NeuroImage* 210 (2020) 116523. doi:10.  
700 1016/j.neuroimage.2020.116523.
- 701 [39] G. Di Fede, M. Catania, E. Maderna, R. Ghidoni, L. Benussi, E. Tonoli,  
702 G. Giaccone, F. Moda, A. Paterlini, I. Campagnani, S. Sorrentino,  
703 L. Colombo, A. Kubis, E. Bistaffa, B. Ghetti, F. Tagliavini, Molec-  
704 ular subtypes of Alzheimer’s disease, *Scientific Reports* 8 (2018) 1–14.  
705 doi:10.1038/s41598-018-21641-1.
- 706 [40] J. Rasmussen, J. Mahler, N. Beschorner, S. A. Kaeser, L. M. Häsler,  
707 F. Baumann, S. Nyström, E. Portelius, K. Blennow, T. Lashley, N. C.  
708 Fox, D. Sepulveda-Falla, M. Glatzel, A. L. Oblak, B. Ghetti, K. P. R.  
709 Nilsson, P. Hammarström, M. Staufenbiel, L. C. Walker, M. Jucker,

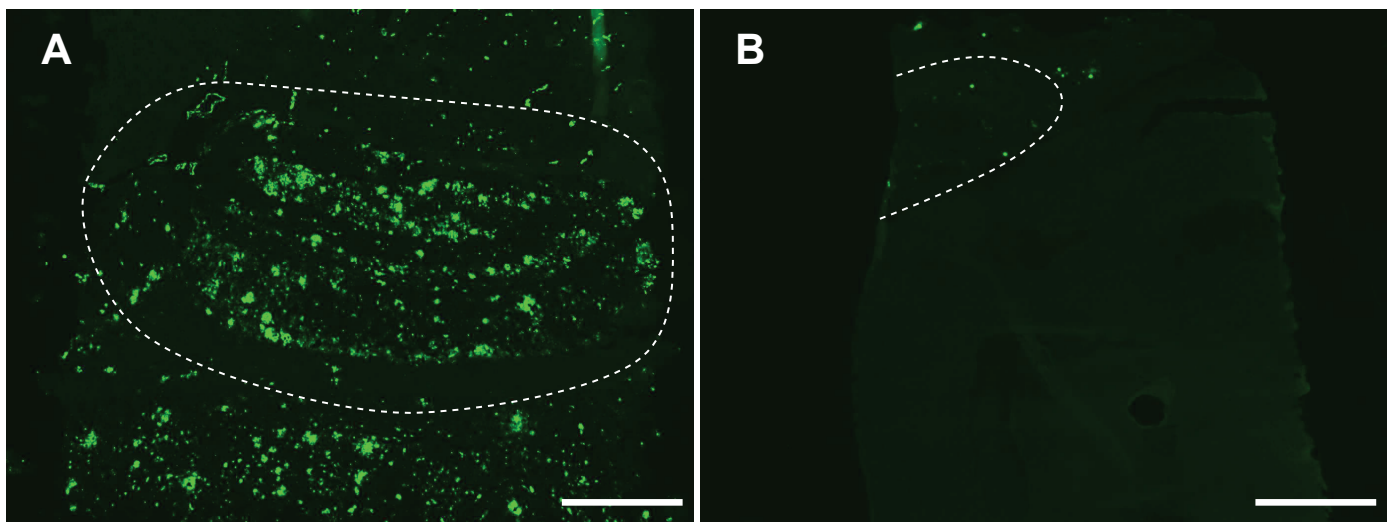
- 710 Amyloid polymorphisms constitute distinct clouds of conformational  
711 variants in different etiological subtypes of Alzheimer’s disease, *Pro-*  
712 *ceedings of the National Academy of Sciences* 114 (2017) 13018–13023.  
713 doi:10.1073/pnas.1713215114.
- 714 [41] D. J. Hare, J. K. Lee, A. D. Beavis, A. van Gramberg, J. George, P. A.  
715 Adlard, D. I. Finkelstein, P. A. Doble, Three-Dimensional Atlas of Iron,  
716 Copper, and Zinc in the Mouse Cerebrum and Brainstem, *Analytical*  
717 *Chemistry* 84 (2012) 3990–3997. doi:10.1021/ac300374x.
- 718 [42] M. Cruz-Alonso, B. Fernandez, A. Navarro, S. Junceda, A. Astudillo,  
719 R. Pereiro, Laser ablation ICP-MS for simultaneous quantitative imag-  
720 ing of iron and ferroportin in hippocampus of human brain tissues  
721 with Alzheimer’s disease, *Talanta* 197 (2019) 413–421. doi:10.1016/  
722 j.talanta.2019.01.056.
- 723 [43] M. Lovell, J. Robertson, W. Teesdale, J. Campbell, W. Markes-  
724 bery, Copper, iron and zinc in Alzheimer’s disease senile plaques,  
725 *Journal of the Neurological Sciences* 158 (1998) 47–52. doi:10.1016/  
726 S0022-510X(98)00092-6.
- 727 [44] X. Zhu, T. W. Victor, A. Ambi, J. K. Sullivan, J. Hatfield, F. Xu,  
728 L. M. Miller, W. E. Van Nostrand, Copper accumulation and the ef-  
729 fect of chelation treatment on cerebral amyloid angiopathy compared  
730 to parenchymal amyloid plaques, *Metallomics* 12 (2020) 539–546.  
731 doi:10.1039/c9mt00306a.
- 732 [45] D. W. Dekens, P. J. W. Naudé, J. N. Keijser, A. S. Boerema, P. P.  
733 De Deyn, U. L. M. Eisel, Lipocalin 2 contributes to brain iron dysreg-  
734 ulation but does not affect cognition, plaque load, and glial activation  
735 in the J20 Alzheimer mouse model, *Journal of Neuroinflammation* 15  
736 (2018) 330. doi:10.1186/s12974-018-1372-5.
- 737 [46] B. Sullivan, G. Robison, Y. Pushkar, J. K. Young, K. F. Manaye, Copper  
738 accumulation in rodent brain astrocytes: A species difference, *Journal of*  
739 *Trace Elements in Medicine and Biology* 39 (2017) 6–13. doi:10.1016/  
740 j.jtemb.2016.06.011.
- 741 [47] E. Drummond, T. Kavanagh, G. Pires, M. Marta-Ariza, E. Kan-  
742 shin, S. Nayak, A. Faustin, V. Berdah, B. Ueberheide, T. Wisniewski,

- 743 The amyloid plaque proteome in early onset Alzheimer's disease and  
744 Down syndrome, *Acta Neuropathologica Communications* 10 (2022) 53.  
745 doi:10.1186/s40478-022-01356-1.
- 746 [48] E. Tsolaki, L. Csincsik, J. Xue, I. Lengyel, S. Bertazzo, Nuclear and  
747 cellular, micro and nano calcification in Alzheimer's disease patients  
748 and correlation to phosphorylated Tau, *Acta Biomaterialia* 143 (2022)  
749 138–144. doi:10.1016/j.actbio.2022.03.003.
- 750 [49] G. E. Barbone, A. Bravin, A. Mittone, A. Pacureanu, G. Mascio,  
751 P. Di Pietro, M. J. Kraiger, M. Eckermann, M. Romano, M. Hrabě  
752 de Angelis, P. Cloetens, V. Bruno, G. Battaglia, P. Coan, X-ray mul-  
753 tiscale 3D neuroimaging to quantify cellular aging and neurodegener-  
754 ation postmortem in a model of Alzheimer's disease, *European Jour-  
755 nal of Nuclear Medicine and Molecular Imaging* (2022). doi:10.1007/  
756 s00259-022-05896-5.
- 757 [50] C. L. Walsh, P. Tafforeau, W. L. Wagner, D. J. Jafree, A. Bellier, C. Wer-  
758 lein, M. P. Kühnel, E. Boller, S. Walker-Samuel, J. L. Robertus, D. A.  
759 Long, J. Jacob, S. Marussi, E. Brown, N. Holroyd, D. D. Jonigk, M. Ack-  
760 ermann, P. D. Lee, Imaging intact human organs with local resolution of  
761 cellular structures using hierarchical phase-contrast tomography, *Nature  
762 Methods* 18 (2021) 1532–1541. doi:10.1038/s41592-021-01317-x.

bioRxiv preprint doi: <https://doi.org/10.1101/2022.09.27.509706>; this version posted March 30, 2023. The copyright holder for this preprint (which was not certified by peer review) is the author/funder, who has granted bioRxiv a license to display the preprint in perpetuity. It is made available under aCC-BY-NC-ND 4.0 International license.

## Supplemental Document — Why are amyloid- $\beta$ plaques detected by X-ray phase-contrast imaging? Role of metals revealed through combined synchrotron infrared and X-ray fluorescence microscopies

Matthieu Chourrout, Christophe Sandt, Timm Weitkamp, Tanja Dučić, David Meyronet, Thierry Baron, Jan Klohs, Nicolas Rama, Hervé Boutin, Shifali Singh, Cécile Olivier, Marlène Wiart, Emmanuel Brun, Sylvain Bohic, Fabien Chauveau



Supplemental Figure 1: Fluorescence microscopy images of p-FTAA-stained sections of a TgF344 rat brain (A) and a J20 mouse brain (B), near hippocampus (shown with dotted line). Both sections were acquired with the same exposure time and rendered with the same value range. One can notice the p-FTAA staining reveals more diffuse structures in the rat brain. Scale bars equal 1000  $\mu\text{m}$ .

### A Extra parameters for synchrotron experiments

| Numerical parameter                     | Values: | Session #1 | Session #2   |
|---|---------|------------|--------------|
| Undulator gap (mm)                      |         | 11.7       | 9.7          |
| Exposure time per projection (ms)       |         | 200        | 50           |
| Gold filter thickness ( $\mu\text{m}$ ) |         | 20         | 20           |
| Detector-to-sample distance (cm)        |         | 113        | 30           |
| Magnification                           |         | 1 $\times$ | 2.1 $\times$ |
| Projection pixel size ( $\mu\text{m}$ ) |         | 6.5        | 3.09         |
| Number of projections                   |         | 2600       | 4000         |
| Weight of unsharp mask filter           |         | 0.5        | 0.5          |
| Radius of unsharp mask filter (px)      |         | 2          | 2            |
| $\delta/\beta$ for Paganin filtering    |         | 1525       | 1400         |

Supplemental Table 1: Acquisition and reconstruction parameters for XPCT (ANATOMIX) per session

bioRxiv preprint doi: <https://doi.org/10.1101/2022.09.27.509706>; this version posted March 30, 2023. The copyright holder for this preprint (which was not certified by peer review) is the author/funder, who has granted bioRxiv a license to display the preprint in perpetuity. It is made available under aCC-BY-NC-ND 4.0 International license.

| Parameter      | Value                |
|----------------|----------------------|
| Mode           | Dual aperture        |
| Apodization    | Strong Norton & Beer |
| Objective type | Schwarzschild        |

| Numerical parameter                      | Value          |
|--|----------------|
| Spectral resolution ( $\text{cm}^{-1}$ ) | 4              |
| Zero-fill factor                         | 2              |
| Aperture size ( $\mu\text{m}^2$ )        | $10 \times 10$ |
| Co-addition                              | 256            |
| Objective numerical aperture             | 0.65           |
| Objective magnification                  | 32             |

Supplemental Table 2: Acquisition parameters for  $\mu\text{FTIR}$  (SMIS)

| Parameter | Value            |
|-----------|------------------|
| Mode      | Flyscan – zigzag |

| Numerical parameter                        | Value            |
|--|------------------|
| Aperture size ( $\mu\text{m}^2$ )          | $100 \times 100$ |
| Piezoelectric motor step ( $\mu\text{m}$ ) | 0.3              |
| Exposure time per position (ms)            | 80               |

Supplemental Table 3: Acquisition parameters for  $\mu\text{XRF}$  (NANOSCOPIUM)

## 6 B Scanning the same positions on SMIS and NANOSCOPIUM

Scanning the same positions on SMIS and NANOSCOPIUM was crucial to associate the FTIR and XRF measures. However, beamtimes were two weeks apart and required different sample holders and orientations. To overcome this challenge, two coordinate systems  $\mathcal{S} := (O, A, B, C)_{\text{FTIR}}$  and  $\mathcal{S}' := (O, A, B, C)_{\text{XRF}}$  were created using the inner corners of the membrane, so that the new points  $p'_i(x'_i, y'_i)$  were obtained from  $p_i(x_i, y_i)$  by solving

$$\begin{bmatrix} -x_O & -y_O & -1 & 0 & 0 & 0 & x_O x'_O & y_O x'_O & x'_O \\ 0 & 0 & 0 & -x_O & -y_O & -1 & x_O y'_O & y_O y'_O & y'_O \\ -x_A & -y_A & -1 & 0 & 0 & 0 & x_A x'_A & y_A x'_A & x'_A \\ 0 & 0 & 0 & -x_A & -y_A & -1 & x_A y'_A & y_A y'_A & y'_A \\ -x_B & -y_B & -1 & 0 & 0 & 0 & x_B x'_B & y_B x'_B & x'_B \\ 0 & 0 & 0 & -x_B & -y_B & -1 & x_B y'_B & y_B y'_B & y'_B \\ -x_C & -y_C & -1 & 0 & 0 & 0 & x_C x'_C & y_C x'_C & x'_C \\ 0 & 0 & 0 & -x_C & -y_C & -1 & x_C y'_C & y_C y'_C & y'_C \\ 0 & 0 & 0 & 0 & 0 & 0 & 0 & 0 & 1 \end{bmatrix} \begin{bmatrix} h_1 \\ h_2 \\ h_3 \\ h_4 \\ h_5 \\ h_6 \\ h_7 \\ h_8 \\ h_9 \end{bmatrix} = \begin{bmatrix} 0 \\ 0 \\ 0 \\ 0 \\ 0 \\ 0 \\ 0 \\ 0 \\ 1 \end{bmatrix} \quad (1)$$

then

$$\begin{bmatrix} x'_i/\lambda \\ y'_i/\lambda \\ \lambda \end{bmatrix} = \overbrace{\begin{bmatrix} h_1 & h_2 & h_3 \\ h_4 & h_5 & h_6 \\ h_7 & h_8 & h_9 \end{bmatrix}}^H \begin{bmatrix} x_i \\ y_i \\ 1 \end{bmatrix} \quad (2)$$

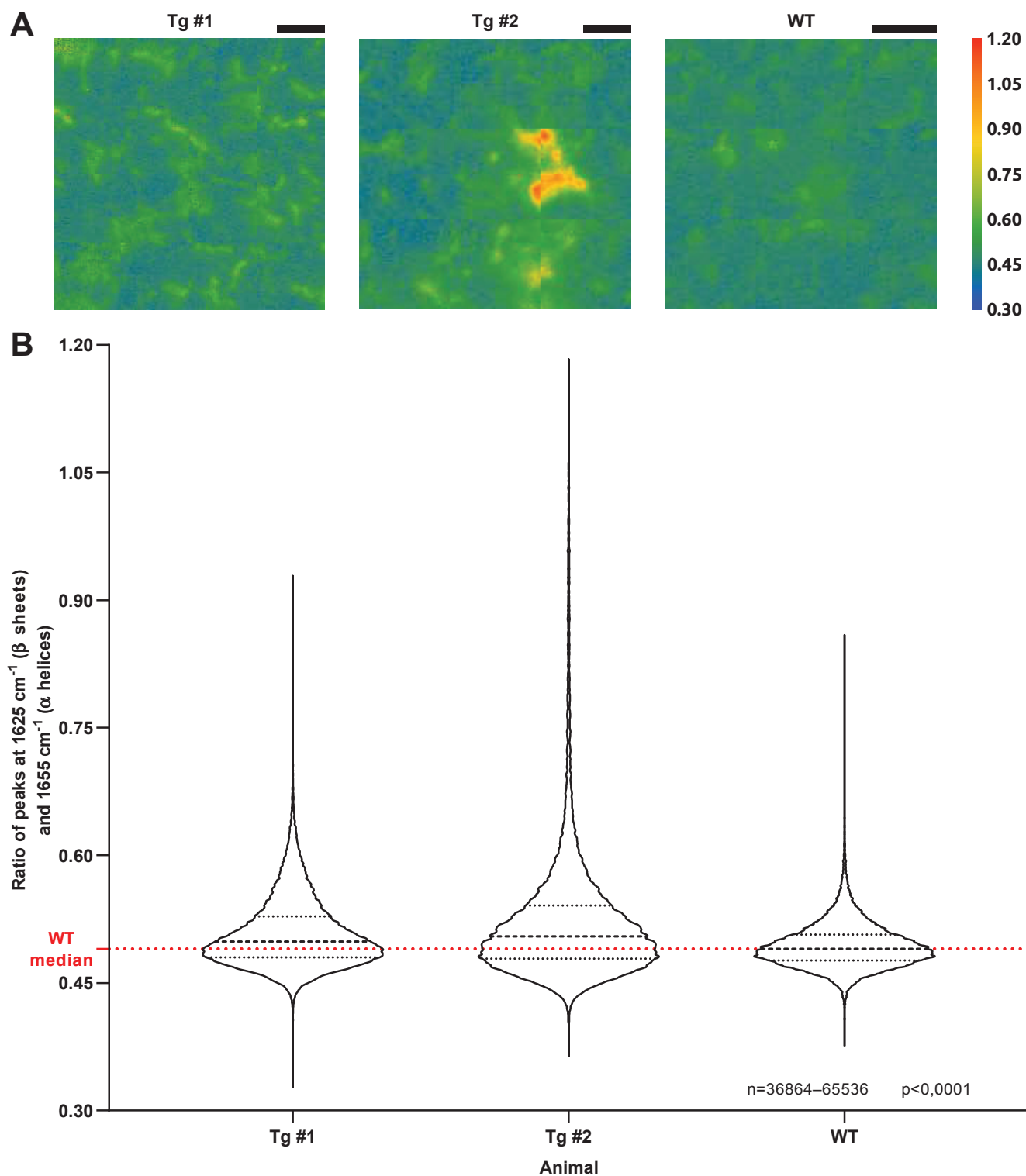
where  $H$  is the homography matrix and  $\lambda$  is a factor.

bioRxiv preprint doi: <https://doi.org/10.1101/2022.09.27.509706>; this version posted March 30, 2023. The copyright holder for this preprint (which was not certified by peer review) is the author/funder, who has granted bioRxiv a license to display the preprint in perpetuity. It is made available under aCC-BY-NC-ND 4.0 International license.

## 13 C Measures at ALBA synchrotron (Barcelona, Spain)

14 Large-field FTIR images were obtained using a  $64 \times 64$  px full-field focal plane array (FPA) detector cooled with liquid  
15 nitrogen. Images were taken by FPA detector on areas of  $210 \times 210 \mu\text{m}^2$  with 128 accumulated spectra per point at  
16  $8 \text{ cm}^{-1}$  spectral resolution and  $10 \mu\text{m}$  pixel size. The spectra were background-corrected using extracellular regions  
17 close to the tissue. From each IR image, the total absorbance cartogram was generated by integrating at specific  
18 peaks in amide I area ( $1600 \text{ cm}^{-1}$ – $1700 \text{ cm}^{-1}$ ), i.e. the ratio of peaks characteristic for  $\beta$ -sheet structures absorbing at  
19  $1625 \text{ cm}^{-1}$  and  $\alpha$ -helix structures assigned at  $1655 \text{ cm}^{-1}$  (Supplemental Figure 2).

bioRxiv preprint doi: <https://doi.org/10.1101/2022.09.27.509706>; this version posted March 30, 2023. The copyright holder for this preprint (which was not certified by peer review) is the author/funder, who has granted bioRxiv a license to display the preprint in perpetuity. It is made available under aCC-BY-NC-ND 4.0 International license.



Supplemental Figure 2: (A) FPA-FTIR maps of the  $\beta$ -sheet content within the hippocampus and (B) measures from TgF344 rats (Tg #1 and Tg #2) and a wild-type rat (WT), acquired at ALBA synchrotron. Mean and standard deviation of Tg #1:  $0.508 \pm 0.041$ ; Tg #2:  $0.523 \pm 0.078$ ; WT:  $0.494 \pm 0.026$ . Scale bars equal 50  $\mu\text{m}$ .

### 5.3. Discussion

In this article, we analyzed the composition of amyloid- $\beta$  plaques, which can be seen with label-free XPCT, in order to determine what makes them stand out from the parenchyma.

We submitted a three-beamline proposal at SOLEIL, the French synchrotron facility, for access to XPCT on the ANATOMIX beamline,  $\mu$ FTIR on the SMIS beamline and  $\mu$ XRF on the NANOSCOPIUM beamline. Experiments took place in November 2020 (XPCT) and March–April 2021 (FTIR & XRF). We acquired samples from AD patients ( $n_{\text{humans}} = 2$ ) and from AD rodent models ( $n_{\text{rodents,AD}} = 12$  and  $n_{\text{rodents,control}} = 2$ ).

The sample preparation was highly discussed when designing the study. The overall consensus in the community is that the elemental analysis of fresh-frozen tissues — brain or frozen-hydrated cells — is the gold standard method for elemental imaging; it is preferable to avoid chemical fixation/perfusion of brain tissues that are reported to disrupt the binding environment of metals, thus enabling their migration and preventing precise/reliable localisation and concentration determination [354]. Hence, following our literature overview, our choice was to separate brain hemispheres, with one part being fixed for whole-brain 3D imaging, and the other part being frozen, cut, and dried without fixation to perform XRF under recommended practices. The XRF-assessed disruption of *in vivo* metal distribution after fixation has been demonstrated on brain sections at the *cellular* or *sub-cellular* scale [355, 356]; in the case of *3D imaging of a whole block* (XPCT), the pixel size was  $3\ \mu\text{m}$  and the effective spatial resolution (not measured) was even higher. So the effect on labile and mobile metallic ions might not be as critical as for XRF. The main disadvantage of using fixed tissue for XPCT is that it hampered a correlative study between the three modalities.

Upon normalization with the total protein content, Leskovjan, Lanzirotti, and Miller [196] showed that Fe and Cu content in the plaques is actually lower than the surrounding neuropil in the APPPS1 mouse, raising the question whether animal models are accurate for AD metallomics. We do not have accurate XRF data outside of the A $\beta$  plaques because our

field of view (FOV) was small and centered on the inclusions — spectra outside of the plaques were extracted for demonstration purposes in the Supplemental Material. We chose to acquire the XRF data at a high resolution (pixel size of 100 nm) for a higher sensitivity but we wonder whether a resolution closer to that of FTIR (pixel size of 10  $\mu\text{m}$ ) and XPCT (isotropic voxel size of 3  $\mu\text{m}$ ) would have been more appropriate. Note that we reported elemental mass fractions in  $\mu\text{g g}^{-1}$  or ppm (“parts per million”) using PyMca [311] for curve fitting and extraction and standard reference materials (SRMs) for calibration. These measures match previous articles [100, 357]; reporting these measures as (normalized) counts is also possible — as shown in Figure 7 and Suppl. Figure 1\* of the article — but they would then require to be weighted with respect to relative intensities of the lines [311]. During the calibration process, one must assume a thickness of dried tissue and a corresponding density: we chose respectively 1  $\mu\text{m}$  (an empirical value for 7  $\mu\text{m}$ -thick frozen slices) and 1.04  $\text{g cm}^{-3}$  (for human tissue, from Stedman and Spyrou [359]). Measures for element analysis are also frequently reported as area densities in  $\text{ng cm}^{-2}$  [99, 360]; but this conversion from our data would require the same assumptions of homogeneous sample thickness and homogeneous density.

\*: This Suppl. Figure 1 is part on the final published version [358].

Our data supports the role of metals in the detection of  $\text{A}\beta$  plaques from rodent models: object intensities and sizes\* match between XRF and XPCT. However, the hypodense rims around  $\text{A}\beta$  plaques in the APPPS1 and Arc $\text{A}\beta$  mouse strains remain unexplained. The density of the tissue may be altered around  $\text{A}\beta$  inclusions because of continuous interaction with  $\text{A}\beta$  oligomers or with the immune cells — adapted histochemistry or density measurements with a compatible technique (because of fixation) might guide us. This could also be an edge effect of the Paganin filter — either the Paganin length could be fine-tuned or we could shift towards an alternative without the mono-material assumption, e.g. another phase-sensitive setup [263, 361] or a new phase-retrieval algorithm [362].

\*: Figure 8, supporting the matching sizes, is part on the final published version [358].

Töpperwien et al. [236] identified mineralized  $\text{A}\beta$  plaques enriched in calcium (Ca) in XPCT images. In our literature review, a Ca accumulation in  $\text{A}\beta$  plaques is only reported in a few studies [125, 196, 216, 363, 364] as it would be associated to rare co-pathologies [365, 366, 367]. Nevertheless, these

results highlight the role of the co-localized accumulation of metals for the detection of A $\beta$  plaques. Still, the intracellular Ca disruption because of A $\beta$  oligomers is well established [368, 369, 370] — the Ca levels are higher in AD neurons, and more specifically in the mitochondria.

We chose to focus our analysis on Cu-Zn-Fe and on the ratio between  $\beta$  sheets and  $\alpha$  helices in the amide region. However, the hyperspectra we acquired at NANOSCOPIUM and SMIS contain information about other elements and other functional groups. This data can be further analyzed, e.g. to assess the load of aluminium (Al) or Ca from XRF, or the lipid content from FTIR.



# Cohort study of human cerebral amyloid angiopathy with XPCT

# 6.

## Article draft with preliminary results

This chapter is a draft of an article for the cohort study of human cerebral amyloid angiopathy with XPCT. Preliminary results are shown and discussed but — contrary to the previous studies — this work has not been peer-reviewed nor submitted as a preprint.

## 6.1. Introduction

Cerebral amyloid angiopathy (CAA) is a cerebrovascular disease with an accumulation of  $A\beta$  peptides. This accumulation in the walls of the blood vessels leads to haemorrhages within a wide range of severity — from microbleeds [164] to larger ischemic areas [371] —, but only for a subgroup of people [372]. The onset of most dementia, including Alzheimer’s disease, has been linked with cerebrovascular diseases [165, 197, 373]; in particular, a recent meta-analysis by Jäkel et al. [374] concluded that almost half (47.5 %) of AD patients had CAA. Most of the affected vessels have a diameter inferior to 100  $\mu\text{m}$ ; gas exchanges are maximized in vessels of this size [375] but the  $A\beta$  deposits impair their activity. The topology of the disease usually starts from the meningeal arteries (cf. Figure 1.3): the perforating arterioles are severely affected in the cortical gray matter; but the disease is only rarely present in the underlying white matter. CAA can be detected indirectly with *in vivo* MRI because of microbleeds (cf. Figure 1.12) [164] or other hallmarks such as enlarged Virchow–Robin spaces [376]. The Boston criteria — introduced in 1995 by Greenberg et al. [377] and modified in 2010 [378] and 2022 [379] — associate MRI with the clinical history of the patient to classify between possible (low chances) and probable (higher chances) CAA. However, the diagnosis is only confirmed upon autopsy: histology will reveal the  $A\beta$  deposits in the walls of blood vessels. These  $A\beta$  deposits are enriched in  $A\beta_{1-40}$  peptides; they are also stained with anti- $A\beta$  antibodies, although  $A\beta$  plaques from AD are enriched in  $A\beta_{1-42}$  peptides. Amyloid- $\beta$  plaques have been widely studied with x-ray phase-contrast imaging since 2006, both in AD models

|       |   |     |
|-------|---|-----|
| 6.1   | Introduction . . .                        | 153 |
| 6.2   | Material & Methods . . . . .              | 154 |
| 6.2.1 | Cohort selection . .                      | 154 |
| 6.2.2 | Immunohistochemistry . . . . .            | 154 |
| 6.2.3 | Sample preparation                        | 156 |
| 6.2.4 | X-ray phase-contrast tomography . . . . . | 156 |
| 6.2.5 | XPCT image analysis . . . . .             | 158 |
| 6.3   | Preliminary results                       | 159 |
| 6.3.1 | CAA hallmark detection . . . . .          | 159 |
| 6.3.2 | Watershed-based segmentation . . . .      | 160 |
| 6.3.3 | Machine learning segmentation . . . .     | 161 |
| 6.4   | Discussion . . . . .                      | 161 |

To get familiar with the human brain anatomy, one can refer to the [Human Brain Atlas](#) [137, 138, 139] on EBRAINS.

[210, 230, 231, 232, 233, 234, 235, 236, 237, 238] and in AD patients [236]. Furthermore, XPCT enables high-resolution 3D angiography [190, 298, 380, 381, 382, 383, 384, 385, 386, 387] — sometimes using gas (CO<sub>2</sub>, microbubbles or ambient air) to improve the contrast between the vessel lumen and the neuropil [388, 389, 390]. The vascular network has been extensively studied in pathological conditions with standard CT, both *in vivo* for medical procedures [391, 392, 393] and *postmortem* for diagnosis [394]; however, it was rarely studied with phase-contrast imaging [234, 395]. In this study, we built a cohort of human CAA patients to determine whether XPCT can detect the hallmarks of the disease by virtual histology. The images were reviewed by a clinical expert. The semi-automatic analysis is work in progress: preliminary segmentation results are shown and discussed; a few metrics are also proposed.

## 6.2. Material & Methods

### 6.2.1. Cohort selection

Patients with different stages of CAA have been identified ( $n = 11$ ) based on the previous histopathological diagnosis (following the routine protocol described in subsection 6.2.2). The clinical information and patient details are shown in Table 6.1. The Thal–Braak staging [37] indicates which brain regions exhibit CAA, ranging from 0 to 3 (cf. Figure 6.1). The Vonsattel score [167] indicates the severity of the CAA at the local scale: mild (1) – intermediate (2) – severe (3). The Thal–Braak type [396] indicates whether there is a cortical capillary A $\beta$  deposition: type 1 if present, type 2 otherwise. Concomittant AD scores are also reported (see table caption).

### 6.2.2. Immunohistochemistry

Immunohistochemistry (IHC) was performed within the eastern neuropathology department of Hospices Civils de Lyon according to the diagnosis routine [397]. One hemisphere per brain was fixed into buffered formalin (10%) for a few days, cut into thick slices for sampling, dehydrated and paraffin-embedded. The paraffin block was cut into 2 to

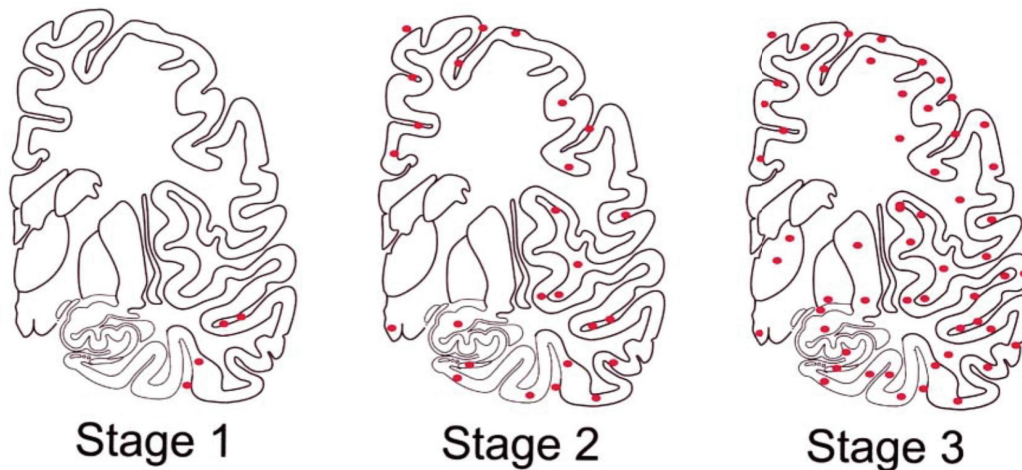


**Figure 6.1.:** Schematic representation of CAA stages in a coronary section through the human brain at the level of the basal ganglia. CAA changes are indicated in red. The first stage of CAA shows vascular A $\beta$  deposits only in a few neocortical areas and involves leptomeningeal and cortical vessels. Stage 2 is characterized by additional vascular A $\beta$  in the hippocampus, amygdala, hypothalamus, midbrain, and in the cerebellum; midbrain and cerebellum are not shown in this figure. In stage 3, CAA is also seen in vessels of the basal ganglia, the thalamus, and the basal forebrain. A $\beta$  deposition in the lower brainstem, another feature of CAA stage 3, is not depicted. Adapted from [37].

**Table 6.1.:** Overview of the cohort with patient ID, age in years at death and histopathological scorings for CAA and AD. CAA scorings are: Thal–Braak stages for regional assessment [37], Vonsattel score for local severity [167] and Thal–Braak type for capillary involvement [396]. AD scorings are in the same order as for the NIA–AA "ABC" descriptors [3]: A $\beta$  Thal phases [182], CERAD score for neuritic plaques (NP) [181] and Braak stages for neurofibrillary tangles (NFT) [184]. F: female; M: male; N/A: not applicable.

✕: rare familial case also studied in Chapter 5;

†: patient without CAA nor AD, with mild tauopathy;

‡: patient without CAA nor AD, diagnosed with Parkinson's disease.

| Patient ID | Age | Sex | CAA   |       |      | AD        |    |      |
|------------|-----|-----|-------|-------|------|-----------|----|------|
|            |     |     | Stage | Score | Type | A $\beta$ | NP | NFT  |
| 16EH01503✕ | 51  | M   | 3     | 3     | 1    | 5         | 3  | VI   |
| 07EH02463  | 52  | M   | 2     | 1     | 1    | 0         | 1  | +    |
| 11EH04091  | 82  | F   | 1     | 1     | 2    | 5         | 3  | V    |
| 11EH09214  | 71  | F   | 3     | 3     | 1    | 4         | 2  | III  |
| 13EJ00001  | 66  | M   | 3     | 1–2   | 2    | 1         | 0  | II   |
| 13EJ00002  | 74  | F   | 2     | 1     | 2    | 0         | 0  | III  |
| 13EJ00003  | 78  | M   | 1     | 1     | 2    | 2         | 3  | V    |
| 16EH08800  | 70  | F   | 2     | 2     | 2    | 3         | 2  | III  |
| 22EH19267  | 60  | M   | 1     | 1     | 1    | 5         | 3  | VI   |
| 12EJ00010† | 54  | M   | 0     | N/A   | N/A  | 0         | 0  | III  |
| 20EH08599‡ | 82  | M   | 0     | N/A   | N/A  | 0         | 0  | None |

4  $\mu$ m-thick slices, which were put on glass slides and stained with:

- ▶ Anti-A $\beta$  A4 antibodies for A $\beta$  load;
- ▶ Anti-phosphorylated-tau antibodies for neurofibrillary

- tangles (NFTs) and P-tau-positive neuritic plaques;
- ▶ Luxol fast blue and periodic acid-Schiff (PAS) stains for myelin and glycogen-rich bodies.

The stained slices were digitalised with a slide scanner (Leica APERIO AT2) and scorings were performed prior to the cohort selection.

### 6.2.3. Sample preparation

The samples were obtained from Tissu-Tumorotheque Est Biobank (CRB-Hospices Civils de Lyon), authorized by the French Ministry of Research (authorizations DC2008-72 & AC2015-2576). The samples were free from prion disease.

As shown in Figure 6.1, the frontal cortex exhibits CAA for all CAA stages 1, 2 and 3 [37]; the cerebellum region has been chosen to differentiate CAA stage 1 from 2 and 3: the cerebellum does not exhibit CAA in CAA stage 1 [37]. For each patient, 2 samples per region were cut from a frozen brain slice into blocks of  $\sim 1 \text{ cm}^3$ . Unfortunately, a few regions were not available because the frozen slices had already been transferred to the national brain bank. Paraffin-embedded samples were also available for one patient.

Samples were kept frozen at  $-80^\circ\text{C}$ . They were unfrozen at room temperature (RT) to be processed. They were immersed overnight in 4% formaldehyde for fixation at  $4^\circ\text{C}$ . They were dehydrated in a series of ethanol baths with increasing concentrations (25%, 25%, 50%, 50%, 75%, 75%, 96%, 96%) for 5 min each. They were put in plastic tubes with a 1 cm-diameter, filled with 96% ethanol; in case they did not fit in the tubes after dehydration, they were cut into smaller pieces. The plastic tubes were stored at RT.

The whole collection is summarized in Table 6.2.

### 6.2.4. X-ray phase-contrast tomography

The XPCT data was acquired at the ANATOMIX beamline [398] of the synchrotron radiation facility SOLEIL (Gif-sur-Yvette, France), within the scope of the proposal #20220319. The formaldehyde-fixed, ethanol-dehydrated samples and a few paraffin-embedded samples were scanned with a pink beam of mean energy 22 keV and a detector pixel size of

| Patient ID             | CAA stage | Number of samples |            |
|------------------------|-----------|-------------------|------------|
|                        |           | Frontal cortex    | Cerebellum |
| 16EH01503 <sup>✕</sup> | 3         | 1                 | 0          |
| 07EH02463              | 2         | 2                 | 0          |
| 11EH04091              | 1         | 3                 | 2          |
| 11EH09214              | 3         | 2                 | 2          |
| 13EJ00001              | 3         | 2                 | 2          |
| 13EJ00002              | 2         | 2                 | 2          |
| 13EJ00003              | 1         | 3                 | 3          |
| 16EH08800 <sup>#</sup> | 2         | 3                 | 1          |
| 22EH19267              | 1         | 1                 | 2          |
| 12EJ00010 <sup>†</sup> | 0         | 2                 | 2          |
| 20EH08599 <sup>‡</sup> | 0         | 1                 | 1          |

**Table 6.2.:** Summary of the samples per patient and per region. The CAA Thal-Braak stage [37] for regional assessment is recalled here for each patient.

<sup>✕</sup>: rare familial case also studied in Chapter 5;

<sup>#</sup>: 2 paraffin-embedded frontal cortex samples from this patient were also scanned;

<sup>†</sup>: patient without CAA nor AD, with mild tauopathy;

<sup>‡</sup>: patient without CAA nor AD, diagnosed with Parkinson’s disease.

6.5  $\mu\text{m}$ . The detector system consisted of a lutetium aluminum garnet (LuAG,  $\text{Lu}_3\text{Al}_5\text{O}_{12}$ ) single-crystal scintillator (600  $\mu\text{m}$  thick) coupled to a CMOS camera (Hamamatsu Orca Flash 4.0 V2,  $2048 \times 2048$  pixels) via a 1.45 : 1.45 lens system consisting of two photo objectives in tandem geometry; this resulted in a magnification of  $2.1\times$  and a projected pixel size of 3.1  $\mu\text{m}$ . Decentered half-acquisitions were performed [399] for the field of view (FOV) to encompass the whole width of the tube at this higher magnification; when it was not needed, standard acquisitions were performed. Complete acquisition parameters are reported in Table 6.3.

| Numerical parameter                     | Values      |
|---|-------------|
| Undulator gap (mm)                      | 9.7         |
| Exposure time per projection (ms)       | 50          |
| Gold filter thickness ( $\mu\text{m}$ ) | 20          |
| Sample-to-detector distance (cm)        | 30          |
| Magnification                           | $2.1\times$ |
| Projection pixel size ( $\mu\text{m}$ ) | 3.09        |
| Number of projections                   | 4000        |
| Weight of unsharp mask filter           | 0.5         |
| Radius of unsharp mask filter (px)      | 2           |
| $\delta/\beta$ for Paganin filtering    | 1400        |

**Table 6.3.:** Acquisition and reconstruction parameters for XPCT

For reconstruction using PyHST2 [271], we set the Paganin length parameter to 216.65  $\mu\text{m}$  ( $\delta/\beta = 1400$ ). We used a motion blur correction algorithm and an unsharp mask filter ( $C_{unsharp} = 0.5$ ,  $\sigma_{unsharp} = 2$  px). 3D volumes from standard acquisitions were  $2048 \times 2048 \times 2048$  px<sup>3</sup>; those from half-acquisitions were  $3348 \times 3348 \times 2048$  px<sup>3</sup>,  $3448 \times 3448 \times 2048$  px<sup>3</sup>

or  $3548 \times 3548 \times 2048 \text{ px}^3$ . The data was reconstructed with a single-float precision (32 bits). It was then converted linearly to unsigned-short-integer precision (16 bits) from the range 0.1 to 0.6 (inferior and superior values were set respectively to 0 and  $2^{16} - 1 = 65535$ ); this range was determined empirically.

### 6.2.5. XPCT image analysis

Ring artifacts were removed using an in-house tool implemented by the company NOVITOM (France; <https://www.novitom.com/en/>) [190].

Scans were examined in 3D and with free-orientation slices (using a cubic interpolation) by a clinical neuropathologist. The software for examination was either Thermo Scientific Amira 2022.3 (ThermoFisher Scientific, USA; <https://www.thermofisher.com>) or Dragonfly 2022.2 for Windows (Object Research Systems (ORS) Inc, Canada; <http://www.theobjects.com/dragonfly>). Two to three perforating arterioles per volume were extracted with a mask under his supervision. For one patient (the familial case #16EH01503), one extracted vessel was segmented semi-automatically with a watershed filter in Amira, into a multi-class label between parenchyma (background), vessel wall, vessel lumen and perivascular spaces.

Preliminary machine learning (ML) trials in Dragonfly were performed. The machine learning algorithms were trained with both raw images and Frangi-3D-filtered images [327], on 3 labeled slices; two of the slices were adjacent to improve the training with 3D features. Two different ML architectures were compared: a random forest [400] and a U-Net [401]. Dragonfly internally uses the class `RandomForestClassifier` from Scikit-learn [403, 404] for its random forest architecture and Keras [405] / TensorFlow 2 [406, 407] for its U-Net architecture.

To get a grasp on ML algorithms, one can refer to the review by Latif et al. [402].

Signal intensity measurements, tortuosity and volume were retrieved with Amira.

## 6.3. Preliminary results

### 6.3.1. CAA hallmark detection

While 3D browsing through the cortical samples, a few hallmarks of cerebrovascular diseases were identified (cf. Figure 6.2). Hemosiderin and enlarged perivascular spaces are shared biomarkers among cerebrovascular diseases. However, double barreling is specific to CAA: the vessel walls get thicker because of the  $A\beta$  burden and the layers of smooth muscle cells progressively disappear. The variations in the signal intensity of the vessel walls suggest that we can detect the  $A\beta$  deposits: their distribution is usually heterogeneous. Note that the patient 16EH01503 has unexplained brighter-than-usual vessels in XPCT images, unless this is a phenotype of the familial AD of the patient (cf. Figure 6.3).

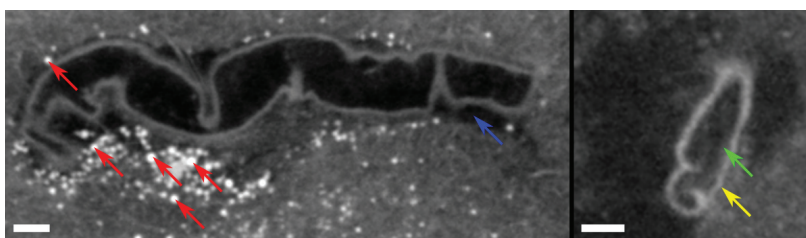


**Figure 6.2.:** Vascular disease hallmarks found while browsing through the XPCT volume. Left: large blood vessel in the cortex surrounded by a high concentration of hemosiderin (red arrows) with a locally-enlarged perivascular space (blue arrow) in patient 13EJ00001. Right: artery in a fissure towards a sulcus presenting double barreling (green and yellow arrows) and variations in the vessel wall intensity from patient 16EH01503. Scale bars equal 100  $\mu\text{m}$ .

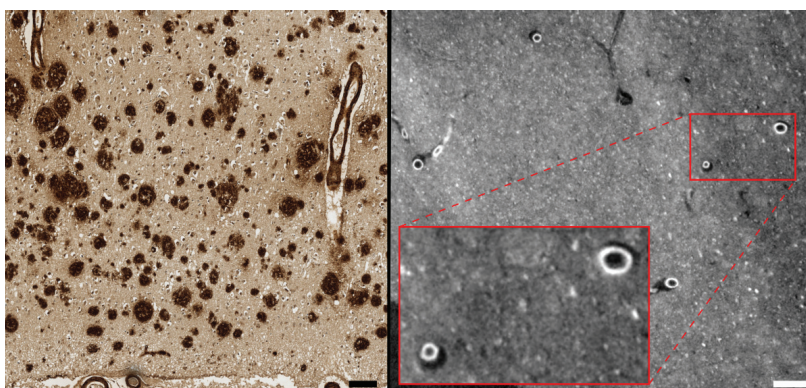


**Figure 6.3.:** Immunohistochemistry with anti- $A\beta_{1-42}$  antibodies (left) and raw XPCT images (right) from the patient 16EH01503. Scale bars equal 100  $\mu\text{m}$ .

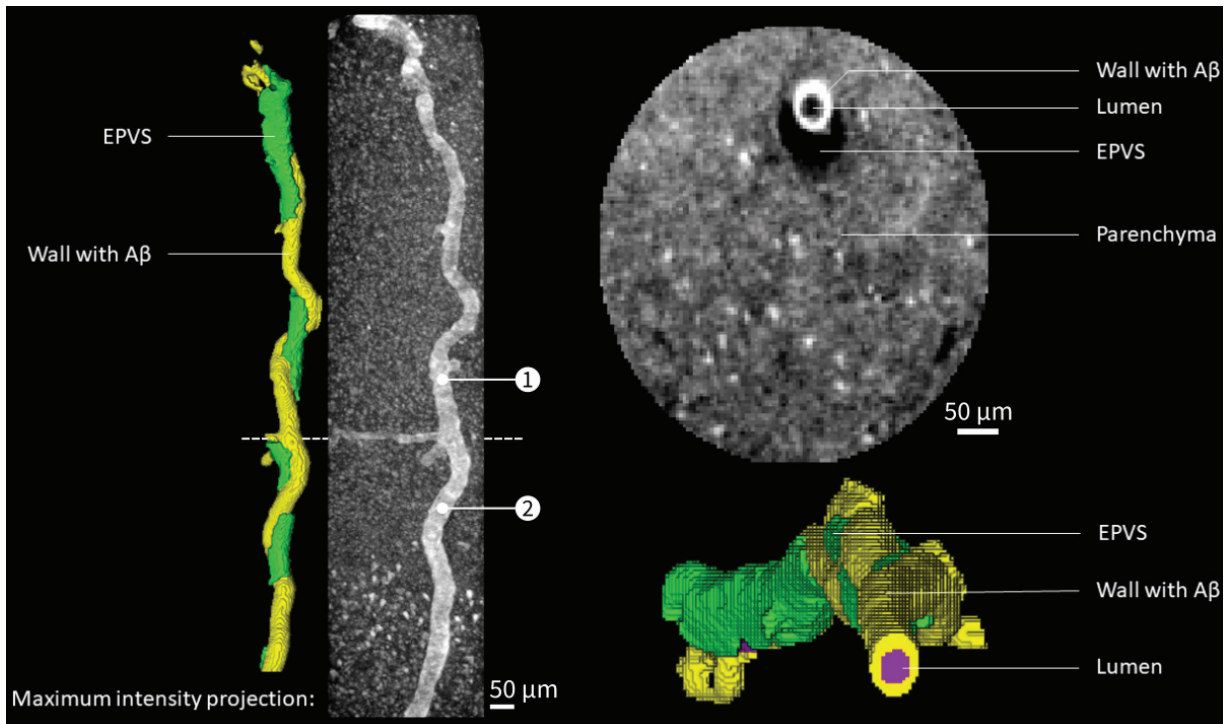


**Figure 6.4.:** Results from watershed-based segmentation on a large vessel from patient 16EH01503. Measurements on segments with labels 1 and 2 are shown in Table 6.4.

### 6.3.2. Watershed-based segmentation

The watershed-based segmentation of a vessel from the patient 16EH01503 is shown in Figure 6.4. Per-segment metrics are shown in Table 6.4. In this sub-volume, the segmented EPVS had a total volume of  $1\,622\,345\ \mu\text{m}^3$ . The signal intensities of EPVS were  $20\,774(958)$  (mean $\pm$ standard deviation, arbitrary units), those of the lumen were  $21\,410(963)$  and those of the vessel walls were  $25\,690(1260)$ . Multiple definitions exist for tortuosity, the computation implemented in Amira is the ratio between curved length and straight length. This watershed-based segmentation was performed on raw XPCT images using a simple gradient as topography input; the topography input could be an image filtered with 3D Frangi.

**Table 6.4.:** Extracted metrics per segment of the segmented vessel from patient 16EH01503. Tortuosity is the ratio between curved length and straight length (not reported). Labels 1 and 2 refer to Figure 6.4.

| Segment | Curved length ( $\mu\text{m}$ ) | Tortuosity | Mean inner radius ( $\mu\text{m}$ ) |
|---------|---------------------------------|------------|-------------------------------------|
| 1       | 1395                            | 1.21       | 9.1                                 |
| 2       | 1098                            | 1.25       | 6.0                                 |

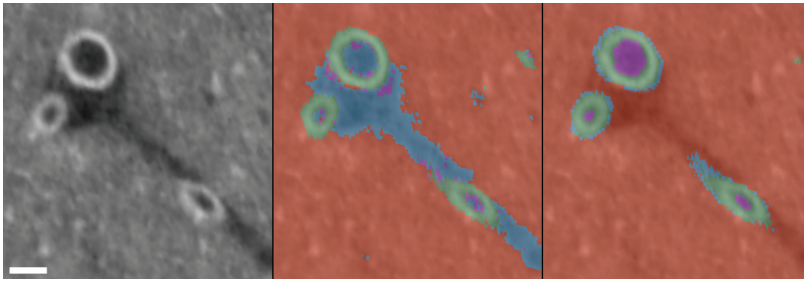


**Figure 6.5.:** Comparative segmentation of a slice with machine learning algorithms. Left: raw XPCT image. Middle: output with a random forest algorithm. Right: output with a U-Net. The parenchyma class is in red, the EPVS class in blue, the vessel wall class in green and the lumen class in purple. Scale bar equals 50  $\mu\text{m}$ .

### 6.3.3. Machine learning segmentation

A comparison between two architectures for machine learning was performed. Results outside of the training set are shown in Figure 6.5. The random forest architecture cannot differentiate EPVS from the lumen. The U-Net architecture did not properly learn the features of EPVS but the lumen and the blood vessel are correctly segmented. A more elaborate training is required.

## 6.4. Discussion

This cohort of CAA patients is of great value towards the assessment of the clinical potential of XPCT. Among the features of the cohort, different levels of CAA severity were available and a sub-group had both AD and CAA while another sub-group was AD-free, along with two controls (neither AD nor CAA). We also obtained a sample from a rare familial AD case (< 5 % of total AD cases), which exhibited a peculiar contrast for all blood vessel walls; in a previous study (cf. Chapter 5 on page 111), we also reported that this patient had detectable  $A\beta$  plaques in the parenchyma. Extensive scoring was fully performed prior to the selection and samples from two regions were collected: the frontal cortex and the cerebellum.

According to our previous study, metals enable the detection of parenchymal plaques. Blood vessels with CAA may have higher levels of copper (3-fold) and zinc (2-fold or more) than parenchymal plaques [408]. Building upon our results from the previous Chapter with respect to metal levels, this suggests we should be able to detect the  $A\beta$  deposits.

The preliminary results showed the limits of the designed segmentation pipelines. The genetic AD case had vessel walls with a very specific signal intensity. This was helpful for semi-automatic watershed-based segmentation. This could not be applied directly to other patients because the signal intensities were homogeneous with the parenchyma. However, as suggested, a Frangi 3D filter can provide the necessary "topology". Other vessel-enhancement filters [409] could be tested such as the Sato vesselness filter [410].

The random forest algorithm was able to segment the lumen and the EPVS separately in the training set, but not in the test set (a few slices away from the training set): this result highlighted the overfitting limit. The U-Net algorithm failed to segment EPVS: it learnt properly that EPVS were located around the vessels, but the signal intensity was not identified as an important feature. The machine learning approach could be extended with the tUbeNet software [411], an open-source Python script using a 3D convolutional neural network pre-trained on datasets from optical imaging, CT and photoacoustic imaging, which was shared on GitHub (<https://github.com/natalie11/tUbeNet>).

Subsequent work on this dataset ought to introduce 3D-based scoring methods that would corroborate with classical 2D histology at different scales. The proposed metrics — tortuosity, inner radius, signal intensities, EPVS volume — need to be optimized and compared between patients. The EPVS volume should be normalized, eventually with the outer diameter of the vessel. The mean vessel wall thickness could be computed as the difference between the mean inner and outer diameters. A method to locally assess the signal intensities would be better than an overall measurement — each vessel could be subdivided, either along its length (e.g. every few pixels) or along its section (e.g. into 4 equal parts of 90° each), or a mix of both methods.

Hemosiderin and double-barreling were identified by our clinical expert; they need to be confirmed with correlative histology. This could be performed on the paraffin blocks from the patient 16EH08800 — or on other scanned samples which could be embedded into paraffin — in order to keep the block orientation and ease pairing. Or the samples could be cleared using the CLARITY system — which is compatible with fixed tissue — and imaged with light-sheet microscopy, with staining for amyloid- $\beta$  deposits, vessel walls and hemosiderin —

hemosiderin can be stained with Prussian blue [412, 413].

This cohort of *ex vivo* human CAA samples can provide original 3D data — which are lost with 2D histology —, but it requires the development of a set of aforementioned techniques and software.



# SYNTHESIS



We will discuss a few developments following the results of the thesis, regarding multi-scale imaging, multi-modal imaging and standardization.

## 7.1. Multi-scale imaging

Among recent advances in XPCT, multi-scale imaging is promising. Indeed, in our studies, we have opted for a trade-off between resolution and the size of the generated data: most of our data was acquired at effective pixel sizes of 3 to 6  $\mu\text{m}$  for a final size of 30 to 50 GB (in 16 bit-format). These pixel sizes were chosen empirically. In the study by Walsh et al. [298], they used a multi-scale approach they called Hierarchical Phase-Contrast Tomography (HiP-CT). A whole human brain was scanned in agarose first with 25  $\mu\text{m}$ , then a subvolume within the cerebellar region was selected and scanned again automatically at 6.5  $\mu\text{m}$  and 2.5  $\mu\text{m}$  — the same strategy was applied to one kidney and two lungs. Along with the achievement about whole-organ imaging (following the aforementioned preparation protocol [334]), they performed quantitative assessments over a large number of objects such as Purkinje cells.

## 7.2. Multi-modal imaging

The work by Johnson et al. [414] associated high-resolution *postmortem* MRI in the skull with light-sheet microscopy (outside of the skull, after clearing) thanks to a specialized registration pipeline they shared on GitHub ([https://github.com/YuqiTianCIVM/MRH\\_LSM\\_registration](https://github.com/YuqiTianCIVM/MRH_LSM_registration)), which could be applied to XPCT. Image registration was not fully investigated during our project, although a wide spectrum of techniques have been developed [415]. This new type of multi-modality goes even beyond simple registration, because it paves the way towards what is called physics-informed machine learning [416]: instead of the sole data-driven machine learning, complex physics or mathematical models can be

given as inputs alongside multi-modal data to get model-accurate results [417].

### 7.3. Standardization

Standardizing the acquisition and reconstruction would ensure the reproducibility of most experiments. Standardizing the acquisition requires a thorough reporting of the settings — e.g. with the NeXus file format [418] — and a common sample preparation protocol — a few protocols have been published [332, 334] and we are preparing a manuscript to that extent with new data. Standardizing the reconstruction processing requires the wide adoption of shared free (open-source) software. A final, crucial step is the ability to easily share data: the neuroimaging community has developed the Brain Imaging Data Structure (BIDS) [419, 420], a data structure that is modality-agnostic and embeds both raw and processed data; BIDS specifications for electroencephalography (EEG), magnetoencephalography (MEG) and MRI have been released and other imaging techniques are to be included — this could be an opportunity for reconstructed XPCT data.

# Conclusion & perspectives

# 8.

This PhD thesis focused on Alzheimer's Disease, the most frequent dementia in the world. Although biomarkers have been identified and associated with the different evidences of the pathological mechanisms —  $A\beta$ , P-tau and the neurodegeneration —, the diagnosis of the disease is performed *postmortem* by a neuropathologist after a laborious process of sampling, slicing and staining. A formerly large set of different neuropathological scorings were pooled ten years ago into an ABC score but it still requires the analysis of microscope slides with three different stainings. Using XPCT, our goal was to advance towards a contrast-agent-free 3D imaging technique for AD *ex vivo* diagnosis. Four studies were reported in this manuscript; corresponding highlights are recalled thereafter.

## 8.1. Methodological contributions

Contributions include sample preparation, software development and data analysis.

### 8.1.1. Sample preparation

In the first study, we optimized the already-known sample preparation by fixation-dehydration for XPCT through a progressive process.

### 8.1.2. Software development

In the first study, we implemented a tool for image-derived orientation extraction with our private collaborators from NOVITOM. An open-source version of the XPCT-derived fiber-tracking technique is being developed.

### 8.1.3. Data analysis

In the first study, we created an AMIRA pipeline for medium-fiber extraction; this processing method and the one by NOVITOM retrieved the volume ratio of fibers and DTI-like parametric maps which were understandable metrics for the neuroscience community. During the second study, we compiled and shared a segmentation pipeline with user-friendly open-source software for the 3D morphological analysis of blob-like objects. For the third study, we combined heterogeneous data from 2D and 3D techniques to correlate molecular and elemental imaging with our label-free technique. The fourth study was a collaborative effort towards the clinical characterization of a cohort of patients with XPCT, that will serve as a proof of concept.

## 8.2. Results provided by this work

Our first results highlighted the role of myelin for the analysis of white-matter tracts in fixed, dehydrated samples. They also demonstrated the feasibility of orientation extraction and lesion assessment with XPCT.

Our second study revealed the 3D morphological differences of A $\beta$  plaques from transgenic strains which develop amyloidosis.

In our third study, we discovered the strong differences of biometal accumulation between two human AD cases and 4 different AD models. We unveiled the ability of XPCT to detect A $\beta$  plaques in a familial AD case. We could link the XPCT signal directly to the metal accumulation in the A $\beta$  plaques.

The data of the fourth study is already acquired: 50 samples were fully scanned and the analysis of the blood vessel network is ongoing.

Paraffin-embedded samples or cleared samples could be studied for correlative analysis. Our collaboration with the local biobank could continue to study other dementia.

### 8.3. Limitations of the studies

Our first and second studies were based on 3 animals per model: we demonstrated the potential of XPCT but larger cohorts would be required for significant assessment. Nevertheless, large numbers of A $\beta$  plaques were segmented.

In our third study, a compatible setup for XPCT such as cryo-CT would have produced a unique dataset: the samples would have been prepared with the same protocol and the same objects would have been scanned with the three techniques — XPCT, FTIR and XRF —, enabling a truly correlative study.

For our fourth study, we need to improve the training of our machine learning algorithms to create an automatic pipeline and process the  $\sim 100$  extracted vessels of interest.



# APPENDIX



# List of publications

# A.

1. Chourrout M, Rositi H, Ong E, Hubert V, Paccalet A, Foucault L, Autret A, Fayard B, Olivier C, Bolbos R, Peyrin F, Crola-da-Silva C, Meyronet D, Raineteau O, Elleaume H, Brun E, Chauveau F, and Wiart M. Brain Virtual Histology with X-ray Phase-Contrast Tomography Part I: Whole-Brain Myelin Mapping in White-Matter Injury Models. *Biomed Opt Express*. 2022 Mar 1; 13  
Co-first author with Rositi H.
2. Chourrout M, Roux M, Boisvert C, Gislard C, Legland D, Arganda-Carreras I, Olivier C, Peyrin F, Boutin H, Rama N, Baron T, Meyronet D, Brun E, Rositi H, Wiart M, and Chauveau F. Brain Virtual Histology with X-ray Phase-Contrast Tomography Part II: 3D Morphologies of Amyloid- $\beta$  Plaques in Alzheimer's Disease Models. *Biomed Opt Express*. 2022 Mar 1; 13  
First author.
3. Dumot C, Po C, Capin L, Hubert V, Ong E, Chourrout M, Bolbos R, Amaz C, Auxenfans C, Canet-Soulas E, Rome C, Chauveau F, and Wiart M. Neurofunctional and Neuroimaging Readouts for Designing a Preclinical Stem-Cell Therapy Trial in Experimental Stroke. *Sci Rep*. 2022 Mar 18; 12
4. Chourrout M, Sandt C, Weitkamp T, Dučić T, Meyronet D, Baron T, Klohs J, Rama N, Boutin H, Singh S, Olivier C, Wiart M, Brun E, Bohic S, and Chauveau F. Virtual Histology of Alzheimer's Disease: Biometal Entrapment within Amyloid- $\beta$  Plaques Allows for Detection via X-ray Phase-Contrast Imaging. *Acta Biomaterialia*. 2023; 170  
First author.
5. Balcaen T, Piens C, Mwema A, Chourrout M, Vandebroek L, Des Rieux A, Chauveau F, De Borggraeve WM, Hoffmann D, and Kerckhofs G. Revealing the Three-Dimensional Murine Brain Microstructure by Contrast-Enhanced Computed Tomography. *Front Neurosci*. 2023 Mar 23; 17. pmid: [37034159](https://pubmed.ncbi.nlm.nih.gov/37034159/)



## List of oral communications

# B.

1. Chourrout M. Brain Virtual Histology with X-ray Phase-Contrast Tomography. Parallel Session. European Molecular Imaging Meeting 2021 (Göttingen, Germany). 2021 Aug 26
2. Chourrout M. Why Do We See Amyloid- $\beta$  Plaques in Phase-Contrast Imaging? Parallel Session. European Molecular Imaging Meeting 2022 (Thessaloniki, Greece). 2022 Mar 17
3. Chourrout M. Virtual Histology of Brain Pathologies: Crucial Impact of Sample Preparation Techniques. Oral Presentation. World Molecular Imaging Congress 2022 (Miami, FL, USA). 2022 Oct 1
4. Chourrout M. Why Do We See Amyloid- $\beta$  Plaques in Phase-Contrast Imaging? Oral Presentation. SOLEIL User Meeting 2023 (Saint-Aubin, France). 2023 Jan 20
5. Chourrout M. Virtual Histology of Human Cerebral Amyloid Angiopathy. Study Group Meeting. European Molecular Imaging Meeting 2023 (Salzburg, Austria). 2023 Mar 14



**Curriculum vitae**

**C.**

# MATTHIEU CHOURROUT

PhD Student at Lyon Neuroscience Research Center (CRNL)

 [orcid.org/0000-0002-2282-6976](https://orcid.org/0000-0002-2282-6976)  [linkedin.com/in/matthieu-chourrout](https://www.linkedin.com/in/matthieu-chourrout)  27 years old (born in 1996)



## EXPERIENCE

PhD Student in Neuro-Imaging

**Lyon Neuroscience Research Center (CRNL)**

 October 2020 – September 2023  Lyon, France

Virtual histology of Alzheimer's disease using synchrotron-radiation phase-contrast x-ray imaging

4 publications and 1 preprint, 4 oral communications in international meetings

Research Engineer in Medical Imaging

**NanoBRAIN project from CREATIS & CarMeN laboratories**

 October 2019 – September 2020  Lyon, France

Synchrotron-radiation phase-contrast x-ray imaging: measurement of white matter anisotropy within mouse brain

Teaching Assistant in Signal Processing

**Claude Bernard University Lyon 1**

 January 2020 – September 2023  Lyon, France

Courses for audio signal processing at Polytech Lyon (engineering school) and ISTR (audioprothesist diploma)

Internship: Research Engineer

**GE Healthcare, Women's Health Advanced Research team**

 February – August 2019  Buc, France

Validation of an x-ray image simulation tool for 2D and 3D breast imaging

Internship: Image Processing for Quality Control

**Leica Microsystems, R&D Department**

 June – August 2018  Wetzlar, Germany

Automatic measurement of chromatic optical errors for microscope lenses through image analysis

## EDUCATION

PhD in Neuro-Imaging

**Claude Bernard University Lyon 1**

 October 2020 – September 2023  Lyon, France

Master of Science in Engineering – Physics & Optics

**Institut d'Optique Graduate School – Paris-Saclay University**

 2016 – 2019  Paris, France

Master of Science in Signal Processing

**Université de Bordeaux**

 2018 – 2019  Bordeaux, France

## STRENGTHS & SKILLS

Hard-working Attention to detail

Curious International mobility

Physics Neuropathologies

Image processing Medical imaging

MATLAB C++ Python

## LANGUAGES

French Native

English TOEIC® L&R 970/990

Spanish Limited working proficiency

## INTERESTS

 **Singing**  
in a choir

 **Acting classes**  
since 2021

 **Rowing**  
on the Saône river

## CERTIFICATIONS

 **Certified Rescuer – French Red Cross**  
for volunteer activities

 **Language Course for Japanese –**  
Toho International College

# Bibliography

Here are the references in citation order.

1. 2023 Alzheimer's Disease Facts and Figures. *Alzheimer's & Dementia*. 2023 Apr; 19:1598–695. doi: [10.1002/alz.13016](https://doi.org/10.1002/alz.13016). [Accessed on: 2023 Apr 26] (cited on pages 5, 7)
2. Reisberg B. Functional Assessment Staging (FAST). *Psychopharmacol Bull*. 1988; 24:653–9 (cited on page 5)
3. Jack CR, Bennett DA, Blennow K, Carrillo MC, Dunn B, Haeberlein SB, Holtzman DM, Jagust W, Jessen F, Karlawish J, Liu E, Molinuevo JL, Montine T, Phelps C, Rankin KP, Rowe CC, Scheltens P, Siemers E, Snyder HM, Sperling R, Contributors, Elliott C, Masliah E, Ryan L, and Silverberg N. NIA-AA Research Framework: Toward a Biological Definition of Alzheimer's Disease. *Alzheimer's & Dementia*. 2018 Apr; 14:535–62. doi: [10.1016/j.jalz.2018.02.018](https://doi.org/10.1016/j.jalz.2018.02.018). [Accessed on: 2023 Apr 26] (cited on pages 5, 6, 155)
4. Hampel H, Cummings J, Blennow K, Gao P, Jack CR, and Vergallo A. Developing the ATX(N) Classification for Use across the Alzheimer Disease Continuum. *Nat Rev Neurol*. 2021 Sep; 17:580–9. doi: [10.1038/s41582-021-00520-w](https://doi.org/10.1038/s41582-021-00520-w). [Accessed on: 2023 Oct 29] (cited on page 5)
5. Jack CR, Knopman DS, Jagust WJ, Petersen RC, Weiner MW, Aisen PS, Shaw LM, Vemuri P, Wiste HJ, Weigand SD, Lesnick TG, Pankratz VS, Donohue MC, and Trojanowski JQ. Tracking Pathophysiological Processes in Alzheimer's Disease: An Updated Hypothetical Model of Dynamic Biomarkers. *The Lancet Neurology*. 2013 Feb; 12:207–16. doi: [10.1016/S1474-4422\(12\)70291-0](https://doi.org/10.1016/S1474-4422(12)70291-0). [Accessed on: 2021 Aug 16] (cited on pages 5, 13, 18, 22)
6. Gordon BA, Blazey TM, Su Y, Hari-Raj A, Dincer A, Flores S, Christensen J, McDade E, Wang G, Xiong C, Cairns NJ, Hassenstab J, Marcus DS, Fagan AM, Jack CR, Hornbeck RC, Paumier KL, Ances BM, Berman SB, Brickman AM, Cash DM, Chhatwal JP, Correia S, Förster S, Fox NC, Graff-Radford NR, la Fougère C, Levin J, Masters CL, Rossor MN, Salloway S, Saykin AJ, Schofield PR, Thompson PM, Weiner MM, Holtzman DM, Raichle ME, Morris JC, Bateman RJ, and Benzinger TLS. Spatial Patterns of Neuroimaging Biomarker Change in Individuals from Families with Autosomal Dominant Alzheimer's Disease: A Longitudinal Study. *The Lancet Neurology*. 2018 Mar; 17:241–50. doi: [10.1016/S1474-4422\(18\)30028-0](https://doi.org/10.1016/S1474-4422(18)30028-0). [Accessed on: 2023 Apr 6] (cited on page 5)
7. Duyckaerts C. Neurodegenerative Lesions: Seeding and Spreading. *Revue Neurologique*. 2013 Oct; 169:825–33. doi: [10.1016/j.neurol.2013.07.018](https://doi.org/10.1016/j.neurol.2013.07.018). [Accessed on: 2023 May 15] (cited on pages 6, 12)

8. Hauw JJ, Haik S, and Duyckaerts C. La transconformation protéique, nouveau paradigme en neurologie. *Revue Neurologique*. 2015 Dec; 171:825–31. doi: [10.1016/j.neurol.2015.09.010](https://doi.org/10.1016/j.neurol.2015.09.010). [Accessed on: 2023 Apr 6] (cited on pages 6, 12, 14)
9. Kang YJ, Diep YN, Tran M, and Cho H. Therapeutic Targeting Strategies for Early-to Late-Staged Alzheimer's Disease. *IJMS*. 2020 Dec 16; 21:9591. doi: [10.3390/ijms21249591](https://doi.org/10.3390/ijms21249591). [Accessed on: 2023 Jun 21] (cited on page 7)
10. Gouilly D, Rafiq M, Nogueira L, Salabert AS, Payoux P, Péran P, and Pariente J. Beyond the Amyloid Cascade: An Update of Alzheimer's Disease Pathophysiology. *Revue Neurologique*. 2023 Mar :S0035378723008706. doi: [10.1016/j.neurol.2022.12.006](https://doi.org/10.1016/j.neurol.2022.12.006). [Accessed on: 2023 Apr 6] (cited on pages 7, 11)
11. Rajan KB, Weuve J, Barnes LL, McAninch EA, Wilson RS, and Evans DA. Population Estimate of People with Clinical Alzheimer's Disease and Mild Cognitive Impairment in the United States (2020–2060). *Alzheimer's & Dementia*. 2021 Dec; 17:1966–75. doi: [10.1002/alz.12362](https://doi.org/10.1002/alz.12362). [Accessed on: 2023 Apr 28] (cited on page 7)
12. Bacigalupo I, Mayer F, Lacorte E, Di Pucchio A, Marzolini F, Canevelli M, Di Fiandra T, and Vanacore N. A Systematic Review and Meta-Analysis on the Prevalence of Dementia in Europe: Estimates from the Highest-Quality Studies Adopting the DSM IV Diagnostic Criteria. *JAD*. 2018 Dec 12; 66. Ed. by Bruni AC:1471–81. doi: [10.3233/JAD-180416](https://doi.org/10.3233/JAD-180416). [Accessed on: 2023 Dec 15] (cited on page 7)
13. World Health Organization. The Global Dementia Observatory Reference Guide. Technical documents. Geneva, Switzerland: World Health Organization, 2018 :74 p. (Cited on page 7)
14. Yip AG, Brayne C, and Matthews FE. Risk Factors for Incident Dementia in England and Wales: The Medical Research Council Cognitive Function and Ageing Study. A Population-Based Nested Case–Control Study. *Age and Ageing*. 2006 Mar 1; 35:154–60. doi: [10.1093/ageing/afj030](https://doi.org/10.1093/ageing/afj030). [Accessed on: 2023 Apr 28] (cited on page 8)
15. James BD, Weuve J, Jackson JW, and Blacker D. "Alcohol Intake." The AlzRisk Database. Alzheimer Research Forum. (Cited on page 8)
16. Koyama A, Weuve J, Jackson JW, and Blacker D. "Dietary Pattern." The AlzRisk Database. Alzheimer Research Forum. (Cited on page 8)
17. Arasaratnam M, Weuve J, Koyama A, Sheu YH, Jackson JW, and Blacker D. "Physical Activity." The AlzRisk Database. Alzheimer Research Forum. (Cited on page 8)
18. Bertram L, McQueen MB, Mullin K, Blacker D, and Tanzi RE. Systematic Meta-Analyses of Alzheimer Disease Genetic Association Studies: The AlzGene Database. *Nat Genet*. 2007 Jan; 39:17–23. doi: [10.1038/ng1934](https://doi.org/10.1038/ng1934). [Accessed on: 2023 Apr 28] (cited on pages 8, 9)

19. Zigman WB, Devenny DA, Krinsky-McHale SJ, Jenkins EC, Urv TK, Wegiel J, Schupf N, and Silverman W. Chapter 4 Alzheimer's Disease in Adults with Down Syndrome. *International Review of Research in Mental Retardation*. Vol. 36. Elsevier, 2008 :103–45. doi: [10.1016/S0074-7750\(08\)00004-9](https://doi.org/10.1016/S0074-7750(08)00004-9). [Accessed on: 2023 Apr 21] (cited on page 8)
20. Cohen AD, Head E, and Lee JH. Alzheimer's Disease in Aging Down Syndrome. *Develop Neurobiol*. 2019 Jul; 79:611–2. doi: [10.1002/dneu.22717](https://doi.org/10.1002/dneu.22717). [Accessed on: 2023 Apr 21] (cited on page 8)
21. Mutations Database. Alzheimer Research Forum. Available from: <https://www.alzforum.org/mutations> [Accessed on: 2023 Apr 3] (cited on page 8)
22. De Strooper B, Iwatsubo T, and Wolfe MS. Presenilins and Gamma-Secretase: Structure, Function, and Role in Alzheimer Disease. *Cold Spring Harbor Perspectives in Medicine*. 2012 Jan 1; 2:a006304–a006304. doi: [10.1101/cshperspect.a006304](https://doi.org/10.1101/cshperspect.a006304). [Accessed on: 2023 May 23] (cited on page 8)
23. Cheng-Hathaway PJ, Reed-Geaghan EG, Jay TR, Casali BT, Bemiller SM, Puntambekar SS, Von Saucken VE, Williams RY, Karlo JC, Moutinho M, Xu G, Ransohoff RM, Lamb BT, and Landreth GE. The Trem2 R47H Variant Confers Loss-of-Function-like Phenotypes in Alzheimer's Disease. *Mol Neurodegeneration*. 2018 Dec; 13:29. doi: [10.1186/s13024-018-0262-8](https://doi.org/10.1186/s13024-018-0262-8). [Accessed on: 2023 May 12] (cited on page 8)
24. Jonsson T, Stefansson H, Steinberg S, Jonsdottir I, Jonsson PV, Snaedal J, Bjornsson S, Huttenlocher J, Levey AI, Lah JJ, Rujescu D, Hampel H, Giegling I, Andreassen OA, Engedal K, Ulstein I, Djurovic S, Ibrahim-Verbaas C, Hofman A, Ikram MA, Van Duijn CM, Thorsteinsdottir U, Kong A, and Stefansson K. Variant of *TREM2* Associated with the Risk of Alzheimer's Disease. *N Engl J Med*. 2013 Jan 10; 368:107–16. doi: [10.1056/NEJMoa1211103](https://doi.org/10.1056/NEJMoa1211103). [Accessed on: 2023 May 12] (cited on page 8)
25. Corder EH, Saunders AM, Strittmatter WJ, Schmechel DE, Gaskell PC, Small GW, Roses AD, Haines JL, and Pericak-Vance MA. Gene Dose of Apolipoprotein E Type 4 Allele and the Risk of Alzheimer's Disease in Late Onset Families. *Science*. 1993 Aug 13; 261:921–3. doi: [10.1126/science.8346443](https://doi.org/10.1126/science.8346443). [Accessed on: 2023 Apr 28] (cited on page 9)
26. Hyman BT, Phelps CH, Beach TG, Bigio EH, Cairns NJ, Carrillo MC, Dickson DW, Duyckaerts C, Frosch MP, Masliah E, Mirra SS, Nelson PT, Schneider JA, Thal DR, Thies B, Trojanowski JQ, Vinters HV, and Montine TJ. National Institute on Aging-Alzheimer's Association Guidelines for the Neuropathologic Assessment of Alzheimer's Disease. *Alzheimer's & Dementia*. 2012 Jan; 8(1):1–13. doi: [10.1016/j.jalz.2011.10.007](https://doi.org/10.1016/j.jalz.2011.10.007). [Accessed on: 2020 Aug 4] (cited on pages 9, 27, 28)
27. Noguchi-Shinohara M and Ono K. The Mechanisms of the Roles of  $\alpha$ -Synuclein, Amyloid- $\beta$ , and Tau Protein in the Lewy Body Diseases: Pathogenesis, Early Detection, and Therapeutics. *IJMS*. 2023 Jun 17; 24:10215. doi: [10.3390/ijms241210215](https://doi.org/10.3390/ijms241210215). [Accessed on: 2023 Jul 2] (cited on page 9)

28. Wüllner U, Borghammer P, Choe Cu, Csoti I, Falkenburger B, Gasser T, Lingor P, and Riederer P. The Heterogeneity of Parkinson's Disease. *J Neural Transm.* 2023 Jun; 130:827–38. doi: [10.1007/s00702-023-02635-4](https://doi.org/10.1007/s00702-023-02635-4). [Accessed on: 2023 Jul 2] (cited on page 9)
29. Irwin DJ, Grossman M, Weintraub D, Hurtig HI, Duda JE, Xie SX, Lee EB, Van Deerlin VM, Lopez OL, Kofler JK, Nelson PT, Jicha GA, Woltjer R, Quinn JF, Kaye J, Leverenz JB, Tsuang D, Longfellow K, Yearout D, Kukull W, Keene CD, Montine TJ, Zabetian CP, and Trojanowski JQ. Neuropathological and Genetic Correlates of Survival and Dementia Onset in Synucleinopathies: A Retrospective Analysis. *Lancet Neurol.* 2017 Jan; 16:55–65. doi: [10.1016/S1474-4422\(16\)30291-5](https://doi.org/10.1016/S1474-4422(16)30291-5) (cited on page 9)
30. Murakami K and Ono K. Interactions of Amyloid Coaggregates with Biomolecules and Its Relevance to Neurodegeneration. *FASEB J.* 2022 Sep; 36:e22493. doi: [10.1096/fj.202200235R](https://doi.org/10.1096/fj.202200235R) (cited on page 9)
31. Ulugut H and Pijnenburg YAL. Frontotemporal Dementia: Past, Present, and Future. *Alzheimer's & Dementia.* 2023 Jun 28 :alz.13363. doi: [10.1002/alz.13363](https://doi.org/10.1002/alz.13363). [Accessed on: 2023 Jul 2] (cited on page 10)
32. Hutton M, Lendon CL, Rizzu P, Baker M, Froelich S, Houlden H, Pickering-Brown S, Chakraverty S, Isaacs A, Grover A, Hackett J, Adamson J, Lincoln S, Dickson D, Davies P, Petersen RC, Stevens M, De Graaff E, Wauters E, Van Baren J, Hillebrand M, Joosse M, Kwon JM, Nowotny P, Che LK, Norton J, Morris JC, Reed LA, Trojanowski J, Basun H, Lannfelt L, Neystat M, Fahn S, Dark F, Tannenberg T, Dodd PR, Hayward N, Kwok JBJ, Schofield PR, Andreadis A, Snowden J, Craufurd D, Neary D, Owen F, Oostra BA, Hardy J, Goate A, Van Swieten J, Mann D, Lynch T, and Heutink P. Association of Missense and 5'-Splice-Site Mutations in Tau with the Inherited Dementia FTDP-17. *Nature.* 1998 Jun; 393:702–5. doi: [10.1038/31508](https://doi.org/10.1038/31508). [Accessed on: 2023 Jul 3] (cited on page 10)
33. Constantinidis J, Richard J, and Tissot R. Pick's Disease. *Eur Neurol.* 1974; 11:208–17. doi: [10.1159/000114320](https://doi.org/10.1159/000114320). [Accessed on: 2023 Jul 3] (cited on page 10)
34. Itoh Y, Yamada M, Hayakawa M, Otomo E, and Miyatake T. Cerebral Amyloid Angiopathy: A Significant Cause of Cerebellar as Well as Lobar Cerebral Hemorrhage in the Elderly. *Journal of the Neurological Sciences.* 1993 Jun; 116:135–41. doi: [10.1016/0022-510X\(93\)90317-R](https://doi.org/10.1016/0022-510X(93)90317-R). [Accessed on: 2023 May 12] (cited on page 10)
35. Ramirez J, Berezuk C, McNeely AA, Gao F, McLaurin J, and Black SE. Imaging the Perivascular Space as a Potential Biomarker of Neurovascular and Neurodegenerative Diseases. *Cell Mol Neurobiol.* 2016 Mar; 36:289–99. doi: [10.1007/s10571-016-0343-6](https://doi.org/10.1007/s10571-016-0343-6). [Accessed on: 2023 Mar 9] (cited on page 11)
36. Allen N, Robinson AC, Snowden J, Davidson YS, and Mann DM. Patterns of Cerebral Amyloid Angiopathy Define Histopathological Phenotypes in Alzheimer's Disease. *Neuropathology and Applied Neurobiology.* 2014; 40(2):136–48. doi: [10.1111/nan.12070](https://doi.org/10.1111/nan.12070) (cited on page 10)

37. Thal DR, Ghebremedhin E, Orantes M, and Wiestler OD. Vascular Pathology in Alzheimer Disease: Correlation of Cerebral Amyloid Angiopathy and Arteriosclerosis/Lipohyalinosis with Cognitive Decline. *J Neuropathol Exp Neurol*. 2003 Dec; 62:1287–301. doi: [10.1093/jnen/62.12.1287](https://doi.org/10.1093/jnen/62.12.1287). [Accessed on: 2023 Jan 26] (cited on pages 10, 154–157)
38. Hardy J and Selkoe DJ. The Amyloid Hypothesis of Alzheimer's Disease: Progress and Problems on the Road to Therapeutics. *Science*. 2002 Jul 19; 297:353–6. doi: [10.1126/science.1072994](https://doi.org/10.1126/science.1072994). [Accessed on: 2023 May 11] (cited on page 11)
39. Selkoe DJ and Hardy J. The Amyloid Hypothesis of Alzheimer's Disease at 25 Years. *EMBO Mol Med*. 2016 Jun; 8:595–608. doi: [10.15252/emmm.201606210](https://doi.org/10.15252/emmm.201606210). [Accessed on: 2023 Jun 20] (cited on page 11)
40. Priller C, Bauer T, Mitteregger G, Krebs B, Kretzschmar HA, and Herms J. Synapse Formation and Function Is Modulated by the Amyloid Precursor Protein. *J Neurosci*. 2006 Jul 5; 26:7212–21. doi: [10.1523/JNEUROSCI.1450-06.2006](https://doi.org/10.1523/JNEUROSCI.1450-06.2006). [Accessed on: 2023 May 15] (cited on page 11)
41. Luca MD. Alpha Beta-and Gamma-Secretases in Alzheimer s Disease. *Front Biosci*. 2012; S4:1126–50. doi: [10.2741/s322](https://doi.org/10.2741/s322). [Accessed on: 2023 May 15] (cited on page 11)
42. Kitazume S, Tachida Y, Oka R, Shirotani K, Saido TC, and Hashimoto Y. Alzheimer's  $\beta$ -Secretase,  $\beta$ -Site Amyloid Precursor Protein-Cleaving Enzyme, Is Responsible for Cleavage Secretion of a Golgi-resident Sialyltransferase. *Proc Natl Acad Sci USA*. 2001 Nov 20; 98:13554–9. doi: [10.1073/pnas.241509198](https://doi.org/10.1073/pnas.241509198). [Accessed on: 2023 May 15] (cited on page 12)
43. Deng Y, Wang Z, Wang R, Zhang X, Zhang S, Wu Y, Staufenbiel M, Cai F, and Song W. Amyloid- $\beta$  Protein ( $A\beta$ ) Glu11 Is the Major  $\beta$ -Secretase Site of  $\beta$ -Site Amyloid- $\beta$  Precursor Protein-Cleaving Enzyme 1(BACE1), and Shifting the Cleavage Site to  $A\beta$  Asp1 Contributes to Alzheimer Pathogenesis. *Eur J Neurosci*. 2013 Jun; 37:1962–9. doi: [10.1111/ejn.12235](https://doi.org/10.1111/ejn.12235). [Accessed on: 2023 May 15] (cited on page 12)
44. Haass C. Take Five—BACE and the  $\gamma$ -Secretase Quartet Conduct Alzheimer's Amyloid  $\beta$ -Peptide Generation. *EMBO J*. 2004 Feb 11; 23:483–8. doi: [10.1038/sj.emboj.7600061](https://doi.org/10.1038/sj.emboj.7600061). [Accessed on: 2023 May 15] (cited on page 12)
45. Muller U and Wil K. Structure and Function of the APP Intracellular Domain in Health and Disease. *Understanding Alzheimer's Disease*. Ed. by Zerr I. InTech, 2013 Feb 27. doi: [10.5772/54543](https://doi.org/10.5772/54543). [Accessed on: 2023 May 15] (cited on page 12)
46. Kuo YM, Emmerling MR, Vigo-Pelfrey C, Kasunic TC, Kirkpatrick JB, Murdoch GH, Ball MJ, and Roher AE. Water-Soluble  $A\beta$ (N-40, N-42) Oligomers in Normal and Alzheimer Disease Brains. *Journal of Biological Chemistry*. 1996 Feb; 271:4077–81. doi: [10.1074/jbc.271.8.4077](https://doi.org/10.1074/jbc.271.8.4077). [Accessed on: 2023 May 25] (cited on page 12)
47. Schmechel DE, Saunders AM, Strittmatter WJ, Crain BJ, Hulette CM, Joo SH, Pericak-Vance MA, Goldgaber D, and Roses AD. Increased Amyloid Beta-Peptide Deposition in Cerebral Cortex as a Consequence of Apolipoprotein E Genotype in Late-Onset Alzheimer Disease. *Proc Natl Acad Sci USA*. 1993 Oct 15; 90:9649–53. doi: [10.1073/pnas.90.20.9649](https://doi.org/10.1073/pnas.90.20.9649). [Accessed on: 2023 Jun 12] (cited on page 12)

48. Bates KA, Verdile G, Li QX, Ames D, Hudson P, Masters CL, and Martins RN. Clearance Mechanisms of Alzheimer's Amyloid- $\beta$  Peptide: Implications for Therapeutic Design and Diagnostic Tests. *Mol Psychiatry*. 2009 May; 14:469–86. doi: [10.1038/mp.2008.96](https://doi.org/10.1038/mp.2008.96). [Accessed on: 2023 May 25] (cited on page 12)
49. Nussbaum JM, Seward ME, and Bloom GS. Alzheimer Disease: A Tale of Two Prions. *Prion*. 2013 Jan; 7:14–9. doi: [10.4161/pri.22118](https://doi.org/10.4161/pri.22118). [Accessed on: 2023 Jun 16] (cited on pages 12, 14)
50. Seeman P and Seeman N. Alzheimer's Disease:  $\beta$ -Amyloid Plaque Formation in Human Brain. *Synapse*. 2011 Dec; 65:1289–97. doi: [10.1002/syn.20957](https://doi.org/10.1002/syn.20957). [Accessed on: 2022 Mar 28] (cited on page 13)
51. Glabe CG and Kaye R. Common Structure and Toxic Function of Amyloid Oligomers Implies a Common Mechanism of Pathogenesis. *Neurology*. 2006 Jan 24; 66(Issue 1, Supplement 1):S74–S78. doi: [10.1212/01.wnl.0000192103.24796.42](https://doi.org/10.1212/01.wnl.0000192103.24796.42). [Accessed on: 2023 May 24] (cited on page 13)
52. Di Fede G, Catania M, Maderna E, Ghidoni R, Benussi L, Tonoli E, Giaccone G, Moda F, Paterlini A, Campagnani I, Sorrentino S, Colombo L, Kubis A, Bistaffa E, Ghetti B, and Tagliavini F. Molecular Subtypes of Alzheimer's Disease. *Scientific Reports*. 2018; 8(1):1–14. doi: [10.1038/s41598-018-21641-1](https://doi.org/10.1038/s41598-018-21641-1) (cited on pages 13, 15, 109)
53. Huang Yr and Liu Rt. The Toxicity and Polymorphism of  $\beta$ -Amyloid Oligomers. *IJMS*. 2020 Jun 24; 21:4477. doi: [10.3390/ijms21124477](https://doi.org/10.3390/ijms21124477). [Accessed on: 2023 May 24] (cited on page 13)
54. Gouras GK, Tampellini D, Takahashi RH, and Capetillo-Zarate E. Intraneuronal  $\beta$ -Amyloid Accumulation and Synapse Pathology in Alzheimer's Disease. *Acta Neuropathol*. 2010 May; 119:523–41. doi: [10.1007/s00401-010-0679-9](https://doi.org/10.1007/s00401-010-0679-9). [Accessed on: 2023 May 24] (cited on page 13)
55. De Felice FG, Velasco PT, Lambert MP, Viola K, Fernandez SJ, Ferreira ST, and Klein WL.  $A\beta$  Oligomers Induce Neuronal Oxidative Stress through an N-methyl-D-aspartate Receptor-Dependent Mechanism That Is Blocked by the Alzheimer Drug Memantine. *Journal of Biological Chemistry*. 2007 Apr; 282:11590–601. doi: [10.1074/jbc.M607483200](https://doi.org/10.1074/jbc.M607483200). [Accessed on: 2023 May 24] (cited on page 13)
56. Kelly BL and Ferreira A. Beta-Amyloid Disrupted Synaptic Vesicle Endocytosis in Cultured Hippocampal Neurons. 2007 (cited on page 13)
57. Demuro A, Mina E, Kaye R, Milton SC, Parker I, and Glabe CG. Calcium Dysregulation and Membrane Disruption as a Ubiquitous Neurotoxic Mechanism of Soluble Amyloid Oligomers. *Journal of Biological Chemistry*. 2005 Apr; 280:17294–300. doi: [10.1074/jbc.M500997200](https://doi.org/10.1074/jbc.M500997200). [Accessed on: 2023 May 24] (cited on page 13)
58. Kaye R and Lasagna-Reeves CA. Molecular Mechanisms of Amyloid Oligomers Toxicity. *JAD*. 2012 Dec 17; 33. Ed. by Perry G, Zhu X, Smith MA, Sorensen A, and Avila J:S67–S78. doi: [10.3233/JAD-2012-129001](https://doi.org/10.3233/JAD-2012-129001). [Accessed on: 2023 May 24] (cited on pages 13, 14)

59. Venegas C and Heneka MT. Danger-Associated Molecular Patterns in Alzheimer's Disease. *Journal of Leukocyte Biology*. 2017 Jan 1; 101:87–98. doi: [10.1189/jlb.3MR0416-204R](https://doi.org/10.1189/jlb.3MR0416-204R). [Accessed on: 2023 Jun 15] (cited on page 13)
60. Heneka MT. Inflammasome Activation and Innate Immunity in Alzheimer's Disease: Innate Immune Activation in AD. *Brain Pathology*. 2017 Mar; 27:220–2. doi: [10.1111/bpa.12483](https://doi.org/10.1111/bpa.12483). [Accessed on: 2023 Jun 15] (cited on page 13)
61. Sarlus H and Heneka MT. Microglia in Alzheimer's Disease. *Journal of Clinical Investigation*. 2017 Sep 1; 127:3240–9. doi: [10.1172/JCI90606](https://doi.org/10.1172/JCI90606). [Accessed on: 2023 May 26] (cited on page 13)
62. Del Bo R, Angeretti N, Lucca E, De Simoni MG, and Forloni G. Reciprocal Control of Inflammatory Cytokines, IL-1 and IL-6, and  $\beta$ -Amyloid Production in Cultures. *Neuroscience Letters*. 1995 Mar; 188:70–4. doi: [10.1016/0304-3940\(95\)11384-9](https://doi.org/10.1016/0304-3940(95)11384-9). [Accessed on: 2023 Jun 16] (cited on page 13)
63. Pan Xd, Zhu Yg, Lin N, Zhang J, Ye Qy, Huang Hp, and Chen Xc. Microglial Phagocytosis Induced by Fibrillar  $\beta$ -Amyloid Is Attenuated by Oligomeric  $\beta$ -Amyloid: Implications for Alzheimer's Disease. *Mol Neurodegeneration*. 2011 Dec; 6:45. doi: [10.1186/1750-1326-6-45](https://doi.org/10.1186/1750-1326-6-45). [Accessed on: 2023 Jun 16] (cited on page 13)
64. Liddelow SA, Guttenplan KA, Clarke LE, Bennett FC, Bohlen CJ, Schirmer L, Bennett ML, Münch AE, Chung WS, Peterson TC, Wilton DK, Frouin A, Napier BA, Panicker N, Kumar M, Buckwalter MS, Rowitch DH, Dawson VL, Dawson TM, Stevens B, and Barres BA. Neurotoxic Reactive Astrocytes Are Induced by Activated Microglia. *Nature*. 2017 Jan; 541:481–7. doi: [10.1038/nature21029](https://doi.org/10.1038/nature21029). [Accessed on: 2023 Jun 16] (cited on page 13)
65. Kamphuis W, Orre M, Kooijman L, Dahmen M, and Hol EM. Differential Cell Proliferation in the Cortex of the Appsweps1de9 Alzheimer's Disease Mouse Model. *Glia*. 2012 Apr; 60:615–29. doi: [10.1002/glia.22295](https://doi.org/10.1002/glia.22295). [Accessed on: 2023 Jun 16] (cited on page 13)
66. Bisht K, Sharma KP, Lecours C, Gabriela Sánchez M, El Hajj H, Milior G, Olmos-Alonso A, Gómez-Nicola D, Luheshi G, Vallières L, Branchi I, Maggi L, Limatola C, Butovsky O, and Tremblay MÈ. Dark Microglia: A New Phenotype Predominantly Associated with Pathological States. *Glia*. 2016 May; 64:826–39. doi: [10.1002/glia.22966](https://doi.org/10.1002/glia.22966). [Accessed on: 2023 Jun 16] (cited on page 13)
67. Busche MA and Hyman BT. Synergy between Amyloid- $\beta$  and Tau in Alzheimer's Disease. *Nat Neurosci*. 2020 Oct; 23:1183–93. doi: [10.1038/s41593-020-0687-6](https://doi.org/10.1038/s41593-020-0687-6). [Accessed on: 2023 Jun 16] (cited on page 13)
68. Takashima A, Noguchi K, Sato K, Hoshino T, and Imahori K. Tau Protein Kinase I Is Essential for Amyloid Beta-Protein-Induced Neurotoxicity. *Proc Natl Acad Sci USA*. 1993 Aug 15; 90:7789–93. doi: [10.1073/pnas.90.16.7789](https://doi.org/10.1073/pnas.90.16.7789). [Accessed on: 2023 May 24] (cited on page 14)

69. Oddo S, Caccamo A, Tseng B, Cheng D, Vasilevko V, Cribbs DH, and LaFerla FM. Blocking A $\beta$ 42 Accumulation Delays the Onset and Progression of Tau Pathology via the C Terminus of Heat Shock Protein70-Interacting Protein: A Mechanistic Link between A $\beta$  and Tau Pathology. *J Neurosci*. 2008 Nov 19; 28:12163–75. doi: [10.1523/JNEUROSCI.2464-08.2008](https://doi.org/10.1523/JNEUROSCI.2464-08.2008). [Accessed on: 2023 Jun 20] (cited on page 14)
70. Meraz-Ríos MA, Lira-De León KI, Campos-Peña V, De Anda-Hernández MA, and Mena-López R. Tau Oligomers and Aggregation in Alzheimer's Disease. *Journal of Neurochemistry*. 2010 Mar; 112:1353–67. doi: [10.1111/j.1471-4159.2009.06511.x](https://doi.org/10.1111/j.1471-4159.2009.06511.x). [Accessed on: 2023 Jun 16] (cited on page 14)
71. DuBoff B, Feany M, and Götz J. Why Size Matters – Balancing Mitochondrial Dynamics in Alzheimer's Disease. *Trends in Neurosciences*. 2013 Jun; 36:325–35. doi: [10.1016/j.tins.2013.03.002](https://doi.org/10.1016/j.tins.2013.03.002). [Accessed on: 2023 Jun 16] (cited on page 14)
72. Lasagna-Reeves CA, Castillo-Carranza DL, Sengupta U, Sarmiento J, Troncoso J, Jackson GR, and Kaye R. Identification of Oligomers at Early Stages of Tau Aggregation in Alzheimer's Disease. *FASEB j*. 2012 May; 26:1946–59. doi: [10.1096/fj.11-199851](https://doi.org/10.1096/fj.11-199851). [Accessed on: 2023 Jun 16] (cited on page 14)
73. Vogel JW et al. Spread of Pathological Tau Proteins through Communicating Neurons in Human Alzheimer's Disease. *Nat Commun*. 2020 May 26; 11:2612. doi: [10.1038/s41467-020-15701-2](https://doi.org/10.1038/s41467-020-15701-2). [Accessed on: 2023 Jun 16] (cited on page 14)
74. Guo JL and Lee VMY. Seeding of Normal Tau by Pathological Tau Conformers Drives Pathogenesis of Alzheimer-like Tangles. *Journal of Biological Chemistry*. 2011 Apr; 286:15317–31. doi: [10.1074/jbc.M110.209296](https://doi.org/10.1074/jbc.M110.209296). [Accessed on: 2023 Jun 16] (cited on page 14)
75. Asai H, Ikezu S, Tsunoda S, Medalla M, Luebke J, Haydar T, Wolozin B, Butovsky O, Kügler S, and Ikezu T. Depletion of Microglia and Inhibition of Exosome Synthesis Halt Tau Propagation. *Nat Neurosci*. 2015 Nov; 18:1584–93. doi: [10.1038/nn.4132](https://doi.org/10.1038/nn.4132). [Accessed on: 2023 Jun 16] (cited on page 14)
76. Vogels T, Murgoci AN, and Hromádka T. Intersection of Pathological Tau and Microglia at the Synapse. *acta neuropathol commun*. 2019 Dec; 7:109. doi: [10.1186/s40478-019-0754-y](https://doi.org/10.1186/s40478-019-0754-y). [Accessed on: 2023 Jun 16] (cited on page 14)
77. Jansen WJ et al. Prevalence of Cerebral Amyloid Pathology in Persons Without Dementia: A Meta-analysis. *JAMA*. 2015 May 19; 313:1924. doi: [10.1001/jama.2015.4668](https://doi.org/10.1001/jama.2015.4668). [Accessed on: 2023 Jun 20] (cited on page 15)
78. Roberts RO, Aakre JA, Kremers WK, Vassilaki M, Knopman DS, Mielke MM, Alhurani R, Geda YE, Machulda MM, Coloma P, Schauble B, Lowe VJ, Jack CR, and Petersen RC. Prevalence and Outcomes of Amyloid Positivity Among Persons Without Dementia in a Longitudinal, Population-Based Setting. *JAMA Neurol*. 2018 Aug 1; 75:970. doi: [10.1001/jamaneurol.2018.0629](https://doi.org/10.1001/jamaneurol.2018.0629). [Accessed on: 2023 Jun 20] (cited on page 15)

79. Sturchio A, Dwivedi AK, Young CB, Malm T, Marsili L, Sharma JS, Mahajan A, Hill EJ, Andaloussi SE, Poston KL, Manfredsson FP, Schneider LS, Ezzat K, and Espay AJ. High Cerebrospinal Amyloid- $\beta$  42 Is Associated with Normal Cognition in Individuals with Brain Amyloidosis. *EClinicalMedicine*. 2021 Jun ;100988. doi: [10.1016/j.eclinm.2021.100988](https://doi.org/10.1016/j.eclinm.2021.100988). [Accessed on: 2021 Aug 17] (cited on page 15)
80. Condello C, Lemmin T, Stöhr J, Nick M, Wu Y, Maxwell AM, Watts JC, Caro CD, Oehler A, Keene CD, Bird TD, van Duinen SG, Lannfelt L, Ingelsson M, Graff C, Giles K, DeGrado WF, and Prusiner SB. Structural Heterogeneity and Intersubject Variability of A $\beta$  in Familial and Sporadic Alzheimer's Disease. *Proc Natl Acad Sci USA*. 2018 Jan 23; 115. doi: [10.1073/pnas.1714966115](https://doi.org/10.1073/pnas.1714966115). [Accessed on: 2022 Apr 11] (cited on page 15)
81. Liu H, Kim C, Haldiman T, Sigurdson CJ, Nyström S, Nilsson KPR, Cohen ML, Wisniewski T, Hammarström P, and Safar JG. Distinct Conformers of Amyloid Beta Accumulate in the Neocortex of Patients with Rapidly Progressive Alzheimer's Disease. *Journal of Biological Chemistry*. 2021 Nov; 297:101267. doi: [10.1016/j.jbc.2021.101267](https://doi.org/10.1016/j.jbc.2021.101267). [Accessed on: 2022 Apr 11] (cited on page 15)
82. Abbaspour N, Hurrell R, and Kelishadi R. Review on Iron and Its Importance for Human Health. *J Res Med Sci*. 2014 Feb; 19:164–74 (cited on page 15)
83. Yu P and Chang YZ. Brain Iron Metabolism and Regulation. *Brain Iron Metabolism and CNS Diseases*. Ed. by Chang YZ. Vol. 1173. Singapore: Springer Singapore, 2019 :33–44. doi: [10.1007/978-981-13-9589-5\\_3](https://doi.org/10.1007/978-981-13-9589-5_3). [Accessed on: 2023 Jun 16] (cited on page 15)
84. Pavelková M, Vysloužil J, Kubová K, and Vetchý D. Biological Role of Copper as an Essential Trace Element in the Human Organism. *Ceska Slov Farm*. 2018; 67:143–53 (cited on page 16)
85. Jomova K, Makova M, Alomar SY, Alwasel SH, Nepovimova E, Kuca K, Rhodes CJ, and Valko M. Essential Metals in Health and Disease. *Chemico-Biological Interactions*. 2022 Nov; 367:110173. doi: [10.1016/j.cbi.2022.110173](https://doi.org/10.1016/j.cbi.2022.110173). [Accessed on: 2023 Jun 21] (cited on page 16)
86. Fukada T, Yamasaki S, Nishida K, Murakami M, and Hirano T. Zinc Homeostasis and Signaling in Health and Diseases: Zinc Signaling. *J Biol Inorg Chem*. 2011 Oct; 16:1123–34. doi: [10.1007/s00775-011-0797-4](https://doi.org/10.1007/s00775-011-0797-4). [Accessed on: 2023 Jun 28] (cited on page 16)
87. Carmona A, Roudeau S, and Ortega R. Molecular Mechanisms of Environmental Metal Neurotoxicity: A Focus on the Interactions of Metals with Synapse Structure and Function. *Toxics*. 2021 Aug 27; 9:198. doi: [10.3390/toxics9090198](https://doi.org/10.3390/toxics9090198). [Accessed on: 2023 Jun 28] (cited on page 16)
88. Benters J, Flögel U, Schäfer T, Leibfritz D, Hechtenberg S, and Beyersmann D. Study of the Interactions of Cadmium and Zinc Ions with Cellular Calcium Homeostasis Using <sup>19</sup>F-NMR Spectroscopy. *Biochemical Journal*. 1997 Mar 15; 322:793–9. doi: [10.1042/bj3220793](https://doi.org/10.1042/bj3220793). [Accessed on: 2023 Jun 22] (cited on page 16)

89. Morel JD, Sauzéat L, Goeminne LJE, Jha P, Williams E, Houtkooper RH, Aebersold R, Auwerx J, and Balter V. The Mouse Metallomic Landscape of Aging and Metabolism. *Nat Commun.* 2022 Dec; 13:607. doi: [10.1038/s41467-022-28060-x](https://doi.org/10.1038/s41467-022-28060-x). [Accessed on: 2022 Feb 21] (cited on page 17)
90. Ellison G, Duong L, Hollings A, Howard D, Jackaman C, and Hackett MJ. Characterising Murine Hippocampal Iron Homeostasis, in Relation to Markers of Brain Inflammation and Metabolism, during Ageing. *Metallomics.* 2022 Oct 8; 14:mfac064. doi: [10.1093/mtomcs/mfac064](https://doi.org/10.1093/mtomcs/mfac064). [Accessed on: 2023 May 24] (cited on page 17)
91. Leskovjan AC, Kretlow A, Lanzirrotti A, Barrea R, Vogt S, and Miller LM. Increased Brain Iron Coincides with Early Plaque Formation in a Mouse Model of Alzheimer's Disease. *NeuroImage.* 2011 Mar; 55(1):32–8. doi: [10.1016/j.neuroimage.2010.11.073](https://doi.org/10.1016/j.neuroimage.2010.11.073). [Accessed on: 2021 Apr 22] (cited on page 17)
92. Wang H, Wang M, Wang B, Li M, Chen H, Yu X, Yang K, Chai Z, Zhao Y, and Feng W. Immunogold Labeling and X-ray Fluorescence Microscopy Reveal Enrichment Ratios of Cu and Zn, Metabolism of APP and Amyloid- $\beta$  Plaque Formation in a Mouse Model of Alzheimer's Disease. *Metallomics.* 2012 Oct; 4:1113–8. doi: [10.1039/c2mt20056b](https://doi.org/10.1039/c2mt20056b) (cited on page 17)
93. Bulk M, Abdelmoula WM, Geut H, Wiarda W, Ronen I, Dijkstra J, and Van Der Weerd L. Quantitative MRI and Laser Ablation-Inductively Coupled Plasma-Mass Spectrometry Imaging of Iron in the Frontal Cortex of Healthy Controls and Alzheimer's Disease Patients. *NeuroImage.* 2020 Jul; 215:116808. doi: [10.1016/j.neuroimage.2020.116808](https://doi.org/10.1016/j.neuroimage.2020.116808). [Accessed on: 2023 Jun 30] (cited on pages 17, 32, 111)
94. Quintana C, Bellefqih S, Laval J, Guerquin-Kern J, Wu T, Avila J, Ferrer I, Arranz R, and Patiño C. Study of the Localization of Iron, Ferritin, and Hemosiderin in Alzheimer's Disease Hippocampus by Analytical Microscopy at the Subcellular Level. *Journal of Structural Biology.* 2006 Jan; 153:42–54. doi: [10.1016/j.jsb.2005.11.001](https://doi.org/10.1016/j.jsb.2005.11.001). [Accessed on: 2023 Jun 30] (cited on page 17)
95. Wang H, Wang M, Wang B, Li M, Chen H, Yu X, Zhao Y, Feng W, and Chai Z. The Distribution Profile and Oxidation States of Biometals in APP Transgenic Mouse Brain: Dyshomeostasis with Age and as a Function of the Development of Alzheimer's Disease. *Metallomics.* 2012; 4:289. doi: [10.1039/c2mt00104g](https://doi.org/10.1039/c2mt00104g). [Accessed on: 2023 Jun 28] (cited on page 17)
96. Bourassa MW, Leskovjan AC, Tappero RV, Farquhar ER, Colton CA, Van Nostrand WE, and Miller LM. Elevated Copper in the Amyloid Plaques and Iron in the Cortex Are Observed in Mouse Models of Alzheimer's Disease That Exhibit Neurodegeneration. *Biomedical Spectroscopy and Imaging.* 2013; 2:129–39. doi: [10.3233/BSI-130041](https://doi.org/10.3233/BSI-130041). [Accessed on: 2023 Jun 30] (cited on page 17)
97. Wang HJ, Wang M, Wang B, Meng XY, Wang Y, Li M, Feng WY, Zhao YL, and Chai ZF. Quantitative Imaging of Element Spatial Distribution in the Brain Section of a Mouse Model of Alzheimer's Disease Using Synchrotron Radiation X-ray Fluorescence Analysis. 2010 :7 (cited on page 17)

98. James S, Churches Q, Bird M, Jonge M, and Streltsov V. P1–259: X-ray Fluorescence Imaging of Metal Ion Content in PSAPP Mouse Brain. *Alzheimer's & Dementia*. 2013 Jul; 9(4S\_Part\_6). doi: [10.1016/j.jalz.2013.05.484](https://doi.org/10.1016/j.jalz.2013.05.484). [Accessed on: 2023 Jun 30] (cited on page 17)
99. James SA, Churches QI, de Jonge MD, Birchall IE, Streltsov V, McColl G, Adlard PA, and Hare DJ. Iron, Copper, and Zinc Concentration in  $A\beta$  Plaques in the APP/PS1 Mouse Model of Alzheimer's Disease Correlates with Metal Levels in the Surrounding Neuropil. *ACS Chem Neurosci*. 2017 Mar 15; 8(3):629–37. doi: [10.1021/acschemneuro.6b00362](https://doi.org/10.1021/acschemneuro.6b00362). [Accessed on: 2021 Apr 22] (cited on pages 17, 111, 150)
100. Lovell M, Robertson J, Teesdale W, Campbell J, and Markesbery W. Copper, Iron and Zinc in Alzheimer's Disease Senile Plaques. *Journal of the Neurological Sciences*. 1998 Jun; 158:47–52. doi: [10.1016/S0022-510X\(98\)00092-6](https://doi.org/10.1016/S0022-510X(98)00092-6). [Accessed on: 2021 Dec 7] (cited on pages 17, 111, 150)
101. Gallagher JJ, Finnegan ME, Grehan B, Dobson J, Collingwood JF, and Lynch MA. Modest Amyloid Deposition Is Associated with Iron Dysregulation, Microglial Activation, and Oxidative Stress. *JAD*. 2012 Jan 12; 28:147–61. doi: [10.3233/JAD-2011-110614](https://doi.org/10.3233/JAD-2011-110614). [Accessed on: 2023 Jun 30] (cited on page 17)
102. Telling ND, Everett J, Collingwood JF, Dobson J, Van Der Laan G, Gallagher JJ, Wang J, and Hitchcock AP. Iron Biochemistry Is Correlated with Amyloid Plaque Morphology in an Established Mouse Model of Alzheimer's Disease. *Cell Chemical Biology*. 2017 Oct; 24:1205–1215.e3. doi: [10.1016/j.chembiol.2017.07.014](https://doi.org/10.1016/j.chembiol.2017.07.014). [Accessed on: 2023 Jun 30] (cited on page 17)
103. Summers KL, Fimognari N, Hollings A, Kiernan M, Lam V, Tidy RJ, Paterson D, Tobin MJ, Takechi R, George GN, Pickering IJ, Mamo JC, Harris HH, and Hackett MJ. A Multimodal Spectroscopic Imaging Method To Characterize the Metal and Macromolecular Content of Proteinaceous Aggregates (“Amyloid Plaques”). *Biochemistry*. 2017 Aug 15; 56:4107–16. doi: [10.1021/acs.biochem.7b00262](https://doi.org/10.1021/acs.biochem.7b00262). [Accessed on: 2022 Jul 6] (cited on pages 17, 32)
104. Miller LM, Wang Q, Telivala TP, Smith RJ, Lanzirotti A, and Miklossy J. Synchrotron-Based Infrared and X-ray Imaging Shows Focalized Accumulation of Cu and Zn Co-Localized with  $\beta$ -Amyloid Deposits in Alzheimer's Disease. *Journal of Structural Biology*. 2006 Jul; 155(1):30–7. doi: [10.1016/j.jsb.2005.09.004](https://doi.org/10.1016/j.jsb.2005.09.004). [Accessed on: 2021 Apr 12] (cited on pages 17, 32)
105. Everett J, Lermyte F, Brooks J, Tjendana-Tjhin V, Plascencia-Villa G, Hands-Portman I, Donnelly JM, Billimoria K, Perry G, Zhu X, Sadler PJ, O'Connor PB, Collingwood JF, and Telling ND. Biogenic Metallic Elements in the Human Brain? *Sci Adv*. 2021 Jun 11; 7:eabf6707. doi: [10.1126/sciadv.abf6707](https://doi.org/10.1126/sciadv.abf6707). [Accessed on: 2022 Jan 18] (cited on page 17)

106. Bush A, Pettingell W, Multhaup G, D Paradis M, Vonsattel J, Gusella J, Beyreuther K, Masters C, and Tanzi R. Rapid Induction of Alzheimer A Beta Amyloid Formation by Zinc. *Science*. 1994 Sep 2; 265:1464–7. doi: [10.1126/science.8073293](https://doi.org/10.1126/science.8073293). [Accessed on: 2023 Jun 30] (cited on page 17)
107. Huang X, Atwood CS, Hartshorn MA, Multhaup G, Goldstein LE, Scarpa RC, Cuajungco MP, Gray DN, Lim J, Moir RD, Tanzi RE, and Bush AI. The A-beta Peptide of Alzheimer's Disease Directly Produces Hydrogen Peroxide through Metal Ion Reduction. *Biochemistry*. 1999 Jun 15; 38:7609–16. doi: [10.1021/bi990438f](https://doi.org/10.1021/bi990438f) (cited on page 17)
108. Bush AI. The Metallobiology of Alzheimer's Disease. *Trends in Neurosciences*. 2003 Apr; 26:207–14. doi: [10.1016/S0166-2236\(03\)00067-5](https://doi.org/10.1016/S0166-2236(03)00067-5). [Accessed on: 2022 Jan 11] (cited on page 17)
109. Collingwood JF, Chong RKK, Kasama T, Cervera-Gontard L, Dunin-Borkowski RE, Perry G, Pósfai M, Siedlak SL, Simpson ET, Smith MA, and Dobson J. Three-Dimensional Tomographic Imaging and Characterization of Iron Compounds within Alzheimer's Plaque Core Material. *JAD*. 2008 Jun 4; 14:235–45. doi: [10.3233/JAD-2008-14211](https://doi.org/10.3233/JAD-2008-14211). [Accessed on: 2023 Jun 30] (cited on page 17)
110. Adlard PA and Bush AI. Metals and Alzheimer's Disease: How Far Have We Come in the Clinic? *JAD*. 2018 Mar 13; 62. Ed. by Perry G, Avila J, Tabaton M, and Zhu X:1369–79. doi: [10.3233/JAD-170662](https://doi.org/10.3233/JAD-170662). [Accessed on: 2023 Jun 30] (cited on page 17)
111. Dong J, Atwood CS, Anderson VE, Siedlak SL, Smith MA, Perry G, and Carey PR. Metal Binding and Oxidation of Amyloid- $\beta$  within Isolated Senile Plaque Cores: Raman Microscopic Evidence. *Biochemistry*. 2003 Mar 1; 42:2768–73. doi: [10.1021/bi0272151](https://doi.org/10.1021/bi0272151). [Accessed on: 2023 Jun 30] (cited on page 17)
112. Bush AI and Tanzi RE. Therapeutics for Alzheimer's Disease Based on the Metal Hypothesis. *Neurotherapeutics*. 2008 Jul; 5:421–32. doi: [10.1016/j.nurt.2008.05.001](https://doi.org/10.1016/j.nurt.2008.05.001). [Accessed on: 2023 Jun 30] (cited on page 17)
113. Crouch PJ, White AR, and Bush AI. The Modulation of Metal Bio-Availability as a Therapeutic Strategy for the Treatment of Alzheimer's Disease: Modulation of Metal Availability for Treating AD. *FEBS Journal*. 2007 Aug; 274:3775–83. doi: [10.1111/j.1742-4658.2007.05918.x](https://doi.org/10.1111/j.1742-4658.2007.05918.x). [Accessed on: 2023 Jun 30] (cited on page 17)
114. Duce JA and Bush AI. Biological Metals and Alzheimer's Disease: Implications for Therapeutics and Diagnostics. *Progress in Neurobiology*. 2010 Sep; 92:1–18. doi: [10.1016/j.pneurobio.2010.04.003](https://doi.org/10.1016/j.pneurobio.2010.04.003). [Accessed on: 2023 Jun 30] (cited on page 17)
115. Streltsov V. X-Ray Absorption and Diffraction Studies of the Metal Binding Sites in Amyloid  $\beta$ -Peptide. *Eur Biophys J*. 2008 Mar; 37:257–63. doi: [10.1007/s00249-007-0232-5](https://doi.org/10.1007/s00249-007-0232-5). [Accessed on: 2023 Jun 30] (cited on page 17)

116. Summers KL, Schilling KM, Roseman G, Markham KA, Dolgova NV, Kroll T, Sokaras D, Millhauser GL, Pickering IJ, and George GN. X-Ray Absorption Spectroscopy Investigations of Copper(II) Coordination in the Human Amyloid  $\beta$  Peptide. *Inorg Chem*. 2019 May 6; 58:6294–311. doi: [10.1021/acs.inorgchem.9b00507](https://doi.org/10.1021/acs.inorgchem.9b00507). [Accessed on: 2023 Jun 30] (cited on page 17)
117. Xie Y, Yu L, Fu Y, Sun H, and Wang J. Evaluating Effect of Metallic Ions on Aggregation Behavior of  $\beta$ -Amyloid Peptides by Atomic Force Microscope and Surface-Enhanced Raman Scattering. *BioMed Eng OnLine*. 2021 Dec; 20:132. doi: [10.1186/s12938-021-00972-7](https://doi.org/10.1186/s12938-021-00972-7). [Accessed on: 2023 Jun 30] (cited on page 17)
118. Stellato F, Menestrina G, Serra MD, Potrich C, Tomazzolli R, Meyer-Klaucke W, and Morante S. Metal Binding in Amyloid  $\beta$ -Peptides Shows Intra- and Inter-Peptide Coordination Modes. *Eur Biophys J*. 2006 Apr; 35:340–51. doi: [10.1007/s00249-005-0041-7](https://doi.org/10.1007/s00249-005-0041-7). [Accessed on: 2023 Jun 30] (cited on page 17)
119. Suwalsky M, Bolognin S, and Zatta P. Interaction between Alzheimer's Amyloid- $\beta$  and Amyloid- $\beta$ -Metal Complexes with Cell Membranes. *JAD*. 2009 May 26; 17:81–90. doi: [10.3233/JAD-2009-1032](https://doi.org/10.3233/JAD-2009-1032). [Accessed on: 2023 Jun 30] (cited on page 17)
120. Streltsov VA and Varghese JN. Substrate Mediated Reduction of Copper-Amyloid- $\beta$  Complex in Alzheimer's Disease. *Chem Commun*. 2008 :3169. doi: [10.1039/b803911a](https://doi.org/10.1039/b803911a). [Accessed on: 2023 Jun 30] (cited on page 17)
121. Grasso G, Giuffrida ML, and Rizzarelli E. Metallostasis and Amyloid  $\beta$ -Degrading Enzymes. *Metallomics*. 2012; 4:937. doi: [10.1039/c2mt20105d](https://doi.org/10.1039/c2mt20105d). [Accessed on: 2023 Jun 29] (cited on page 17)
122. Luo Y, Zhang J, Liu N, Luo Y, and Zhao B. Copper Ions Influence the Toxicity of  $\beta$ -Amyloid(1–42) in a Concentration-Dependent Manner in a *Caenorhabditis Elegans* Model of Alzheimer's Disease. *Sci China Life Sci*. 2011 Jun; 54:527–34. doi: [10.1007/s11427-011-4180-z](https://doi.org/10.1007/s11427-011-4180-z). [Accessed on: 2023 Jun 30] (cited on page 17)
123. Martic S, Rains MK, and Kraatz HB. Probing Copper/Tau Protein Interactions Electrochemically. *Analytical Biochemistry*. 2013 Nov; 442:130–7. doi: [10.1016/j.ab.2013.07.015](https://doi.org/10.1016/j.ab.2013.07.015). [Accessed on: 2023 Jul 1] (cited on page 17)
124. Landsberg JP, McDonald B, and Watt F. Absence of Aluminium in Neuritic Plaque Cores in Alzheimer's Disease. *Nature*. 1992 Nov; 360(6399):65–8. doi: [10.1038/360065a0](https://doi.org/10.1038/360065a0). [Accessed on: 2023 Apr 26] (cited on page 17)
125. Yumoto S, Kakimi S, Ohsaki A, and Ishikawa A. Demonstration of Aluminum in Amyloid Fibers in the Cores of Senile Plaques in the Brains of Patients with Alzheimer's Disease. *Journal of Inorganic Biochemistry*. 2009 Nov; 103:1579–84. doi: [10.1016/j.jinorgbio.2009.07.023](https://doi.org/10.1016/j.jinorgbio.2009.07.023). [Accessed on: 2023 Jun 30] (cited on pages 17, 150)
126. Das N, Raymick J, and Sarkar S. Role of Metals in Alzheimer's Disease. *Metab Brain Dis*. 2021 Oct; 36:1627–39. doi: [10.1007/s11011-021-00765-w](https://doi.org/10.1007/s11011-021-00765-w). [Accessed on: 2023 Jul 1] (cited on page 17)

127. Li K, Li A, Mei Y, Zhao J, Zhou Q, Li Y, Yang M, and Xu Q. Trace Elements and Alzheimer Dementia in Population-Based Studies: A Bibliometric and Meta-Analysis. *Environmental Pollution*. 2023 Feb; 318:120782. doi: [10.1016/j.envpol.2022.120782](https://doi.org/10.1016/j.envpol.2022.120782). [Accessed on: 2023 Jul 1] (cited on page 17)
128. Dubois B, Touchon J, Portet F, Ousset PJ, Vellas B, and Michel B. ["The 5 words": a simple and sensitive test for the diagnosis of Alzheimer's disease]. *Presse Med*. 2002 Nov 9; 31:1696–9 (cited on page 18)
129. Cahn DA, Salmon DP, Monsch AU, Butters N, Wiederholt WC, Corey-Bloom J, and Barrett-Connor E. Screening for Dementia of the Alzheimer Type in the Community: The Utility of the Clock Drawing Test. *Archives of Clinical Neuropsychology*. 1996 Jan 1; 11:529–39. doi: [10.1016/0887-6177\(95\)00041-0](https://doi.org/10.1016/0887-6177(95)00041-0). [Accessed on: 2023 Apr 26] (cited on page 19)
130. Folstein MF, Folstein SE, and McHugh PR. "Mini-mental State". *Journal of Psychiatric Research*. 1975 Nov; 12:189–98. doi: [10.1016/0022-3956\(75\)90026-6](https://doi.org/10.1016/0022-3956(75)90026-6). [Accessed on: 2023 May 2] (cited on page 19)
131. Galasko D, Klauber MR, Hofstetter CR, Salmon DP, Lasker B, and Thal LJ. The Mini-Mental State Examination in the Early Diagnosis of Alzheimer's Disease. *Archives of Neurology*. 1990 Jan 1; 47:49–52. doi: [10.1001/archneur.1990.00530010061020](https://doi.org/10.1001/archneur.1990.00530010061020). [Accessed on: 2023 May 2] (cited on page 19)
132. Clark CM. Variability in Annual Mini-Mental State Examination Score in Patients With Probable Alzheimer Disease: A Clinical Perspective of Data From the Consortium to Establish a Registry for Alzheimer's Disease. *Arch Neurol*. 1999 Jul 1; 56:857. doi: [10.1001/archneur.56.7.857](https://doi.org/10.1001/archneur.56.7.857). [Accessed on: 2023 May 2] (cited on page 19)
133. Harrell LE, Marson D, Chatterjee A, and Parrish JA. The Severe Mini-Mental State Examination: A New Neuropsychologic Instrument for the Bedside Assessment of Severely Impaired Patients With Alzheimer Disease: Alzheimer Disease and Associated Disorders. 2000 Jul; 14:168–75. doi: [10.1097/00002093-200007000-00008](https://doi.org/10.1097/00002093-200007000-00008). [Accessed on: 2023 May 2] (cited on page 19)
134. Nasreddine ZS, Phillips NA, Bédirian V, Charbonneau S, Whitehead V, Collin I, Cummings JL, and Chertkow H. The Montreal Cognitive Assessment, MoCA: A Brief Screening Tool For Mild Cognitive Impairment. *Journal of the American Geriatrics Society*. 2005 Apr; 53:695–9. doi: [10.1111/j.1532-5415.2005.53221.x](https://doi.org/10.1111/j.1532-5415.2005.53221.x). [Accessed on: 2023 May 11] (cited on page 20)
135. Wattmo C, Minthon L, and Wallin ÅK. Mild versus Moderate Stages of Alzheimer's Disease: Three-Year Outcomes in a Routine Clinical Setting of Cholinesterase Inhibitor Therapy. *Alz Res Therapy*. 2016 Dec; 8:7. doi: [10.1186/s13195-016-0174-1](https://doi.org/10.1186/s13195-016-0174-1). [Accessed on: 2023 Jul 10] (cited on page 20)
136. Li B, Cheng J, Cheng G, Zhu H, Liu B, Yang Y, Dai Q, Li W, Bao W, and Rong S. The Effect of Grape Seed Procyanidins Extract on Cognitive Function in Elderly People with Mild Cognitive Impairment: A Randomized, Double-Blind, Placebo-Controlled Clinical Trial. *Heliyon*. 2023 Jun; 9:e16994. doi: [10.1016/j.heliyon.2023.e16994](https://doi.org/10.1016/j.heliyon.2023.e16994). [Accessed on: 2023 Jul 10] (cited on page 20)

137. Eickhoff SB, Stephan KE, Mohlberg H, Grefkes C, Fink GR, Amunts K, and Zilles K. A New SPM Toolbox for Combining Probabilistic Cytoarchitectonic Maps and Functional Imaging Data. *NeuroImage*. 2005 May; 25:1325–35. doi: [10.1016/j.neuroimage.2004.12.034](https://doi.org/10.1016/j.neuroimage.2004.12.034). [Accessed on: 2023 Nov 7] (cited on pages 20, 111, 153)
138. Evans AC, Janke AL, Collins DL, and Baillet S. Brain Templates and Atlases. *NeuroImage*. 2012 Aug; 62:911–22. doi: [10.1016/j.neuroimage.2012.01.024](https://doi.org/10.1016/j.neuroimage.2012.01.024). [Accessed on: 2023 Nov 7] (cited on pages 20, 111, 153)
139. Amunts K, Mohlberg H, Bludau S, Caspers S, Lewis LB, Eickhoff SB, and Pieperhoff P. Julich-Brain Atlas, Cytoarchitectonic Maps (v3.0.3). In collab. with Amunts K. EBRAINS, 2023 Jul 13. doi: [10.25493/56EM-75H](https://doi.org/10.25493/56EM-75H). [Accessed on: 2023 Nov 7] (cited on pages 20, 111, 153)
140. Goldman JS and Hou CE. Early-Onset Alzheimer Disease: When Is Genetic Testing Appropriate? *Alzheimer Disease & Associated Disorders*. 2004; 18:65–7. doi: [10.1097/01.wad.0000126616.77653.71](https://doi.org/10.1097/01.wad.0000126616.77653.71). [Accessed on: 2023 Oct 29] (cited on page 20)
141. Goldman JS, Hahn SE, Catania JW, Larusse-Eckert S, Butson MB, Rumbaugh M, Strecker MN, Roberts JS, Burke W, Mayeux R, and Bird T. Genetic Counseling and Testing for Alzheimer Disease: Joint Practice Guidelines of the American College of Medical Genetics and the National Society of Genetic Counselors. *Genetics in Medicine*. 2011 Jun; 13:597–605. doi: [10.1097/GIM.0b013e31821d69b8](https://doi.org/10.1097/GIM.0b013e31821d69b8). [Accessed on: 2023 Oct 29] (cited on page 20)
142. Valotassiou V, Malamitsi J, Papatriantafyllou J, Dardiotis E, Tsougos I, Psimadas D, Alexiou S, Hadjigeorgiou G, and Georgoulas P. SPECT and PET Imaging in Alzheimer’s Disease. *Ann Nucl Med*. 2018 Nov; 32:583–93. doi: [10.1007/s12149-018-1292-6](https://doi.org/10.1007/s12149-018-1292-6). [Accessed on: 2023 May 2] (cited on page 20)
143. Toyonaga T, Smith LM, Finnema SJ, Gallezot JD, Naganawa M, Bini J, Mulnix T, Cai Z, Ropchan J, Huang Y, Strittmatter SM, and Carson RE. In Vivo Synaptic Density Imaging with <sup>11</sup>C-UCB-J Detects Treatment Effects of Saracatinib in a Mouse Model of Alzheimer Disease. *J Nucl Med*. 2019 Dec; 60:1780–6. doi: [10.2967/jnumed.118.223867](https://doi.org/10.2967/jnumed.118.223867). [Accessed on: 2023 May 2] (cited on page 21)
144. Klunk WE, Engler H, Nordberg A, Wang Y, Blomqvist G, Holt DP, Bergström M, Savitcheva I, Huang GF, Estrada S, Ausén B, Debnath ML, Barletta J, Price JC, Sandell J, Lopresti BJ, Wall A, Koivisto P, Antoni G, Mathis CA, and Långström B. Imaging Brain Amyloid in Alzheimer’s Disease with Pittsburgh Compound-B: Imaging Amyloid in AD with PIB. *Ann Neurol*. 2004 Mar; 55:306–19. doi: [10.1002/ana.20009](https://doi.org/10.1002/ana.20009). [Accessed on: 2023 May 2] (cited on page 21)
145. Kolanko MA, Win Z, Loreto F, Patel N, Carswell C, Gontsarova A, Perry RJ, and Malhotra PA. Amyloid PET Imaging in Clinical Practice. *Pract Neurol*. 2020 Dec; 20:451–62. doi: [10.1136/practneurol-2019-002468](https://doi.org/10.1136/practneurol-2019-002468). [Accessed on: 2023 May 3] (cited on page 21)

146. Leuzy A, Chiotis K, Lemoine L, Gillberg PG, Almkvist O, Rodriguez-Vieitez E, and Nordberg A. Tau PET Imaging in Neurodegenerative Tauopathies—Still a Challenge. *Mol Psychiatry*. 2019 Aug; 24:1112–34. doi: [10.1038/s41380-018-0342-8](https://doi.org/10.1038/s41380-018-0342-8). [Accessed on: 2023 May 3] (cited on page 21)
147. Chien DT, Bahri S, Szardenings AK, Walsh JC, Mu F, Su MY, Shankle WR, Elizarov A, and Kolb HC. Early Clinical PET Imaging Results with the Novel PHF-Tau Radioligand [F-18]-T807. *JAD*. 2013 Jun 20; 34:457–68. doi: [10.3233/JAD-122059](https://doi.org/10.3233/JAD-122059). [Accessed on: 2023 May 3] (cited on page 21)
148. Knezevic D and Mizrahi R. Molecular Imaging of Neuroinflammation in Alzheimer’s Disease and Mild Cognitive Impairment. *Progress in Neuro-Psychopharmacology and Biological Psychiatry*. 2018 Jan; 80:123–31. doi: [10.1016/j.pnpbp.2017.05.007](https://doi.org/10.1016/j.pnpbp.2017.05.007). [Accessed on: 2023 May 4] (cited on page 21)
149. Wang ZB, Tan L, Wang HF, Chen SD, Fu Y, Gao PY, Ma YH, Guo Y, Hou JH, Zhang DD, Yu JT, and for the Alzheimer’s Disease Neuroimaging Initiative. Differences between *Ante Mortem* Alzheimer’s Disease Biomarkers in Predicting Neuropathology at Autopsy. *Alzheimer’s & Dementia*. 2023 Feb 25 :alz.12997. doi: [10.1002/alz.12997](https://doi.org/10.1002/alz.12997). [Accessed on: 2023 May 3] (cited on page 21)
150. Blennow K and Zetterberg H. Fluid Biomarker-Based Molecular Phenotyping of Alzheimer’s Disease Patients in Research and Clinical Settings. *Progress in Molecular Biology and Translational Science*. Vol. 168. Elsevier, 2019 :3–23. doi: [10.1016/bs.pmbts.2019.07.006](https://doi.org/10.1016/bs.pmbts.2019.07.006). [Accessed on: 2023 May 3] (cited on page 21)
151. Almkvist O and Nordberg A. A Biomarker-Validated Time Scale in Years of Disease Progression Has Identified Early- and Late-Onset Subgroups in Sporadic Alzheimer’s Disease. *Alz Res Therapy*. 2023 May 2; 15:89. doi: [10.1186/s13195-023-01231-8](https://doi.org/10.1186/s13195-023-01231-8). [Accessed on: 2023 May 3] (cited on page 21)
152. Bos I, Vos S, Verhey F, Scheltens P, Teunissen C, Engelborghs S, Sleegers K, Frisoni G, Blin O, Richardson JC, Bordet R, Tsolaki M, Popp J, Peyratout G, Martinez-Lage P, Tainta M, Lleó A, Johannsen P, Freund-Levi Y, Frölich L, Vandenberghe R, Westwood S, Dobricic V, Barkhof F, Legido-Quigley C, Bertram L, Lovestone S, Streffer J, Andreasson U, Blennow K, Zetterberg H, and Visser PJ. Cerebrospinal Fluid Biomarkers of Neurodegeneration, Synaptic Integrity, and Astroglial Activation across the Clinical Alzheimer’s Disease Spectrum. *Alzheimer’s & Dementia*. 2019 May; 15:644–54. doi: [10.1016/j.jalz.2019.01.004](https://doi.org/10.1016/j.jalz.2019.01.004). [Accessed on: 2023 Oct 25] (cited on page 21)
153. Mattsson N, Rosen E, Hansson O, Andreasen N, Parnetti L, Jonsson M, Herukka SK, Van Der Flier WM, Blankenstein MA, Ewers M, Rich K, Kaiser E, Verbeek MM, Olde Rikkert M, Tsolaki M, Mulugeta E, Aarsland D, Visser PJ, Schroder J, Marcusson J, De Leon M, Hampel H, Scheltens P, Wallin A, Eriksson-Jonhagen M, Minthon L, Winblad B, Blennow K, and Zetterberg H. Age and Diagnostic Performance of Alzheimer Disease CSF Biomarkers. *Neurology*. 2012 Feb 14; 78:468–76. doi: [10.1212/WNL.0b013e3182477eed](https://doi.org/10.1212/WNL.0b013e3182477eed). [Accessed on: 2023 Oct 25] (cited on page 21)

154. Ni M, Zhu ZH, Gao F, Dai LB, Lv XY, Wang Q, Zhu XX, Xie JK, Shen Y, Wang SC, Xie Q, and CANDI Consortium. Plasma Core Alzheimer's Disease Biomarkers Predict Amyloid Deposition Burden by Positron Emission Tomography in Chinese Individuals with Cognitive Decline. *ACS Chem Neurosci*. 2023 Jan 4; 14:170–9. doi: [10.1021/acscchemneuro.2c00636](https://doi.org/10.1021/acscchemneuro.2c00636). [Accessed on: 2023 May 3] (cited on page 22)
155. Bellaver B, Puig-Pijoan A, Ferrari-Souza JP, Leffa DT, Lussier FZ, Ferreira PCL, Tissot C, Povala G, Therriault J, Benedet AL, Ashton NJ, Servaes S, Chamoun M, Stevenson J, Rahmouni N, Vermeiren M, Macedo AC, Fernández-Lebrero A, García-Escobar G, Navalpotro-Gómez I, Lopez O, Tudorascu DL, Cohen A, Villemagne VL, Klunk WE, Gauthier S, Zimmer ER, Karikari TK, Blennow K, Zetterberg H, Suárez-Calvet M, Rosa-Neto P, and Pascoal TA. Blood-brain Barrier Integrity Impacts the Use of Plasma Amyloid- $\beta$  as a Proxy of Brain Amyloid- $\beta$  Pathology. *Alzheimer's & Dementia*. 2023 Mar 15 :alz.13014. doi: [10.1002/alz.13014](https://doi.org/10.1002/alz.13014). [Accessed on: 2023 May 3] (cited on page 22)
156. Desikan RS, Cabral HJ, Hess CP, Dillon WP, Glastonbury CM, Weiner MW, Schmansky NJ, Greve DN, Salat DH, Buckner RL, Fischl B, and Alzheimer's Disease Neuroimaging Initiative. Automated MRI Measures Identify Individuals with Mild Cognitive Impairment and Alzheimer's Disease. *Brain*. 2009 Aug; 132(Pt 8):2048–57. doi: [10.1093/brain/awp123](https://doi.org/10.1093/brain/awp123) (cited on page 22)
157. Grundman M, Sencakova D, Jack CR, Petersen RC, Kim HT, Schultz A, Weiner MF, DeCarli C, DeKosky ST, van Dyck C, Thomas RG, Thal LJ, and Alzheimer's Disease Cooperative Study. Brain MRI Hippocampal Volume and Prediction of Clinical Status in a Mild Cognitive Impairment Trial. *J Mol Neurosci*. 2002; 19:23–7. doi: [10.1007/s12031-002-0006-6](https://doi.org/10.1007/s12031-002-0006-6) (cited on page 22)
158. Chandra A, Dervenoulas G, Politis M, and Alzheimer's Disease Neuroimaging Initiative. Magnetic Resonance Imaging in Alzheimer's Disease and Mild Cognitive Impairment. *J Neurol*. 2019 Jun; 266:1293–302. doi: [10.1007/s00415-018-9016-3](https://doi.org/10.1007/s00415-018-9016-3). [Accessed on: 2023 May 23] (cited on page 22)
159. Capizzano AA. White Matter Hyperintensities Are Significantly Associated with Cortical Atrophy in Alzheimer's Disease. *Journal of Neurology, Neurosurgery & Psychiatry*. 2004 Jun 1; 75:822–7. doi: [10.1136/jnnp.2003.019273](https://doi.org/10.1136/jnnp.2003.019273). [Accessed on: 2023 Jul 3] (cited on page 22)
160. Nesteruk M, Nesteruk T, Styczyńska M, Barczak A, Mandecka M, Walecki J, and Barcikowska-Kotowicz M. Predicting the Conversion of Mild Cognitive Impairment to Alzheimer's Disease Based on the Volumetric Measurements of the Selected Brain Structures in Magnetic Resonance Imaging. *Neurologia i Neurochirurgia Polska*. 2015 Nov; 49:349–53. doi: [10.1016/j.pjnns.2015.09.003](https://doi.org/10.1016/j.pjnns.2015.09.003). [Accessed on: 2023 Jul 3] (cited on page 22)
161. Van Straaten ECW, Harvey D, Scheltens P, Barkhof F, Petersen RC, Thal LJ, Jack CR, DeCarli C, and Alzheimer's Disease Cooperative Study Group. Periventricular White Matter Hyperintensities Increase the Likelihood of Progression from Amnestic

- Mild Cognitive Impairment to Dementia. *J Neurol*. 2008 Sep; 255:1302. doi: [10.1007/s00415-008-0874-y](https://doi.org/10.1007/s00415-008-0874-y). [Accessed on: 2023 Jul 3] (cited on page 22)
162. Tam CW, Burton EJ, McKeith IG, Burn DJ, and O'Brien JT. Temporal Lobe Atrophy on MRI in Parkinson Disease with Dementia: A Comparison with Alzheimer Disease and Dementia with Lewy Bodies. *Neurology*. 2005 Mar 8; 64:861–5. doi: [10.1212/01.WNL.0000153070.82309.D4](https://doi.org/10.1212/01.WNL.0000153070.82309.D4). [Accessed on: 2023 Jul 3] (cited on page 22)
163. Dai W, Lopez OL, Carmichael OT, Becker JT, Kuller LH, and Gach HM. Mild Cognitive Impairment and Alzheimer Disease: Patterns of Altered Cerebral Blood Flow at MR Imaging. *Radiology*. 2009 Mar; 250:856–66. doi: [10.1148/radiol.2503080751](https://doi.org/10.1148/radiol.2503080751). [Accessed on: 2023 Jul 3] (cited on page 22)
164. Greenberg SM, Vernooij MW, Cordonnier C, Viswanathan A, Al-Shahi Salman R, Warach S, Launer LJ, Van Buchem MA, and Breteler MM. Cerebral Microbleeds: A Guide to Detection and Interpretation. *The Lancet Neurology*. 2009 Feb; 8:165–74. doi: [10.1016/S1474-4422\(09\)70013-4](https://doi.org/10.1016/S1474-4422(09)70013-4). [Accessed on: 2022 Feb 8] (cited on pages 23, 153)
165. Sadowski M, Pankiewicz J, Scholtzova H, Li Ys, Quartermain D, Duff K, and Wisniewski T. Links Between the Pathology of Alzheimer's Disease and Vascular Dementia. *Neurochem Res*. 2004 Jun; 29:1257–66. doi: [10.1023/B:NERE.0000023612.66691.e6](https://doi.org/10.1023/B:NERE.0000023612.66691.e6). [Accessed on: 2023 May 2] (cited on pages 23, 153)
166. Ghostine S, Raghavan R, Khanlou N, Vinters HV, Tong KA, Johnson WD, Oyoyo U, and Kido D. Cerebral Amyloid Angiopathy: Micro-Haemorrhages Demonstrated by Magnetic Resonance Susceptibility-Weighted Imaging. *Neuropathol Appl Neurobiol*. 2009 Feb; 35:116–9. doi: [10.1111/j.1365-2990.2008.00976.x](https://doi.org/10.1111/j.1365-2990.2008.00976.x) (cited on page 23)
167. Vonsattel JPG, Myers RH, Tessa Hedley-Whyte E, Ropper AH, Bird ED, and Richardson EP. Cerebral Amyloid Angiopathy without and with Cerebral Hemorrhages: A Comparative Histological Study. *Ann Neurol*. 1991 Nov; 30:637–49. doi: [10.1002/ana.410300503](https://doi.org/10.1002/ana.410300503). [Accessed on: 2022 Feb 8] (cited on pages 23, 154, 155)
168. Idée G, Plaisant O, and Guédon A. Étude des coupes dites « de Charcot » et « de Flechsig » : des descriptions princeps au recalage dans le BigBrain. *Morphologie*. 2019 Nov; 103:118. doi: [10.1016/j.morpho.2019.09.027](https://doi.org/10.1016/j.morpho.2019.09.027). [Accessed on: 2023 May 3] (cited on page 23)
169. Rauramaa T, Pikkarainen M, Englund E, Ince PG, Jellinger K, Paetau A, and Alafuzoff I. Consensus Recommendations on Pathologic Changes in the Hippocampus: A Postmortem Multicenter Inter-Rater Study. *J Neuropathol Exp Neurol*. 2013 Jun; 72:452–61. doi: [10.1097/NEN.0b013e318292492a](https://doi.org/10.1097/NEN.0b013e318292492a). [Accessed on: 2023 May 3] (cited on page 24)
170. Alafuzoff I, Pikkarainen M, Arzberger T, Thal DR, Al-Sarraj S, Bell J, Bodi I, Budka H, Capetillo-Zarate E, Ferrer I, Gelpi E, Gentleman S, Giaccone G, Kavantzias N, King A, Korkolopoulou P, Kovács GG, Meyronet D, Monoranu C, Parchi P, Patsouris E, Roggendorf W, Stadelmann C, Streichenberger N, Tagliavini F, and Kretschmar H. Inter-Laboratory Comparison of Neuropathological Assessments of  $\beta$ -Amyloid

- Protein: A Study of the BrainNet Europe Consortium. *Acta Neuropathol.* 2008 May; 115:533–46. DOI: [10.1007/s00401-008-0358-2](https://doi.org/10.1007/s00401-008-0358-2). [Accessed on: 2022 Nov 26] (cited on page 25)
171. Divry P. Etude Histochimique Des Plaques Seniles. *J Belge Neurol Psychiat.* 1927; 27:643–57 (cited on page 25)
  172. Johansson GA and Pfeiffer HH. On the Amyloid-Congo Red Complex in Histological Sections and the Genesis of the Amyloid Substance. *Cells Tissues Organs.* 1954; 20:285–90. DOI: [10.1159/000140904](https://doi.org/10.1159/000140904). [Accessed on: 2023 May 4] (cited on page 25)
  173. Puchtler H and Sweat F. Congo Red as a Stain for Fluorescence Microscopy of Amyloid. *J Histochem Cytochem.* 1965 Nov; 13:693–4. DOI: [10.1177/13.8.693](https://doi.org/10.1177/13.8.693). [Accessed on: 2023 May 4] (cited on page 25)
  174. Hewlett BR. Studies on the Staining of Amyloid with Congo Red. *Can J Med Technol.* 1966 Dec; 28:248–61 (cited on page 25)
  175. Kelényi G. Thioflavin S Fluorescent and Congo Red Anisotropic Stainings in the Histologic Demonstration of Amyloid. *Acta Neuropathol.* 1967; 7:336–48. DOI: [10.1007/BF00688089](https://doi.org/10.1007/BF00688089). [Accessed on: 2023 May 4] (cited on page 25)
  176. Hobbs JR and Morgan AD. Fluorescence Microscopy with Thioflavine-T in the Diagnosis of Amyloid. *J Pathol.* 1963 Oct; 86:437–42. DOI: [10.1002/path.1700860218](https://doi.org/10.1002/path.1700860218). [Accessed on: 2023 May 4] (cited on page 25)
  177. Gallyas F. Silver Staining of Alzheimer's Neurofibrillary Changes by Means of Physical Development. *Acta Morphol Acad Sci Hung.* 1971; 19:1–8 (cited on page 25)
  178. Wisniewski HM, Wen GY, and Kim KS. Comparison of Four Staining Methods on the Detection of Neuritic Plaques. *Acta Neuropathol.* 1989; 78:22–7. DOI: [10.1007/BF00687398](https://doi.org/10.1007/BF00687398). [Accessed on: 2023 May 4] (cited on page 25)
  179. Braak H, Braak E, Ohm T, and Bohl J. Silver Impregnation of Alzheimer's Neurofibrillary Changes Counterstained for Basophilic Material and Lipofuscin Pigment. *Stain Technology.* 1988 Jan; 63:197–200. DOI: [10.3109/10520298809107184](https://doi.org/10.3109/10520298809107184). [Accessed on: 2023 May 4] (cited on page 25)
  180. Alafuzoff I, Pikkarainen M, Al-Sarraj S, Arzberger T, Bell J, Bodi I, Bogdanovic N, Budka H, Bugiani O, Ferrer I, Gelpi E, Giaccone G, Graeber MB, Hauw JJ, Kamphorst W, King A, Kopp N, Korkolopoulou P, Kovács GG, Meyronet D, Parchi P, Patsouris E, Preusser M, Ravid R, Roggendorf W, Seilhean D, Streichenberger N, Thal DR, and Kretschmar H. Interlaboratory Comparison of Assessments of Alzheimer Disease-Related Lesions: A Study of the BrainNet Europe Consortium. *J Neuropathol Exp Neurol.* 2006 Aug; 65:740–57. DOI: [10.1097/01.jnen.0000229986.17548.27](https://doi.org/10.1097/01.jnen.0000229986.17548.27). [Accessed on: 2022 Nov 26] (cited on page 25)

181. Mirra SS, Heyman A, McKeel D, Sumi SM, Crain BJ, Brownlee LM, Vogel FS, Hughes JP, Belle G v., Berg L, and participating CERAD neuropathologists. The Consortium to Establish a Registry for Alzheimer's Disease (CERAD). Part II. Standardization of the Neuropathologic Assessment of Alzheimer's Disease. *Neurology*. 1991 Apr 1; 41:479–9. doi: [10.1212/WNL.41.4.479](https://doi.org/10.1212/WNL.41.4.479). [Accessed on: 2021 Aug 17] (cited on pages 26, 155)
182. Thal DR, Rüb U, Orantes M, and Braak H. Phases of A Beta-Deposition in the Human Brain and Its Relevance for the Development of AD. *Neurology*. 2002 Jun 25; 58:1791–800. doi: [10.1212/wnl.58.12.1791](https://doi.org/10.1212/wnl.58.12.1791) (cited on pages 26, 27, 155)
183. Braak H and Braak E. Neuropathological Staging of Alzheimer-related Changes. *Acta Neuropathol*. 1991; 82:239–59. doi: [10.1007/BF00308809](https://doi.org/10.1007/BF00308809) (cited on page 27)
184. Braak H, Alafuzoff I, Arzberger T, Kretschmar H, and Del Tredici K. Staging of Alzheimer Disease-Associated Neurofibrillary Pathology Using Paraffin Sections and Immunocytochemistry. *Acta Neuropathol*. 2006 Oct; 112:389–404. doi: [10.1007/s00401-006-0127-z](https://doi.org/10.1007/s00401-006-0127-z) (cited on pages 27, 28, 155)
185. Consensus Recommendations for the Postmortem Diagnosis of Alzheimer's Disease. The National Institute on Aging, and Reagan Institute Working Group on Diagnostic Criteria for the Neuropathological Assessment of Alzheimer's Disease. *Neurobiol Aging*. 1997; 18(4 Suppl):S1–2 (cited on page 27)
186. Stucht D, Danishad KA, Schulze P, Godenschweger F, Zaitsev M, and Speck O. Highest Resolution In Vivo Human Brain MRI Using Prospective Motion Correction. *PLoS ONE*. 2015 Jul 30; 10. Ed. by Kassubek J:e0133921. doi: [10.1371/journal.pone.0133921](https://doi.org/10.1371/journal.pone.0133921). [Accessed on: 2023 Oct 29] (cited on page 29)
187. Sloots JJ, Biessels GJ, and Zwanenburg JJ. Cardiac and Respiration-Induced Brain Deformations in Humans Quantified with High-Field MRI. *NeuroImage*. 2020 Apr; 210:116581. doi: [10.1016/j.neuroimage.2020.116581](https://doi.org/10.1016/j.neuroimage.2020.116581). [Accessed on: 2023 Oct 29] (cited on page 29)
188. Croton L, Crossley K, McDonald C, Morgan K, Penny T, Galinsky R, Hooper S, Ruben G, Pollock J, Schaff F, Croughan M, Sutherland A, and Kitchen M. Pre-Clinical Phase-Contrast Imaging of the Whole Brain in Situ: From Traumatic to Diffuse White Matter Injury. *Developments in X-Ray Tomography XIV*. *Developments in X-Ray Tomography XIV*. Ed. by Müller B and Wang G. San Diego, United States: SPIE, 2022 Nov 10:45. doi: [10.1117/12.2633340](https://doi.org/10.1117/12.2633340). [Accessed on: 2023 Oct 29] (cited on page 29)
189. Stewart F, Akleyev A, Hauer-Jensen M, Hendry J, Kleiman N, MacVittie T, Aleman B, Edgar A, Mabuchi K, Muirhead C, Shore R, and Wallace W. ICRP PUBLICATION 118: ICRP Statement on Tissue Reactions and Early and Late Effects of Radiation in Normal Tissues and Organs — Threshold Doses for Tissue Reactions in a Radiation Protection Context. *Ann ICRP*. 2012 Feb; 41. Ed. by Clement C:1–322. doi: [10.1016/j.icrp.2012.02.001](https://doi.org/10.1016/j.icrp.2012.02.001). [Accessed on: 2023 Oct 29] (cited on page 29)

190. Chourrout M, Rositi H, Ong E, Hubert V, Paccalet A, Foucault L, Autret A, Fayard B, Olivier C, Bolbos R, Peyrin F, Crola-da-Silva C, Meyronet D, Raineteau O, Elleaume H, Brun E, Chauveau F, and Wiart M. Brain Virtual Histology with X-ray Phase-Contrast Tomography Part I: Whole-Brain Myelin Mapping in White-Matter Injury Models. *Biomed Opt Express*. 2022 Mar 1; 13:1620. doi: [10.1364/B0E.438832](https://doi.org/10.1364/B0E.438832) (cited on pages 29, 58, 111, 154, 158, 175)
191. Wang Q, Ding SL, Li Y, Royall J, Feng D, Lesnar P, Graddis N, Naemi M, Facer B, Ho A, Dolbeare T, Blanchard B, Dee N, Wakeman W, Hirokawa KE, Szafer A, Sunkin SM, Oh SW, Bernard A, Phillips JW, Hawrylycz M, Koch C, Zeng H, Harris JA, and Ng L. The Allen Mouse Brain Common Coordinate Framework: A 3D Reference Atlas. *Cell*. 2020 May; 181:936–953.e20. doi: [10.1016/j.cell.2020.04.007](https://doi.org/10.1016/j.cell.2020.04.007). [Accessed on: 2023 Nov 7] (cited on pages 29, 57, 89, 111)
192. Waxholm Space Atlas of the Sprague Dawley Rat Brain. RRID: SCR\_017124 (cited on pages 29, 57, 89, 111)
193. Papp EA, Leergaard TB, Calabrese E, Johnson GA, and Bjaalie JG. Waxholm Space Atlas of the Sprague Dawley Rat Brain. *Neuroimage*. 2014 Aug 15; 97:374–86. doi: [10.1016/j.neuroimage.2014.04.001](https://doi.org/10.1016/j.neuroimage.2014.04.001) (cited on pages 29, 57, 89, 111)
194. Papp EA, Leergaard TB, Calabrese E, Allan Johnson G, and Bjaalie JG. Addendum to “Waxholm Space Atlas of the Sprague Dawley Rat Brain” [*NeuroImage* 97 (2014) 374–386]. *NeuroImage*. 2015 Jan; 105:561–2. doi: [10.1016/j.neuroimage.2014.10.017](https://doi.org/10.1016/j.neuroimage.2014.10.017). [Accessed on: 2023 Nov 7] (cited on pages 29, 57, 89, 111)
195. Research Models Database. Alzheimer Research Forum. Available from: <https://www.alzforum.org/research-models/alzheimers-disease> [Accessed on: 2023 Apr 3] (cited on pages 29, 30)
196. Leskovjan AC, Lanzirotti A, and Miller LM. Amyloid Plaques in PSAPP Mice Bind Less Metal than Plaques in Human Alzheimer’s Disease. *NeuroImage*. 2009 Oct; 47(4):1215–20. doi: [10.1016/j.neuroimage.2009.05.063](https://doi.org/10.1016/j.neuroimage.2009.05.063). [Accessed on: 2021 Apr 12] (cited on pages 30, 32, 149, 150)
197. Scheffer S, Hermkens DM, Van Der Weerd L, De Vries HE, and Daemen MJ. Vascular Hypothesis of Alzheimer Disease: Topical Review of Mouse Models. *ATVB*. 2021 Apr; 41:1265–83. doi: [10.1161/ATVBAHA.120.311911](https://doi.org/10.1161/ATVBAHA.120.311911). [Accessed on: 2023 Jul 4] (cited on pages 30, 153)
198. Fu H and Cui M. Fluorescent Imaging of Amyloid- $\beta$  Deposits in Brain: An Overview of Probe Development and a Highlight of the Applications for In Vivo Imaging. *CMC*. 2018 Jul 4; 25:2736–59. doi: [10.2174/0929867325666180214110024](https://doi.org/10.2174/0929867325666180214110024). [Accessed on: 2023 Jul 4] (cited on page 31)
199. Tao R, Wang N, Shen T, Tan Y, Ren Y, Wei W, Liao M, Tan D, Tang C, Xu N, Wang H, Liu X, and Li X. High-Fidelity Imaging of Amyloid-Beta Deposits with an Ultrasensitive Fluorescent Probe Facilitates the Early Diagnosis and Treatment of Alzheimer’s Disease. *Theranostics*. 2022; 12:2549–59. doi: [10.7150/thno.68743](https://doi.org/10.7150/thno.68743). [Accessed on: 2023 Jul 4] (cited on page 31)

200. Cao Y, Liu X, Zhang J, Liu Z, Fu Y, Zhang D, Zheng M, Zhang H, and Xu MH. Design of a Coumarin-Based Fluorescent Probe for Efficient *In Vivo* Imaging of Amyloid- $\beta$  Plaques. *ACS Chem Neurosci*. 2023 Mar 1; 14:829–38. doi: [10.1021/acscchemneuro.2c00468](https://doi.org/10.1021/acscchemneuro.2c00468). [Accessed on: 2023 Jul 4] (cited on page 31)
201. Ni R, Chen Z, Deán-Ben XL, Voigt FF, Kirschenbaum D, Shi G, Villois A, Zhou Q, Crimi A, Arosio P, Nitsch RM, Nilsson KPR, Aguzzi A, Helmchen F, Klohs J, and Razansky D. Multiscale Optical and Optoacoustic Imaging of Amyloid- $\beta$  Deposits in Mice. *Nat Biomed Eng*. 2022 Jul 14; 6:1031–44. doi: [10.1038/s41551-022-00906-1](https://doi.org/10.1038/s41551-022-00906-1). [Accessed on: 2023 Mar 29] (cited on page 31)
202. Cheng KK, Chan PS, Fan S, Kwan SM, Yeung KL, Wáng YXJ, Chow AHL, Wu EX, and Baum L. Curcumin-Conjugated Magnetic Nanoparticles for Detecting Amyloid Plaques in Alzheimer’s Disease Mice Using Magnetic Resonance Imaging (MRI). *Biomaterials*. 2015 Mar; 44:155–72. doi: [10.1016/j.biomaterials.2014.12.005](https://doi.org/10.1016/j.biomaterials.2014.12.005). [Accessed on: 2023 May 25] (cited on page 31)
203. Lerouge F, Ong E, Rositi H, Mpambani F, Berner LP, Bolbos R, Olivier C, Peyrin F, Apputukan VK, Monnereau C, Andraud C, Chaput F, Berthezène Y, Braun B, Jucker M, Åslund AK, Nyström S, Hammarström P, R Nilsson KP, Lindgren M, Wiart M, Chauveau F, and Parola S. In Vivo Targeting and Multimodal Imaging of Cerebral Amyloid- $\beta$  Aggregates Using Hybrid GdF3 Nanoparticles. *Nanomedicine (Lond)*. 2022 Dec; 17:2173–87. doi: [10.2217/nnm-2022-0252](https://doi.org/10.2217/nnm-2022-0252) (cited on page 31)
204. Lombardo SM, Schneider M, Türeli AE, and Günday Türeli N. Key for Crossing the BBB with Nanoparticles: The Rational Design. *Beilstein J Nanotechnol*. 2020 Jun 4; 11:866–83. doi: [10.3762/bjnano.11.72](https://doi.org/10.3762/bjnano.11.72). [Accessed on: 2023 Jul 11] (cited on page 31)
205. Lim JKH, Li QX, Ryan T, Bedggood P, Metha A, Vingrys AJ, Bui BV, and Nguyen CTO. Retinal Hyperspectral Imaging in the 5xFAD Mouse Model of Alzheimer’s Disease. *Sci Rep*. 2021 Mar 18; 11:6387. doi: [10.1038/s41598-021-85554-2](https://doi.org/10.1038/s41598-021-85554-2). [Accessed on: 2023 May 25] (cited on page 31)
206. Song A, Johnson N, Ayala A, and Thompson AC. Optical Coherence Tomography in Patients with Alzheimer’s Disease: What Can It Tell Us? *EB*. 2021 Jan; Volume 13:1–20. doi: [10.2147/EB.S235238](https://doi.org/10.2147/EB.S235238). [Accessed on: 2023 Oct 29] (cited on page 31)
207. Miller LM, Bourassa MW, and Smith RJ. FTIR Spectroscopic Imaging of Protein Aggregation in Living Cells. *Biochim Biophys Acta*. 2013 Oct; 1828:2339–46. doi: [10.1016/j.bbamem.2013.01.014](https://doi.org/10.1016/j.bbamem.2013.01.014) (cited on page 32)
208. Collingwood JF and Adams F. Chemical Imaging Analysis of the Brain with X-ray Methods. *Spectrochimica Acta Part B: Atomic Spectroscopy*. 2017 Apr; 130:101–18. doi: [10.1016/j.sab.2017.02.013](https://doi.org/10.1016/j.sab.2017.02.013). [Accessed on: 2023 May 26] (cited on pages 32, 52)
209. Surowka AD, Czyzycki M, Ziomber-Lisiak A, Migliori A, and Szczerbowska-Boruchowska M. On 2D-FTIR-XRF Microscopy – A Step Forward Correlative Tissue Studies by Infrared and Hard X-ray Radiation. *Ultramicroscopy*. 2022 Jan; 232:113408. doi: [10.1016/j.ultramicro.2021.113408](https://doi.org/10.1016/j.ultramicro.2021.113408). [Accessed on: 2022 Apr 7] (cited on page 32)

210. Noda-Saita K, Yoneyama A, Shitaka Y, Hirai Y, Terai K, Wu J, Takeda T, Hyodo K, Osakabe N, Yamaguchi T, and Okada M. Quantitative Analysis of Amyloid Plaques in a Mouse Model of Alzheimer's Disease by Phase-Contrast X-ray Computed Tomography. *Neuroscience*. 2006; 138(4):1205–13. doi: [10.1016/j.neuroscience.2005.12.036](https://doi.org/10.1016/j.neuroscience.2005.12.036) (cited on pages 32, 33, 108, 111, 154)
211. Albers J, Pacilé S, Markus MA, Wiart M, Vande Velde G, Tromba G, and Dullin C. X-Ray-Based 3D Virtual Histology-Adding the Next Dimension to Histological Analysis. *Mol Imaging Biol*. 2018 Oct; 20(5):732–41. doi: [10.1007/s11307-018-1246-3](https://doi.org/10.1007/s11307-018-1246-3) (cited on page 32)
212. Bulk M, Abdelmoula WM, Nabuurs RJA, van der Graaf LM, Mulders CWH, Mulder AA, Jost CR, Koster AJ, van Buchem MA, Natté R, Dijkstra J, and van der Weerd L. Postmortem MRI and Histology Demonstrate Differential Iron Accumulation and Cortical Myelin Organization in Early- and Late-Onset Alzheimer's Disease. *Neurobiol Aging*. 2018 Feb; 62:231–42. doi: [10.1016/j.neurobiolaging.2017.10.017](https://doi.org/10.1016/j.neurobiolaging.2017.10.017) (cited on page 32)
213. Gómez-Gaviro MV, Sanderson D, Ripoll J, and Desco M. Biomedical Applications of Tissue Clearing and Three-Dimensional Imaging in Health and Disease. *iScience*. 2020 Aug; 23:101432. doi: [10.1016/j.isci.2020.101432](https://doi.org/10.1016/j.isci.2020.101432). [Accessed on: 2021 Oct 19] (cited on page 32)
214. Bulk M, van der Weerd L, Breimer W, Lebedev N, Webb A, Goeman JJ, Ward RJ, Huber M, Oosterkamp TH, and Bossoni L. Quantitative Comparison of Different Iron Forms in the Temporal Cortex of Alzheimer Patients and Control Subjects. *Sci Rep*. 2018 May 2; 8:6898. doi: [10.1038/s41598-018-25021-7](https://doi.org/10.1038/s41598-018-25021-7) (cited on page 32)
215. De Barros A, Arribarat G, Combis J, Chaynes P, and Péran P. Matching Ex Vivo MRI With Iron Histology: Pearls and Pitfalls. *Front Neuroanat*. 2019 Jul 3; 13:68. doi: [10.3389/fnana.2019.00068](https://doi.org/10.3389/fnana.2019.00068). [Accessed on: 2023 Jul 11] (cited on page 32)
216. Dhenain M, El Tannir El Tayara N, Wu TD, Guégan M, Volk A, Quintana C, and Delatour B. Characterization of in Vivo MRI Detectable Thalamic Amyloid Plaques from APP/PS1 Mice. *Neurobiol Aging*. 2009 Jan; 30:41–53. doi: [10.1016/j.neurobiolaging.2007.05.018](https://doi.org/10.1016/j.neurobiolaging.2007.05.018) (cited on pages 32, 111, 150)
217. Duffeffant C, Vandesquille M, Herbert K, Garin CM, Alves S, Blanchard V, Comoy EE, Petit F, and Dhenain M. Contrast-Enhanced MR Microscopy of Amyloid Plaques in Five Mouse Models of Amyloidosis and in Human Alzheimer's Disease Brains. *Sci Rep*. 2017 Jul 10; 7:4955. doi: [10.1038/s41598-017-05285-1](https://doi.org/10.1038/s41598-017-05285-1). [Accessed on: 2023 Jul 11] (cited on page 32)
218. Costantini I, Cicchi R, Silvestri L, Vanzi F, and Pavone FS. In-Vivo and Ex-Vivo Optical Clearing Methods for Biological Tissues: Review. *Biomed Opt Express*. 2019 Oct 1; 10:5251. doi: [10.1364/B0E.10.005251](https://doi.org/10.1364/B0E.10.005251). [Accessed on: 2023 Mar 29] (cited on page 32)
219. Genina EA. Tissue Optical Clearing: State of the Art and Prospects. *Diagnostics*. 2022 Jun 23; 12:1534. doi: [10.3390/diagnostics12071534](https://doi.org/10.3390/diagnostics12071534). [Accessed on: 2023 Mar 29] (cited on pages 32, 48)

220. Ando K, Laborde Q, Lazar A, Godefroy D, Youssef I, Amar M, Pooler A, Potier MC, Delatour B, and Duyckaerts C. Inside Alzheimer Brain with CLARITY: Senile Plaques, Neurofibrillary Tangles and Axons in 3-D. *Acta Neuropathol.* 2014 Sep; 128(3):457–9. DOI: [10.1007/s00401-014-1322-y](https://doi.org/10.1007/s00401-014-1322-y). [Accessed on: 2020 Aug 4] (cited on page 32)
221. Liebmann T, Renier N, Bettayeb K, Greengard P, Tessier-Lavigne M, and Flajolet M. Three-Dimensional Study of Alzheimer’s Disease Hallmarks Using the iDISCO Clearing Method. *Cell Reports.* 2016 Jul; 16:1138–52. DOI: [10.1016/j.celrep.2016.06.060](https://doi.org/10.1016/j.celrep.2016.06.060). [Accessed on: 2021 Jul 23] (cited on page 32)
222. Merlini M, Sozmen EG, Subramanian KS, Nana AL, Seeley WW, and Akassoglou K. Three-Dimensional Imaging of Fibrinogen and Neurovascular Alterations in Alzheimer’s Disease. *Alzheimer’s Disease.* Ed. by Chun J. Vol. 2561. New York, NY: Springer US, 2023 :87–101. DOI: [10.1007/978-1-0716-2655-9\\_5](https://doi.org/10.1007/978-1-0716-2655-9_5). [Accessed on: 2023 Jul 4] (cited on pages 32, 33)
223. Kirschenbaum D, Dadgar-Kiani E, Catto F, Voigt FF, Trevisan C, Bichsel O, Shirani H, Nilsson KPR, Frontzek KJ, Paganetti P, Helmchen F, Lee JH, and Aguzzi A. Whole-brain Microscopy Reveals Distinct Temporal and Spatial Efficacy of anti-A $\beta$  Therapies. *EMBO Mol Med.* 2023 Jan 11; 15:e16789. DOI: [10.15252/emmm.202216789](https://doi.org/10.15252/emmm.202216789). [Accessed on: 2023 Jul 4] (cited on page 32)
224. Di Giovanna AP, Tibo A, Silvestri L, Müllenbroich MC, Costantini I, Sacconi L, Frasconi P, and Pavone FS. Optimal Staining and Clearing Protocol for Whole Mouse Brain Vasculature Imaging with Light-Sheet Microscopy. *European Conferences on Biomedical Optics.* Ed. by Beaurepaire E, Pavone FS, and So PTC. Munich, Germany, 2017 Jul 28:104140N. DOI: [10.1117/12.2285044](https://doi.org/10.1117/12.2285044). [Accessed on: 2023 Jul 4] (cited on page 32)
225. Bennett HC and Kim Y. Advances in Studying Whole Mouse Brain Vasculature Using High-Resolution 3D Light Microscopy Imaging. *Neurophoton.* 2022 Apr 5; 9. DOI: [10.1117/1.NPh.9.2.021902](https://doi.org/10.1117/1.NPh.9.2.021902). [Accessed on: 2023 Jul 4] (cited on page 32)
226. Zhang X, Yin X, Zhang J, Li A, Gong H, Luo Q, Zhang H, Gao Z, and Jiang H. High-Resolution Mapping of Brain Vasculature and Its Impairment in the Hippocampus of Alzheimer’s Disease Mice. *National Science Review.* 2019 Nov 1; 6:1223–38. DOI: [10.1093/nsr/nwz124](https://doi.org/10.1093/nsr/nwz124). [Accessed on: 2023 Jul 4] (cited on page 33)
227. Sarri B, Poizat F, Heuke S, Wojak J, Franchi F, Caillol F, Giovannini M, and Rigneault H. Stimulated Raman Histology: One to One Comparison with Standard Hematoxylin and Eosin Staining. *Biomed Opt Express.* 2019 Oct 1; 10:5378–84. DOI: [10.1364/B0E.10.005378](https://doi.org/10.1364/B0E.10.005378) (cited on page 33)
228. Kavkova M, Zikmund T, Kala A, Salplachta J, Proskauer Pena SL, Kaiser J, and Jezek K. Contrast Enhanced X-ray Computed Tomography Imaging of Amyloid Plaques in Alzheimer Disease Rat Model on Lab Based Micro CT System. *Sci Rep.* 2021 Dec; 11:5999. DOI: [10.1038/s41598-021-84579-x](https://doi.org/10.1038/s41598-021-84579-x). [Accessed on: 2022 Jul 7] (cited on page 33)

229. Balcaen T, Piens C, Mwema A, Chourrout M, Vandebroek L, Des Rieux A, Chauveau F, De Borggraeve WM, Hoffmann D, and Kerckhofs G. Revealing the Three-Dimensional Murine Brain Microstructure by Contrast-Enhanced Computed Tomography. *Front Neurosci.* 2023 Mar 23; 17:1141615. doi: [10.3389/fnins.2023.1141615](https://doi.org/10.3389/fnins.2023.1141615) (cited on pages 33, 86, 175)
230. Barbone GE, Bravin A, Mittone A, Pacureanu A, Mascio G, Di Pietro P, Kraiger MJ, Eckermann M, Romano M, Hrabě de Angelis M, Cloetens P, Bruno V, Battaglia G, and Coan P. X-Ray Multiscale 3D Neuroimaging to Quantify Cellular Aging and Neurodegeneration Postmortem in a Model of Alzheimer's Disease. *Eur J Nucl Med Mol Imaging.* 2022 Jul 19. doi: [10.1007/s00259-022-05896-5](https://doi.org/10.1007/s00259-022-05896-5). [Accessed on: 2022 Aug 29] (cited on pages 33, 108, 111, 154)
231. Pinzer B, Cacquevel M, Modregger P, McDonald S, Bensadoun J, Thuering T, Aebischer P, and Stampanoni M. Imaging Brain Amyloid Deposition Using Grating-Based Differential Phase Contrast Tomography. *NeuroImage.* 2012 Jul; 61(4):1336–46. doi: [10.1016/j.neuroimage.2012.03.029](https://doi.org/10.1016/j.neuroimage.2012.03.029). [Accessed on: 2020 Aug 4] (cited on pages 33, 108, 111, 154)
232. Astolfo A, Lathuilière A, Laversenne V, Schneider B, and Stampanoni M. Amyloid- $\beta$  Plaque Deposition Measured Using Propagation-Based X-ray Phase Contrast CT Imaging. *J Synchrotron Rad.* 2016 May 1; 23(3):813–9. doi: [10.1107/S1600577516004045](https://doi.org/10.1107/S1600577516004045). [Accessed on: 2020 Aug 4] (cited on pages 33, 108, 111, 154)
233. Töpferwien M, Krenkel M, Vincenz D, Stöber F, Oelschlegel AM, Goldschmidt J, and Salditt T. Three-Dimensional Mouse Brain Cytoarchitecture Revealed by Laboratory-Based x-Ray Phase-Contrast Tomography. *Sci Rep.* 2017 Feb 27; 7:42847. doi: [10.1038/srep42847](https://doi.org/10.1038/srep42847) (cited on pages 33, 85, 108, 111, 154)
234. Massimi L, Bukreeva I, Santamaria G, Fratini M, Corbelli A, Brun F, Fumagalli S, Maugeri L, Pacureanu A, Cloetens P, Pieroni N, Fiordaliso F, Forloni G, Uccelli A, Kerlero de Rosbo N, Balducci C, and Cedola A. Exploring Alzheimer's Disease Mouse Brain through X-ray Phase Contrast Tomography: From the Cell to the Organ. *NeuroImage.* 2019 Jan; 184:490–5. doi: [10.1016/j.neuroimage.2018.09.044](https://doi.org/10.1016/j.neuroimage.2018.09.044). [Accessed on: 2020 Aug 4] (cited on pages 33, 108, 111, 154)
235. Massimi L, Pieroni N, Maugeri L, Fratini M, Brun F, Bukreeva I, Santamaria G, Medici V, Poloni TE, Balducci C, and Cedola A. Assessment of Plaque Morphology in Alzheimer's Mouse Cerebellum Using Three-Dimensional X-ray Phase-Based Virtual Histology. *Scientific reports.* 2020; 10(1):11233. doi: [10.1038/s41598-020-68045-8](https://doi.org/10.1038/s41598-020-68045-8) (cited on pages 33, 108, 111, 154)
236. Töpferwien M, van der Meer F, Stadelmann C, and Salditt T. Correlative X-Ray Phase-Contrast Tomography and Histology of Human Brain Tissue Affected by Alzheimer's Disease. *NeuroImage.* 2020 Apr; 210:116523. doi: [10.1016/j.neuroimage.2020.116523](https://doi.org/10.1016/j.neuroimage.2020.116523). [Accessed on: 2020 Aug 4] (cited on pages 33, 86, 108, 111, 150, 154)

237. Palermo F, Pieroni N, Maugeri L, Provinciali GB, Sanna A, Massimi L, Catalano M, Olbinado MP, Bukreeva I, Fratini M, Uccelli A, Gigli G, Kerlero de Rosbo N, Balducci C, and Cedola A. X-Ray Phase Contrast Tomography Serves Preclinical Investigation of Neurodegenerative Diseases. *Front Neurosci.* 2020; 14:584161. doi: [10.3389/fnins.2020.584161](https://doi.org/10.3389/fnins.2020.584161) (cited on pages 33, 108, 111, 154)
238. Chourrout M, Roux M, Boisvert C, Gislard C, Legland D, Arganda-Carreras I, Olivier C, Peyrin F, Boutin H, Rama N, Baron T, Meyronet D, Brun E, Rositi H, Wiart M, and Chauveau F. Brain Virtual Histology with X-ray Phase-Contrast Tomography Part II: 3D Morphologies of Amyloid- $\beta$  Plaques in Alzheimer's Disease Models. *Biomed Opt Express.* 2022 Mar 1; 13:1640. doi: [10.1364/B0E.438890](https://doi.org/10.1364/B0E.438890) (cited on pages 33, 89, 111, 154, 175)
239. Balerna A and Mobilio S. Introduction to Synchrotron Radiation. *Synchrotron Radiation*. Ed. by Mobilio S, Boscherini F, and Meneghini C. Berlin, Heidelberg: Springer Berlin Heidelberg, 2015 :3–28. doi: [10.1007/978-3-642-55315-8\\_1](https://doi.org/10.1007/978-3-642-55315-8_1). [Accessed on: 2023 Jun 23] (cited on pages 35, 37)
240. Margaritondo G. Introduction to Synchrotron Radiation. New York: Oxford Univ. Press, 1988. 280 pp. (cited on page 35)
241. Bharti A and Goyal N. Fundamental of Synchrotron Radiations. *Synchrotron Radiation - Useful and Interesting Applications*. Ed. by Joseph D. IntechOpen, 2019 May 10. doi: [10.5772/intechopen.82202](https://doi.org/10.5772/intechopen.82202). [Accessed on: 2023 Jun 23] (cited on page 36)
242. Von Bohlen A and Tolan M. Editorial for Synchrotron Radiation. *J Anal At Spectrom.* 2008; 23:790. doi: [10.1039/b804010a](https://doi.org/10.1039/b804010a). [Accessed on: 2023 Jun 23] (cited on page 36)
243. Mitchell E, Kuhn P, and Garman E. Demystifying the Synchrotron Trip: A First Time User's Guide. *Structure.* 1999 May; 7:R111–R121. doi: [10.1016/S0969-2126\(99\)80063-X](https://doi.org/10.1016/S0969-2126(99)80063-X). [Accessed on: 2023 Jun 23] (cited on page 37)
244. Jackson JD. Classical Electrodynamics. 3rd ed. New York: Wiley, 1999. 808 pp. (cited on page 38)
245. Hwu Y, Margaritondo G, and Chiang AS. Q&A: Why Use Synchrotron x-Ray Tomography for Multi-Scale Connectome Mapping? *BMC Biol.* 2017 Dec 21; 15(1):122. doi: [10.1186/s12915-017-0461-8](https://doi.org/10.1186/s12915-017-0461-8) (cited on page 38)
246. Pithan L. On the Role of External Stimuli to Tailor Growth of Organic Thin Films. PhD thesis. Humboldt-Universität zu Berlin, Mathematisch-Naturwissenschaftliche Fakultät, 2017 Apr 13. doi: [10.18452/17749](https://doi.org/10.18452/17749). [Accessed on: 2023 Jun 26] (cited on page 38)
247. Motz H. Applications of the Radiation from Fast Electron Beams. *Journal of Applied Physics.* 1951 May; 22:527–35. doi: [10.1063/1.1700002](https://doi.org/10.1063/1.1700002). [Accessed on: 2023 Jun 23] (cited on page 38)
248. Kulipanov GN. Ginzburg's Invention of Undulators and Their Role in Modern Synchrotron Radiation Sources and Free Electron Lasers. *Phys-Usp.* 2007 Apr 30; 50:368–76. doi: [10.1070/PU2007v050n04ABEH006237](https://doi.org/10.1070/PU2007v050n04ABEH006237). [Accessed on: 2023 Jun 23] (cited on page 38)

249. Margaritondo G. Characteristics and Properties of Synchrotron Radiation. *Synchrotron Radiation*. Ed. by Mobilio S, Boscherini F, and Meneghini C. Berlin, Heidelberg: Springer Berlin Heidelberg, 2015 :29–63. doi: [10.1007/978-3-642-55315-8\\_2](https://doi.org/10.1007/978-3-642-55315-8_2). [Accessed on: 2023 Jun 23] (cited on page 38)
250. Weitkamp T, Scheel M, Giorgetta J, Joyet V, Le Roux V, Cauchon G, Moreno T, Polack F, Thompson A, and Samama J. The Tomography Beamline ANATOMIX at Synchrotron SOLEIL. *J Phys: Conf Ser.* 2017 Jun; 849:012037. doi: [10.1088/1742-6596/849/1/012037](https://doi.org/10.1088/1742-6596/849/1/012037). [Accessed on: 2023 Jun 28] (cited on page 39)
251. Braag WH and Braag L. The Reflection of X-rays by Crystals. *Proc R Soc Lond A.* 1913 Jul; 88:428–38. doi: [10.1098/rspa.1913.0040](https://doi.org/10.1098/rspa.1913.0040). [Accessed on: 2023 Jun 28] (cited on page 39)
252. Shin S. New Era of Synchrotron Radiation: Fourth-Generation Storage Ring. *AAPPS Bull.* 2021 Dec; 31:21. doi: [10.1007/s43673-021-00021-4](https://doi.org/10.1007/s43673-021-00021-4). [Accessed on: 2023 Jun 27] (cited on page 39)
253. Raimondi P, Benabderrahmane C, Berkvens P, Biasci JC, Borowiec P, Bouteille JF, Brochard T, Brookes NB, Carmignani N, Carver LR, Chaize JM, Chavanne J, Checchia S, Chushkin Y, Cianciosi F, Di Michiel M, Dimper R, D’Elia A, Einfeld D, Ewald F, Farvacque L, Goirand L, Hardy L, Jacob J, Jolly L, Krisch M, Le Bec G, Leconte I, Liuzzo SM, Maccarrone C, Marchial T, Martin D, Mezouar M, Nevo C, Perron T, Plouviez E, Reichert H, Renaud P, Revol JL, Roche B, Scheidt KB, Serriere V, Sette F, Susini J, Torino L, Versteegen R, White S, and Zontone F. The Extremely Brilliant Source Storage Ring of the European Synchrotron Radiation Facility. *Commun Phys.* 2023 Apr 24; 6:82. doi: [10.1038/s42005-023-01195-z](https://doi.org/10.1038/s42005-023-01195-z). [Accessed on: 2023 Jun 23] (cited on page 39)
254. McNeil BWJ and Thompson NR. X-Ray Free-Electron Lasers. *Nature Photon.* 2010 Dec; 4:814–21. doi: [10.1038/nphoton.2010.239](https://doi.org/10.1038/nphoton.2010.239). [Accessed on: 2023 Jul 18] (cited on page 40)
255. Weise H and Decking W. Commissioning and First Lasing of the European XFEL. *Proceedings of the 38th Int Free Electron Laser Conf.* 2018; FEL2017. In collab. with Kip (Ed.) B, Bruce (Ed.) C, and RW (Ed.) Volker S:5 pages, 1.953 MB. doi: [10.18429/JACOW-FEL2017-MOC03](https://doi.org/10.18429/JACOW-FEL2017-MOC03). [Accessed on: 2023 Jul 18] (cited on page 40)
256. Seibert JA and Boone JM. X-Ray Imaging Physics for Nuclear Medicine Technologists. Part 2: X-ray Interactions and Image Formation. *J Nucl Med Technol.* 2005 Mar; 33:3–18 (cited on page 40)
257. Mobilio S. Introduction to Matter Radiation Interaction. *Synchrotron Radiation*. Ed. by Mobilio S, Boscherini F, and Meneghini C. Berlin, Heidelberg: Springer Berlin Heidelberg, 2015 :107–43. doi: [10.1007/978-3-642-55315-8\\_4](https://doi.org/10.1007/978-3-642-55315-8_4). [Accessed on: 2023 Jun 27] (cited on pages 42, 43)
258. Cesareo R. X-Ray Physics: Interaction with Matter, Production, Detection. *Riv Nuovo Cim.* 2000 Jul; 23:1–231. doi: [10.1007/BF03548887](https://doi.org/10.1007/BF03548887). [Accessed on: 2023 Jun 28] (cited on page 42)

259. Seltzer S. XCOM-Photon Cross Sections Database, NIST Standard Reference Database 8. National Institute of Standards and Technology, 1987. doi: [10.18434/T48G6X](https://doi.org/10.18434/T48G6X). [Accessed on: 2023 Jun 28] (cited on page 42)
260. Willmott P. An Introduction to Synchrotron Radiation: Techniques and Applications. 1st ed. Wiley, 2019 Mar 20. [Accessed on: 2023 Jun 27] (cited on page 43)
261. Paganin D, Mayo SC, Gureyev TE, Miller PR, and Wilkins SW. Simultaneous Phase and Amplitude Extraction from a Single Defocused Image of a Homogeneous Object. *J Microsc.* 2002 Apr; 206(Pt 1):33–40. doi: [10.1046/j.1365-2818.2002.01010.x](https://doi.org/10.1046/j.1365-2818.2002.01010.x) (cited on pages 43, 47)
262. Griffiths DJ. Introduction to Quantum Mechanics. Englewood Cliffs (N.J.): Prentice Hall, 1995 (cited on page 43)
263. Birnbacher L, Braig EM, Pfeiffer D, Pfeiffer F, and Herzen J. Quantitative X-ray Phase Contrast Computed Tomography with Grating Interferometry: Biomedical Applications of Quantitative X-ray Grating-Based Phase Contrast Computed Tomography. *Eur J Nucl Med Mol Imaging.* 2021 Dec; 48:4171–88. doi: [10.1007/s00259-021-05259-6](https://doi.org/10.1007/s00259-021-05259-6). [Accessed on: 2023 Jul 17] (cited on pages 43, 150)
264. Chantler CT. Detailed Tabulation of Atomic Form Factors, Photoelectric Absorption and Scattering Cross Section, and Mass Attenuation Coefficients in the Vicinity of Absorption Edges in the Soft X-Ray ( $Z=30-36$ ,  $Z=60-89$ ,  $E=0.1$  keV–10 keV), Addressing Convergence Issues of Earlier Work. *Journal of Physical and Chemical Reference Data.* 2000 Jul 1; 29:597–1056. doi: [10.1063/1.1321055](https://doi.org/10.1063/1.1321055). [Accessed on: 2023 Jun 28] (cited on pages 43, 44)
265. Seltzer S. X-Ray Form Factor, Attenuation and Scattering Tables, NIST Standard Reference Database 66. National Institute of Standards and Technology, 1995. doi: [10.18434/T4HS32](https://doi.org/10.18434/T4HS32). [Accessed on: 2023 Jun 28] (cited on page 43)
266. Vo NT, Drakopoulos M, Atwood RC, and Reinhard C. Reliable Method for Calculating the Center of Rotation in Parallel-Beam Tomography. *Opt Express.* 2014 Aug 11; 22:19078. doi: [10.1364/OE.22.019078](https://doi.org/10.1364/OE.22.019078). [Accessed on: 2023 Jul 6] (cited on page 44)
267. Tomography. Salditt T, Aspelmeier T, and Aeffner S. *Biomedical Imaging: Principles of Radiography, Tomography and Medical Physics*. De Gruyter, 2017 Oct 23:111–67. doi: [10.1515/9783110426694-004](https://doi.org/10.1515/9783110426694-004). [Accessed on: 2023 Jul 6] (cited on pages 44–46)
268. Radon J. On the Determination of Functions from Their Integral Values along Certain Manifolds. *IEEE Trans Med Imaging.* 1986 Dec; 5:170–6. doi: [10.1109/TMI.1986.4307775](https://doi.org/10.1109/TMI.1986.4307775). [Accessed on: 2023 Jul 6] (cited on page 45)
269. Bracewell R. Strip Integration in Radio Astronomy. *Aust J Phys.* 1956; 9:198. doi: [10.1071/PH560198](https://doi.org/10.1071/PH560198). [Accessed on: 2023 Oct 30] (cited on page 45)
270. Schofield R, King L, Tayal U, Castellano I, Stirrup J, Pontana F, Earls J, and Nicol E. Image Reconstruction: Part 1 – Understanding Filtered Back Projection, Noise and Image Acquisition. *Journal of Cardiovascular Computed Tomography.* 2020 May; 14:219–25. doi: [10.1016/j.jcct.2019.04.008](https://doi.org/10.1016/j.jcct.2019.04.008). [Accessed on: 2023 Jul 6] (cited on pages 45, 46)

271. Mirone A, Brun E, Gouillart E, Tafforeau P, and Kieffer J. The PyHST2 Hybrid Distributed Code for High Speed Tomographic Reconstruction with Iterative Reconstruction and a Priori Knowledge Capabilities. *Nuclear Instruments and Methods in Physics Research Section B: Beam Interactions with Materials and Atoms*. 2014 Apr; 324:41–8. doi: [10.1016/j.nimb.2013.09.030](https://doi.org/10.1016/j.nimb.2013.09.030). [Accessed on: 2021 Jul 23] (cited on pages 46, 157)
272. Van Aarle W, Palenstijn WJ, Cant J, Janssens E, Bleichrodt F, Dabravolski A, De Beenhouwer J, Joost Batenburg K, and Sijbers J. Fast and Flexible X-ray Tomography Using the ASTRA Toolbox. *Opt Express*. 2016 Oct 31; 24:25129. doi: [10.1364/OE.24.025129](https://doi.org/10.1364/OE.24.025129). [Accessed on: 2023 Jul 6] (cited on page 46)
273. Pelt DM and Batenburg KJ. Accurately Approximating Algebraic Tomographic Reconstruction by Filtered Backprojection. *Proceedings of the 13th International Meeting on Fully Three-Dimensional Image Reconstruction in Radiology and Nuclear Medicine*. 2015 :158–61 (cited on page 46)
274. Snigirev A, Snigireva I, Kohn V, Kuznetsov S, and Schelokov I. On the Possibilities of X-ray Phase Contrast Microimaging by Coherent High-energy Synchrotron Radiation. *Review of Scientific Instruments*. 1995 Dec; 66:5486–92. doi: [10.1063/1.1146073](https://doi.org/10.1063/1.1146073). [Accessed on: 2023 Jul 6] (cited on page 46)
275. Quenot L, Bohic S, and Brun E. X-Ray Phase Contrast Imaging from Synchrotron to Conventional Sources: A Review of the Existing Techniques for Biological Applications. *Applied Sciences*. 2022 Sep 23; 12:9539. doi: [10.3390/app12199539](https://doi.org/10.3390/app12199539). [Accessed on: 2023 Jul 6] (cited on pages 47, 48)
276. Yu B, Weber L, Pacureanu A, Langer M, Olivier C, Cloetens P, and Peyrin F. Evaluation of Phase Retrieval Approaches in Magnified X-ray Phase Nano Computerized Tomography Applied to Bone Tissue. *Opt Express*. 2018 Apr 30; 26:11110. doi: [10.1364/OE.26.011110](https://doi.org/10.1364/OE.26.011110). [Accessed on: 2023 Jul 17] (cited on pages 47, 51)
277. Weitkamp T, Diaz A, David C, Pfeiffer F, Stampanoni M, Cloetens P, and Ziegler E. X-Ray Phase Imaging with a Grating Interferometer. *Opt Express*. 2005 Aug 8; 13:6296. doi: [10.1364/OPEX.13.006296](https://doi.org/10.1364/OPEX.13.006296). [Accessed on: 2023 Jul 6] (cited on page 47)
278. Eckermann M, Frohn J, Reichardt M, Osterhoff M, Sprung M, Westermeier F, Tzankov A, Werlein C, Kühnel M, Jonigk D, and Salditt T. 3D Virtual Pathohistology of Lung Tissue from Covid-19 Patients Based on Phase Contrast X-ray Tomography. *eLife*. 2020 Aug 20; 9:e60408. doi: [10.7554/eLife.60408](https://doi.org/10.7554/eLife.60408). [Accessed on: 2023 Jul 17] (cited on pages 48, 49)
279. Rougé-Labriet H, Quenot L, Bohic S, Fayard B, Paganin DM, Brun E, and Berujon S. Comparison of X-ray Speckle Based Imaging Deflection Retrieval Algorithms for the Optimization of Radiation Dose. *Phys Med Biol*. 2020 Apr 8. doi: [10.1088/1361-6560/ab87f7](https://doi.org/10.1088/1361-6560/ab87f7). [Accessed on: 2020 Aug 4] (cited on page 48)
280. Zdora MC. State of the Art of X-ray Speckle-Based Phase-Contrast and Dark-Field Imaging. *Journal of Imaging*. 2018; 4(5). doi: [10.3390/jimaging4050060](https://doi.org/10.3390/jimaging4050060) (cited on page 48)

281. Viermetz M, Gustschin N, Schmid C, Haeusele J, von Teuffenbach M, Meyer P, Bergner F, Lasser T, Proksa R, Koehler T, and Pfeiffer F. Dark-Field Computed Tomography Reaches the Human Scale. *Proc Natl Acad Sci U S A*. 2022 Feb 22; 119:e2118799119. doi: [10.1073/pnas.2118799119](https://doi.org/10.1073/pnas.2118799119) (cited on page 48)
282. Zhou SA and Brahme A. Development of Phase-Contrast X-ray Imaging Techniques and Potential Medical Applications. *Physica Medica*. 2008 Sep; 24:129–48. doi: [10.1016/j.ejmp.2008.05.006](https://doi.org/10.1016/j.ejmp.2008.05.006). [Accessed on: 2023 Jul 9] (cited on pages 48, 50)
283. Takeda T, Kunii T, Sirai R, Ohizumi T, Maruyama H, Hyodo K, Yoneyama A, and Ueda K. Ethanol Fixed Brain Imaging by Phase-Contrast X-ray Technique. *J Phys: Conf Ser*. 2013 Mar 22; 425:022004. doi: [10.1088/1742-6596/425/2/022004](https://doi.org/10.1088/1742-6596/425/2/022004). [Accessed on: 2023 Jul 9] (cited on pages 48, 87)
284. Lwin TT, Yoneyama A, Kokubo S, Maruyama H, Hyodo K, and Takeda T. White Matter Imaging of Ethanol-Fixed Rat Brain by Phase-Contrast X-ray Computed Tomography. *Acta Radiol*. 2022 Aug; 63:1102–9. doi: [10.1177/02841851211030776](https://doi.org/10.1177/02841851211030776). [Accessed on: 2023 Apr 4] (cited on pages 48, 85)
285. Buytaert J, Goyens J, De Greef D, Aerts P, and Dirckx J. Volume Shrinkage of Bone, Brain and Muscle Tissue in Sample Preparation for Micro-CT and Light Sheet Fluorescence Microscopy (LSFM). *Microsc Microanal*. 2014 Aug; 20(4):1208–17. doi: [10.1017/S1431927614001329](https://doi.org/10.1017/S1431927614001329) (cited on page 48)
286. Rodgers G, Kuo W, Schulz G, Scheel M, Migga A, Bikis C, Tanner C, Kurtcuoglu V, Weitkamp T, and Müller B. Virtual Histology of an Entire Mouse Brain from Formalin Fixation to Paraffin Embedding. Part 1: Data Acquisition, Anatomical Feature Segmentation, Tracking Global Volume and Density Changes. *J Neurosci Methods*. 2021 Sep 13; 364:109354. doi: [10.1016/j.jneumeth.2021.109354](https://doi.org/10.1016/j.jneumeth.2021.109354) (cited on pages 48, 85, 87)
287. Weitkamp T, Haas D, Wegrzynek D, and Rack A. *ANKAphase* : Software for Single-Distance Phase Retrieval from Inline X-ray Phase-Contrast Radiographs. *J Synchrotron Rad*. 2011 Jul 1; 18:617–29. doi: [10.1107/S0909049511002895](https://doi.org/10.1107/S0909049511002895). [Accessed on: 2023 Nov 8] (cited on pages 49, 50)
288. Strotton MC, Bodey AJ, Wanelik K, Hobbs C, Rau C, and Bradbury EJ. The Spatiotemporal Spread of Cervical Spinal Cord Contusion Injury Pathology Revealed by 3D In-Line Phase Contrast Synchrotron X-ray Microtomography. *Experimental Neurology*. 2021 Feb; 336:113529. doi: [10.1016/j.expneurol.2020.113529](https://doi.org/10.1016/j.expneurol.2020.113529). [Accessed on: 2023 Jun 29] (cited on page 49)
289. Xian RP, Walsh CL, Verleden SE, Wagner WL, Bellier A, Marussi S, Ackermann M, Jonigk DD, Jacob J, Lee PD, and Tafforeau P. A Multiscale X-ray Phase-Contrast Tomography Dataset of a Whole Human Left Lung. *Sci Data*. 2022 Jun 2; 9:264. doi: [10.1038/s41597-022-01353-y](https://doi.org/10.1038/s41597-022-01353-y). [Accessed on: 2023 Jul 17] (cited on page 49)
290. Tao Q, Li D, Zhang L, and Luo S. Using X-Ray In-Line Phase-Contrast Imaging for the Investigation of Nude Mouse Hepatic Tumors. *PLoS ONE*. 2012 Jun 28; 7. Ed. by Singh SR:e39936. doi: [10.1371/journal.pone.0039936](https://doi.org/10.1371/journal.pone.0039936). [Accessed on: 2023 Jul 17] (cited on page 49)

291. Kaneko Y, Shinohara G, Hoshino M, Morishita H, Morita K, Oshima Y, Takahashi M, Yagi N, Okita Y, and Tsukube T. Intact Imaging of Human Heart Structure Using X-ray Phase-Contrast Tomography. *Pediatr Cardiol.* 2017 Feb; 38:390–3. doi: [10.1007/s00246-016-1527-z](https://doi.org/10.1007/s00246-016-1527-z). [Accessed on: 2023 Jul 17] (cited on page 49)
292. Planinc I, Ilic I, Dejea H, Garcia-Canadilla P, Gasparovic H, Jurin H, Milicic D, Skoric B, Stampanoni M, Bijmens B, Bonnin A, and Cikes M. A Novel Three-Dimensional Approach Towards Evaluating Endomyocardial Biopsies for Follow-Up After Heart Transplantation: X-Ray Phase Contrast Imaging and Its Agreement With Classical Histopathology. *Transpl Int.* 2023 Jan 24; 36:11046. doi: [10.3389/ti.2023.11046](https://doi.org/10.3389/ti.2023.11046). [Accessed on: 2023 Jul 20] (cited on page 49)
293. Pingel J, Kjer HM, Biering-Sørensen F, Feidenhans'l R, and Dyrby TB. 3D Synchrotron Imaging of Muscle Tissues at Different Atrophic Stages in Stroke and Spinal Cord Injury: A Proof-of-Concept Study. *Sci Rep.* 2022 Oct 14; 12:17289. doi: [10.1038/s41598-022-21741-z](https://doi.org/10.1038/s41598-022-21741-z). [Accessed on: 2023 Jun 29] (cited on page 49)
294. Hooper SB, Kitchen MJ, Siew ML, Lewis RA, Fouras A, B Te Pas A, Siu KK, Yagi N, Uesugi K, and Wallace MJ. Imaging Lung Aeration and Lung Liquid Clearance at Birth Using Phase Contrast X-ray Imaging. *Clinical and Experimental Pharmacology and Physiology.* 2009 Jan; 36:117–25. doi: [10.1111/j.1440-1681.2008.05109.x](https://doi.org/10.1111/j.1440-1681.2008.05109.x). [Accessed on: 2023 Jul 17] (cited on page 49)
295. Murrie RP, Morgan KS, Maksimenko A, Fouras A, Paganin DM, Hall C, Siu KKW, Parsons DW, and Donnelley M. Live Small-Animal X-ray Lung Velocimetry and Lung Micro-Tomography at the Australian Synchrotron Imaging and Medical Beamline. *J Synchrotron Rad.* 2015 Jul 1; 22:1049–55. doi: [10.1107/S1600577515006001](https://doi.org/10.1107/S1600577515006001). [Accessed on: 2023 Jul 17] (cited on page 49)
296. Broche L, Perchiazzi G, Porra L, Tannoia A, Pellegrini M, Derosa S, Sindaco A, Batista Borges J, Degrugilliers L, Larsson A, Hedenstierna G, Wexler AS, Bravin A, Verbanck S, Smith BJ, Bates JHT, and Bayat S. Dynamic Mechanical Interactions Between Neighboring Airspaces Determine Cyclic Opening and Closure in Injured Lung: *Critical Care Medicine.* 2017 Apr; 45:687–94. doi: [10.1097/CCM.0000000000002234](https://doi.org/10.1097/CCM.0000000000002234). [Accessed on: 2023 Jul 17] (cited on page 49)
297. Donnelley M, Morgan KS, Gradl R, Klein M, Hausermann D, Hall C, Maksimenko A, and Parsons DW. Live-Pig-Airway Surface Imaging and Whole-Pig CT at the Australian Synchrotron Imaging and Medical Beamline. *J Synchrotron Rad.* 2019 Jan 1; 26:175–83. doi: [10.1107/S1600577518014133](https://doi.org/10.1107/S1600577518014133). [Accessed on: 2023 Jul 17] (cited on page 49)
298. Walsh CL, Tafforeau P, Wagner WL, Jafree DJ, Bellier A, Werlein C, Kühnel MP, Boller E, Walker-Samuel S, Robertus JL, Long DA, Jacob J, Marussi S, Brown E, Holroyd N, Jonigk DD, Ackermann M, and Lee PD. Imaging Intact Human Organs with Local Resolution of Cellular Structures Using Hierarchical Phase-Contrast Tomography. *Nat Methods.* 2021 Dec; 18:1532–41. doi: [10.1038/s41592-021-01317-x](https://doi.org/10.1038/s41592-021-01317-x). [Accessed on: 2022 Sep 5] (cited on pages 51, 154, 167)

299. Chappard C, Peyrin F, Bonnassie A, Lemineur G, Brunet-Imbault B, Lespessailles E, and Benhamou CL. Subchondral Bone Micro-Architectural Alterations in Osteoarthritis: A Synchrotron Micro-Computed Tomography Study. *Osteoarthritis and Cartilage*. 2006 Mar; 14:215–23. doi: [10.1016/j.joca.2005.09.008](https://doi.org/10.1016/j.joca.2005.09.008). [Accessed on: 2023 Jul 17] (cited on page 51)
300. Madi K, Staines KA, Bay BK, Javaheri B, Geng H, Bodey AJ, Cartmell S, Pitsillides AA, and Lee PD. In Situ Characterization of Nanoscale Strains in Loaded Whole Joints via Synchrotron X-ray Tomography. *Nat Biomed Eng*. 2019 Nov 25; 4:343–54. doi: [10.1038/s41551-019-0477-1](https://doi.org/10.1038/s41551-019-0477-1). [Accessed on: 2023 Jul 17] (cited on page 51)
301. Rougé-Labriet H, Berujon S, Mathieu H, Bohic S, Fayard B, Ravey JN, Robert Y, Gaudin P, and Brun E. X-Ray Phase Contrast Osteo-Articular Imaging: A Pilot Study on Cadaveric Human Hands. *Sci Rep*. 2020 Dec; 10:1911. doi: [10.1038/s41598-020-58168-3](https://doi.org/10.1038/s41598-020-58168-3). [Accessed on: 2021 Jul 23] (cited on page 51)
302. Broche L, Favier B, Rougé-Labriet H, Drevet S, Lardy B, Brun E, and Lemasson B. Calcified Cartilage Revealed in Whole Joint by X-ray Phase Contrast Imaging. *Osteoarthritis and Cartilage Open*. 2021 Jun; 3:100168. doi: [10.1016/j.ocarto.2021.100168](https://doi.org/10.1016/j.ocarto.2021.100168). [Accessed on: 2023 Jul 17] (cited on page 51)
303. Drevet S, Favier B, Lardy B, Gavazzi G, and Brun E. New Imaging Tools for Mouse Models of Osteoarthritis. *GeroScience*. 2022 Apr; 44:639–50. doi: [10.1007/s11357-022-00525-3](https://doi.org/10.1007/s11357-022-00525-3). [Accessed on: 2023 Jul 17] (cited on page 51)
304. Giglio A, Vommaro ML, Agostino RG, Lo LK, and Donato S. Exploring Compound Eyes in Adults of Four Coleopteran Species Using Synchrotron X-ray Phase-Contrast Microtomography (SR-PhC Micro-CT). *Life*. 2022 May 17; 12:741. doi: [10.3390/life12050741](https://doi.org/10.3390/life12050741). [Accessed on: 2023 Jun 29] (cited on page 51)
305. Friis EM, Crane PR, Pedersen KR, Bengtson S, Donoghue PCJ, Grimm GW, and Stampanoni M. Phase-Contrast X-ray Microtomography Links Cretaceous Seeds with Gnetales and Bennettitales. *Nature*. 2007 Nov; 450:549–52. doi: [10.1038/nature06278](https://doi.org/10.1038/nature06278). [Accessed on: 2023 Jul 17] (cited on page 51)
306. Rousseau D, Widiez T, Di Tommaso S, Rositi H, Adrien J, Maire E, Langer M, Olivier C, Peyrin F, and Rogowsky P. Fast Virtual Histology Using X-ray in-Line Phase Tomography: Application to the 3D Anatomy of Maize Developing Seeds. *Plant Methods*. 2015 Dec; 11:55. doi: [10.1186/s13007-015-0098-y](https://doi.org/10.1186/s13007-015-0098-y). [Accessed on: 2023 Jul 17] (cited on page 51)
307. Piovesan A, Vancauwenberghe V, Van De Looverbosch T, Verboven P, and Nicolai B. X-Ray Computed Tomography for 3D Plant Imaging. *Trends in Plant Science*. 2021 Nov; 26:1171–85. doi: [10.1016/j.tplants.2021.07.010](https://doi.org/10.1016/j.tplants.2021.07.010). [Accessed on: 2023 Jul 17] (cited on page 51)
308. Romell J, Vågberg W, Romell M, Häggman S, Ikram S, and Hertz HM. Soft-Tissue Imaging in a Human Mummy: Propagation-based Phase-Contrast CT. *Radiology*. 2018 Dec; 289:670–6. doi: [10.1148/radiol.2018180945](https://doi.org/10.1148/radiol.2018180945). [Accessed on: 2023 Jul 17] (cited on page 51)

309. Berruyer C, Porcier SM, and Tafforeau P. Synchrotron “Virtual Archaeozoology” Reveals How Ancient Egyptians Prepared a Decaying Crocodile Cadaver for Mummification. *PLoS ONE*. 2020 Feb 21; 15. Ed. by Wong WO:e0229140. doi: [10.1371/journal.pone.0229140](https://doi.org/10.1371/journal.pone.0229140). [Accessed on: 2023 Jul 17] (cited on page 51)
310. Mocella V, Brun E, Ferrero C, and Delattre D. Revealing Letters in Rolled Herculaneum Papyri by X-ray Phase-Contrast Imaging. *Nat Commun*. 2015 Jan 20; 6:5895. doi: [10.1038/ncomms6895](https://doi.org/10.1038/ncomms6895). [Accessed on: 2023 Jul 17] (cited on page 51)
311. Solé V, Papillon E, Cotte M, Walter Ph, and Susini J. A Multiplatform Code for the Analysis of Energy-Dispersive X-ray Fluorescence Spectra. *Spectrochimica Acta Part B: Atomic Spectroscopy*. 2007 Jan; 62:63–8. doi: [10.1016/j.sab.2006.12.002](https://doi.org/10.1016/j.sab.2006.12.002). [Accessed on: 2022 Jan 11] (cited on pages 52, 53, 150)
312. Jenkins R, Manne R, Robin R, and Senemaud C. Nomenclature, Symbols, Units and Their Usage in Spectrochemical Analysis - VIII. Nomenclature System for X-ray Spectroscopy (Recommendations 1991). *Pure and Applied Chemistry*. 1991 Jan 1; 63:735–46. doi: [10.1351/pac199163050735](https://doi.org/10.1351/pac199163050735). [Accessed on: 2023 Jul 3] (cited on page 53)
313. Siegbahn M. Relations between the K and L Series of the High-Frequency Spectra. *Nature*. 1916 Feb; 96:676–6. doi: [10.1038/096676b0](https://doi.org/10.1038/096676b0). [Accessed on: 2023 Jul 3] (cited on page 53)
314. Louthback K, Birarda G, Chen L, and N. Holman HY. Microfluidic Approaches to Synchrotron Radiation-Based Fourier Transform Infrared (SR-FTIR) Spectral Microscopy of Living Biosystems. *PPL*. 2016 Feb 15; 23:273–82. doi: [10.2174/0929866523666160106154035](https://doi.org/10.2174/0929866523666160106154035). [Accessed on: 2023 Jul 10] (cited on page 54)
315. Greci G, Birarda G, Mitri E, Businaro L, Pacor S, Vaccari L, and Tormen M. Optimization of Microfluidic Systems for IRMS Long Term Measurement of Living Cells. *Microelectronic Engineering*. 2012 Oct; 98:698–702. doi: [10.1016/j.mee.2012.05.049](https://doi.org/10.1016/j.mee.2012.05.049). [Accessed on: 2023 Jul 10] (cited on page 54)
316. Töpperwien M, Van Der Meer F, Stadelmann C, and Salditt T. Three-Dimensional Virtual Histology of Human Cerebellum by X-ray Phase-Contrast Tomography. *Proc Natl Acad Sci USA*. 2018 Jul 3; 115:6940–5. doi: [10.1073/pnas.1801678115](https://doi.org/10.1073/pnas.1801678115). [Accessed on: 2023 Jul 12] (cited on page 85)
317. Arregui M, Fernández A, Paz-Sánchez Y, Santana Á, Sacchini S, Sierra E, Arbelo M, and De Quirós YB. Comparison of Three Histological Techniques for Fat Emboli Detection in Lung Cetacean’s Tissue. *Sci Rep*. 2020 May 19; 10:8251. doi: [10.1038/s41598-020-64821-8](https://doi.org/10.1038/s41598-020-64821-8). [Accessed on: 2023 Jul 11] (cited on page 85)
318. Sherman DL and Brophy PJ. Mechanisms of Axon Ensheatment and Myelin Growth. *Nat Rev Neurosci*. 2005 Sep; 6:683–90. doi: [10.1038/nrn1743](https://doi.org/10.1038/nrn1743). [Accessed on: 2023 Jul 11] (cited on page 85)
319. Bartels M, Krenkel M, Cloetens P, Möbius W, and Salditt T. Myelinated Mouse Nerves Studied by X-ray Phase Contrast Zoom Tomography. *Journal of Structural Biology*. 2015 Dec; 192:561–8. doi: [10.1016/j.jsb.2015.11.001](https://doi.org/10.1016/j.jsb.2015.11.001). [Accessed on: 2023 Jul 9] (cited on page 85)

320. Da Silva JC, Pacureanu A, Yang Y, Fus F, Hubert M, Bloch L, Salome M, Bohic S, and Cloetens P. High-Energy Cryo x-Ray Nano-Imaging at the ID16A Beamline of ESRF. *X-Ray Nanoimaging: Instruments and Methods III*. X-Ray Nanoimaging: Instruments and Methods III. Ed. by Lai B and Somogyi A. San Diego, United States: SPIE, 2017 Sep 7:14. doi: [10.1117/12.2275739](https://doi.org/10.1117/12.2275739). [Accessed on: 2023 May 17] (cited on page 85)
321. Bravin A, Coan P, and Suortti P. X-Ray Phase-Contrast Imaging: From Pre-Clinical Applications towards Clinics. *Phys Med Biol*. 2013 Jan 7; 58:R1–R35. doi: [10.1088/0031-9155/58/1/R1](https://doi.org/10.1088/0031-9155/58/1/R1). [Accessed on: 2022 Jul 7] (cited on page 85)
322. Bukreeva I, Asadchikov V, Buzmakov A, Grigoryev V, Bravin A, and Cedola A. High-Resolution Investigation of Spinal Cord and Spine. 2017 Feb 27. doi: [10.48550/arXiv.1702.08538](https://doi.org/10.48550/arXiv.1702.08538). Available from: <http://arxiv.org/abs/1702.08538> [Accessed on: 2023 Jul 9]. preprint (cited on page 85)
323. Saccomano M, Albers J, Tromba G, Dobrivojević Radmilović M, Gajović S, Alves F, and Dullin C. Synchrotron Inline Phase Contrast  $\mu$ CT Enables Detailed Virtual Histology of Embedded Soft-Tissue Samples with and without Staining. *J Synchrotron Rad*. 2018 Jul 1; 25:1153–61. doi: [10.1107/S1600577518005489](https://doi.org/10.1107/S1600577518005489). [Accessed on: 2021 Jul 23] (cited on page 85)
324. Barbone GE, Bravin A, Mittone A, Grosu S, Ricke J, Cavaletti G, Djonov V, and Coan P. High-Spatial-Resolution Three-dimensional Imaging of Human Spinal Cord and Column Anatomy with Postmortem X-ray Phase-Contrast Micro-CT. *Radiology*. 2021 Jan; 298:135–46. doi: [10.1148/radiol.2020201622](https://doi.org/10.1148/radiol.2020201622). [Accessed on: 2023 Apr 19] (cited on page 85)
325. Barbone GE, Bravin A, Mittone A, Kraiger MJ, Hrabě de Angelis M, Bossi M, Ballarini E, Rodriguez-Menendez V, Ceresa C, Cavaletti G, and Coan P. Establishing Sample-Preparation Protocols for X-ray Phase-Contrast CT of Rodent Spinal Cords: Aldehyde Fixations and Osmium Impregnation. *Journal of Neuroscience Methods*. 2020 Jun; 339:108744. doi: [10.1016/j.jneumeth.2020.108744](https://doi.org/10.1016/j.jneumeth.2020.108744). [Accessed on: 2022 Nov 30] (cited on page 85)
326. Gonzalezballester M. Estimation of the Partial Volume Effect in MRI. *Medical Image Analysis*. 2002 Dec; 6:389–405. doi: [10.1016/S1361-8415\(02\)00061-0](https://doi.org/10.1016/S1361-8415(02)00061-0). [Accessed on: 2023 Jul 9] (cited on page 85)
327. Frangi AF, Niessen WJ, Vincken KL, and Viergever MA. Multiscale Vessel Enhancement Filtering. *Medical Image Computing and Computer-Assisted Intervention — MICCAI'98*. Ed. by Wells WM, Colchester A, and Delp S. Vol. 1496. Berlin, Heidelberg: Springer Berlin Heidelberg, 1998 :130–7. doi: [10.1007/BFb0056195](https://doi.org/10.1007/BFb0056195). [Accessed on: 2021 Jul 23] (cited on pages 86, 158)
328. Wang R, Benner T, Sorensen AG, and Wedeen VJ. Diffusion Toolkit: A Software Package for Diffusion Imaging Data Processing and Tractography. *Proc. Intl. Soc. Mag. Reson. Med*. International Society for Magnetic Resonance in Medicine. Vol. 15. 2007 (cited on page 86)

329. Garyfallidis E, Brett M, Amirbekian B, Rokem A, Van Der Walt S, Descoteaux M, Nimmo-Smith I, and Dipy Contributors. Dipy, a Library for the Analysis of Diffusion MRI Data. *Front Neuroinform.* 2014 Feb 21; 8. doi: [10.3389/fninf.2014.00008](https://doi.org/10.3389/fninf.2014.00008). [Accessed on: 2023 Jul 11] (cited on page 86)
330. Mohajerani P, Hipp A, Willner M, Marschner M, Trajkovic-Arsic M, Ma X, Burton NC, Klemm U, Radrich K, Ermolayev V, Tzoumas S, Siveke JT, Bech M, Pfeiffer F, and Ntziachristos V. FMT-PCCT: Hybrid Fluorescence Molecular Tomography—X-Ray Phase-Contrast CT Imaging of Mouse Models. *IEEE Trans Med Imaging.* 2014 Jul; 33:1434–46. doi: [10.1109/TMI.2014.2313405](https://doi.org/10.1109/TMI.2014.2313405). [Accessed on: 2023 Jul 9] (cited on page 86)
331. Eckermann M and Salditt T. Towards Correlative Imaging of Neuronal Tissue by Phase-Contrast x-Ray Tomography and SEM. *Developments in X-Ray Tomography XIII*. *Developments in X-Ray Tomography XIII*. Ed. by Müller B and Wang G. San Diego, United States: SPIE, 2021 Sep 9:2. doi: [10.1117/12.2596133](https://doi.org/10.1117/12.2596133). [Accessed on: 2023 Jul 9] (cited on page 86)
332. Zhang Y, Ackels T, Pacureanu A, Zdora MC, Bonnin A, Schaefer AT, and Bosch C. Sample Preparation and Warping Accuracy for Correlative Multimodal Imaging in the Mouse Olfactory Bulb Using 2-Photon, Synchrotron X-Ray and Volume Electron Microscopy. *Front Cell Dev Biol.* 2022 Jun 8; 10:880696. doi: [10.3389/fcell.2022.880696](https://doi.org/10.3389/fcell.2022.880696). [Accessed on: 2023 Jun 29] (cited on pages 86, 168)
333. Bosch C, Ackels T, Pacureanu A, Zhang Y, Peddie CJ, Berning M, Rzepka N, Zdora MC, Whiteley I, Storm M, Bonnin A, Rau C, Margrie T, Collinson L, and Schaefer AT. Functional and Multiscale 3D Structural Investigation of Brain Tissue through Correlative in Vivo Physiology, Synchrotron Microtomography and Volume Electron Microscopy. *Nat Commun.* 2022 May 25; 13:2923. doi: [10.1038/s41467-022-30199-6](https://doi.org/10.1038/s41467-022-30199-6). [Accessed on: 2023 Jun 29] (cited on page 86)
334. Brunet J, Walsh CL, Wagner WL, Bellier A, Werlein C, Marussi S, Jonigk DD, Verleden SE, Ackermann M, Lee PD, and Tafforeau P. Preparation of Large Biological Samples for High-Resolution, Hierarchical, Synchrotron Phase-Contrast Tomography with Multimodal Imaging Compatibility. *Nat Protoc.* 2023 Mar 1. doi: [10.1038/s41596-023-00804-z](https://doi.org/10.1038/s41596-023-00804-z). [Accessed on: 2023 Apr 19] (cited on pages 86, 167, 168)
335. Shirai R, Kunii T, Yoneyama A, Oozumi T, Maruyama H, Lwin TT, Hyodo K, and Takeda T. Enhanced Renal Image Contrast by Ethanol Fixation in Phase-Contrast X-ray Computed Tomography. *J Synchrotron Rad.* 2014 Jul 1; 21(4):795–800. doi: [10.1107/S1600577514010558](https://doi.org/10.1107/S1600577514010558). [Accessed on: 2020 Nov 9] (cited on page 87)
336. Dudak J, Zemlicka J, Karch J, Patzelt M, Mrzilkova J, Zach P, Hermanova Z, Kvacek J, and Krejci F. High-Contrast X-ray Micro-Radiography and Micro-CT of Ex-Vivo Soft Tissue Murine Organs Utilizing Ethanol Fixation and Large Area Photon-Counting Detector. *Sci Rep.* 2016 Sep; 6(1):30385. doi: [10.1038/srep30385](https://doi.org/10.1038/srep30385). [Accessed on: 2020 Nov 9] (cited on page 87)

337. Patzelt M, Mrzilkova J, Dudak J, Krejci F, Zemlicka J, Karch J, Musil V, Rosina J, Sykora V, Horehledova B, and Zach P. Ethanol Fixation Method for Heart and Lung Imaging in Micro-CT. *Jpn J Radiol.* 2019 Jun; 37:500–10. doi: [10.1007/s11604-019-00830-6](https://doi.org/10.1007/s11604-019-00830-6). [Accessed on: 2023 Jul 9] (cited on page 87)
338. Rodgers G, Tanner C, Schulz G, Migga A, Kuo W, Bikis C, Scheel M, Kurtcuoglu V, Weitkamp T, and Müller B. Virtual Histology of an Entire Mouse Brain from Formalin Fixation to Paraffin Embedding. Part 2: Volumetric Strain Fields and Local Contrast Changes. *Journal of Neuroscience Methods.* 2022 Jan; 365:109385. doi: [10.1016/j.jneumeth.2021.109385](https://doi.org/10.1016/j.jneumeth.2021.109385). [Accessed on: 2022 Feb 8] (cited on page 87)
339. Lein ES et al. Genome-Wide Atlas of Gene Expression in the Adult Mouse Brain. *Nature.* 2007 Jan; 445:168–76. doi: [10.1038/nature05453](https://doi.org/10.1038/nature05453). [Accessed on: 2023 Jul 12] (cited on page 87)
340. Paxinos G and Watson C. *The Rat Brain in Stereotaxic Coordinates*. 6th ed. Amsterdam: Elsevier, 2007 (cited on page 87)
341. Van Heel M and Schatz M. Fourier Shell Correlation Threshold Criteria. *Journal of Structural Biology.* 2005 Sep; 151:250–62. doi: [10.1016/j.jsb.2005.05.009](https://doi.org/10.1016/j.jsb.2005.05.009). [Accessed on: 2023 Jul 11] (cited on page 108)
342. Tao S, He C, Hao X, Kuang C, and Liu X. Factors Affecting the Spatial Resolution in 2D Grating-Based X-Ray Phase Contrast Imaging. *Front Phys.* 2021 Jun 17; 9:672207. doi: [10.3389/fphy.2021.672207](https://doi.org/10.3389/fphy.2021.672207). [Accessed on: 2023 Jul 11] (cited on page 108)
343. Witten IH, Frank E, and Hall MA. *Data Mining: Practical Machine Learning Tools and Techniques*. 3rd ed. Morgan Kaufmann Series in Data Management Systems. Burlington, MA: Morgan Kaufmann, 2011. 629 pp. (cited on page 108)
344. Schindelin J, Arganda-Carreras I, Frise E, Kaynig V, Longair M, Pietzsch T, Preibisch S, Rueden C, Saalfeld S, Schmid B, Tinevez JY, White DJ, Hartenstein V, Eliceiri K, Tomancak P, and Cardona A. Fiji: An Open-Source Platform for Biological-Image Analysis. *Nat Methods.* 2012 Jul; 9:676–82. doi: [10.1038/nmeth.2019](https://doi.org/10.1038/nmeth.2019). [Accessed on: 2021 Jul 23] (cited on page 108)
345. Arganda-Carreras I, Kaynig V, Rueden C, Eliceiri KW, Schindelin J, Cardona A, and Sebastian Seung H. Trainable Weka Segmentation: A Machine Learning Tool for Microscopy Pixel Classification. *Bioinformatics.* 2017 Aug 1; 33. Ed. by Murphy R:2424–6. doi: [10.1093/bioinformatics/btx180](https://doi.org/10.1093/bioinformatics/btx180). [Accessed on: 2021 Jul 23] (cited on page 108)
346. Legland D, Arganda-Carreras I, and Andrey P. MorphoLibJ: Integrated Library and Plugins for Mathematical Morphology with ImageJ. *Bioinformatics.* 2016 Jul 13 :btw413. doi: [10.1093/bioinformatics/btw413](https://doi.org/10.1093/bioinformatics/btw413). [Accessed on: 2021 Jul 23] (cited on page 108)
347. Ollion J, Cochenec J, Loll F, Escudé C, and Boudier T. TANGO: A Generic Tool for High-Throughput 3D Image Analysis for Studying Nuclear Organization. *Bioinformatics.* 2013 Jul 15; 29:1840–1. doi: [10.1093/bioinformatics/btt276](https://doi.org/10.1093/bioinformatics/btt276). [Accessed on: 2021 Jul 23] (cited on page 108)

348. Chourrout M, Roux M, Gislard C, Arganda-Carreras I, Legland D, Rositi H, Wiart M, and Chauveau F. A Fiji Pipeline to Segment 3D Objects and Retrieve Shape Parameters in Biomedical Images. Zenodo, 2021 Mar 15. doi: [10.5281/zenodo.4584752](https://doi.org/10.5281/zenodo.4584752). Available from: <https://zenodo.org/record/4584752> [Accessed on: 2021 Oct 6] (cited on page 108)
349. Tycko R. Amyloid Polymorphism: Structural Basis and Neurobiological Relevance. *Neuron*. 2015 May; 86:632–45. doi: [10.1016/j.neuron.2015.03.017](https://doi.org/10.1016/j.neuron.2015.03.017). [Accessed on: 2022 Jun 27] (cited on page 109)
350. Rasmussen J, Mahler J, Beschorner N, Kaeser SA, Häsler LM, Baumann F, Nyström S, Portelius E, Blennow K, Lashley T, Fox NC, Sepulveda-Falla D, Glatzel M, Oblak AL, Ghetti B, Nilsson KPR, Hammarström P, Staufenbiel M, Walker LC, and Jucker M. Amyloid Polymorphisms Constitute Distinct Clouds of Conformational Variants in Different Etiological Subtypes of Alzheimer’s Disease. *Proc Natl Acad Sci USA*. 2017 Dec 5; 114:13018–23. doi: [10.1073/pnas.1713215114](https://doi.org/10.1073/pnas.1713215114). [Accessed on: 2022 Apr 11] (cited on page 109)
351. Watts JC, Condello C, Stohr J, Oehler A, Lee J, DeArmond SJ, Lannfelt L, Ingelsson M, Giles K, and Prusiner SB. Serial Propagation of Distinct Strains of A $\beta$  Prions from Alzheimer’s Disease Patients. *Proceedings of the National Academy of Sciences*. 2014 Jul 15; 111:10323–8. doi: [10.1073/pnas.1408900111](https://doi.org/10.1073/pnas.1408900111). [Accessed on: 2021 Jul 23] (cited on page 109)
352. Baron T, Arzac JN, Verchère J, Tlili H, Aufauvre C, and Bétemps D. Co-Expression of APP/PS1 Disrupts the Distribution of Brain Lesions in a Synucleinopathy Transgenic Mouse Model (M83). *Acta Neuropathol*. 2022 Apr; 143:527–9. doi: [10.1007/s00401-022-02410-x](https://doi.org/10.1007/s00401-022-02410-x). [Accessed on: 2023 Jul 12] (cited on page 109)
353. Chourrout M, Sandt C, Weitkamp T, Dučić T, Meyronet D, Baron T, Klohs J, Rama N, Boutin H, Singh S, Olivier C, Wiart M, Brun E, Bohic S, and Chauveau F. Why Are Amyloid- $\beta$  Plaques Detected by X-ray Phase-Contrast Imaging? Role of Metals Revealed through Combined Synchrotron Infrared and X-ray Fluorescence Microscopies. 2023 Jan 1. doi: [10.1101/2022.09.27.509706](https://doi.org/10.1101/2022.09.27.509706). Available from: <http://biorxiv.org/content/early/2023/03/30/2022.09.27.509706.abstract>. preprint (cited on page 112)
354. Pushie MJ, Sylvain NJ, Hou H, Hackett MJ, Kelly ME, and Webb SM. X-Ray Fluorescence Microscopy Methods for Biological Tissues. *Metallomics*. 2022 Jun 23; 14:mfac032. doi: [10.1093/mtomcs/mfac032](https://doi.org/10.1093/mtomcs/mfac032). [Accessed on: 2023 Jun 9] (cited on page 149)
355. Chwiej J, Szczerbowska-Boruchowska M, Lankosz M, Wojcik S, Falkenberg G, Stegowski Z, and Setkowicz Z. Preparation of Tissue Samples for X-ray Fluorescence Microscopy. *Spectrochimica Acta Part B: Atomic Spectroscopy*. 2005 Dec; 60:1531–7. doi: [10.1016/j.sab.2005.10.002](https://doi.org/10.1016/j.sab.2005.10.002). [Accessed on: 2023 Jun 1] (cited on page 149)

356. Pushie MJ, Hollings A, Reinhardt J, Webb SM, Lam V, Takechi R, Mamo JC, Paterson PG, Kelly ME, George GN, Pickering IJ, and Hackett MJ. Sample Preparation with Sucrose Cryoprotection Dramatically Alters Zn Distribution in the Rodent Hippocampus, as Revealed by Elemental Mapping. *J Anal At Spectrom.* 2020; 35:2498–508. doi: [10.1039/D0JA00323A](https://doi.org/10.1039/D0JA00323A). [Accessed on: 2023 Jun 1] (cited on page 149)
357. Hare DJ, Lee JK, Beavis AD, van Gramberg A, George J, Adlard PA, Finkelstein DI, and Doble PA. Three-Dimensional Atlas of Iron, Copper, and Zinc in the Mouse Cerebrum and Brainstem. *Anal Chem.* 2012 May 1; 84:3990–7. doi: [10.1021/ac300374x](https://doi.org/10.1021/ac300374x). [Accessed on: 2022 Jan 10] (cited on page 150)
358. Chourrout M, Sandt C, Weitkamp T, Dučić T, Meyronet D, Baron T, Klohs J, Rama N, Boutin H, Singh S, Olivier C, Wiart M, Brun E, Bohic S, and Chauveau F. Virtual Histology of Alzheimer’s Disease: Biometal Entrapment within Amyloid- $\beta$  Plaques Allows for Detection via X-ray Phase-Contrast Imaging. *Acta Biomaterialia.* 2023; 170:260–72. doi: [10.1016/j.actbio.2023.07.046](https://doi.org/10.1016/j.actbio.2023.07.046) (cited on pages 150, 175)
359. Stedman JD and Spyrou NM. Hierarchical Clustering into Groups of Human Brain Regions According to Elemental Composition. *J Radioanal Nucl Chem.* 1998 Oct; 236:11b–14. doi: [10.1007/BF02386309](https://doi.org/10.1007/BF02386309). [Accessed on: 2022 Jan 18] (cited on page 150)
360. Mathieu E, Bernard AS, Quévrain E, Zoumpoulaki M, Iriart S, Lung-Soong C, Lai B, Medjoubi K, Henry L, Nagarajan S, Poyer F, Scheitler A, Ivanović-Burmazović I, Marco S, Somogyi A, Seksik P, Delsuc N, and Policar C. Intracellular Location Matters: Rationalization of the Anti-Inflammatory Activity of a Manganese( II ) Superoxide Dismutase Mimic Complex. *Chem Commun.* 2020; 56:7885–8. doi: [10.1039/D0CC03398G](https://doi.org/10.1039/D0CC03398G). [Accessed on: 2023 Nov 7] (cited on page 150)
361. Mayo SC, Stevenson AW, and Wilkins SW. In-Line Phase-Contrast X-ray Imaging and Tomography for Materials Science. *Materials.* 2012 May 24; 5:937–65. doi: [10.3390/ma5050937](https://doi.org/10.3390/ma5050937). [Accessed on: 2023 Jul 17] (cited on page 150)
362. Alloo SJ, Paganin DM, Morgan KS, Gureyev TE, Mayo SC, Mohammadi S, Lockie D, Menk RH, Arfelli F, Zanconati F, Tromba G, and Pavlov KM. Tomographic Phase and Attenuation Extraction for a Sample Composed of Unknown Materials Using X-ray Propagation-Based Phase-Contrast Imaging. *Opt Lett.* 2022 Apr 15; 47:1945. doi: [10.1364/OL.445802](https://doi.org/10.1364/OL.445802). [Accessed on: 2022 Nov 7] (cited on page 150)
363. Everett J, F. Collingwood J, Tjendana-Tjhin V, Brooks J, Lermyte F, Plascencia-Villa G, Hands-Portman I, Dobson J, Perry G, and D. Telling N. Nanoscale Synchrotron X-ray Speciation of Iron and Calcium Compounds in Amyloid Plaque Cores from Alzheimer’s Disease Subjects. *Nanoscale.* 2018; 10:11782–96. doi: [10.1039/C7NR06794A](https://doi.org/10.1039/C7NR06794A). [Accessed on: 2022 Apr 12] (cited on page 150)
364. Stern AM, Liu L, Jin S, Liu W, Meunier AL, Ericsson M, Miller MB, Batson M, Sun T, Kathuria S, Reczek D, Pradier L, and Selkoe DJ. A Calcium-Sensitive Antibody Isolates Soluble Amyloid- $\beta$  Aggregates and Fibrils from Alzheimer’s Disease Brain. *Brain.* 2022 Jul 29; 145:2528–40. doi: [10.1093/brain/awac023](https://doi.org/10.1093/brain/awac023). [Accessed on: 2023 Jul 17] (cited on page 150)

365. Imamura K, Sawada M, Ozaki N, Naito H, Iwata N, Ishihara R, Takeuchi T, and Shibayama H. Activation Mechanism of Brain Microglia in Patients With Diffuse Neurofibrillary Tangles With Calcification: A Comparison With Alzheimer Disease: Alzheimer Disease and Associated Disorders. 2001 Jan; 15:45–50. doi: [10.1097/00002093-200101000-00006](https://doi.org/10.1097/00002093-200101000-00006). [Accessed on: 2023 Jul 17] (cited on page 150)
366. Kitamura K, Nakayama T, Ohata K, Wakasa K, and Miki Y. Computed Tomography and Magnetic Resonance Imaging Appearance of Prolactinoma With Spheroid-Type Amyloid Deposition: Journal of Computer Assisted Tomography. 2011 Mar; 35:313–5. doi: [10.1097/RCT.0b013e31820d7bdf](https://doi.org/10.1097/RCT.0b013e31820d7bdf). [Accessed on: 2023 Jul 17] (cited on page 150)
367. Schober R, Hilbrich I, Jäger C, and Holzer M. Senile Plaque Calcification of the Lamina Circumvoluta Medullaris in Alzheimer's Disease. Neuropathology. 2021 Oct; 41:366–70. doi: [10.1111/neup.12742](https://doi.org/10.1111/neup.12742). [Accessed on: 2023 Jul 17] (cited on page 150)
368. Chen M. The Alzheimer's Plaques Tangles and Memory Deficits May Have a Common Origin - Part III Animal Model. Front Biosci. 1998; 3:a47–51. doi: [10.2741/A251](https://doi.org/10.2741/A251). [Accessed on: 2023 Jul 17] (cited on page 151)
369. Busche MA. In Vivo Two-Photon Calcium Imaging of Hippocampal Neurons in Alzheimer Mouse Models. *Biomarkers for Alzheimer's Disease Drug Development*. Ed. by Perneczky R. Vol. 1750. New York, NY: Springer New York, 2018 :341–51. doi: [10.1007/978-1-4939-7704-8\\_23](https://doi.org/10.1007/978-1-4939-7704-8_23). [Accessed on: 2023 Jul 17] (cited on page 151)
370. Di Benedetto G, Burgaletto C, Bellanca CM, Munafò A, Bernardini R, and Cantarella G. Role of Microglia and Astrocytes in Alzheimer's Disease: From Neuroinflammation to Ca<sup>2+</sup> Homeostasis Dysregulation. Cells. 2022 Sep 1; 11:2728. doi: [10.3390/cells11172728](https://doi.org/10.3390/cells11172728). [Accessed on: 2023 Jul 17] (cited on page 151)
371. Banerjee G, Carare R, Cordonnier C, Greenberg SM, Schneider JA, Smith EE, Buchem MV, Grund JVD, Verbeek MM, and Werring DJ. The Increasing Impact of Cerebral Amyloid Angiopathy: Essential New Insights for Clinical Practice. J Neurol Neurosurg Psychiatry. 2017 Nov; 88:982–94. doi: [10.1136/jnnp-2016-314697](https://doi.org/10.1136/jnnp-2016-314697). [Accessed on: 2023 Jul 7] (cited on page 153)
372. Knudsen KA, Rosand J, Karluk D, and Greenberg SM. Clinical Diagnosis of Cerebral Amyloid Angiopathy: Validation of the Boston Criteria. Neurology. 2001 Feb 27; 56:537–9. doi: [10.1212/WNL.56.4.537](https://doi.org/10.1212/WNL.56.4.537). [Accessed on: 2022 Feb 8] (cited on page 153)
373. Thal DR, Griffin WST, De Vos RAI, and Ghebremedhin E. Cerebral Amyloid Angiopathy and Its Relationship to Alzheimer's Disease. Acta Neuropathol. 2008 Jun; 115:599–609. doi: [10.1007/s00401-008-0366-2](https://doi.org/10.1007/s00401-008-0366-2). [Accessed on: 2023 May 12] (cited on page 153)
374. Jäkel L, De Kort AM, Klijn CJ, Schreuder FH, and Verbeek MM. Prevalence of Cerebral Amyloid Angiopathy: A Systematic Review and Meta-analysis. Alzheimer's & Dementia. 2022 Jan; 18:10–28. doi: [10.1002/alz.12366](https://doi.org/10.1002/alz.12366). [Accessed on: 2023 Jul 8] (cited on page 153)

375. Jespersen SN and Østergaard L. The Roles of Cerebral Blood Flow, Capillary Transit Time Heterogeneity, and Oxygen Tension in Brain Oxygenation and Metabolism. *J Cereb Blood Flow Metab.* 2012 Feb; 32:264–77. doi: [10.1038/jcbfm.2011.153](https://doi.org/10.1038/jcbfm.2011.153). [Accessed on: 2023 Jul 7] (cited on page 153)
376. Kwee RM and Kwee TC. Virchow-Robin Spaces at MR Imaging. *RadioGraphics.* 2007 Jul; 27:1071–86. doi: [10.1148/rg.274065722](https://doi.org/10.1148/rg.274065722). [Accessed on: 2023 Jul 8] (cited on page 153)
377. Greenberg SM, William Rebeck G, Vonsattel JPG, Gomez-Isla T, and Hyman BT. Apolipoprotein E E4 and Cerebral Hemorrhage Associated with Amyloid Angiopathy. *Ann Neurol.* 1995 Aug; 38:254–9. doi: [10.1002/ana.410380219](https://doi.org/10.1002/ana.410380219). [Accessed on: 2023 Jul 8] (cited on page 153)
378. Linn J, Halpin A, Demaerel P, Ruhland J, Giese AD, Dichgans M, Van Buchem MA, Bruckmann H, and Greenberg SM. Prevalence of Superficial Siderosis in Patients with Cerebral Amyloid Angiopathy. *Neurology.* 2010 Apr 27; 74:1346–50. doi: [10.1212/WNL.0b013e3181dad605](https://doi.org/10.1212/WNL.0b013e3181dad605). [Accessed on: 2023 Jul 8] (cited on page 153)
379. Charidimou A, Boulouis G, Frosch MP, Baron JC, Pasi M, Albucher JF, Banerjee G, Barbato C, Bonneville F, Brandner S, Calviere L, Caparros F, Casolla B, Cordonnier C, Delisle MB, Deramecourt V, Dichgans M, Gokcal E, Herms J, Hernandez-Guillamon M, Jäger HR, Jaunmuktane Z, Linn J, Martinez-Ramirez S, Martínez-Sáez E, Mawrin C, Montaner J, Moulin S, Olivot JM, Piazza F, Puy L, Raposo N, Rodrigues MA, Roeber S, Romero JR, Samarasekera N, Schneider JA, Schreiber S, Schreiber F, Schwall C, Smith C, Szalardy L, Varlet P, Viguier A, Wardlaw JM, Warren A, Wollenweber FA, Zedde M, Van Buchem MA, Gurol ME, Viswanathan A, Al-Shahi Salman R, Smith EE, Werring DJ, and Greenberg SM. The Boston Criteria Version 2.0 for Cerebral Amyloid Angiopathy: A Multicentre, Retrospective, MRI–Neuropathology Diagnostic Accuracy Study. *The Lancet Neurology.* 2022 Aug; 21:714–25. doi: [10.1016/S1474-4422\(22\)00208-3](https://doi.org/10.1016/S1474-4422(22)00208-3). [Accessed on: 2023 Jul 8] (cited on page 153)
380. Momose A, Takeda T, and Itai Y. Blood Vessels: Depiction at Phase-Contrast X-ray Imaging without Contrast Agents in the Mouse and Rat—Feasibility Study. *Radiology.* 2000 Nov; 217:593–6. doi: [10.1148/radiology.217.2.r00oc14593](https://doi.org/10.1148/radiology.217.2.r00oc14593). [Accessed on: 2023 Jul 9] (cited on page 154)
381. Lee JY, Mack AF, Shiozawa T, Longo R, Tromba G, Scheffler K, and Hagberg GE. Microvascular Imaging of the Unstained Human Superior Colliculus Using Synchrotron-Radiation Phase-Contrast Microtomography. *Sci Rep.* 2022 Jun 2; 12:9238. doi: [10.1038/s41598-022-13282-2](https://doi.org/10.1038/s41598-022-13282-2). [Accessed on: 2023 Jun 29] (cited on page 154)
382. Takeda T, Momose A, Wu J, Yu Q, Zeniya T, Lwin TT, Yoneyama A, and Itai Y. Vessel Imaging by Interferometric Phase-Contrast X-Ray Technique. *Circulation.* 2002 Apr 9; 105:1708–12. doi: [10.1161/01.CIR.0000012752.35225.6C](https://doi.org/10.1161/01.CIR.0000012752.35225.6C). [Accessed on: 2023 Jul 9] (cited on page 154)

383. Takeda T, Yoneyama A, Wu J, Thet-Thet-Lwin, Momose A, and Hyodo K. *In Vivo* Physiological Saline-Infused Hepatic Vessel Imaging Using a Two-Crystal-Interferometer-Based Phase-Contrast X-ray Technique. *J Synchrotron Rad.* 2012 Mar 1; 19:252–6. doi: [10.1107/S0909049511056226](https://doi.org/10.1107/S0909049511056226). [Accessed on: 2023 Jul 9] (cited on page 154)
384. Holme MN, Schulz G, Deyhle H, Weitkamp T, Beckmann F, Lobrinus JA, Rikhtegar F, Kurtcuoglu V, Zanette I, Saxer T, and Müller B. Complementary X-ray Tomography Techniques for Histology-Validated 3D Imaging of Soft and Hard Tissues Using Plaque-Containing Blood Vessels as Examples. *Nat Protoc.* 2014 Jun; 9(6):1401–15. doi: [10.1038/nprot.2014.091](https://doi.org/10.1038/nprot.2014.091). [Accessed on: 2020 Aug 4] (cited on page 154)
385. Song M. Imaging Three-Dimensional Microvascular Networks of Brain with Synchrotron Radiation Microangiography. *Neurosci Bull.* 2020 Apr; 36:331–2. doi: [10.1007/s12264-020-00491-w](https://doi.org/10.1007/s12264-020-00491-w). [Accessed on: 2023 Jul 9] (cited on page 154)
386. Schwarzenberg FL, Schütz P, Hammel JU, Riedel M, Bartl J, Bordbari S, Frank SC, Walkenfort B, Busse M, Herzen J, Lohr C, Wülfig C, and Henne S. Three-Dimensional Analyses of Vascular Network Morphology in a Murine Lymph Node by X-ray Phase-Contrast Tomography with a 2D Talbot Array. *Front Immunol.* 2022 Nov 29; 13:947961. doi: [10.3389/fimmu.2022.947961](https://doi.org/10.3389/fimmu.2022.947961). [Accessed on: 2023 Jul 9] (cited on page 154)
387. Zeng C, Chen Z, Yang H, Fan Y, Fei L, Chen X, and Zhang M. Advanced High Resolution Three-Dimensional Imaging to Visualize the Cerebral Neurovascular Network in Stroke. *Int J Biol Sci.* 2022; 18:552–71. doi: [10.7150/ijbs.64373](https://doi.org/10.7150/ijbs.64373). [Accessed on: 2023 Jun 29] (cited on page 154)
388. Laperle CM, Hamilton TJ, Wintermeyer P, Walker EJ, Shi D, Anastasio MA, Derdak Z, Wands JR, Diebold G, and Rose-Petrucci C. Low Density Contrast Agents for X-Ray Phase Contrast Imaging: The Use of Ambient Air for x-Ray Angiography of Excised Murine Liver Tissue. *Phys Med Biol.* 2008 Dec 7; 53:6911–23. doi: [10.1088/0031-9155/53/23/017](https://doi.org/10.1088/0031-9155/53/23/017). [Accessed on: 2023 Jul 9] (cited on page 154)
389. Tang R, Xi Y, Chai WM, Wang Y, Guan Y, Yang GY, Xie H, and Chen KM. Microbubble-Based Synchrotron Radiation Phase Contrast Imaging: Basic Study and Angiography Applications. *Phys Med Biol.* 2011 Jun 21; 56:3503–12. doi: [10.1088/0031-9155/56/12/004](https://doi.org/10.1088/0031-9155/56/12/004). [Accessed on: 2023 Jul 9] (cited on page 154)
390. Lundström U, Larsson DH, Burvall A, Scott L, Westermarck UK, Wilhelm M, Arsenian Henriksson M, and Hertz HM. X-Ray Phase-Contrast CO<sub>2</sub> Angiography for Sub-10 Mm Vessel Imaging. *Phys Med Biol.* 2012 Nov 21; 57:7431–41. doi: [10.1088/0031-9155/57/22/7431](https://doi.org/10.1088/0031-9155/57/22/7431). [Accessed on: 2023 Jul 9] (cited on page 154)
391. Wannamaker R, Buck B, and Butcher K. Multimodal CT in Acute Stroke. *Curr Neurol Neurosci Rep.* 2019 Sep; 19:63. doi: [10.1007/s11910-019-0978-z](https://doi.org/10.1007/s11910-019-0978-z). [Accessed on: 2023 Jul 9] (cited on page 154)

392. Bienstock S, Lin F, Blankstein R, Leipsic J, Cardoso R, Ahmadi A, Gelijns A, Patel K, Baldassarre LA, Hadley M, LaRocca G, Sanz J, Narula J, Chandrashekhara Y, Shaw LJ, and Fuster V. Advances in Coronary Computed Tomographic Angiographic Imaging of Atherosclerosis for Risk Stratification and Preventive Care. *JACC: Cardiovascular Imaging*. 2023 May ;S1936878X23000918. DOI: [10.1016/j.jcmg.2023.02.002](https://doi.org/10.1016/j.jcmg.2023.02.002). [Accessed on: 2023 Jul 9] (cited on page 154)
393. Tonet E, Boccadoro A, Micillo M, Cocco M, Cossu A, Pompei G, Giganti M, and Campo G. Coronary Computed Tomography Angiography: Beyond Obstructive Coronary Artery Disease. *Life*. 2023 Apr 26; 13:1086. DOI: [10.3390/life13051086](https://doi.org/10.3390/life13051086). [Accessed on: 2023 Jul 9] (cited on page 154)
394. Stassi C, Mondello C, Baldino G, Cardia L, Gualniera P, Calapai F, Sapienza D, Asmundo A, and Ventura Spagnolo E. State of the Art on the Role of Postmortem Computed Tomography Angiography and Magnetic Resonance Imaging in the Diagnosis of Cardiac Causes of Death: A Narrative Review. *Tomography*. 2022 Apr 1; 8:961–73. DOI: [10.3390/tomography8020077](https://doi.org/10.3390/tomography8020077). [Accessed on: 2023 Jul 9] (cited on page 154)
395. Barbone GE, Bravin A, Romanelli P, Mittone A, Bucci D, Gaaß T, Le Duc G, Auweter S, Reiser MF, Kraiger MJ, Hrabě de Angelis M, Battaglia G, and Coan P. Micro-Imaging of Brain Cancer Radiation Therapy Using Phase-contrast Computed Tomography. *Int J Radiat Oncol Biol Phys*. 2018 Jul 15; 101(4):965–84. DOI: [10.1016/j.ijrobp.2018.03.063](https://doi.org/10.1016/j.ijrobp.2018.03.063) (cited on page 154)
396. Thal DR, Ghebremedhin E, Rüb U, Yamaguchi H, Del Tredici K, and Braak H. Two Types of Sporadic Cerebral Amyloid Angiopathy. *J Neuropathol Exp Neurol*. 2002 Mar; 61:282–93. DOI: [10.1093/jnen/61.3.282](https://doi.org/10.1093/jnen/61.3.282). [Accessed on: 2022 Feb 8] (cited on pages 154, 155)
397. Alafuzoff I, Thal DR, Arzberger T, Bogdanovic N, Al-Sarraj S, Bodi I, Boluda S, Bugiani O, Duyckaerts C, Gelpi E, Gentleman S, Giaccone G, Graeber M, Hortobagyi T, Höftberger R, Ince P, Ironside JW, Kavantzias N, King A, Korkolopoulou P, Kovács GG, Meyronet D, Monoranu C, Nilsson T, Parchi P, Patsouris E, Pikkarainen M, Revesz T, Rozemuller A, Seilhean D, Schulz-Schaeffer W, Streichenberger N, Wharton SB, and Kretschmar H. Assessment of  $\beta$ -Amyloid Deposits in Human Brain: A Study of the BrainNet Europe Consortium. *Acta Neuropathol*. 2009 Mar; 117:309–20. DOI: [10.1007/s00401-009-0485-4](https://doi.org/10.1007/s00401-009-0485-4). [Accessed on: 2021 Aug 17] (cited on page 154)
398. Weitkamp T, Scheel M, Perrin J, Daniel G, King A, Le Roux V, Giorgetta J, Carcy A, Langlois F, Desjardins K, Meneglier C, Cerato M, Engblom C, Cauchon G, Moreno T, Rivard C, Gohon Y, and Polack F. Microtomography on the ANATOMIX Beamline at Synchrotron SOLEIL. *J Phys: Conf Ser*. 2022 Dec 1; 2380(1):012122. DOI: [10.1088/1742-6596/2380/1/012122](https://doi.org/10.1088/1742-6596/2380/1/012122). [Accessed on: 2023 Aug 2] (cited on page 156)
399. Vo NT, Atwood RC, Drakopoulos M, and Connolley T. Data Processing Methods and Data Acquisition for Samples Larger than the Field of View in Parallel-Beam

- Tomography. *Opt Express*. 2021 Jun 7; 29:17849. doi: [10.1364/OE.418448](https://doi.org/10.1364/OE.418448). [Accessed on: 2023 Jun 23] (cited on page 157)
400. Geurts P, Ernst D, and Wehenkel L. Extremely Randomized Trees. *Mach Learn*. 2006 Apr; 63:3–42. doi: [10.1007/s10994-006-6226-1](https://doi.org/10.1007/s10994-006-6226-1). [Accessed on: 2023 Oct 30] (cited on page 158)
401. Ronneberger O, Fischer P, and Brox T. U-Net: Convolutional Networks for Biomedical Image Segmentation. 2015 May 18. Available from: <http://arxiv.org/abs/1505.04597> [Accessed on: 2023 Oct 30]. preprint (cited on page 158)
402. Latif J, Xiao C, Imran A, and Tu S. Medical Imaging Using Machine Learning and Deep Learning Algorithms: A Review. *2019 2nd International Conference on Computing, Mathematics and Engineering Technologies (iCoMET)*. 2019 2nd International Conference on Computing, Mathematics and Engineering Technologies (iCoMET). Sukkur, Pakistan: IEEE, 2019 Jan :1–5. doi: [10.1109/ICOMET.2019.8673502](https://doi.org/10.1109/ICOMET.2019.8673502). [Accessed on: 2023 Oct 31] (cited on page 158)
403. Pedregosa F, Varoquaux G, Gramfort A, Michel V, Thirion B, Grisel O, Blondel M, Prettenhofer P, Weiss R, Dubourg V, Vanderplas J, Passos A, Cournapeau D, Brucher M, Perrot M, and Duchesnay E. Scikit-Learn: Machine Learning in Python. *Journal of Machine Learning Research*. 2011; 12:2825–30 (cited on page 158)
404. Buitinck L, Louppe G, Blondel M, Pedregosa F, Mueller A, Grisel O, Niculae V, Prettenhofer P, Gramfort A, Grobler J, Layton R, Vanderplas J, Joly A, Holt B, and Varoquaux G. API Design for Machine Learning Software: Experiences from the Scikit-Learn Project. Version 1 2013. doi: [10.48550/ARXIV.1309.0238](https://doi.org/10.48550/ARXIV.1309.0238). [Accessed on: 2023 Oct 30] (cited on page 158)
405. Chollet F et al. Keras. 2015. Available from: <https://keras.io> (cited on page 158)
406. Abadi M, Agarwal A, Barham P, Brevdo E, Chen Z, Citro C, Corrado GS, Davis A, Dean J, Devin M, Ghemawat S, Goodfellow I, Harp A, Irving G, Isard M, Jia Y, Jozefowicz R, Kaiser L, Kudlur M, Levenberg J, Mané D, Monga R, Moore S, Murray D, Olah C, Schuster M, Shlens J, Steiner B, Sutskever I, Talwar K, Tucker P, Vanhoucke V, Vasudevan V, Viégas F, Vinyals O, Warden P, Wattenberg M, Wicke M, Yu Y, and Zheng X. TensorFlow: Large-scale Machine Learning on Heterogeneous Systems. 2015. Available from: <https://www.tensorflow.org/> (cited on page 158)
407. TensorFlow Developers. TensorFlow. Version v2.14.0. Zenodo, 2023 Sep 26. doi: [10.5281/ZENODO.4724125](https://doi.org/10.5281/ZENODO.4724125). [Accessed on: 2023 Oct 30] (cited on page 158)
408. Zhu X, Victor TW, Ambi A, Sullivan JK, Hatfield J, Xu F, Miller LM, and Van Nostrand WE. Copper Accumulation and the Effect of Chelation Treatment on Cerebral Amyloid Angiopathy Compared to Parenchymal Amyloid Plaques. *Metallomics*. 2020 Apr 1; 12:539–46. doi: [10.1039/c9mt00306a](https://doi.org/10.1039/c9mt00306a). [Accessed on: 2022 Sep 5] (cited on page 161)
409. Phellan R and Forkert ND. Comparison of Vessel Enhancement Algorithms Applied to Time-of-Flight MRA Images for Cerebrovascular Segmentation. *Med Phys*. 2017 Nov; 44:5901–15. doi: [10.1002/mp.12560](https://doi.org/10.1002/mp.12560). [Accessed on: 2023 Jul 17] (cited on page 162)

410. Sato M, Bitter I, Bender M, Kaufman A, and Nakajima M. TEASAR: Tree-Structure Extraction Algorithm for Accurate and Robust Skeletons. *Proceedings the Eighth Pacific Conference on Computer Graphics and Applications*. The Eighth Pacific Conference on Computer Graphics and Applications. Hong Kong, China: IEEE Comput. Soc, 2000 :281–449. doi: [10.1109/PCCGA.2000.883951](https://doi.org/10.1109/PCCGA.2000.883951). [Accessed on: 2021 Jul 23] (cited on page 162)
411. Holroyd NA, Walsh CL, and Walker-Samuel S. tUbeNet. Version 1.0-alpha. 2023. [Accessed on: 2023 Jul 17] (cited on page 162)
412. Liu S, Grigoryan MM, Vasilevko V, Sumbria RK, Paganini-Hill A, Cribbs DH, and Fisher MJ. Comparative Analysis of H&E and Prussian Blue Staining in a Mouse Model of Cerebral Microbleeds. *J Histochem Cytochem*. 2014 Nov; 62:767–73. doi: [10.1369/0022155414546692](https://doi.org/10.1369/0022155414546692). [Accessed on: 2023 Jul 18] (cited on page 163)
413. Lo P, Crouzet C, Vasilevko V, and Choi B. Visualization of Microbleeds with Optical Histology in Mouse Model of Cerebral Amyloid Angiopathy. *Microvascular Research*. 2016 May; 105:109–13. doi: [10.1016/j.mvr.2016.02.002](https://doi.org/10.1016/j.mvr.2016.02.002). [Accessed on: 2023 Jul 18] (cited on page 163)
414. Johnson GA, Tian Y, Ashbrook DG, Cofer GP, Cook JJ, Gee JC, Hall A, Hornburg K, Kaczorowski CC, Qi Y, Yeh FC, Wang N, White LE, and Williams RW. Merged Magnetic Resonance and Light Sheet Microscopy of the Whole Mouse Brain. *Proc Natl Acad Sci USA*. 2023 Apr 25; 120:e2218617120. doi: [10.1073/pnas.2218617120](https://doi.org/10.1073/pnas.2218617120). [Accessed on: 2023 Jul 4] (cited on page 167)
415. Keszei AP, Berkels B, and Deserno TM. Survey of Non-Rigid Registration Tools in Medicine. *J Digit Imaging*. 2017 Feb; 30:102–16. doi: [10.1007/s10278-016-9915-8](https://doi.org/10.1007/s10278-016-9915-8). [Accessed on: 2023 Apr 20] (cited on page 167)
416. Karniadakis GE, Kevrekidis IG, Lu L, Perdikaris P, Wang S, and Yang L. Physics-Informed Machine Learning. *Nat Rev Phys*. 2021 May 24; 3:422–40. doi: [10.1038/s42254-021-00314-5](https://doi.org/10.1038/s42254-021-00314-5). [Accessed on: 2023 Jul 18] (cited on page 167)
417. Berg M, Holroyd N, Walsh C, West H, Walker-Samuel S, and Shipley R. Challenges and Opportunities of Integrating Imaging and Mathematical Modelling to Interrogate Biological Processes. *The International Journal of Biochemistry & Cell Biology*. 2022 May; 146:106195. doi: [10.1016/j.biocel.2022.106195](https://doi.org/10.1016/j.biocel.2022.106195). [Accessed on: 2023 Jul 18] (cited on page 168)
418. Könnecke M, Akeroyd FA, Bernstein HJ, Brewster AS, Campbell SI, Clausen B, Cottrell S, Hoffmann JU, Jemian PR, Männicke D, Osborn R, Peterson PF, Richter T, Suzuki J, Watts B, Wintersberger E, and Wuttke J. The NeXus Data Format. *J Appl Crystallogr*. 2015 Feb 1; 48:301–5. doi: [10.1107/S1600576714027575](https://doi.org/10.1107/S1600576714027575). [Accessed on: 2023 Jul 18] (cited on page 168)
419. Gorgolewski KJ, Auer T, Calhoun VD, Craddock RC, Das S, Duff EP, Flandin G, Ghosh SS, Glatard T, Halchenko YO, Handwerker DA, Hanke M, Keator D, Li X, Michael Z, Maumet C, Nichols BN, Nichols TE, Pellman J, Poline JB, Rokem A, Schaefer G, Sochat V, Triplett W, Turner JA, Varoquaux G, and Poldrack RA. The Brain Imaging Data Structure, a Format for Organizing and Describing Outputs of Neuroimaging

- Experiments. *Sci Data*. 2016 Jun 21; 3:160044. doi: [10.1038/sdata.2016.44](https://doi.org/10.1038/sdata.2016.44). [Accessed on: 2023 Jul 18] (cited on page 168)
420. Gorgolewski KJ, Alfaro-Almagro F, Auer T, Bellec P, Capotă M, Chakravarty MM, Churchill NW, Cohen AL, Craddock RC, Devenyi GA, Eklund A, Esteban O, Flandin G, Ghosh SS, Guntupalli JS, Jenkinson M, Keshavan A, Kiar G, Liem F, Raamana PR, Raffelt D, Steele CJ, Quirion PO, Smith RE, Strother SC, Varoquaux G, Wang Y, Yarkoni T, and Poldrack RA. BIDS Apps: Improving Ease of Use, Accessibility, and Reproducibility of Neuroimaging Data Analysis Methods. *PLoS Comput Biol*. 2017 Mar 9; 13. Ed. by Schneidman D:e1005209. doi: [10.1371/journal.pcbi.1005209](https://doi.org/10.1371/journal.pcbi.1005209). [Accessed on: 2023 Jul 18] (cited on page 168)
421. Dumot C, Po C, Capin L, Hubert V, Ong E, Chourrout M, Bolbos R, Amaz C, Auxenfans C, Canet-Soulas E, Rome C, Chauveau F, and Wiart M. Neurofunctional and Neuroimaging Readouts for Designing a Preclinical Stem-Cell Therapy Trial in Experimental Stroke. *Sci Rep*. 2022 Mar 18; 12:4700. doi: [10.1038/s41598-022-08713-z](https://doi.org/10.1038/s41598-022-08713-z) (cited on page 175)
422. Chourrout M. Brain Virtual Histology with X-ray Phase-Contrast Tomography. Parallel Session. European Molecular Imaging Meeting 2021 (Göttingen, Germany). 2021 Aug 26 (cited on page 177)
423. Chourrout M. Why Do We See Amyloid- $\beta$  Plaques in Phase-Contrast Imaging? Parallel Session. European Molecular Imaging Meeting 2022 (Thessaloniki, Greece). 2022 Mar 17 (cited on page 177)
424. Chourrout M. Virtual Histology of Brain Pathologies: Crucial Impact of Sample Preparation Techniques. Oral Presentation. World Molecular Imaging Congress 2022 (Miami, FL, USA). 2022 Oct 1 (cited on page 177)
425. Chourrout M. Why Do We See Amyloid- $\beta$  Plaques in Phase-Contrast Imaging? Oral Presentation. SOLEIL User Meeting 2023 (Saint-Aubin, France). 2023 Jan 20 (cited on page 177)
426. Chourrout M. Virtual Histology of Human Cerebral Amyloid Angiopathy. Study Group Meeting. European Molecular Imaging Meeting 2023 (Salzburg, Austria). 2023 Mar 14 (cited on page 177)



# Terms & Acronyms

## Numbers

**3xTg** a triple-transgenic mouse model of Alzheimer's disease (cf. <https://www.alzforum.org/research-models/3xtg>).

**5xFAD** a double-transgenic mouse model of Alzheimer's disease (cf. <https://www.alzforum.org/research-models/5xfad-b6sjl>).

## A

**A $\beta$**  amyloid- $\beta$ .

**A $\beta$ <sub>1-40</sub>** amyloid- $\beta$  peptide of 40 amino acids.

**A $\beta$ <sub>1-42</sub>** amyloid- $\beta$  peptide of 42 amino acids.

**AA** U.S. Alzheimer's Association.

**absorption index ( $\beta$ )** an index which describes absorption properties of an object for x-ray interactions.

**AD** Alzheimer's disease.

**ADAD** autosomal dominant form of AD.

**Al** aluminium.

**$\alpha$ -syn**  $\alpha$ -synuclein.

**ANSES** French Agency for Food, Environmental and Occupational Health & Safety.

**APOE** apolipoprotein E.

**APP** amyloid- $\beta$  precursor protein.

**APP/PS1** a double-transgenic mouse model of Alzheimer's disease (cf. <https://www.alzforum.org/research-models/appswepsen1de9-line-85>).

**APPPS1** a double-transgenic mouse model of Alzheimer's disease (cf. <https://www.alzforum.org/research-models/appps1>).

**ArcA $\beta$**  a mono-transgenic mouse model of Alzheimer's disease (cf. <https://www.alzforum.org/research-models/arcav>).

**ASL** arterial spin labelling.

## B

**BBB** blood-brain barrier.

**BIDS** Brain Imaging Data Structure.

**BM** bending magnet.

**BOLD** blood-oxygen-level-dependent imaging.

**BW** bandwidth.

## C

**Ca** calcium.

**CAA** cerebral amyloid angiopathy.

**carbon 11** (<sup>11</sup>C) a radioactive carbon atom with a half-life of 20 min.

**CBF** cerebral blood flow.

**CDT** clock-drawing test.

**celerity** (*c*) the speed of light and EM waves in a vacuum.

**CERAD** Consortium to Establish a Registry for Alzheimer's Disease.

**complex index of refraction** (*n*) an index which describes x-ray interactions with matter.

**CRCL** Cancer Research Center of Lyon.

**CSF** cerebrospinal fluid.

**CT** computed tomography.

**Cu** copper.

## D

**DCM** double-crystal monochromator.

**DMM** double-multilayer monochromator.

**DTI** diffusion tensor imaging.

## E

**EEG** electroencephalography.

**EM** electromagnetic.

**EOAD** early-onset Alzheimer's disease.

**EPVS** enlarged perivascular space.

**ESRF** European Synchrotron Radiation Facility.

## F

**FA** fractional anisotropy.

**FBP** filtered back projection.

**FDA** U.S. Food & Drug Agency.

**FDG** fluorodeoxyglucose.

**Fe** iron.

**fluorine 18** (<sup>18</sup>F) a radioactive fluorine atom with a half-life of 110 min.

**FOV** field of view.

**FTD** frontotemporal dementia.

**FTIR** Fourier-transform infrared spectroscopy.

## G

**Gd** gadolinium.

## H

**H&E** hematoxylin-eosin.

**HiP-CT** hierarchical phase-contrast tomography.

## I

**ICP-MS** induced coupled plasma mass spectroscopy.

**ID** insertion device.

**IHC** immunohistochemistry.

**index of refraction** ( $n$ ) an index which describes light interactions with matter in the ranges of infrared, visible light and ultraviolet.

## J

**J20** a mono-transgenic mouse model of Alzheimer's disease (cf. <https://www.alzforum.org/research-models/j20-pd-gf-appswind>).

## L

**LB** Lewy body.

**LBD** Lewy body dementia.

**linear attenuation coefficient** ( $\mu$ ) a coefficient for the Beer–Lambert law.

**LOAD** late-onset Alzheimer's disease.

**Lorentz factor** ( $\gamma$ ) a factor that represents the relativistic effects.

**LPC** lysophosphatidylcholine (a.k.a. lysolecithin).

**LSM** light-sheet (fluorescence) microscopy.

## M

**MAPT** microtubule-associated protein tau.

**MCI** mild cognitive impairment.

**MD** mean diffusivity.

**MEG** magnetoencephalography.

**ML** machine learning.

**MMSE** Mini-Mental State Examination.

**MoCA** Montreal Cognitive Assessment.

**MRI** magnetic resonance imaging.

## N

**NFT** neurofibrillary tangle.

**NIA** U.S. National Institute on Aging.

**NIST** U.S. National Institute of Standards and Technology.

**NP** nanoparticle / neuritic plaque.

## O

**OCT** optical coherence tomography.

## P

**PART** primary-age-related tauopathy.

**PD** Parkinson's disease.

**PET** positron emission tomography.

**PHF** paired helical filament.

**ppm** part per million, e.g.  $\mu\text{g g}^{-1}$ .

**PRR** pattern recognition receptor.

**PSAPP** a double-transgenic mouse model of Alzheimer's disease (cf. <https://www.alzforum.org/research-models/psapp>).

**PSEN1** presenilin 1.

**PSEN2** presenilin 2.

**P-tau** hyperphosphorylated tau protein.

## R

**Radon transform** ( $\mathcal{R}$ ) a mathematical operator which describes the transformation from a line integral to a projection.

**RD** radial diffusivity.

**refractive-index decrement** ( $\delta$ ) an index which describes phase-shift properties of an object for x-ray interactions.

**RF** radiofrequency.

**RI** Reagan Institute.

**ROI** region of interest.

**ROS** reactive oxygen species.

## S

**SOLEIL** French national synchrotron facility.

**SPECT** single-photon emission computed tomography.

**SR** synchrotron radiation.

**SRM** standard reference material.

**SUV** standardized uptake value.

**SUVR** standardized uptake value ratio.

## T

**tau** tau protein.

**TgF344** a double-transgenic rat model of Alzheimer's disease (cf. <https://www.alzforum.org/research-models/tgf344-ad>).

**TOMM40** a mitochondrial protein encoded by the gene *TOMM40*.

**TREM2** triggering receptor expressed on myeloid cells 2.

**TSPO** Translocator Protein 18kDa.

## U

**U-Net** a convolutional neural network for machine learning.

## W

**WMH** white matter hyperintensity.

## X

**XFEL** x-ray free-electron laser.

**XPCT** x-ray phase-contrast tomography.

**XRF** x-ray fluorescence microscopy.

**Z**

Z atomic number.

**Zn** zinc.

